Electronic ISSN: 1309-0267

I
J
E
A
S

International Journal of Engineering & Applied Sciences

IJEAS

Volume 9, Issue 2

Special Issue: "Composite Structures"

2017

Published by Akdeniz University

Abstracting & Indexing

CONTENTS

International Journal of Engineering & Applied Sciences (IJEAS)
Vol.9, Issue 2 (Special Issue: Composite Structures) (2017) 1-21
http://dx.doi.org/10.24107/ijeas.304376
Int J Eng Appl Sci 9(2) (2017) 1-21

Finite Elements Based on Strong and Weak Formulations for Structural Mechanics: Stability, Accuracy and Reliability

†Francesco Tornabene[1], Nicholas Fantuzzi[1], and Michele Bacciocchi[1]

[1]DICAM - Department, University of Bologna, Viale del Risorgimento 2, 40136 Bologna, Italy
†E-mail address: francesco.tornabene@unibo.it

Received date: April 2017

Abstract

The authors are presenting a novel formulation based on the Differential Quadrature (DQ) method which is used to approximate derivatives and integrals. The resulting scheme has been termed strong and weak form finite elements (SFEM or WFEM), according to the numerical scheme employed in the computation. Such numerical methods are applied to solve some structural problems related to the mechanical behavior of plates and shells, made of isotropic or composite materials.

The main differences between these two approaches rely on the initial formulation – which is strong or weak (variational) – and the implementation of the boundary conditions, that for the former include the continuity of stresses and displacements, whereas in the latter can consider the continuity of the displacements or both.

The two methodologies consider also a mapping technique to transform an element of general shape described in Cartesian coordinates into the same element in the computational space. Such technique can be implemented by employing the classic Lagrangian-shaped elements with a fixed number of nodes along the element edges or blending functions which allow an "exact mapping" of the element. In particular, the authors are employing NURBS (Not-Uniform Rational B-Splines) for such nonlinear mapping in order to use the "exact" shape of CAD designs.

Keywords: Structural analysis, Numerical methods, Strong formulation finite element method, Weak formulation finite element method, Differential and integral quadrature, Numerical stability and accuracy

1. Introduction

It is well-known that a physical phenomenon can be modeled by a system of differential equations, which are obtained once the proper hypotheses are introduced [1]-[4]. The solution of these complex differential equations cannot be reached analytically, thus a numerical method is needed for this purpose. This statement is especially true when a structural problem is taken into account, such as the vibrational or static behavior of laminated composite structures.

With reference to the papers by Tornabene et al. [5][6], it should be noted that the numerical approaches that can be employed in these circumstances are categorized according to the formulation. In general, the solution of problem governed by a set of differential equations can be achieved by solving the strong or the weak form of the equations in hand. The governing equations are changed directly into a discrete system if the strong formulation is considered, since a numerical technique is introduced to approximate the derivatives. To this aim, different techniques can be used, such as some spectral methods for instance [7]-[9]. Among them, the Differential Quadrature (DQ) method should be mentioned due to its versatility and accuracy features [10]-[13]. A more stable and reliable approach was developed by Shu [14], and it is known in the literature as Generalized Differential Quadrature (GDQ) method. In this paper, only the main aspects of the DQ and GDQ techniques are presented. For the sake of completeness, the reader can find a more complete treatise about these methods in the review paper by Tornabene et al. [5].

On the other hand, the main aim of solving the weak formulation is to obtain an equivalent form of the governing equations by introducing a weighted-integral statement, which allows to reduce (or weaken) the order of differentiability of the differential equations. For this purpose, a numerical method able to compute integrals must be used. In the present paper, the Generalized Integral Quadrature (GIQ) is introduced to this aim [5][14]. Nevertheless, it should be mentioned that different weak form-based methods can be employed, as illustrated in the book by Reddy [4]. For the sake of completeness, it should be recalled that the weak form of the governing equations is solved also in the well-known Finite Element (FE) method [4][15].

In general, many practical applications require that the reference domain in which the governing equations are written is subdivided into several subdomains (or finite elements), due to the presence of geometric and mechanical discontinuities. At this point, a peculiar mapping technique can be developed to deal with arbitrarily shaped elements. Different approaches can be introduced for this purpose [16][17]. Recently, the theoretical framework provided by the Isogeometric Analysis (IGA) appears to be one of the most exploited approaches to study geometries with arbitrary edges [18][19]. Indeed, the use of blending functions based on NURBS (Non-Uniform Rational B-Splines) curves facilitates the analysis of generic domains. Both the domain decomposition and the mapping procedure are broadly used in classic FE method. Nevertheless, the same processes can be employed also when the strong form of the governing equations is considered [20]-[25]. The authors employ the names Strong Formulation Finite Element Method (SFEM) and Weak Formulation Finite Element Method (WFEM) to classify two different approaches based on the strong and weak forms of the governing equations, respectively.

In this paper, the accuracy, reliability and stability characteristics of SFEM and WFEM are discussed and compared by means of some numerical examples related to structural problems. A brief theoretical treatise is also presented for the sake of completeness. Further details concerning the structural models, as well as the governing equations, can be found in the works [26]-[30].

2. Numerical methods

The main aspects of the numerical methods used in the computations are presented briefly in this section. In particular, the fundamentals of DQ are introduced firstly. Then, the corresponding technique used to approximate integrals is illustrated starting from the concepts employed for the numerical evaluation of derivatives.

Approximation of derivatives

The derivative of a generic function can be approximated numerically by means of the DQ method. The key points of this technique are the evaluation of the weighting coefficients and the choice of a discrete distribution of grid points within the reference domain. Let us consider a one-dimensional function $f(x)$ defined in the closed interval $[a,b]$. Such domain must be preventively discretized by placing I_N discrete grid points $x_k \in [a,b]$, according to the following relation

$$x_k = \frac{b-a}{d-c}(\zeta_k - c) + a \tag{1}$$

for $k = 1, 2, ..., I_N$, where $\zeta_k \in [c,d]$ denotes the points of a generic distributions. The most typical grid employed in many engineering problems are listed in Table 1, assuming

$$\zeta_k = \frac{r_k - r_1}{r_N - r_1} \tag{2}$$

where not specified. On the other hand, the basis polynomials required to evaluate the corresponding distribution will be indicated in the following. A more complete list of discrete grid distributions is presented in the books [31][32] and in the review paper by Tornabene et al. [5].

It should be recalled that a smooth function $f(x)$ can be approximated by a set of basis functions $\psi_j(x)$, for $j = 1, 2, ..., I_N$. From the mathematical point of view, one gets

$$f(x) \cong \sum_{j=1}^{I_N} \lambda_j \psi_j(x) \tag{3}$$

in which λ_j are unknown coefficients. By using a compact matrix form, Eq. (3) can be written as follows

$$\mathbf{f} = \mathbf{A}\boldsymbol{\lambda} \tag{4}$$

where $\mathbf{f}$ represents the vector of the values that the function assumes in each grid point, whereas the vector $\boldsymbol{\lambda}$ collects the terms λ_j. On the other hand, $\mathbf{A}$ is the coefficient matrix, whose elements are given by $A_{ij} = \psi_j(x_i)$, for $i, j = 1, 2, ..., I_N$. Since the unknown parameters λ_j do not depend on x, the n-th order derivative of $f(x)$ can be computed as

$$\frac{d^n f(x)}{dx^n} = \sum_{j=1}^{I_N} \lambda_j \frac{d^n \psi_j(x)}{dx^n} \tag{5}$$

for $n = 1, 2, ..., I_N - 1$. Analogously, a compact matrix form can be conveniently used

$$\mathbf{f}^{(n)} = \mathbf{A}^{(n)}\boldsymbol{\lambda} \tag{6}$$

where $\mathbf{f}^{(n)}$ collects the values of the n-th order derivatives computed at each grid point. The coefficients of the matrix $\mathbf{A}^{(n)}$ are clearly given by

$$A_{ij}^{(n)} = \left. \frac{d^n \psi_j(x)}{dx^n} \right|_{x_i} \tag{7}$$

for $i, j = 1, 2, ..., I_N$. Having in mind Eq. (4), the unknown vector $\boldsymbol{\lambda}$ can be computed as

$$\boldsymbol{\lambda} = \mathbf{A}^{-1}\mathbf{f} \tag{8}$$

Table 1. Grid point distributions. The symbol $\boldsymbol{N}$ denotes the total number of points

Unifor (Unif)	Chebyshev-Gauss-Lobatto (Cheb-Gau-Lob)
$\zeta_k = \frac{k-1}{N-1}, \ k = 1,2,...,N$	$r_k = \cos\left(\frac{N-k}{N-1}\pi\right), \ k = 1,2,...,N, \ r \in [-1,1]$
Quadratic (Quad)	Chebyshev I kind (Cheb I)
$\begin{cases} \zeta_k = 2\left(\frac{k-1}{N-1}\right)^2, \ k = 1,2,...,\frac{N+1}{2} \\ \zeta_k = -2\left(\frac{k-1}{N-1}\right)^2 + 4\left(\frac{k-1}{N-1}\right) - 1, \ k = \frac{N+1}{2}+1,...,N-1,N \end{cases}$	$r_k = \cos\left(\frac{2(N-k)+1}{2N}\pi\right), \ k = 1,2,...,N, \ r \in [-1,1]$
Chebyshev II kind (Cheb II)	Approximate Legendre (App Leg)
$r_k = \cos\left(\frac{N-k+1}{N+1}\pi\right), \ k = 1,2,...,N, \ r \in [-1,1]$	$r_k = \left(1 - \frac{1}{8N^2} + \frac{1}{8N^3}\right)\cos\left(\frac{4(N-k)+3}{4N+2}\pi\right),$ $k = 1,2,...,N, \ r \in [-1,1]$
Legendre-Gauss (Leg-Gau)	Radau I kind (Rad I)
$r_k =$ roots of $(1-r^2)L_{N-1}(r), \ k = 1,2,...,N, \ r \in [-1,1]$	$r_k =$ roots of $(1-r)\left(L_N(-r) + L_{N-1}(-r)\right),$ $k = 1,2,...,N, \ r \in [-1,1]$
Chebyshev-Gauss (Cheb-Gau)	Legendre-Gauss-Lobatto (Leg-Gau-Lob)
$r_1 = -1, \ r_N = 1, \ r_k = \cos\left(\frac{2(N-k)-1}{2(N-2)}\pi\right),$ $k = 2,3,...,N-1, \ r \in [-1,1]$	$r_k =$ roots of $(1-r^2)A_{N-1}(r), \ k = 1,2,...,N, \ r \in [-1,1]$
Hermite (Her)	Laguerre (Lague)
$r_k =$ roots of $H_{N+1}(r), \ k = 1,2,...,N \ r \in]-\infty, +\infty[$	$r_k =$ roots of $G_{N+1}(r), \ k = 1,2,...,N, \ r \in [0, +\infty[$
Chebyshev-Gauss-Radau (Cheb-Gau-Rad)	Non uniform Ding (Ding)
$r_k = \cos\left(\frac{2(N-k)}{2N-1}\pi\right), \quad k = 1,2,...,N, \quad r \in [-1,1]$	$\zeta_k = \frac{1}{2}\left(1 - \sqrt{2}\cos\left(\frac{\pi}{4} + \frac{\pi}{2}\frac{k-1}{N-1}\right)\right), \ k = 1,2,...,N$
Legendre (Leg)	Chebyshev III kind (Cheb III)
$r_k =$ roots of $L_{N+1}(r), \ k = 1,2,...,N, \ r \in [-1,1]$	$r_k = \cos\left(\frac{2(N-k)+1}{2N+1}\pi\right), \ k = 1,2,...,N, \ r \in [-1,1]$
Chebyshev IV kind (Cheb IV)	Lobatto (Lob)
$r_k = \cos\left(\frac{2(N-k+1)}{2N+1}\pi\right), \ k = 1,2,...,N, \ r \in [-1,1]$	$r_k =$ roots of $A_{N+1}(r), \ k = 1,2,...,N, \ r \in [-1,1]$
Legendre-Gauss-Radau (Leg-Gau-Rad)	Radau II kind (Rad II)
$r_k =$ roots of $L_{N+1}(r) + L_N(r), \ k = 1,2,...,N, \ r \in [-1,1]$	$r_k =$ roots of $(1-r)\left(L_N(r) + L_{N-1}(r)\right),$ $k = 1,2,...,N, \ r \in [-1,1]$
Jacobi (Jac)	Jacobi-Gauss (Jac-Gau)
$r_k =$ roots of $J_{N-1}^{(\gamma,\delta)}(r), \ k = 1,2,...,N \ r \in [-1,1]$	$r_k =$ roots of $(1-r^2)J_{N-1}^{(\gamma,\delta)}(r), \ k = 1,2,...,N, \ r \in [-1,1]$

Thus, Eq. (8) allows to write the following definition

$$\mathbf{f}^{(n)} = \mathbf{A}^{(n)}\mathbf{A}^{-1}\mathbf{f} \tag{9}$$

According to the differentiation matrix procedure provided by the DQ method, the n-th order derivatives are given by

$$\mathbf{f}^{(n)} = \mathbf{D}^{(n)}\mathbf{f} \tag{10}$$

in which $\mathbf{D}^{(n)}$ is the matrix that collects the so called weighting coefficients for the derivation. By comparing Eq. (9) and Eq. (10), it is evident that

$$\mathbf{D}^{(n)} = \mathbf{A}^{(n)}\mathbf{A}^{-1} \tag{11}$$

Therefore, it should be noted that the differentiation matrix $\mathbf{D}^{(n)}$ can be computed as the matrix product between the matrix $\mathbf{A}^{(n)}$ that collects the n-th order derivatives of the chosen basis functions at each discrete point of the domain and the inverse matrix of the operator $\mathbf{A}$ that includes the values that the basis functions assume in every grid point. For completeness purpose, some of the basis functions that can be used for this purpose are listed in Table 2.
As highlighted in the review paper by Tornabene et al. [5], it is possible also to employ the well-known Radial Basis Functions (RBFs) for the functional approximation. Analogously, the same approximation can be achieved through the so-called Moving Least Squares (MLS) method [5]. For the sake of clarity, Eq. (10) assumes the following aspect

$$\left.\frac{d^n f(x)}{dx^n}\right|_{x_i} = \sum_{j=1}^{I_N} D_{ij}^{(n)} f(x_j) \tag{12}$$

for $i = 1, 2, ..., I_N$, where $D_{ij}^{(n)}$ denotes the elements collected in the differentiation matrix. It should be noted that Eq. (12) is analogous to the definition of numerical derivative provided by the Generalized Differential Quadrature (GDQ) method

$$\left.\frac{d^n f(x)}{dx^n}\right|_{x_i} = \sum_{j=1}^{I_N} \varsigma_{ij}^{(n)} f(x_j) \tag{13}$$

where $\varsigma_{ij}^{(n)}$ are the weighting coefficients that can be collected in the corresponding matrix $\boldsymbol{\varsigma}^{(n)}$, so that one gets

$$\mathbf{f}^{(n)} = \boldsymbol{\varsigma}^{(n)}\mathbf{f} \tag{14}$$

Eq. (14) is equivalent to the definition shown in Eq. (10). The coefficients $\varsigma_{ij}^{(n)}$ can be computed by means of the recursive expressions provided by Shu [5], whereas a matrix multiplication and an inversion of a matrix are required to evaluate $D_{ij}^{(n)}$. It should be highlighted that the matrix $\mathbf{A}$ could become ill-conditioned if the number of grid points I_N is increased, since it appears to be similar to the well-known Vandermonde matrix. It is proven that this problem happens for $I_N > 13$. It should be observed anyway that the number of discrete points is low when the reference domain is subdivided into finite elements, since the unknown field is well-approximated by using lower-order basis functions. However, the choice of particular basis functions such as Lagrange polynomials, Lagrange trigonometric polynomials, or the Sinc function, allows to overcome this issue since the coefficient matrix is equal to the corresponding identity matrix (in other words, one gets $\mathbf{A}=\mathbf{I}$). Thus, when the solution is obtained by using a single element, the unknown field requires higher-order basis functions for its approximation. Consequently, the numerical problems related to the ill-conditioned matrix can be avoided by choosing the aforementioned basis functions.

Table 2. Basis function employed for the functional approximation

Lagrange polynomials	Lagrange trigonometric polynomials
$\psi_j = l_j(r) = \dfrac{\mathcal{L}(r)}{(r-r_j)L^{(1)}(r_j)}$, $r \in]-\infty,+\infty[$, $j=1,2,...,N$ $\mathcal{L}(r)=\prod_{k=1}^{N}(r-r_k)$, $\mathcal{L}^{(1)}(r_j)=\prod_{k=1,\, j\neq k}^{N}(r_j-r_k)$	$\psi_j = g_j(r) = \dfrac{G(r)}{\sin\left(\frac{r-r_j}{2}\right)S^{(1)}(r_j)}$, $r\in[0,2\pi]$, $j=1,2,...,N$ $G(r)=\prod_{k=1}^{N}\sin\left(\frac{r-r_k}{2}\right)$, $G^{(1)}(r_j)=\prod_{k=1,\, j\neq k}^{N}\sin\left(\frac{r_j-r_k}{2}\right)$
Bernstein polynomials	**Lobatto polynomials**
$\psi_j = B_j(r) = \dfrac{(N-1)!}{(j-1)!(N-j)!}r^{j-1}(1-r)^{N-j}$ $r\in[0,1]$, $j=1,2,...,N$	$\psi_j = A_j(r) = \dfrac{d}{dr}\left(L_{j+1}(r)\right)$, $r\in[-1,1]$, $j=1,2,...,N$
Exponential functions	**Monomial polynomials**
$\psi_j = E_j(r) = e^{(j-1)r}$, $r\in]-\infty,+\infty[$, $j=1,2,...,N$	$\psi_j = Z_j(r) = r^{j-1}$, $r\in]-\infty,+\infty[$, $j=1,2,...,N$
Bessel polynomials	**Sinc functions**
$\psi_1 = P_1(r)=1$, $\psi_j = P_j(r) = \sum_{k=0}^{j-1}\dfrac{(j-1+k)!}{(j-1-k)!k!}\left(\dfrac{r}{2}\right)^k$, $r\in[-\infty,+\infty]$, $j=2,3,...,N$	$\psi_j = S_j = \mathrm{Sinc}_j(r) = \dfrac{\sin\left(\pi(N-1)(r-r_j)\right)}{\pi(N-1)(r-r_j)}$ $r\in[0,1]$, $j=1,2,...,N$
Fourier functions	**Boubaker polynomials**
$\psi_1 = F_1(r)=1$, $\psi_j = F_j(r)=\cos\left(\dfrac{j}{2}r\right)$ for j even $\psi_j = F_j(r)=\sin\left(\dfrac{j-1}{2}r\right)$ for j odd $r\in[0,2\pi]$, $j=2,3,...,N$	$\psi_1 = Q_1(r)=1$, $r\in[-\infty,+\infty]$, $j=2,3,...,N$ $\psi_j = Q_j(r) = \sum_{k=0}^{\phi(j-1)}(-1)^k\binom{j-1-k}{k}\dfrac{j-1-4k}{j-1-k}r^{j-1-2k}$ $\phi(j-1)=\dfrac{2(j-1)+\left((-1)^{j-1}-1\right)}{4}$
Jacobi Polynomials	**Legendre polynomials**
$\psi_j = J_j^{(\gamma,\delta)}(r) = \dfrac{(-1)^{j-1}}{2^{j-1}(j-1)!(1-r)^{\gamma}(1+r)^{\delta}}\dfrac{d^{j-1}}{dr^{j-1}}\left((1-r)^{j-1+\gamma}(1+r)^{j-1+\delta}\right)$ $r\in[-1,1]$, $j=1,2,...,N$, $\gamma,\delta>-1$	$\psi_j = L_j(r) = \dfrac{(-1)^{j-1}}{2^{j-1}(j-1)!}\dfrac{d^{j-1}}{dr^{j-1}}\left((1-r^2)^{j-1}\right)$ $r\in[-1,1]$ $j=1,2,...,N$
Chebyshev polynomials (I kind)	**Chebyshev polynomials (II kind)**
$\psi_j = T_j(r) = \cos\left((j-1)\arccos(r)\right)$, $r\in[-1,1]$, $j=1,2,...,N$	$\psi_j = U_j(r) = \dfrac{\sin\left(j\arccos(r)\right)}{\sin\left(\arccos(r)\right)}$, $r\in[-1,1]$, $j=1,2,...,N$
Chebyshev polynomials (III kind)	**Chebyshev polynomials (IV kind)**
$\psi_j = V_j(r) = \dfrac{\cos\left(\frac{(2j-1)\arccos(r)}{2}\right)}{\cos\left(\frac{\arccos(r)}{2}\right)}$, $r\in[-1,1]$, $j=1,2,...,N$	$\psi_j = W_j(r) = \dfrac{\sin\left(\frac{(2j-1)\arccos(r)}{2}\right)}{\sin\left(\frac{\arccos(r)}{2}\right)}$, $r\in[-1,1]$, $j=1,2,...,N$
Laguerre polynomials	**Hermite polynomials**
$\psi_j = G_j(r) = \dfrac{1}{(j-1)!e^{-r}}\dfrac{d^{j-1}}{dr^{j-1}}\left(r^{j-1}e^{-r}\right)$, $r\in[0,+\infty[$, $j=1,2,...,N$	$\psi_j = H_j(r) = (-1)^{j-1}e^{r^2}\dfrac{d^{j-1}}{dr^{j-1}}\left(e^{-r^2}\right)$, $r\in]-\infty,+\infty[$, $j=1,2,...,N$

For the sake of completeness, it should be noted that the following linear coordinate transformation is required to define the weighting coefficients in the physical domain

$$\varsigma_{ij}^{(n)} = \left(\frac{r_N - r_1}{x_N - x_1} \right)^n \tilde{\varsigma}_{ij}^{(n)} \tag{15}$$

for $i, j = 1, 2, \ldots, I_N$ and $n = 1, 2, \ldots, I_N - 1$, where $\varsigma_{ij}^{(n)}$ are the weighting coefficients related to the physical domain, whereas $\tilde{\varsigma}_{ij}^{(n)}$ are the ones computed in the definition domain. The values of r_1, r_N can be found using the expressions shown in Table 1.

This approach can be easily extended to two-dimensional domains, such as the ones that characterize the structural problem of plates and shells. Firstly, the reference domain must be discretized by placing I_N, I_M grid points along the two principal directions, respectively. Then, the same procedure illustrated above should be used to obtain the weighting coefficients for the numerical derivatives along both the main coordinates of the domain x, y. In this circumstance, a two-dimensional function $f(x, y)$ is considered. In order to facilitate the implementation of the technique in hand, the values that this function assumes in each discrete point of the domain can be conveniently collected according to the following scheme

$$\begin{aligned} \mathbf{f} = \Big[& \underbrace{f(x_1, y_1)_1 \quad f(x_2, y_1)_2 \quad \cdots \quad f(x_{I_N}, y_1)_{I_N}}_{\text{first column}} \cdots\cdots \\ & \cdots\cdots \underbrace{f(x_1, y_2)_{I_N+1} \quad \cdots \quad f(x_{I_N}, y_2)_{2I_N}}_{\text{second column}} \cdots\cdots \\ & \cdots\cdots \underbrace{f(x_1, y_{I_M})_{I_N \cdot I_M - I_N + 1} \quad \cdots \quad f(x_{I_N}, y_{I_M})_{I_N \cdot I_M}}_{\text{last column}} \Big]^T \end{aligned} \tag{16}$$

in which $f_k = f(x_i, y_j)_k$, for $i = 1, 2, ..., I_N$ and $j = 1, 2, ..., I_M$. For the sake of clarity, this aspect is depicted graphically in the scheme of Figure 1.

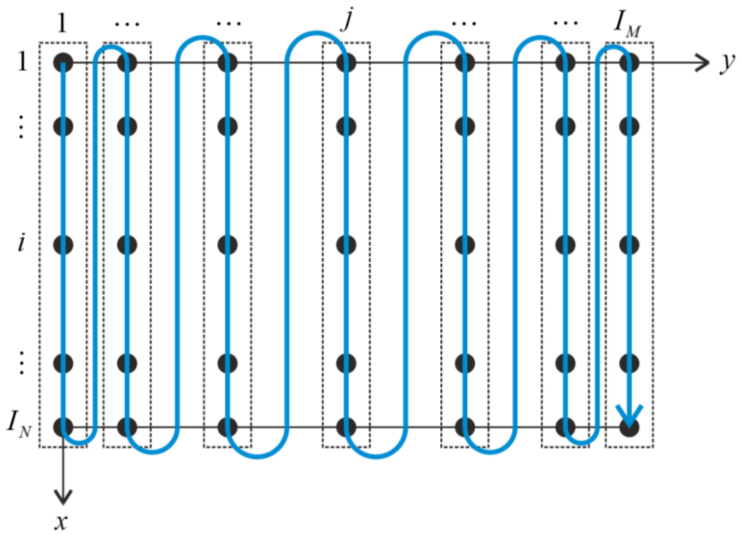

Fig. 1. DQ implementation for a two-dimensional domain

The weighting coefficients can be computed by using the Kronecker product $\otimes$ as follows

$$\underset{(I_N \cdot I_M)\times(I_N \cdot I_M)}{\mathbf{C}_x^{(n)}} = \underset{I_M \times I_M}{\mathbf{I}} \otimes \underset{I_N \times I_N}{\mathbf{D}_x^{(n)}} \tag{17}$$

$$\underset{(I_N \cdot I_M)\times(I_N \cdot I_M)}{\mathbf{C}_y^{(m)}} = \underset{I_M \times I_M}{\mathbf{D}_y^{(m)}} \otimes \underset{I_N \times I_N}{\mathbf{I}} \tag{18}$$

$$\underset{(I_N \cdot I_M)\times(I_N \cdot I_M)}{\mathbf{C}_{xy}^{(n+m)}} = \underset{I_M \times I_M}{\mathbf{D}_y^{(m)}} \otimes \underset{I_N \cdot I_N}{\mathbf{D}_x^{(n)}} \tag{19}$$

in which $\mathbf{I}$ represents the identity matrix, whereas $\mathbf{D}_x^{(n)}, \mathbf{D}_y^{(m)}$ collect the weighting coefficients along the two principal coordinates, which can be evaluated as shown above. The size of every operator is indicated under the corresponding matrix for the sake of completeness. Once the weighting coefficients related to the current scheme are computed and collected in the corresponding matrices $\mathbf{C}_x^{(n)}, \mathbf{C}_y^{(m)}, \mathbf{C}_{xy}^{(n+m)}$, the derivatives of the considered function are given by the following matrix products

$$\mathbf{f}_x^{(n)} = \mathbf{C}_x^{(n)} \mathbf{f} \tag{20}$$

$$\mathbf{f}_y^{(m)} = \mathbf{C}_y^{(m)} \mathbf{f} \tag{21}$$

$$\mathbf{f}_{xy}^{(n+m)} = \mathbf{C}_{xy}^{(n+m)} \mathbf{f} \tag{22}$$

In particular, $\mathbf{f}_x^{(n)}$ collects the n-th order derivatives with respect to x, $\mathbf{f}_y^{(m)}$ is the vector of the m-th order derivatives with respect to y, whereas $\mathbf{f}_{xy}^{(n+m)}$ represents $(n+m)$-th order mixed derivatives. The size of all these vectors, as well as of $\mathbf{f}$, is given by $(I_N \cdot I_M)\times 1$.

At this point, it should be mentioned that the present approach is used to obtain and solve the strong form of the governing equations. If a subdivision of the reference domain into finite elements is required, the technique is termed Strong Formulation Finite Element Method (SFEM). It is clear that the vector $\mathbf{f}$ denotes the unknown field of the partial differential equations of the fundamental system, which is transformed directly into a system of discrete equations by means of the DQ method.

Approximation of integrals

Starting from the ideas and definitions illustrated for the numerical evaluation of derivatives, a numerical scheme for the computation of integrals can be developed. In this section, the main aspects of this integral quadrature are presented briefly. Since the Lagrange polynomials are used as basis functions for the functional approximation, the technique at issue is known in the literature as Generalized Integral Quadrature (GIQ). Nevertheless, it should be recalled that different basis functions can be chosen for the same purpose.

Let us consider the same one-dimensional function $f(x)$ defined in the closed interval $[a,b]$ introduced in the previous section. As shown in Eq. (1), the reference domain is discretized so that one gets $x_k \in [a,b]$. All the grid distributions listed in Table 1 could be employed. By definition, the integral of $f(x)$ within the closed interval $[x_i, x_j]$, with $x_i, x_j \in [a,b]$, can be approximated as follows

$$\int_{x_i}^{x_j} f(x)\,dx = \sum_{k=1}^{I_N} w_k^{ij} f(x_k) \tag{23}$$

where I_N denotes the total number of discrete points, whereas w_k^{ij} are the weighting coefficients for the integration. It should be noted that the numerical integration in Eq. (23) requires to consider all the sampling points of the domain independently from the integration limits. Eq. (23) becomes a conventional integral for $x_i = a$ and $x_j = b$. In order to evaluate the weighting coefficients, the following quantities must be introduced

$$\begin{aligned} \bar{\varsigma}_{ij}^{(1)} &= \frac{x_i - c}{x_j - c} \varsigma_{ij}^{(1)} \quad \text{for } i \neq j \\ \bar{\varsigma}_{ij}^{(1)} &= \varsigma_{ii}^{(1)} + \frac{1}{x_i - c} \quad \text{for } i = j \end{aligned} \tag{24}$$

for $i = 1, 2, ..., I_N$. It is clear that $\varsigma_{ij}^{(1)}$ stands for the weighting coefficients for the first-order derivatives, computable through the recursive formulae provided by Shu as explained in the previous section. The arbitrary constant c should be set equal to $c = b + 10^{-10}$ to guarantee the accuracy and stability of the numerical solution. The coefficients introduced in Eq. (24) can be collected in the corresponding matrix $\bar{\boldsymbol{\varsigma}}^{(1)}$ of size $I_N \times I_N$. At this point, this last matrix must be inverted as follows to obtain the matrix of the weighting coefficients for the integration

$$\mathbf{W} = \left(\bar{\boldsymbol{\varsigma}}^{(1)}\right)^{-1} \tag{25}$$

A generic term of $\mathbf{W}$ is specified by the notation w_{ij}, for $i, j = 1, 2, ..., I_N$. Finally, the weighting coefficients w_k^{ij} needed in Eq. (23) are given by

$$w_k^{ij} = w_{jk} - w_{ik} \tag{26}$$

for $k = 1, 2, ..., I_N$. These I_N coefficients can be conveniently collected in a row vector $\mathbf{W}_x$, whose size is $1 \times I_N$. In compact matrix form, the numerical integral I is computed as a vector product

$$I = \mathbf{W}_x \mathbf{f} \tag{27}$$

If the integration limits are set equal to $x_i = a$ and $x_j = b$, or in other words $x_i = x_1$ and $x_j = x_{I_N}$, the numerical integration can be performed by using the weighting coefficients $w_k^{1I_N}$, which are defined as follows

$$w_k^{1I_N} = w_{I_N k} - w_{1k} \tag{28}$$

A transformation of these weighting coefficients must be performed to switch from the reference interval $[\alpha, \beta]$ to a generic one $[a, b]$. The weighting coefficients $w_k^{1I_N}$ in the physical interval $[a, b]$ are given by

$$w_k^{1I_N} = \frac{b - a}{\beta - \alpha} \tilde{w}_k^{1I_N} \tag{29}$$

where $\tilde{w}_k^{1I_N}$ represents the weighting coefficients related to the shifted interval $[\alpha, \beta]$. It is important to underline that this approach can be applied without any restriction on the grid point distributions employed to discretize the reference domain.

As shown above, the two-dimensional counterpart can be easily deducted. Let us consider a generic smooth function $f(x, y)$ defined in a two-dimensional domain, where the main coordinates x, y are given by $x \in [a, b]$ and $y \in [c, d]$. The numerical integral performed in the whole domain is defined as follows

$$\int_c^d \int_a^b f(x, y)\, dx dy = \sum_{i=1}^{I_N} \sum_{j=1}^{I_M} w_i^{1I_N} w_j^{1I_M} f(x_i, y_j) \tag{30}$$

in which the weighting coefficients $w_i^{1I_N}, w_j^{1I_M}$ can be evaluated by applying the same procedure just illustrated along the two principal coordinates. In order to facilitate the implementation process, these coefficients can be collected in the corresponding vectors denoted by $\mathbf{W}_x, \mathbf{W}_y$, respectively. Even in this circumstance, the same scheme used before to order the grid points should be used (Figure 1). By using the Kronecker product, the vector of the weighting coefficients for the two-dimensional integration is obtained

$$\underset{1\times(I_N \cdot I_M)}{\mathbf{W}_{xy}} = \underset{1\times I_M}{\mathbf{W}_y} \otimes \underset{1\times I_N}{\mathbf{W}_x} \tag{31}$$

A simple matrix product is required to evaluate the numerical integration shown in Eq. (30). Analogously to the one-dimensional scheme, the integral I is given by

$$I = \mathbf{W}_{xy}\mathbf{f} \tag{32}$$

where $\mathbf{f}$ assumes the meaning shown in Eq. (16). The current approach is employed to obtain and solve the weak form of the governing equations. When the reference domain is decomposed into finite elements, the technique in hand is named Weak Formulation Finite Element Method (WFEM).

3. Applications

In this section, some applications related to the structural analysis of plates and shells are presented. Both the strong and weak formulations are employed and the numerical results are obtained by using different basis functions and grid distributions.

Isotropic plates

The numerical tests shown in this paragraph are related to the convergence analysis of simply-supported plates in terms of the first circular frequency ω_1. The reference solution ω_{1ex} for this structure is shown in the review paper by Tornabene et al. [5]. The square plates of side $L = 1\text{m}$ and thickness $h = 0.1\text{m}$ are made of isotropic material ($E = 70\,\text{GPa}$, $\nu = 0.3$, $\rho = 2707\,\text{kg/m}^3$). In the first applications, the two formulations are employed by varying grid distributions and basis functions in the theoretical framework provided by the Reissner-Mindlin theory, increasing the number of grid points $I_N = I_M = N$. The structural model is composed by a sole element due to its regular shape. Figure 2 and Figure 3 show the convergence analyses for the weak and strong formulations, respectively. It is easy to note that some grid distributions do not provide accurate results. This aspect is even more evident for the strong formulation (Figure 3). In general, the solutions converge by using a reduced number of points ($N = 11 \div 15$). On the other hand, the MLS method gives inaccurate results, especially for the weak form. For this technique, the Gaussian quadric function is used as basis function.

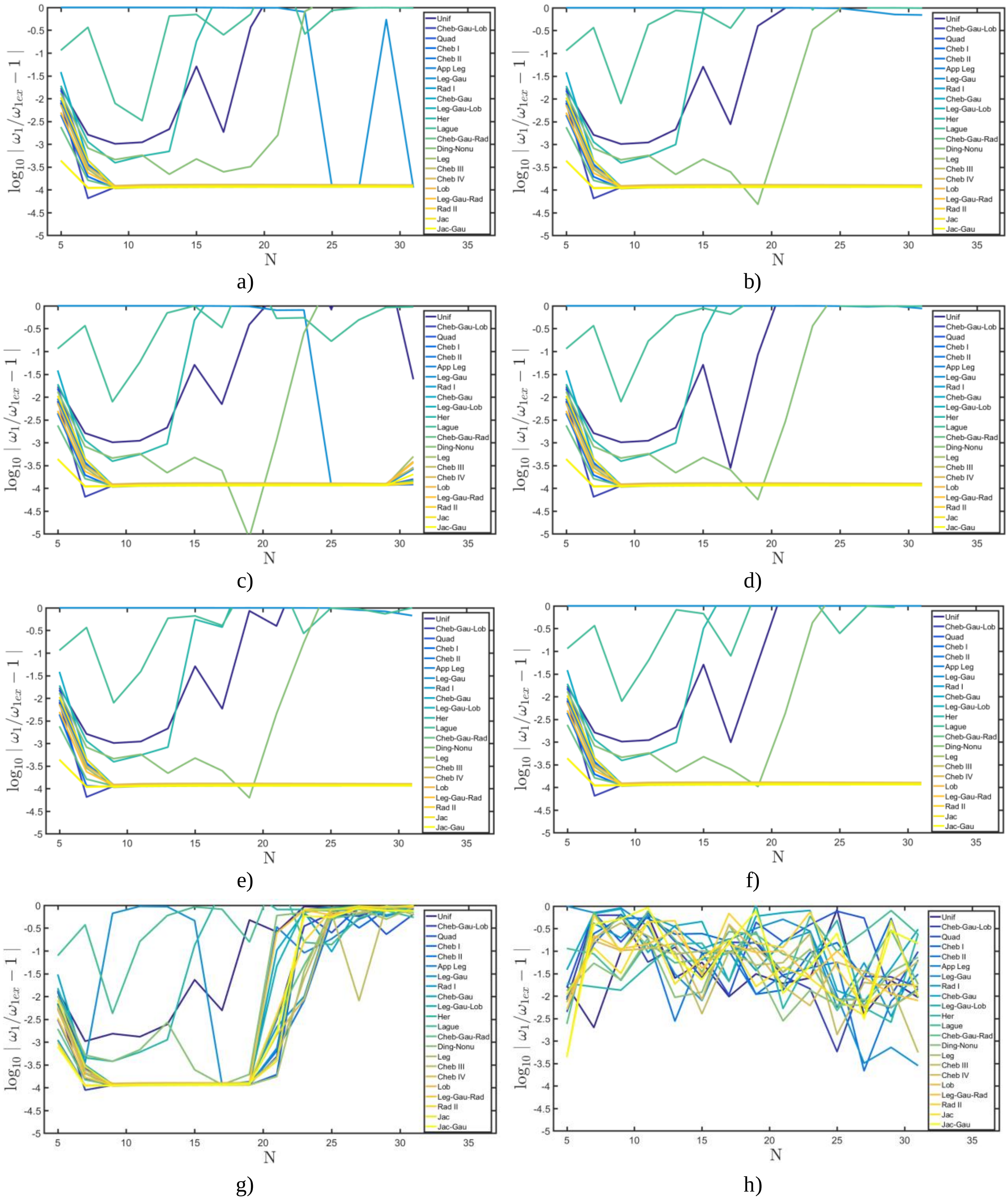

Fig. 2. Relative error for the first frequency of a simply-supported square plate. The weak formulation is employed considering different basis functions: a) Bernstein polynomials; b) Bessel polynomials; c) Boubaker polynomials; d) Chebyshev (I kind) polynomials; e) Exponential functions; f) Lagrange polynomials; g) Fourier basis functions; h) MLS method (Gaussian quadric basis functions)

A second set of convergence analyses is performed considering an isotropic rectangular plate ($L_x = 2\,\text{m}$, $L_y = 1.5\,\text{m}$, $h = 0.1\,\text{m}$) characterized by the same mechanical properties and boundary conditions of the previous tests.

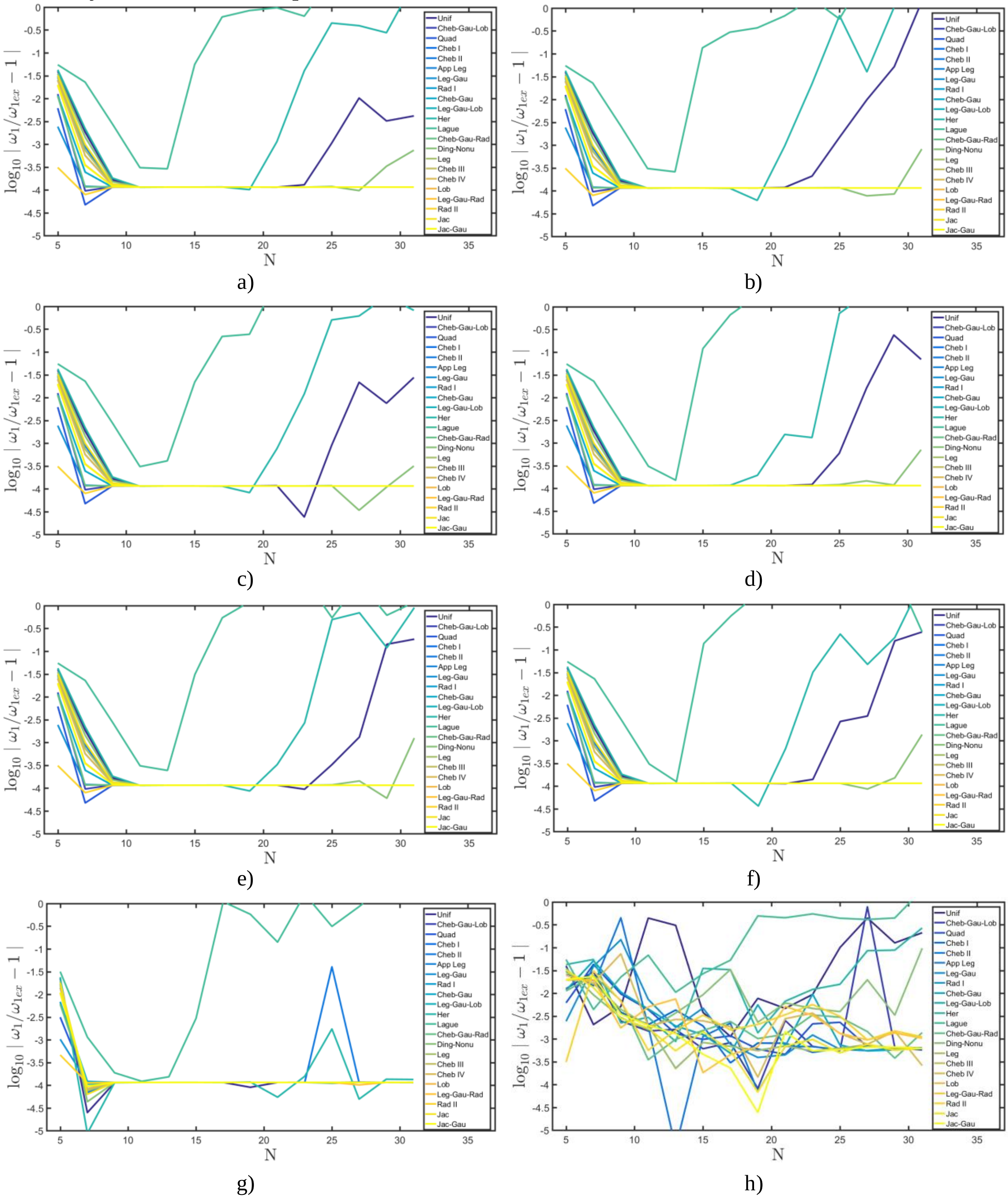

Fig. 3. Relative error for the first frequency of a simply-supported square plate. The strong formulation is employed considering different basis functions: a) Bernstein polynomials; b) Bessel polynomials; c) Boubaker polynomials; d) Chebyshev (I kind) polynomials; e) Exponential functions; f) Lagrange polynomials; g) Fourier basis functions; h) MLS method (Gaussian quadric basis functions)

If f_{ref} denotes the reference solution in term of natural frequency, the relative error is

$$\varepsilon = \frac{f_n}{f_{ref}} - 1 \tag{33}$$

where n stands for the considered vibration mode. For the sake of completeness, the Navier type solution can be found in [5]. The same analyses are performed by means of two finite element commercial codes (Strand7 and Abaqus) by using several kinds of plate elements, as specified in Table 3. A complete description of these elements can be found in the corresponding documentation of the software.

Table 3. Finite elements available in the commercial codes used in the computations

	Strand7	
Quadrangular		Triangular
Quad4 (4 nodes)		*Tri3* (3 nodes)
Quad8 (8 nodes)		*Tri6* (6 nodes)
Quad9 (9 nodes)		-
	Abaqus	
General purpose	Thin structures	Thick structures
S4 (quadrangular, 4 nodes)	*S8R5* (quadrangular, 8 nodes)	*S8R* (quadrangular, 8 nodes)
S4R (quadrangular, 4 nodes)	*STRI65* (triangular, 6 nodes)	-
S3 (triangular, 3 nodes)	-	-

As far as the present approaches are concerned, the strong formulation is used with the Cheb-Gau-Lob (CGL) grid, whereas the Leg-Gau-Lob (LGL) is employed for the weak form. The Lagrange polynomials are employed for both the formulations. In this example, the reference domain is divided into elements and the notations SFEM*j* and WFEM*j* are introduced. The symbol j stands for the number of elements ($j = 1, 2, 4, 8, 16$) used for the computation. The results are shown in Figure 4 for the first three mode shapes of the isotropic rectangular plate, where the relative error is given as a function of the degrees of freedom of the problem ($DOFS$). It can be observed that the present approaches show a rapid convergence if compared to the commercial codes, independently from the number of finite elements. Thus, the current approaches require a reduced number of degrees of freedom to obtain accurate results. The strong and the weak based methodologies are characterized by the same level of accuracy, when the corresponding structural models are considered. It is important to note that both the SFEM and WFEM are able to capture the reference solutions and the machine epsilon is reached. This aspect is highlighted by the horizontal lines in the graphs of Figure 4. Finally, it should be specified that the theoretical model is provided by the Reissner-Mindlin theory [25].

Laminated plates

The same structure is considered in this paragraph to perform the convergence analyses for a laminated plate, whose stacking sequence is given by $(90/0/90/0/90)$. The orthotropic mechanical properties are the following ones

$$\begin{gathered} E_1 = 137.9\,\mathrm{GPa},\; E_2 = E_3 = \frac{E_1}{40},\; \mathrm{G}_{12} = G_{13} = 0.6E_2, \\ G_{23} = 0.6E_2,\; \nu_{12} = \nu_{13} = \nu_{23} = 0.25,\; \rho = 1450\,\mathrm{kg/m^3} \end{gathered} \tag{34}$$

As shown above, the results are given in terms of the relative error (33) related to the Navier solution specified in [5], for the Reissner-Mindlin theory. The notations and considerations of these tests are the same of the previous application. The convergence graphs are depicted in Figure 5.

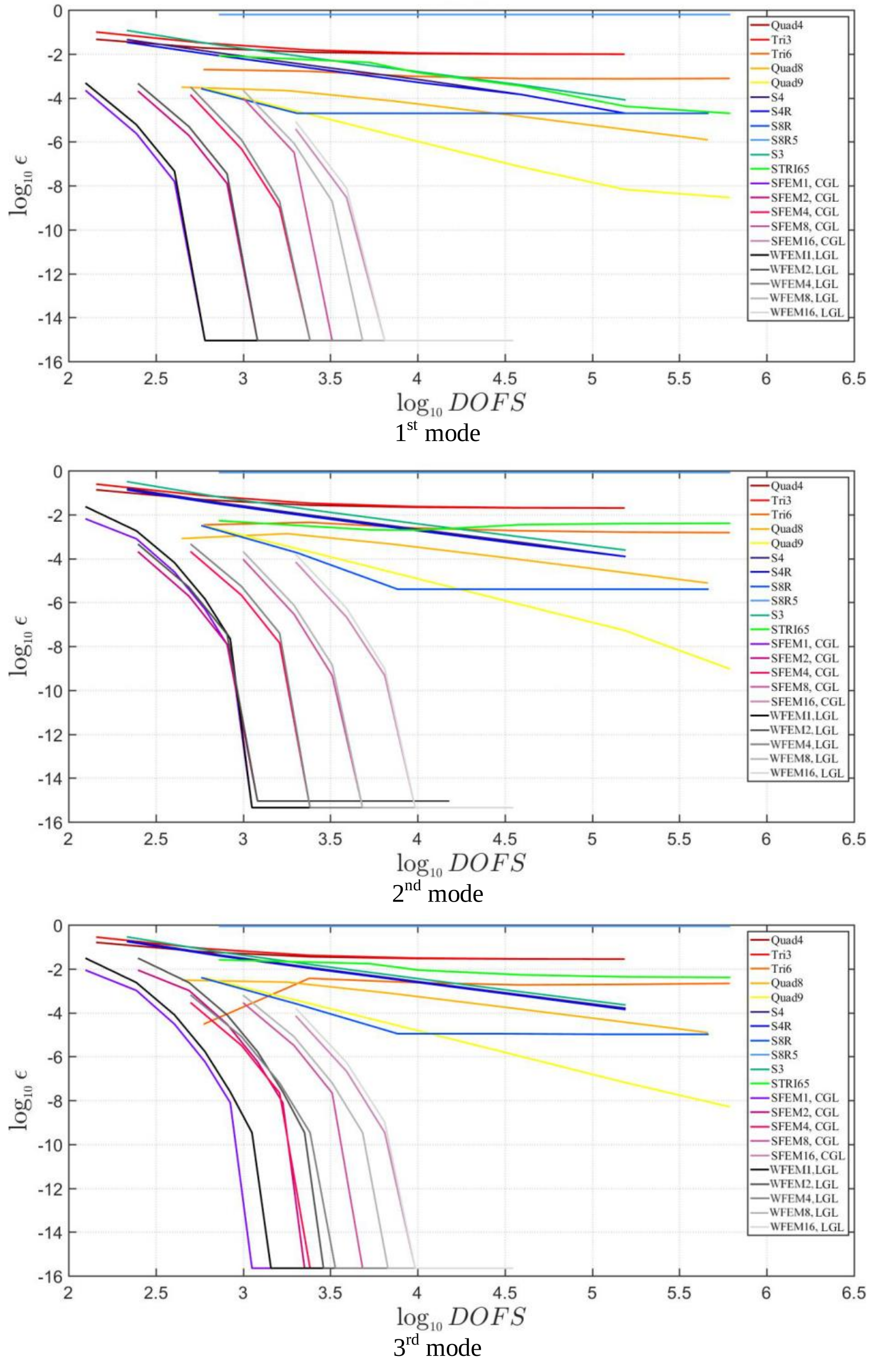

Fig. 4. Relative error for the first three natural frequencies of a simply-supported isotropic rectangular plate increasing the number of degrees of freedom (*DOFS*). Both the strong and weak formulations are employed by dividing the domain into finite elements. The present solutions are compared with the ones obtained by different models obtained through several plate elements provided by two finite element commercial codes.

It should be noted that the machine epsilon is reached in each model for the present solution. On the other hand, the accuracy of the commercial codes is decreased if compared to the corresponding isotropic case.

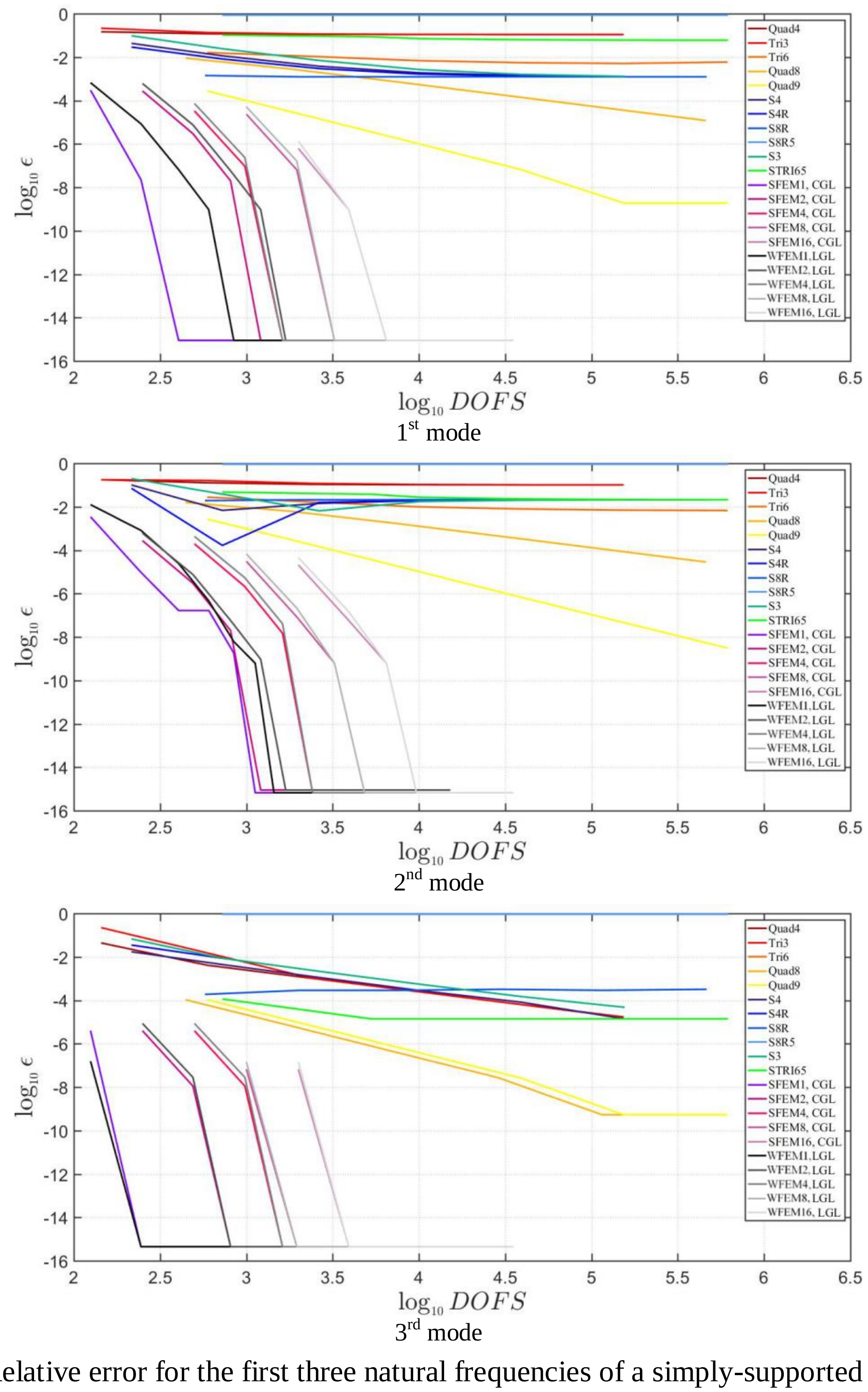

Fig. 5. Relative error for the first three natural frequencies of a simply-supported laminated rectangular plate increasing the number of degrees of freedom (*DOFS*). Both the strong and weak formulations are employed by dividing the domain into finite elements. The present solutions are compared with the ones obtained by different models obtained through several plate elements provided by two finite element commercial codes.

In the applications just presented there is no need of a mapping procedure, since the domain has a regular shape. In the following, a fully clamped circular plate of radius $R = 1\text{m}$ and thickness h is analyzed. The lamination scheme is given by $(30/45)$ and the two layers have the properties shown in (34) and the same thickness. The convergence analyses are shown in Figure 6 for two ratios R/h to deal with thick and thin structures, respectively.

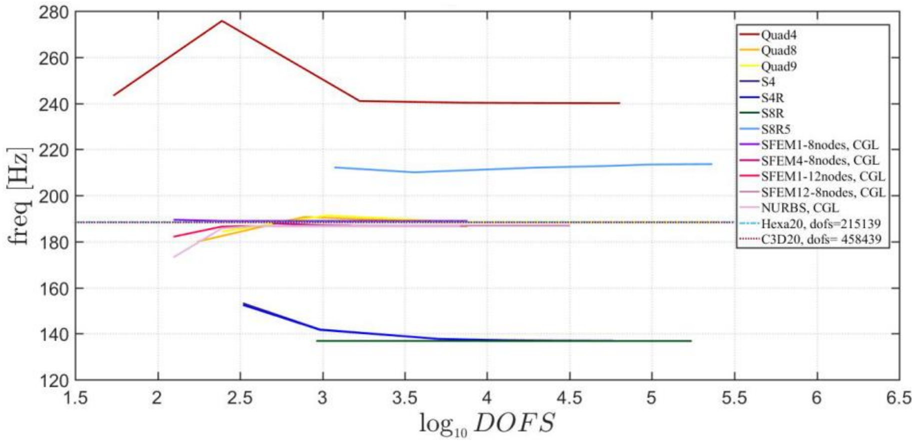

a) $R/h = 10$

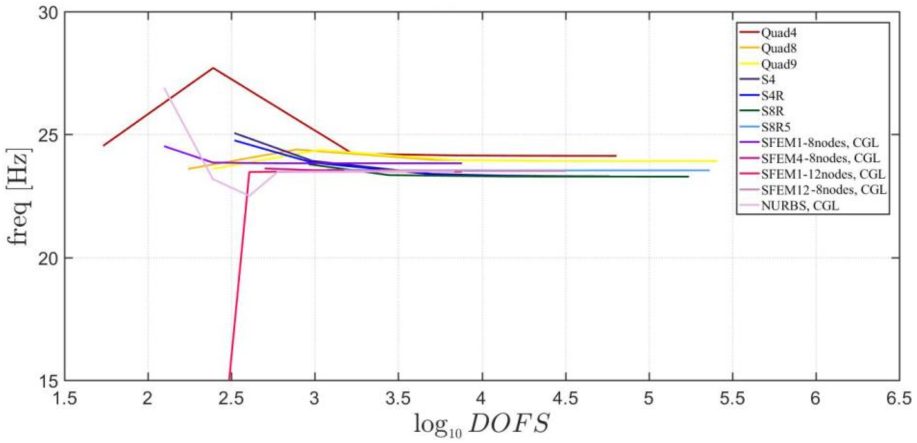

b) $R/h = 100$

Fig. 6. First natural frequency for a fully clamped laminated circular plate increasing the number of degrees of freedom (*DOFS*), for two different thickness values: a) $\boldsymbol{R/h = 10}$; b) $\boldsymbol{R/h = 100}$

As shown above, several kinds of plate elements are considered when the solutions are obtained by means of the finite element commercial codes. As far as the present approach is concerned, only the strong formulation is solved by using different element configurations, as specified in the legend of the corresponding graphs, where the number of nodes required for the mapping of the curved edges of the structure is indicated too. An isogeometric mapping based on NURBS curves is also implemented and compared with the other results. Only for the thicker case, a three-dimensional finite element solution (achieved by means of Strand7 and Abaqus) is computed and taken as a reference. These models are obtained through brick elements made of 20 nodes, named Hexa20 and C3D20 respectively. Both the SFEM and NURBS graphs tend to this solution with a reduced number of degrees of freedom. On the other hand, some types of elements provide convergence plots that are considerably detached from the reference ones, since they are not suitable to deal with this particular problem. Indeed, a similar tendency is achieved by means of each element for the thin plate. Finally, it should be specified that the solutions are obtained in the framework of the Reissner-Mindlin theory.

Laminated shells

The last example is focused on the free vibration analysis of a doubly-curved laminated translational shell made of two orthotropic layers of equal thickness, whose geometry is widely described in the paper by Tornabene et al. [26]. The stacking sequence is given by $(30/45)$, and their mechanical properties are the following ones

$$\begin{gathered} E_1 = 137.9\,\mathrm{GPa},\ E_2 = E_3 = 8.96\,\mathrm{GPa},\ \mathrm{G}_{12} = G_{13} = 7.1\mathrm{GPa}, \\ G_{23} = 6.21\mathrm{GPa},\ \nu_{12} = \nu_{13} = 0.3,\ \nu_{23} = 0.49,\ \rho = 1450\,\mathrm{kg/m^3} \end{gathered} \tag{35}$$

The overall thickness is assumed as $h = 0.1\mathrm{m}$. In this case, the first ten natural frequencies are obtained by solving only the weak formulation of the governing equations. A unified formulation is used to deal with higher-order shear deformation theories, as illustrated in the paper [30], where the reader can find a complete treatise about these structural models, as well as the nomenclature to denote them. The Leg-Gau-Lob grid distribution is employed by setting $I_N = 30$ and $I_M = 60$ as number of discrete points along the two principal directions. The first ten natural frequencies are presented in Table 4, together with the reference solution obtained by Abaqus (three-dimensional finite element model). All the numerical solutions are in good agreement with the reference one. For the sake of completeness, the first three mode shapes are depicted in Figure 7, where it is easy to note also the adopted boundary conditions. In particular, only one of the two external edges is fully clamped, whereas the other one is free.

Table 4. First ten frequencies for a doubly-curved laminated panel

Mode [Hz]	FSDT	TSDT	ED1	ED2	ED3	3D FEM Abaqus
f_1	21.808	21.821	22.134	21.798	21.826	21.811
f_2	22.323	22.347	22.388	22.186	22.207	22.205
f_3	22.576	22.589	22.883	22.557	22.584	22.566
f_4	33.055	33.089	33.013	32.824	32.857	32.854
f_5	43.251	43.287	43.622	43.053	43.109	43.085
f_6	44.870	44.874	45.932	44.957	45.027	44.986
f_7	45.641	45.641	46.774	45.754	45.832	45.783
f_8	52.459	52.489	52.837	52.251	52.308	52.263
f_9	54.176	54.186	54.694	54.570	54.571	54.561
f_{10}	64.235	64.258	64.290	64.001	64.039	64.006

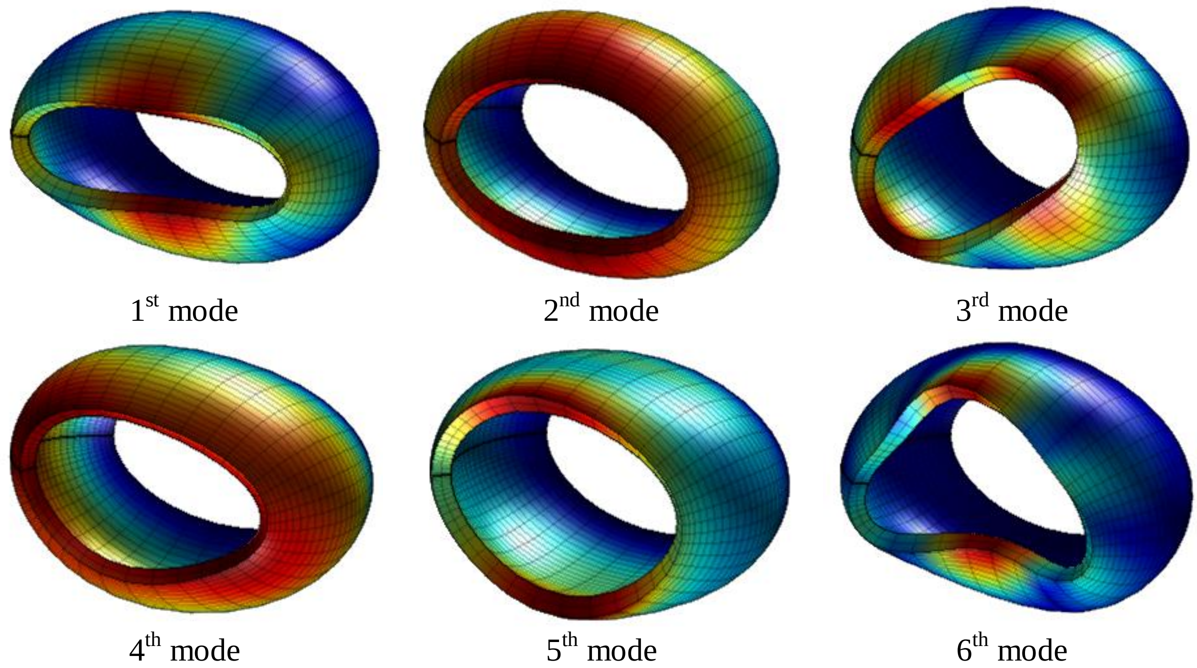

Fig. 7. First six mode shapes for a doubly-curved laminated shell of translation

4. Conclusions

The authors have presented two numerical approaches based on the DQ method to approximate derivatives and integrals, respectively. These techniques have been applied to solve some structural problems related to the mechanical behavior of plates and shells made of isotropic and composite materials. In particular, the accuracy and stability features of a strong formulation (SFEM) and a weak formulation (WFEM) have been discussed by means of some numerical analyses. Several basis polynomials for the functional approximation and different discrete grid distributions have been tested and compared. For this purpose, some convergence analyses have been performed by increasing the number of sampling points within the elements, for both a single element domain and a multi-element domain. The present solutions have been compared also with the results obtained through two commercial codes. These finite element models have been achieved by using several kinds of plate elements available in the software libraries. In general, the present methodologies have proven to be more accurate and characterized by a faster convergence ratio than the commercial codes.

Acknowledgements

The research topic is one of the subjects of the Centre of Study and Research for the Identification of Materials and Structures (CIMEST)-"M. Capurso" of the University of Bologna (Italy).

References

[1] Oden, J.T., and Reddy, J.N., *An introduction to the mathematical theory of finite elements*, John Wiley & Sons, 1976.

[2] Ochoa, O.O. and Reddy, J.N., *Finite Element Analysis of Composite Laminates,* Springer, 1992.

[3] Zienkiewicz, O.C. and Taylor R.L., *The Finite Element Method for Solid and Structural Mechanics,* 6th edition, Elsevier, 2005.

[4] Reddy, J.N., *An introduction to the finite element method*, 3rd edition, McGraw-Hill, 2006.

[5] Tornabene, F., Fantuzzi, N., Ubertini, F. and Viola, E., Strong Formulation Finite Element Method Based on Differential Quadrature: A Survey, *Applied Mechanics Reviews*, 67, 020801-1-55, 2015.

[6] Tornabene, F., Fantuzzi, N., and Bacciocchi, M., The Strong Formulation Finite Element Method: Stability and Accuracy, *Fracture and Structural Integrity,* 29, 251-265, 2014.

[7] Gottlieb, D., and Orszag, S.A., Numerical Analysis of Spectral Methods: Theory and Applications, CBMS-NSF Regional Conference Series in Applied Mathematics., SIAM, 1977.

[8] Boyd, J.P., *Chebyshev and Fourier Spectral Methods*, Dover Publications, 2001.

[9] Canuto, C., Hussaini, M.Y., Quarteroni, A., and Zang, T.A., *Spectral Method. Fundamentals in Single Domains,* Springer, 2006.

[10] Bellman, R., and Casti, J., Differential quadrature and long-term integration, *Journal of Mathematical Analysis and Applications*, 34, 235-238, 1971.

[11] Bert, C.W., and Malik, M., Differential quadrature method in computational mechanics, *Applied Mechanics Reviews,* 49, 1-27, 1996.

[12] Quan, J.R., and Chang, C.T., New insights in solving distributed system equations by the quadrature method - I. Analysis, *Computers & Chemical Engineering*, 13, 779-788, 1989.

[13] Striz, A.G., Chen, W.L., and Bert, C.W., Static analysis of structures by the quadrature element method (QEM), *International Journal of Solids and Structures*, 31, 2807-2818, 1994.

[14] Shu, C., *Differential Quadrature and Its Application in Engineering*, Springer, 2000.

[15] Reddy, J.N., *Mechanics of Laminated Composites Plates and Shells*, 2nd edition, CRC Press, New York, 2004.

[16] Chen, C.-N., *Discrete Element Analysis Methods of Generic Differential Quadratures*, Springer, 2006.

[17] Zong, Z., and Zhang, Y.Y., *Advanced Differential Quadrature Methods*, CRC Press, 2009.

[18] Cottrell, J.A., Hughes, T.J.R. and Bazilevs, Y., *Isogeometric Analysis. Toward Integration of CAD and FEA*, John Wiley & Sons, 2009.

[19] Reali, A., An isogeometric analysis approach for the study of structural vibrations, *Journal of Earthquake Engineering*, 10, 1-30, 2006.

[20] Tornabene, F., Fantuzzi, N. and Bacciocchi M., The GDQ Method for the Free Vibration Analysis of Arbitrarily Shaped Laminated Composite Shells Using a NURBS-Based Isogeometric Approach, *Composite Structures*, 154, 190-218, 2016.

[21] Fantuzzi, N. and Tornabene F., Strong Formulation Isogeometric Analysis (SFIGA) for Laminated Composite Arbitrarily Shaped Plates, *Composites Part B Engineering* 96, 173-203, 2016.

[22] Viola, E., Tornabene, F. and Fantuzzi N., Generalized Differential Quadrature Finite Element Method for Cracked Composite Structures of Arbitrary Shape, *Composite Structures*, 106, 815-834, 2013.

[23] Fantuzzi, N., Bacciocchi, M., Tornabene, F., Viola, E. and Ferreira, A.J.M., Radial Basis Functions Based on Differential Quadrature Method for the Free Vibration of Laminated Composite Arbitrary Shaped Plates, *Composites Part B Engineering* 78, 65-78, 2015.

[24] Tornabene, F., Fantuzzi, N., Bacciocchi, M., Neves, A.M.A. and Ferreira, A.J.M., MLSDQ Based on RBFs for the Free Vibrations of Laminated Composite Doubly-Curved Shells, *Composites Part B: Engineering* 99, 30-47, 2016.

[25] Fantuzzi, N., Tornabene, F., Bacciocchi, M., Neves, A.M.A. and A.J.M. Ferreira, Stability and Accuracy of Three Fourier Expansion-Based Strong Form Finite Elements for the Free Vibration Analysis of Laminated Composite Plates, *International Journal for Numerical Methods in Engineering* (in press), 2017.

[26] Tornabene, F., Fantuzzi, N. and Bacciocchi, M., The local GDQ method applied to general higher-order theories of doubly-curved laminated composite shells and panels: The free vibration analysis, *Composite Structures*, 116, 637-660, 2014.

[27] Tornabene, F., Brischetto, S., Fantuzzi, N., and Bacciocchi M., Boundary Conditions in 2D Numerical and 3D Exact Models for Cylindrical Bending Analysis of Functionally Graded Structures, *Shock and Vibration Vol.* 2016, Article ID 2373862, 1-17, 2016.

[28] Tornabene, F., Fantuzzi, N., Bacciocchi, M. and Reddy J.N., An Equivalent Layer-Wise Approach for the Free Vibration Analysis of Thick and Thin Laminated Sandwich Shells, *Applied Sciences,* 7, 17, 1-34, 2017.

[29] Brischetto, S., Tornabene, F., Fantuzzi, N. and Bacciocchi, M., Interpretation of Boundary Conditions in the Analytical and Numerical Shell Solutions for Mode Analysis of Multilayered Structures, *International Journal of Mechanical Sciences,* 122, 18-28, 2017.

[30] Tornabene, F., Fantuzzi, N., Bacciocchi, M., Viola, E. and Reddy J.N., A Numerical Investigation on the Natural Frequencies of FGM Sandwich Shells with Variable Thickness by the Local Generalized Differential Quadrature Method, *Applied Sciences,* 7, 131, 1-39, 2017.

[31] Tornabene, F., Fantuzzi, N., Bacciocchi, M. and Viola, E., *Laminated Composite Doubly-Curved Shell Structures. Differential Geometry. Higher-Order Structural Theories*, Esculapio, 2016.

[32] Tornabene, F., Fantuzzi, N., Bacciocchi, M. and Viola, E., *Laminated Composite Doubly-Curved Shell Structures. Differential and Integral Quadrature. Strong Formulation Finite Element Method*, Esculapio, 2016.

International Journal of Engineering & Applied Sciences (IJEAS)
Vol.9, Issue 2 (Special Issue: Composite Structures) (2017) 22-38
http://dx.doi.org/10.24107/ijeas.305348
Int J Eng Appl Sci 9(2) (2017) 22-38

Longitudinal Vibration of CNTs Viscously Damped in Span

Mustafa Arda [a*] *and Metin Aydogdu* [b]

[a,b]*Trakya University, Department of Mechanical Engineering*
[*]*E-mail address*: mustafaarda@trakya.edu.tr

Received date: April 2017

Abstract

In this study, longitudinal vibration of a carbon nanotube with an attached damper has been investigated using the nonlocal stress gradient elasticity theory. Equations of motions have been solved analytically and frequencies of clamped-clamped and clamped-free nanotubes have been obtained explicitly in terms of damping coefficient, nonlocal parameter, the attachment point of damper and nanotube length. The nonlocal effects have important effects on the dynamics of a CNT with an attached damper.

Keywords: longitudinal vibration; viscously damped; carbon nanotubes; nonlocal elasticity

1. Introduction

Discovery of carbon nanotubes (CNTs) by Iijima [1] has important results on nanotechnology. With superior properties like electrical and heat conductivity, strength, density etc., scientists have considered use of CNTs in many areas: nano-electromechanical devices, nano-pharmaceutical products, nano-bearings, nano-sensors, etc.

Dynamic behavior of CNTs at different areas is very important in design of nano-products. Nowadays, scientists try to use CNTs in medical applications [2,3], bearing-like products [4,5], electromagnetic damping process [6] and molecular transportation [7,8] etc.

Generally, two modeling techniques are used in nano-mechanics: continuum model and discrete model. Because of the size independence, classical theories are not suitable at nanoscale. Nonlocal Elasticity, a modified continuum model, was firstly proposed by Eringen [9,10]. In this theory mechanical behavior of materials is size dependent. Also Molecular Dynamics (MD) Simulations are used as a discrete model in nano-mechanics. Both models give more acceptable results than the classical theory when compared to the lattice dynamics results.

Recently, wave propagation in SWCNTs has been compared for the nonlocal continuum models and MD Simulations [11]. Very close results were obtained between two results. Lattice Dynamic results for longitudinal wave propagation in nanotubes have been investigated in previous studies [12].

Thermal, concentration or electromagnetic fields can cause a damping effect on CNTs [13] . Wang et al. [14] have studied asymmetric vibration of a single-walled carbon nanotubes (SWCNTs) immersed in water. Assuming that, water can establish a viscous damping effect on axisymmetric radial, longitudinal and torsional vibration. Rinaldi et al. [15] investigated the fluid conveying micro scale pipes with the effects of flow velocity on damping, stability and frequency shift. Vibration and instability analysis of CNTs with a fluid flow is studied by Ghavanloo et al. [16] and microtubules in surrounding cytoplasm is investigated by Ghavanloo et al. [17]. In plane and flexural vibration of fluid conveying CNTs in viscoelastic medium is studied by [18] and in viscous fluid is studied by Ghavanloo et al. [19]. Yun et al. [20] have obtained the free vibration and flow-induced flutter instability of fluid conveying multi-walled carbon nanotubes (MWCNTs). Vibrations and instability of fluid conveying double-walled carbon nanotubes (DWCNTs) is studied using the modified couple stress theory by Zeighampour and Tadi Beni [21]. Martin and Houston [22] investigated the gas damping effect on CNT based nano-resonator operating in low vacuum conditions. The natural frequencies of aligned SWCNT reinforced composite beams were obtained using shear deformable composite beam theories by Aydogdu [23]. Chemi et al. [24] investigated elastic buckling of chiral DWCNTs under axial compression. Longitudinal forced vibration of nanorods studied by Aydogdu and Arda [25] using the nonlocal elasticity theory of Eringen. They considered uniform, linear and sinusoidal loads on axial direction.

One of the possible medical applications of CNTs is the viscous fluid conveying SWCNT embedded in biological soft tissue. Transverse vibrational model is studied by Soltani et al. [26]. They simulated the viscoelastic behavior of surrounding tissue using Kevin-Voigt model. In addition to mentioned work, transverse vibration of fluid conveying DWCNTs embedded in biological soft tissue is investigated by Zhen et al. [27].

Hoseinzadeh and Khadem [28] studied the thermoelastic vibration and damping of DWCNT upon interlayer van der Waals interaction and initial axial stress. Same authors also investigated the thermoelastic vibration behavior and damping of DWCNTs using nonlocal shell theory [29]. Thermoelastic damping in a DWCNT under electrostatic actuation is obtained through an analytical method by Hajnayeb and Khadem [30].

Magnetic damping effect on CNTs as a nanoelectromechanical resonators is studied by Schmid et al. [31] at cryogenic temperature. Chang and Lee [32] investigated vibration behavior of CNTs using non-local viscoelasticity theory including thermal and foundation effects.

Damping effect on rods for various boundary conditions is investigated at macro scale by [33–35]. Viscoelastic properties of SWCNTs are investigated with a semi-analytical approach and associated damping mechanism at nano scale by Zhou et al. [36]. Jeong et al. [37] modeled the nonlinear damping behavior of micro cantilever-nanotube system and compared with measurement results. Adhikari et al. [38] investigated free and forced axial vibrations of strain-rate depended viscous damping and velocity dependent viscous damped nonlocal rods. The asymptotic frequencies of four kinds of nonlocal viscoelastic damped structures, including an Euler-Bernoulli beam with rotary inertia, a Timoshenko beam, a Kirchhoff plate with rotary inertia and a Mindlin plate are studied by Lei et al. [39]. Arani et al. [40] investigated the vibration of double viscoelastic CNTs conveying viscous fluid coupled by visco-Pasternak medium using the surface nonlocal theory. Karličić et al. [41] studied free longitudinal vibration of a nonlocal viscoelastic double-nanorod system as a complementary study at nano scale to Erol and Gürgöze's paper [42].

Mechanical response of a CNT atomic force microscope (AFM) probe tip contact is an important problem (Fig.1). This response can be modeled as a spring [43] or damping element according continuum mechanics. Damping of a mechanical resonators based on CNTs is studied by Eichler et al. [44]. Li et al. [45] investigated the mechanical oscillatory behaviors of MWCNT oscillators in gaseous environment using MD simulation. Suspended carbon nanotube resonators behavior over a broad range of temperatures to explore the physics of semi flexible polymers in underdamped environments simulated by Barnard et al. [46]. Hüttel et al. [47] observed the transversal vibration mode of suspended CNTs at miliKelvin temperatures by measuring the single electron tunneling current. The measured magnitude and temperature dependence of the Q factor shown a remarkable agreement with the intrinsic damping predicted for a suspended carbon nanotube. According to author's literature knowledge, vibration of a nanorod with an attached viscous damper has not been considered in the previous studies.

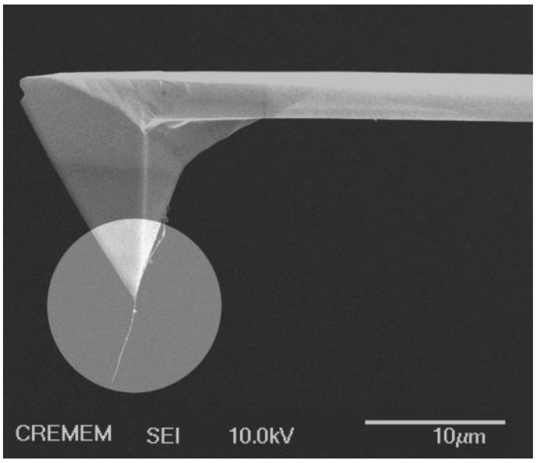

Fig. 1. SEM Image of a MWCNT Attached to Pyramidal Si Tip [43]

2. Analysis

A nanorod of length L and diameter ϕ is considered. A viscous damper is attached at an arbitrary point of the rod (Fig. 2). The equation of motion in the longitudinal direction can be expressed as:

$$EA\frac{\partial^2 u}{\partial x^2} = m\frac{\partial^2 u}{\partial t^2} \tag{1}$$

where A is the cross-section area , E is the Young Modulus and m is the mass per unit length. In Fig. (2), η defines the attachment point of the viscous damper, L is the length of nanorod, d is the damping coefficient of viscous damper and $u(x,t)$ is the displacement in longitudinal direction.

2.1. Equation of motion of nanorod in nonlocal model

The nonlocal constitute relation can be given as [9,10] :

$$(1-\mu\nabla^2)\tau_{kl} = \lambda\varepsilon_{rr}\delta_{kl} + 2G\varepsilon_{kl} \tag{2}$$

where τ_{kl} is the nonlocal stress tensor, ε_{kl} is the strain tensor, λ and G are the lame constants, $\mu=(e_0a)^2$. μ *is* called the nonlocal parameter, a is an internal characteristic length and e_0 is a constant. In this study, $\mu \leq 2nm^2$ is accepted for SWCNTs. Using the Nonlocal Elasticity Theory in one dimensional form leads following equation of motion:

$$EA\frac{\partial^2 u}{\partial x^2} = \left(1-\mu\frac{\partial^2}{\partial x^2}\right)m\frac{\partial^2 u}{\partial t^2} \tag{3}$$

If the nonlocal parameter μ is assumed identically zero, Eq. (3) reduces to classical rod model. In order to study the equation of motion of a nanorod with an attached viscous damper, the nanorod is divided into two parts. The equation of motion for each segment can be written as:

$$EA\frac{\partial^2 u_i}{\partial x^2} = \left(1 - \mu\frac{\partial^2}{\partial x^2}\right) m \frac{\partial^2 u_i}{\partial t^2} \quad , \quad (i = 1{,}2) \tag{4}$$

where u_1 and u_2 denote displacement of the left and the right segments of the nanorod respectively. The corresponding boundary and continuity conditions are written as:

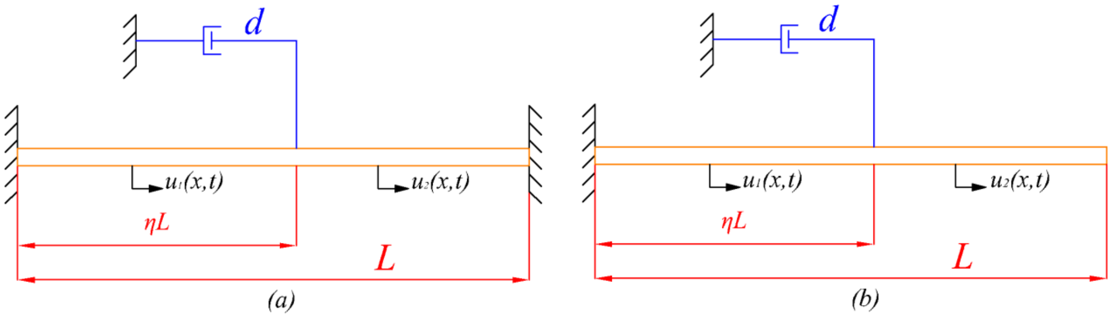

Fig. 2 Nanorod model with a viscous damper in a)C-C boundary condition b)C-F boundary condition

Clamped-Clamped (C-C):

$$\begin{gathered} u_1(0,t) = 0, \\ u_1(\eta L,t) = u_2(\eta L,t), \\ EA\frac{\partial u_1(\eta L,t)}{\partial x} + \mu m\frac{\partial^3 u_1(\eta L,t)}{\partial x\,\partial t^2} - EA\frac{\partial u_2(\eta L,t)}{\partial x} - \mu m\frac{\partial^3 u_2(\eta L,t)}{\partial x\,\partial t^2} + d\frac{\partial u_1(\eta L,t)}{\partial t} - \mu d\frac{\partial^3 u_1(\eta L,t)}{\partial x^2\,\partial t} = 0, \\ u_2(L,t) = 0 \end{gathered} \tag{5}$$

Clamped-Free (C-F):

$$\begin{gathered} u_1(0,t) = 0, \\ u_1(\eta L,t) = u_2(\eta L,t), \\ EA\frac{\partial u_1(\eta L,t)}{\partial x} + \mu m\frac{\partial^3 u_1(\eta L,t)}{\partial x\,\partial t^2} - EA\frac{\partial u_2(\eta L,t)}{\partial x} - \mu m\frac{\partial^3 u_2(\eta L,t)}{\partial x\,\partial t^2} + d\frac{\partial u_1(\eta L,t)}{\partial t} - \mu d\frac{\partial^3 u_1(\eta L,t)}{\partial x^2\,\partial t} = 0, \\ EA\frac{\partial u_2(L,t)}{\partial x} + \mu m\frac{\partial^3 u_2(L,t)}{\partial x\,\partial t^2} = 0 \end{gathered} \tag{6}$$

The longitudinal displacement u_i can be expressed as:

$$u_i(x,t) = U_i(x)\, e^{\lambda t} \quad , \quad (i = 1{,}2) \tag{7}$$

where $U_i(x)$ and λ is the amplitude function and characteristic value respectively. Inserting Eq.(7) into Eq.(4) gives following dimensionless equations of motion:

$$\frac{\partial^2 U_i}{\partial x^2} - \beta^2 U_i = 0 \quad , \quad (i = 1{,}2) \tag{8}$$

where:

$$\beta^2 = \frac{m\lambda^2}{EA + \mu m\lambda^2} \tag{9}$$

The solutions of Eq.(8) are:

$$U_1(x) = C_1 e^{\beta x} + C_2 e^{-\beta x} \tag{10}$$
$$U_2(x) = C_3 e^{\beta x} + C_4 e^{-\beta x} \tag{11}$$

where C_1, C_2, C_3 and C_4 are the undetermined coefficients. For the C-C boundary condition, eigenvalue equation is obtained using Eq.(5), Eq.(10) and Eq.(11):

$$\begin{bmatrix} CC_{11} & CC_{12} & CC_{13} & CC_{14} \\ CC_{21} & CC_{22} & CC_{23} & CC_{24} \\ CC_{31} & CC_{32} & CC_{33} & CC_{34} \\ CC_{41} & CC_{42} & CC_{43} & CC_{44} \end{bmatrix} \begin{bmatrix} C_1 \\ C_2 \\ C_3 \\ C_4 \end{bmatrix} = 0 \tag{12}$$

where

$$\begin{gathered} CC_{11} = 1 \ , \quad CC_{12} = 1 \ , \quad CC_{13} = 0 \ , \quad CC_{14} = 0 \ , \\ CC_{21} = 0 \ , \quad CC_{22} = 0 \ , \quad CC_{23} = e^{\beta L} \ , \quad CC_{24} = e^{-\beta L} \ , \\ CC_{31} = e^{\beta\eta L} \ , \quad CC_{32} = e^{-\beta\eta L} \ , \quad CC_{33} = -e^{\beta\eta L} \ , \quad CC_{34} = -e^{\beta\eta L} \\ CC_{41} = e^{\beta\eta L}\left(1 + \alpha + D(1 - \mu\beta^2)^{1/2}\right) \ , \\ CC_{42} = e^{-\beta\eta L}\left(-1 - \alpha + D(1 - \mu\beta^2)^{1/2}\right) \ , \\ CC_{43} = e^{\beta\eta L}(-1 - \alpha) \ , \\ CC_{44} = e^{-\beta\eta L}(1 + \alpha) \end{gathered} \tag{13}$$

and for the C-F boundary condition, eigenvalue equation is obtained using Eq.(6), Eq.(10) and Eq.(11):

$$\begin{bmatrix} CF_{11} & CF_{12} & CF_{13} & CF_{14} \\ CF_{21} & CF_{22} & CF_{23} & CF_{24} \\ CF_{31} & CF_{32} & CF_{33} & CF_{34} \\ CF_{41} & CF_{42} & CF_{43} & CF_{44} \end{bmatrix} \begin{bmatrix} C_1 \\ C_2 \\ C_3 \\ C_4 \end{bmatrix} = 0 \tag{14}$$

where

$$\begin{gathered} CF_{11} = 1 \ , \quad CF_{12} = 1 \ , \quad CF_{13} = 0 \ , \quad CF_{14} = 0 \ , \\ CF_{21} = 0 \ , \quad CF_{22} = 0 \ , \quad CF_{23} = (1 + a)e^{\beta L} \ , \quad CF_{24} = (-1 - a)e^{-\beta L} \ , \\ CF_{31} = e^{\beta\eta L} \ , \quad CF_{32} = e^{-\beta\eta L} \ , \quad CF_{33} = -e^{\beta\eta L} \ , \quad CF_{34} = -e^{\beta\eta L} \ , \\ CF_{41} = e^{\beta\eta L}\left(1 + \alpha + D(1 - \mu\beta^2)^{1/2}\right) \ , \\ CF_{42} = e^{-\beta\eta L}\left(-1 - \alpha + D(1 - \mu\beta^2)^{1/2}\right) \ , \\ CF_{43} = e^{\beta\eta L}(-1 - \alpha) \ , \\ CF_{44} = e^{-\beta\eta L}(1 + \alpha) \end{gathered} \tag{15}$$

For a nontrivial solution the determinant of the coefficient matrix in Eq.(12) and Eq.(14) must be zero. If these determinant equations are rearranged, following characteristic equations are obtained for each boundary conditions considered:

$$2(\alpha + 1)\sinh(\bar{\beta}) + D\left(1 - \frac{\mu}{L^2}\bar{\beta}^2\right)^{\frac{1}{2}}\left\{\cosh(\bar{\beta}) - \cosh\left[(1 - 2\eta)\bar{\beta}\right]\right\} = 0 \ \rightarrow \ (C - C) \tag{16}$$

$$2(\alpha + 1)\cosh(\bar{\beta}) + D\left(1 - \frac{\mu}{L^2}\bar{\beta}^2\right)^{\frac{1}{2}}\left\{\sinh(\bar{\beta}) - \sinh\left[(1 - 2\eta)\bar{\beta}\right]\right\} = 0 \ \rightarrow \ (C - F) \tag{17}$$

where

$$\alpha = \frac{\mu}{L^2}\frac{\bar{\beta}^2}{\left(1-\frac{\mu}{L^2}\bar{\beta}^2\right)} \quad , \quad D = \frac{dc}{EA} \quad , \quad c = \sqrt{\frac{E}{\rho}} \quad , \quad \bar{\beta} = \beta L \tag{18}$$

where α is the dimensionless coefficient, D is the dimensionless damping coefficient, c is the velocity of the wave propagation along the nanorod and $\bar{\beta}$ is the dimensionless characteristic parameter. $\bar{\beta}$ is a complex number and its imaginary part defines the non-dimensional frequency (NDF) and real part defines the non-dimensional damping coefficient (NDD) of nanorod. Damping ratio (ξ) of nanorod is defined in the following form:

$$\xi = \frac{|\mathrm{NDD}|}{\sqrt{\mathrm{NDF}^2+\mathrm{NDD}^2}} \tag{19}$$

3. Numerical Results and Discussion

In this section, the non-dimensional frequency (NDF) and non-dimensional damping coefficient (NDD) of the nanorod are investigated for different dimensionless damping coefficient, nanotube length, nonlocal parameter and the attachment point of viscous damper. Geometrical and material properties of the CNT are taken from Ref. [48]. The validity of present work is checked in the next section.

3.1. Validation of the Present Results

By assuming nonlocal parameter is identically zero (μ=0), the local model solutions are obtained. The dimensionless characteristic values are compared with local model from Ref. [33] and Ref. [34] for C-C and C-F boundary conditions in Table 1. Good agreement is observed between two results.

Table 1 Comparison of characteristic values with literature (η = 0.6)

	Present Work		[34]	[33]
	C-C	C-F	C-C	C-F
$\bar{\beta}_1$	-0.020352+3.141619i	-0.001439+1.570796i	-0.020349+3.141619i	-0.001472+1.570796i
$\bar{\beta}_2$	-0.007773+6.283168i	-0.000210+4.712389i	-0.007772+6.283168i	-0.000214+4.712389i
$\bar{\beta}_3$	-0.007773+9.424794i	-0.002200+7.853981i	-0.007772+9.424794i	-0.002249+7.853981i

3.2. Dimensionless Damping Effect on NDF and NDD

In Figs. (3-14) and Tables (2-3), variations of NDF and NDD with dimensionless damping coefficient for C-C and C-F boundary condition are depicted. According to these results following conclusions are obtained:

The fundamental NDF value increases but the second and third NDF decrease with increasing D for the C-C boundary condition. However, for the C-F boundary condition, variation of NDF depends on η. First and second NDF increase whereas third NDF decreases with increasing D when η < 0.5. On the other hand, first and second NDF decrease and third NDF increase with increasing D when η > 0.5 (See Table (2) and (3)). Generally, NDD increases with increasing D except for some cases. For smaller nanotube length, nonlocal effect is more pronounced and it reduces the NDD (See Figs. (4) and (6)).

NDF decreases with increasing the nonlocal parameter for both C-C and C-F boundary condition. The nonlocal effect decreases with increasing nanotube length. NDD increases with increasing μ for both C-C and C-F boundary condition (See Figs. (3-10)).

The attachment point of damper has different effects on NDF for C-C and C-F cases. In C-C boundary condition, fundamental NDF decreases, however second and third NDF increase when $\eta < 0.5$. The obtained results for NDF and NDD are symmetric with respect to $\eta = 0.5$ (i.e. results of $\eta = 0.1$ are equal to $\eta = 0.9$, etc.). The NDD is maximum at $\eta = 0.5$.

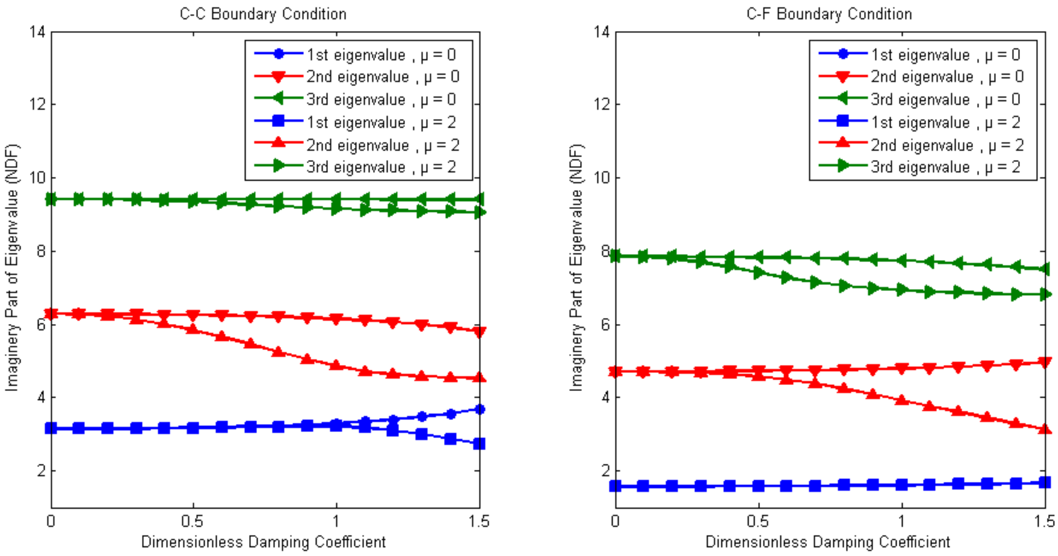

Fig. 3. Variation of NDF with dimensionless damping coefficient ξ ($\eta = 0.3$, L = 10 nm)

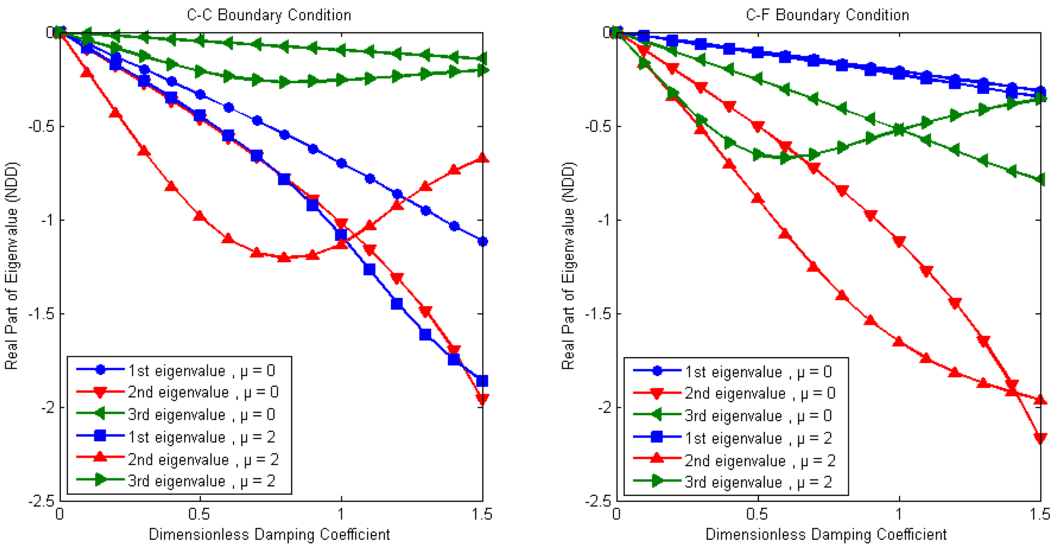

Fig. 4. Variation of NDD with dimensionless damping coefficient ξ ($\eta = 0.3$, L = 10 nm)

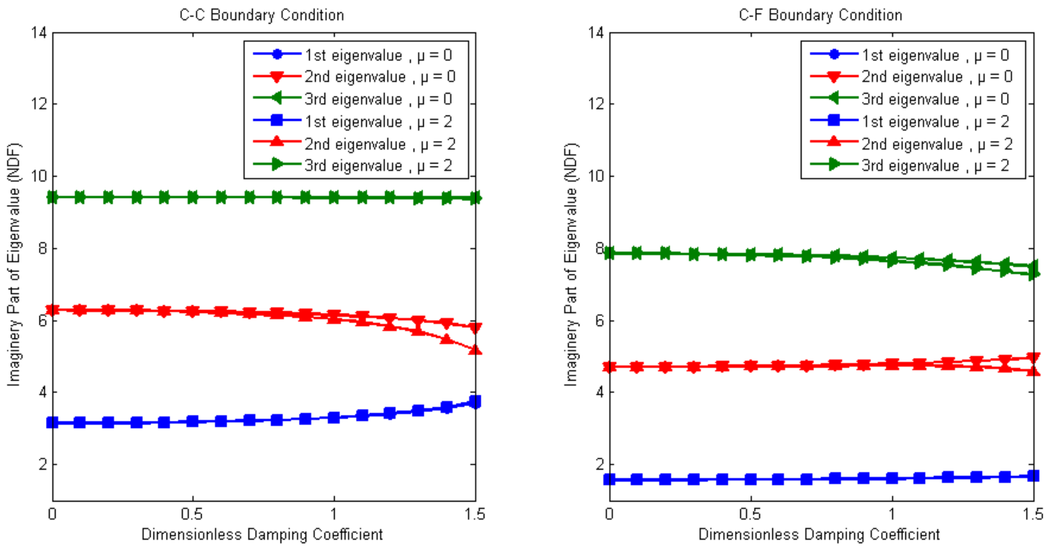

Fig. 5. Variation of NDF with dimensionless damping coefficient ξ (η = 0.3 , L = 30 nm)

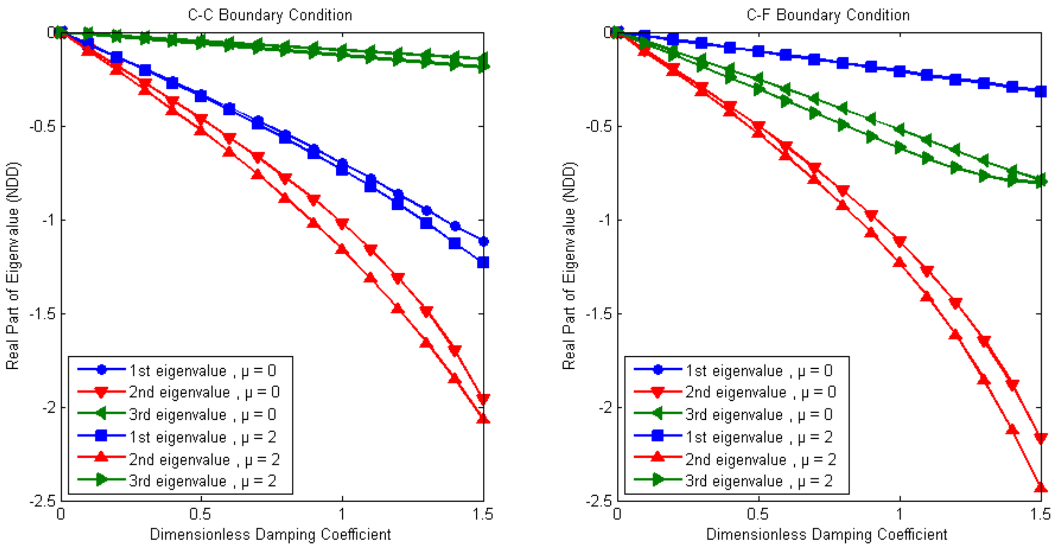

Fig. 6. Variation of NDD with dimensionless damping coefficient ξ (η = 0.3 , L = 30 nm)

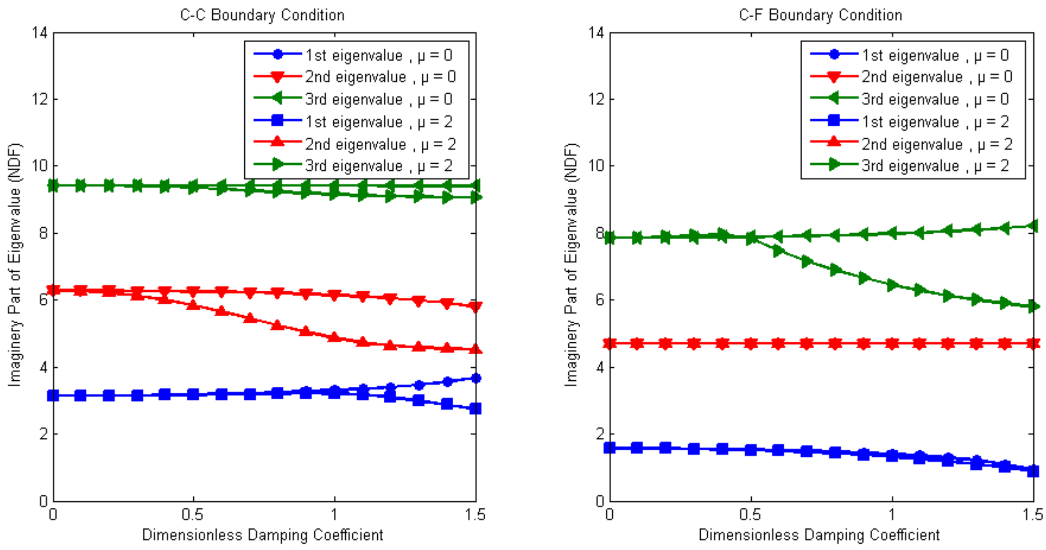

Fig. 7. Variation of NDF with dimensionless damping coefficient ξ (η = 0.7 , L = 10 nm)

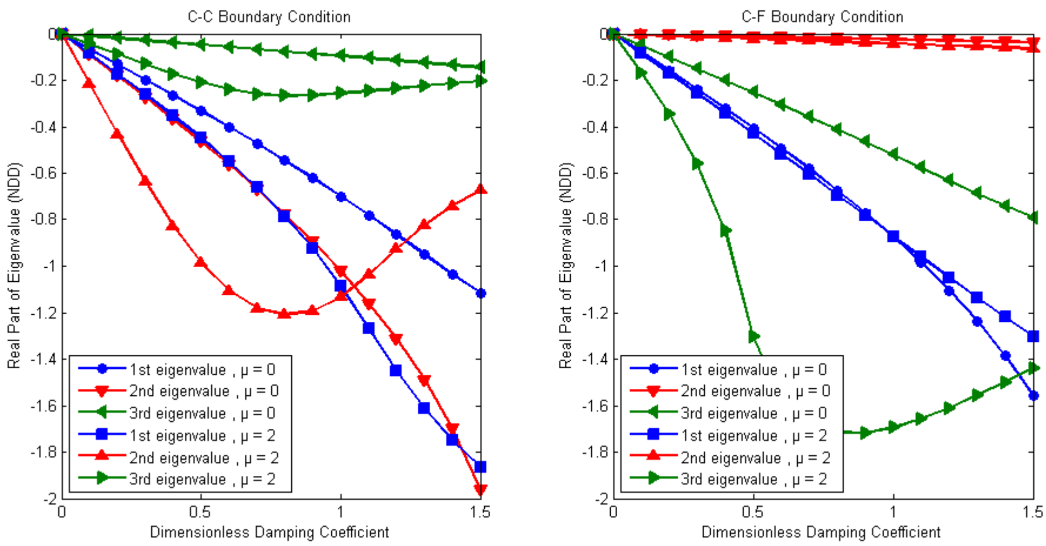

Fig. 8. Variation of NDD with dimensionless damping coefficient ξ (η = 0.7 , L = 10 nm)

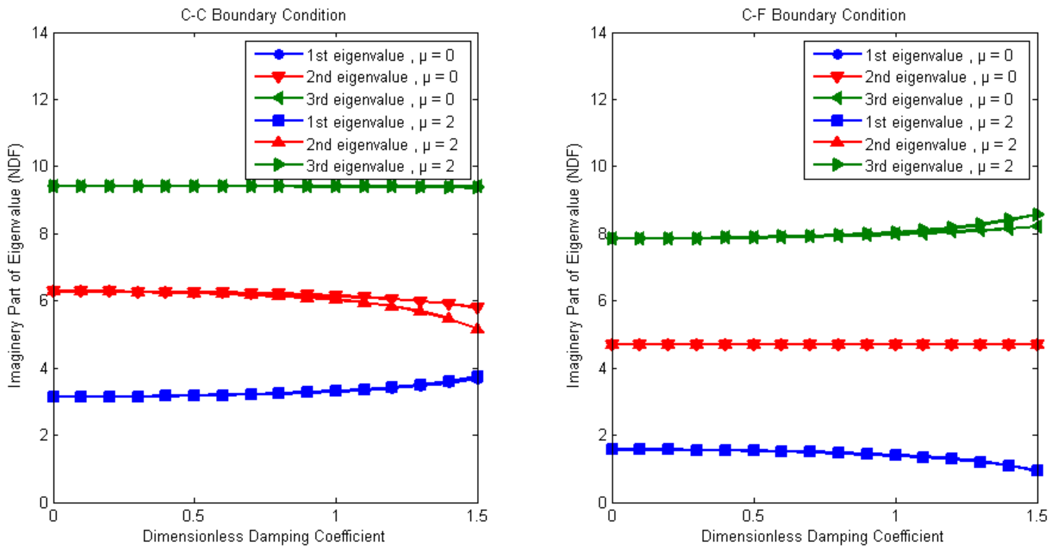

Fig. 9. Variation of NDF with dimensionless damping coefficient ξ (η = 0.7 , L = 30 nm)

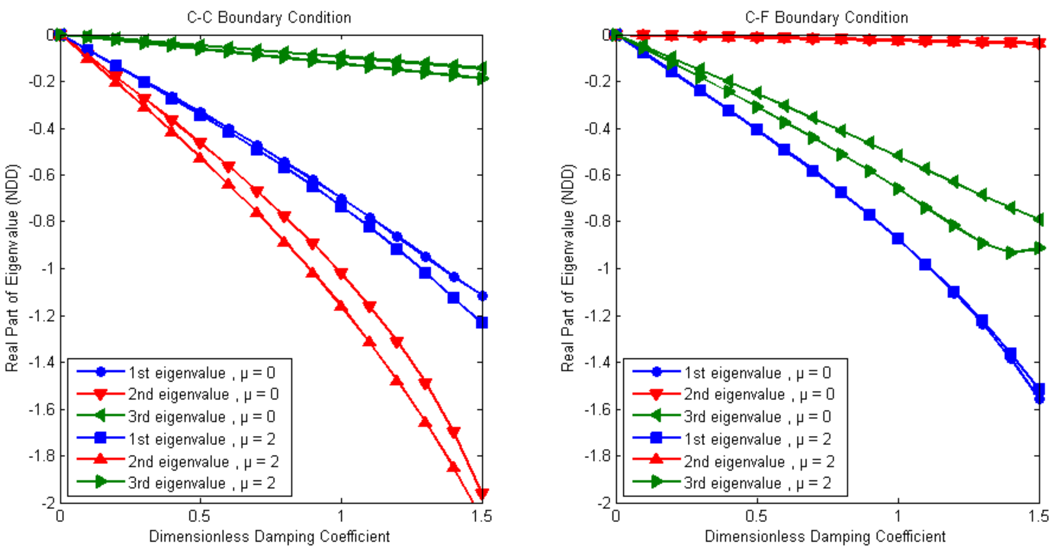

Fig. 10. Variation of NDD with dimensionless damping coefficient ξ (η = 0.7 , L = 30 nm)

For the C-F boundary condition, first and second NDF decreases and third NDF increases with increasing η and reaches a maximum value at η = 1 (See Table (2) and (3)).

Nanotube length has effect on NDF and NDD only for the nonlocal results. The local results (μ=0) are not affected by change of nanotube length (See Table (2) and (3)). This is an expected result from the classical theory. The NDF increases and the NDD decreases with increasing nanotube length in the nonlocal case.

Damping ratio (ξ) increases with increasing dimensionless damping coefficient (D) generally. Attachment point of damper increases damping ratio in C-F case when η is approaching to 1. In C-C case, damping ratio reaches maximum value at η = 0.5. For longer nanotube length, local and nonlocal damping ratios have very close values, since bigger nanotube length reduces the nonlocal effect.

Table 2 Characteristic values of nanorod for C-C boundary condition

			Dimensionless Damping Coefficient (D)			
			$\xi = 0.5$		$\xi = 1.5$	
η	L (nm)		μ=0 nm^2	μ=2 nm^2	μ=0 nm^2	μ=2 nm^2
0.3	10	$\overline{\beta_1}$	-0.3326+3.1744i	-0.4490+3.1663i	-1.1147+3.6824i	-1.8652+2.7424i
		$\overline{\beta_2}$	-0.4647+6.2550i	-0.9872+5.8387i	-1.9599+5.7909i	-0.6720+4.5281i
		$\overline{\beta_3}$	-0.0478+9.4219i	-0.2102+9.3442i	-0.1444+9.3969i	-0.2031+9.0587i
	30	$\overline{\beta_1}$	-0.3326+3.1744i	-0.3446+3.1742i	-1.1147+3.6824i	-1.2340+3.7502i
		$\overline{\beta_2}$	-0.4647+6.2550i	-0.5283+6.2350i	-1.9599+5.7909i	-2.0674+5.1729i
		$\overline{\beta_3}$	-0.0478+9.4219i	-0.0626+9.4197i	-0.1444+9.3969i	-0.1875+9.3721i
0.5	10	$\overline{\beta_1}$	-0.5108+3.1416i	-0.6617+3.0680i	-1.9459+3.1416i	-1.8301+2.2991i
		$\overline{\beta_2}$	0+6.2832i	0+6.2832i	0+6.2832i	0+6.2832i
		$\overline{\beta_3}$	-0.5108+9.4248i	-1.6761+8.1626i	-1.9459+9.4248i	-1.0926+6.6017i
	30	$\overline{\beta_1}$	-0.5108+3.1416i	-0.5279+3.1356i	-1.9459+3.1416i	-1.9958+2.9986i
		$\overline{\beta_2}$	0+6.2832i	0+6.2832i	0+6.2832i	0+6.2832i
		$\overline{\beta_3}$	-0.5108+9.4248i	-0.6780+9.3988i	-1.9459+9.4248i	-2.5840+8.4288i
0.7	10	$\overline{\beta_1}$	-0.3326+3.1744i	-0.4490+3.1663i	-1.1147+3.6824i	-1.8652+2.7424i
		$\overline{\beta_2}$	-0.4647+6.2550i	-0.9872+5.8387i	-1.9599+5.7909i	-0.6720+4.5281i
		$\overline{\beta_3}$	-0.0478+9.4219i	-0.2102+9.3442i	-0.1444+9.3969i	-0.2031+9.0587i
	30	$\overline{\beta_1}$	-0.3326+3.1744i	-0.3446+3.1742i	-1.1147+3.6824i	-1.2340+3.7502i
		$\overline{\beta_2}$	-0.4647+6.2550i	-0.5283+6.2350i	-1.9599+5.7909i	-2.0674+5.1729i
		$\overline{\beta_3}$	-0.0478+9.4219i	-0.0626+9.4197i	-0.1444+9.3969i	-0.1875+9.3721i

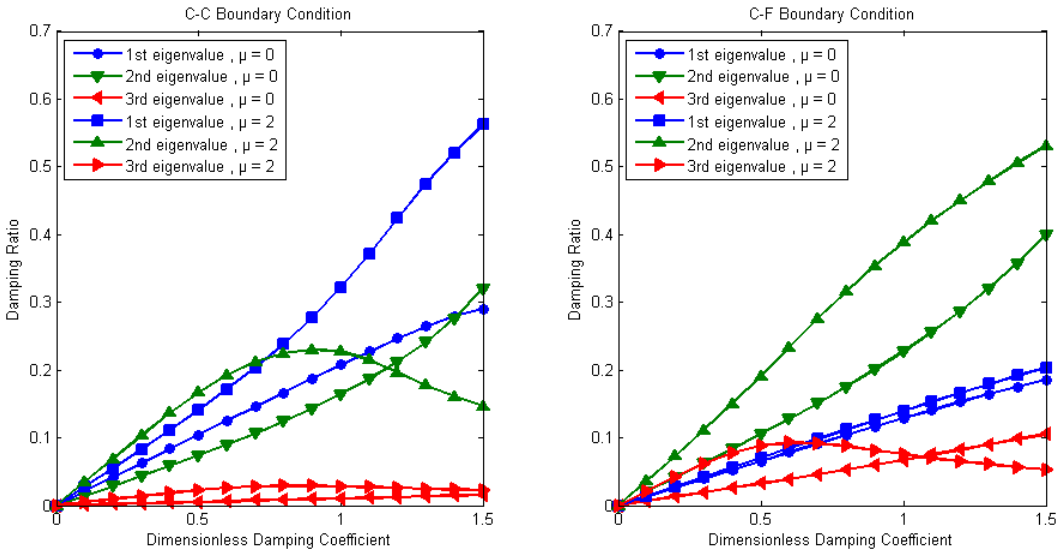

Fig. 11. Variation of damping ratio (ξ) with dimensionless damping coefficient D (η = 0.3, L = 10 nm)

Table 3 Characteristic values of nanorod for C-F boundary condition

			Dimensionless Damping Coefficient (D)			
			ξ = 0.5		ξ = 1.5	
η	L (nm)		μ=0 nm^2	μ=2 nm^2	μ=0 nm^2	μ=2 nm^2
0.3	10	$\overline{\beta_1}$	-0.1034+1.5793i	-0.1114+1.5796i	-0.3136+1.6625i	-0.3472+1.6707i
		$\overline{\beta_2}$	-0.5029+4.7284i	-0.8914+4.5744i	-2.1677+4.9632i	-1.9622+3.1264i
		$\overline{\beta_3}$	-0.2527+7.8278i	-0.6570+7.4139i	-0.7900+7.4916i	-0.3603+6.8108i
	30	$\overline{\beta_1}$	-0.1034+1.5793i	-0.1043+1.5793i	-0.3136+1.6625i	-0.3171+1.6634i
		$\overline{\beta_2}$	-0.5029+4.7284i	-0.5435+4.7215i	-2.1677+4.9632i	-2.4331+4.5761i
		$\overline{\beta_3}$	-0.2527+7.8278i	-0.3060+7.8105i	-0.7900+7.4916i	-0.8028+7.2631i
0.5	10	$\overline{\beta_1}$	-0.2554+1.5708i	-0.2746+1.5637i	-0.9730+1.5708i	-1.0051+1.4147i
		$\overline{\beta_2}$	-0.2554+4.7124i	-0.4559+4.6657i	-0.9730+4.7124i	-1.1215+3.7590i
		$\overline{\beta_3}$	-0.2554+7.8540i	-0.9220+7.5255i	-0.9730+7.8540i	-0.6012+6.3805i
	30	$\overline{\beta_1}$	-0.2554+1.5708i	-0.2575+1.5701i	-0.9730+1.5708i	-0.9810+1.5531i
		$\overline{\beta_2}$	-0.2554+4.7124i	-0.2754+4.7100i	-0.9730+4.7124i	-1.0979+4.6400i
		$\overline{\beta_3}$	-0.2554+7.8540i	-0.3128+7.8492i	-0.9730+7.8540i	-1.3783+7.5994i
0.7	10	$\overline{\beta_1}$	-0.4058+1.5368i	-0.4298+1.5150i	-1.5566+0.9318i	-1.3030+0.8760i
		$\overline{\beta_2}$	-0.0122+4.7120i	-0.0212+4.7112i	-0.0368+4.7089i	-0.0636+4.7006i
		$\overline{\beta_3}$	-0.2527+7.8801i	-1.3054+7.8292i	-0.7900+8.2164i	-1.4398+5.7877i
	30	$\overline{\beta_1}$	-0.4058+1.5368i	-0.4086+1.5345i	-1.5566+0.9318i	-1.5149+0.9222i
		$\overline{\beta_2}$	-0.0122+4.7120i	-0.0132+4.7119i	-0.0368+4.7089i	-0.0396+4.7083i
		$\overline{\beta_2}$	-0.2527+7.8801i	-0.3095+7.8888i	-0.7900+8.2164i	-0.9144+8.5625i

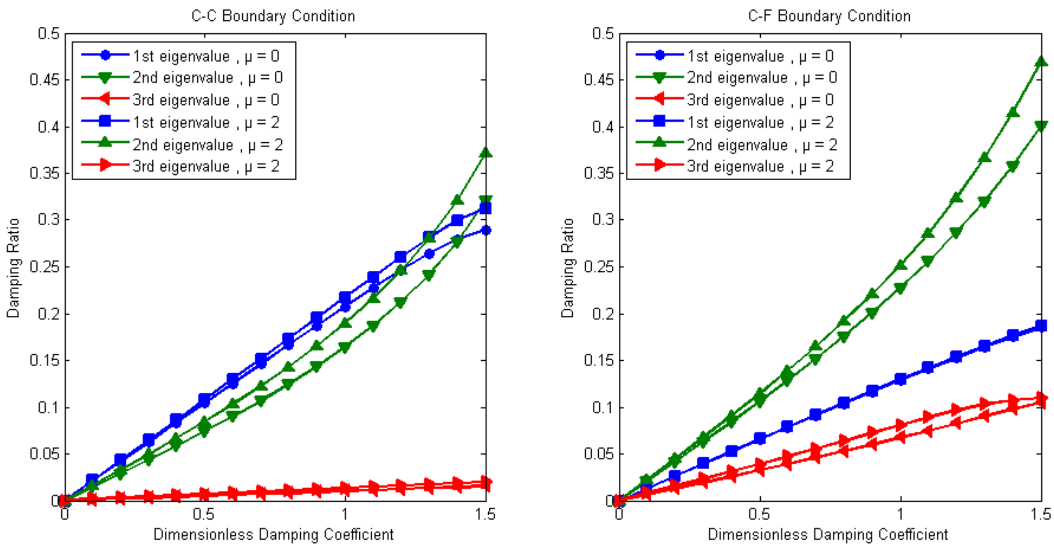

Fig. 12. Variation of damping ratio (ξ) with dimensionless damping coefficient D (η = 0.3, L = 30 nm)

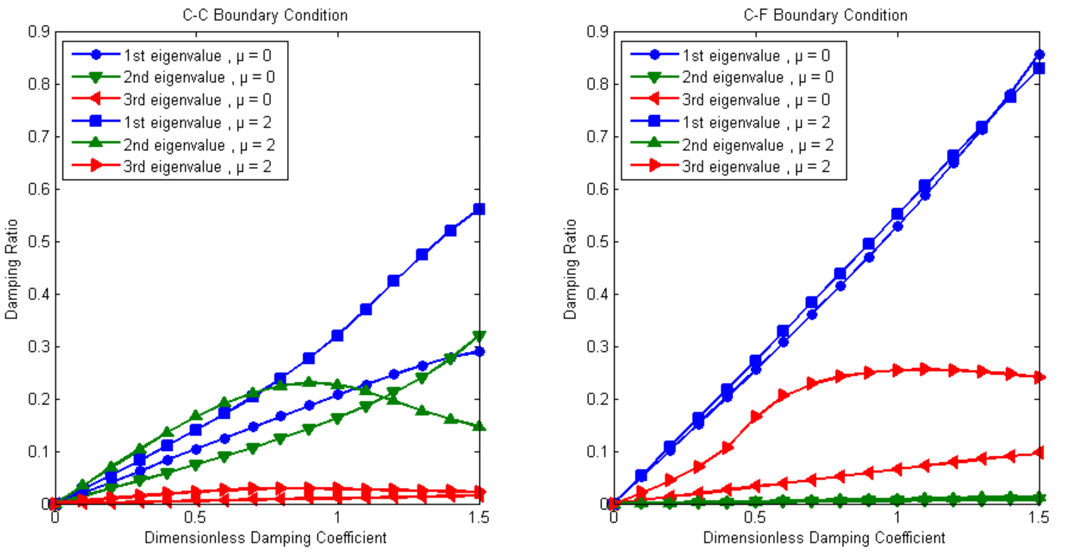

Fig. 13. Variation of damping ratio (ξ) with dimensionless damping coefficient D (η = 0.7, L = 10 nm)

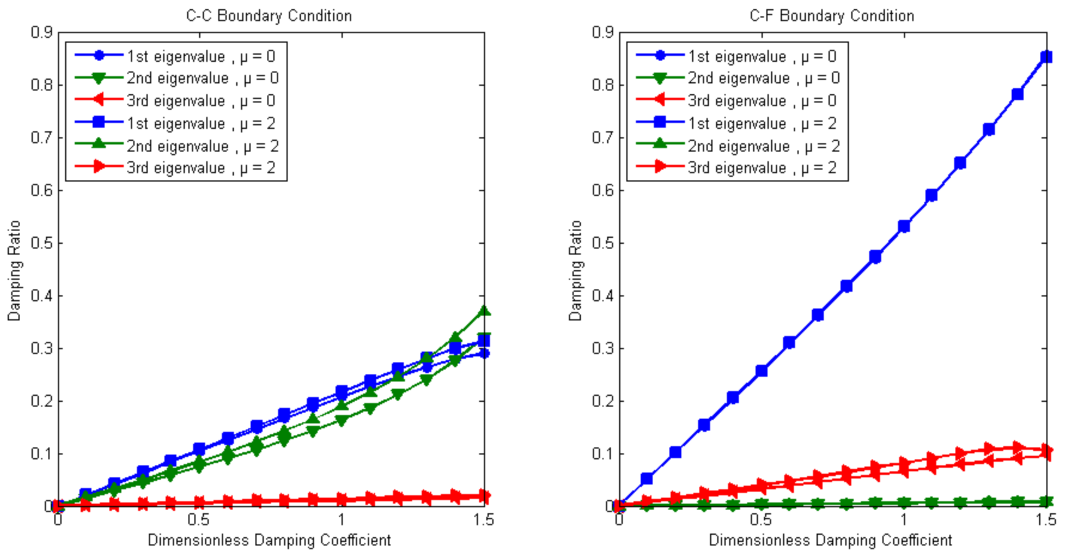

Fig. 14. Variation of damping ratio (ξ) with dimensionless damping coefficient D (η = 0.7, L = 30 nm)

Damping ratio (ξ) increases with increasing dimensionless damping coefficient (D) generally. Attachment point of damper increases damping ratio in C-F case when η is approaching to 1. In C-C case, damping ratio reaches maximum value at η = 0.5. For longer nanotube length, local and nonlocal damping ratios have very close values, since bigger nanotube length reduces the nonlocal effect.

4. Conclusions

Free longitudinal vibration of damped nanotube with attached a viscous damper is investigated in the present study. Effects of some parameters like dimensionless damping coefficient (D), nonlocal parameter (μ), attachment point of damper (η) and nanotube length (L) to the non-dimensional frequency (NDF), non-dimensional damping (NDD) and damping ratio (ξ) of nanorod is studied. Following results are obtained from the present study:

- The dimensionless damping coefficient (D) is effected by NDF differently depending on the attachment point of damper (η). NDD always increases with increasing D.
- The Nonlocal parameter (μ) has a decreasing effect on NDF whereas it has an increasing effect on NDD. Also μ is more effective in smaller nanotube length.
- NDD reaches a maximum value at $\eta = 0.5$ in C-C case and $\eta = 1$ in C-F case.
- Nanotube length (L) is effective only in nonlocal case ($\mu \neq 0$). NDF increases and NDD decreases with increasing L.
- Damping ratio (ξ) increases with increasing dimensionless damping coefficient (D) in C-F case. In C-C case, it reaches a maximum value at $\eta = 0.5$. Bigger nanotube length reduces nonlocal effect.

References

[1] Iijima, S., Helical microtubules of graphitic carbon, Nature, 354, 56–8, 1991. doi:10.1038/354056a0

[2] He, H., Pham-Huy, L.A., Dramou, P., Xiao, D., Zuo, P., Pham-Huy, C., Carbon nanotubes: Applications in pharmacy and medicine, BioMed Research International, 2013, 2013. doi:10.1155/2013/578290

[3] Marchesan, S., Kostarelos, K., Bianco, A., Prato, M., The winding road for carbon nanotubes in nanomedicine, Materials Today, 18, 12–9, 2015. doi:10.1016/j.mattod.2014.07.009

[4] Bourlon, B., Glattli, D.C., Miko, C., Forró, L., Bachtold, A., Carbon Nanotube Based Bearing for Rotational Motions, Nano Letters, 4, 709–12, 2004. doi:10.1021/nl035217g

[5] Kimoto, Y., Mori, H., Mikami, T., Akita, S., Nakayama, Y., Higashi, K., et al., Molecular Dynamics Study of Double-Walled Carbon Nanotubes for Nano-Mechanical Manipulation, Japanese Journal of Applied Physics, 44, 1641, 2005. doi:10.1143/JJAP.44.1641

[6] Von Oppen, F., Guinea, F., Mariani, E., Synthetic electric fields and phonon damping in carbon nanotubes and graphene, Physical Review B - Condensed Matter and Materials Physics, 80, 1–11, 2009. doi:10.1103/PhysRevB.80.075420

[7] Falk, K., Sedlmeier, F., Joly, L., Netz, R.R., Bocquet, L., Molecular origin of fast water transport in carbon nanotube membranes: Superlubricity versus curvature dependent friction, Nano Letters, 10, 4067–73, 2010. doi:10.1021/nl1021046

[8] Miyako, E., Kono, K., Yuba, E., Hosokawa, C., Nagai, H., Hagihara, Y., Carbon nanotube-liposome supramolecular nanotrains for intelligent molecular-transport systems., Nature Communications, 3, 1226, 2012. doi:10.1038/ncomms2233

[9] Eringen, A.C., Nonlocal polar elastic continua, International Journal of Engineering Science, 10, 1–16, 1972. doi:10.1016/0020-7225(72)90070-5

[10] Eringen, A.C., On differential equations of nonlocal elasticity and solutions of screw dislocation and surface waves, Journal of Applied Physics, 54, 4703–10, 1983. doi:10.1063/1.332803

[11] Khademolhosseini, F., Phani, A.S., Nojeh, A., Rajapakse, N., Nonlocal continuum modeling and molecular dynamics simulation of torsional vibration of carbon nanotubes, IEEE Transactions on Nanotechnology, 11, 34–43, 2012. doi:10.1109/TNANO.2011.2111380

[12] Aydogdu, M., Longitudinal wave propagation in multiwalled carbon nanotubes, Composite Structures, 107, 578–84, 2014. doi:10.1016/j.compstruct.2013.08.031

[13] Chen, C., Ma, M., Zhe Liu, J., Zheng, Q., Xu, Z., Viscous damping of nanobeam resonators: Humidity, thermal noise, and a paddling effect, Journal of Applied Physics, 110, 2011. doi:10.1063/1.3619854

[14] Wang, C.Y.Y., Li, C.F.F., Adhikari, S., Axisymmetric vibration of single-walled carbon nanotubes in water, Physics Letters A, 374, 2467–74, 2010. doi:10.1016/j.physleta.2010.04.002

[15] Rinaldi, S., Prabhakar, S., Vengallatore, S., Païdoussis, M.P., Dynamics of microscale pipes containing internal fluid flow: Damping, frequency shift, and stability, Journal of Sound and Vibration, 329, 1081–8, 2010. doi:10.1016/j.jsv.2009.10.025

[16] Ghavanloo, E., Daneshmand, F., Rafiei, M., Vibration and instability analysis of carbon nanotubes conveying fluid and resting on a linear viscoelastic Winkler foundation, Physica E: Low-Dimensional Systems and Nanostructures, 42, 2218–24, 2010. doi:10.1016/j.physe.2010.04.024

[17] Ghavanloo, E., Daneshmand, F., Amabili, M., Vibration analysis of a single microtubule surrounded by cytoplasm, Physica E: Low-Dimensional Systems and Nanostructures, 43, 192–8, 2010. doi:10.1016/j.physe.2010.07.016

[18] Ghavanloo, E., Rafiei, M., Daneshmand, F., In-plane vibration analysis of curved carbon nanotubes conveying fluid embedded in viscoelastic medium, Physics Letters A, 375, 1994–9, 2011. doi:10.1016/j.physleta.2011.03.025

[19] Ghavanloo, E., Fazelzadeh, S.A., Flow-thermoelastic vibration and instability analysis of viscoelastic carbon nanotubes embedded in viscous fluid, Physica E: Low-Dimensional Systems and Nanostructures, 44, 17–24, 2011. doi:10.1016/j.physe.2011.06.024

[20] Yun, K., Choi, J., Kim, S.-K., Song O, Flow-induced vibration and stability analysis of multi-wall carbon nanotubes, Journal of Mechanical Science and Technology, 26, 3911–20, 2012. doi:10.1007/s12206-012-0888-3

[21] Zeighampour, H., Tadi Beni, Y., Size-dependent vibration of fluid-conveying double-walled carbon nanotubes using couple stress shell theory, Physica E: Low-Dimensional Systems and Nanostructures, 61, 28–39, 2014. doi:10.1016/j.physe.2014.03.011

[22] Martin, M.J., Houston, B.H., Gas damping of carbon nanotube oscillators, Applied Physics Letters, 91, 103116, 2007. doi:10.1063/1.2779973

[23] Aydogdu, M., On the vibration of aligned carbon nanotube reinforced composite beams, Advances in Nano Research, 2, 199–210, 2014

[24] Chemi, A., Heireche, H., Zidour, M., Rakrak, K., Bousahla, A.A., Critical buckling load of chiral double-walled carbon nanotube using non-local theory elasticity, Advances in Nano

Research, 3, 193–206, 2015. doi:10.12989/anr.2015.3.4.193

[25] Aydogdu, M., Arda, M., Forced vibration of nanorods using nonlocal elasticity, Advances in Nano Research, 4, 265–79, 2016. doi:10.12989/anr.2016.4.4.265

[26] Soltani, P., Taherian, M.M., Farshidianfar, A., Vibration and instability of a viscous-fluid-conveying single-walled carbon nanotube embedded in a visco-elastic medium, Journal of Physics D: Applied Physics, 43, 425401, 2010. doi:10.1088/0022-3727/43/42/425401

[27] Zhen, Y.-X., Fang, B., Tang, Y., Thermal–mechanical vibration and instability analysis of fluid-conveying double walled carbon nanotubes embedded in visco-elastic medium, Physica E: Low-Dimensional Systems and Nanostructures, 44, 379–85, 2011. doi:10.1016/j.physe.2011.09.004

[28] Hoseinzadeh, M.S., Khadem, S.E., Thermoelastic vibration and damping analysis of double-walled carbon nanotubes based on shell theory, Physica E: Low-Dimensional Systems and Nanostructures, 43, 1146–54, 2011. doi:10.1016/j.physe.2011.01.013

[29] Hoseinzadeh, M.S., Khadem, S.E., A nonlocal shell theory model for evaluation of thermoelastic damping in the vibration of a double-walled carbon nanotube, Physica E: Low-Dimensional Systems and Nanostructures, 57, 6–11, 2014. doi:10.1016/j.physe.2013.10.009

[30] Hajnayeb, A., Khadem, S.E., Zamanian, M., Thermoelastic damping of a double-walled carbon nanotube under electrostatic force, Micro & Nano Letters, 6, 698, 2011. doi:10.1049/mnl.2011.0193

[31] Schmid, D.R., Stiller, P.L., Strunk, C., Hüttel, a K., Magnetic damping of a carbon nanotube nano-electromechanical resonator, New Journal of Physics, 14, 83024, 2012. doi:10.1088/1367-2630/14/8/083024

[32] Chang, W.-J., Lee, H.-L., Vibration analysis of viscoelastic carbon nanotubes, Micro & Nano Letters, 7, 1308–12, 2012. doi:10.1049/mnl.2012.0612

[33] Hizal, N.A., Gürgöze, M., Lumped parameter representation of a longitudinally vibrating elastic rod viscously damped in-span, Journal of Sound and Vibration, 216, 328–36, 1998. doi:10.1006/jsvi.1998.1685

[34] Yüksel, Ş., Gürgöze, M., Continuous and discrete models for longitudinally vibrating elastic rods viscously damped in-span, Journal of Sound and Vibration, 257, 996–1006, 2002. doi:10.1006/jsvi.5032

[35] Yüksel, Ş., Dalli, U., Longitudinally vibrating elastic rods with locally and non-locally reacting viscous dampers, Shock and Vibration, 12, 109–18, 2005

[36] Zhou, Z., Qian, D., Yu, M.-F., A Computational Study on the Transversal Visco-Elastic Properties of Single Walled Carbon Nanotubes and Their Relation to the Damping Mechanism, Journal of Computational and Theoretical Nanoscience, 8, 820–30, 2010

[37] Jeong, B., Cho, H., Yu, M.-F., Vakakis, A.F., McFarland, D.M., Bergman, L.A., Modeling and Measurement of Geometrically Nonlinear Damping in a Microcantilever–Nanotube System, ACS Nano, 7, 8547–53, 2013. doi:10.1021/nn402479d

[38] Adhikari, S., Murmu, T., McCarthy, M.A., Dynamic finite element analysis of axially vibrating nonlocal rods, Finite Elements in Analysis and Design, 63, 42–50, 2013. doi:10.1016/j.finel.2012.08.001

[39] Lei, Y., Adhikari, S., Murmu, T., Friswell, M.I., Asymptotic frequencies of various damped nonlocal beams and plates, Mechanics Research Communications, 62, 94–101, 2014. doi:10.1016/j.mechrescom.2014.08.002

[40] Ghorbanpour Arani, A., Amir, S., Dashti, P., Yousefi, M., Flow-induced vibration of double bonded visco-CNTs under magnetic fields considering surface effect, Computational Materials Science, 86, 144–54, 2014. doi:10.1016/j.commatsci.2014.01.047

[41] Karličić, D., Cajić, M., Murmu, T., Adhikari, S., Nonlocal longitudinal vibration of viscoelastic coupled double-nanorod systems, European Journal of Mechanics - A/Solids, 49, 183–96, 2015. doi:10.1016/j.euromechsol.2014.07.005

[42] Erol, H., Gürgöze, M., Longitudinal vibrations of a double-rod system coupled by springs and dampers, Journal of Sound and Vibration, 276, 419–30, 2004. doi:10.1016/j.jsv.2003.10.043

[43] Buchoux, J., Aimé, J.-P., Boisgard, R., Nguyen, C.V., Buchaillot, L., Marsaudon, S., Investigation of the carbon nanotube AFM tip contacts: free sliding versus pinned contact., Nanotechnology, 20, 475701/8pp, 2009. doi:10.1088/0957-4484/20/47/475701

[44] Eichler, A., Moser, J., Chaste, J., Zdrojek, M., Wilson-Rae, I., Bachtold, A., Nonlinear damping in mechanical resonators made from carbon nanotubes and graphene, Nat Nano, 6, 339–42, 2011

[45] Li, J., Bi, K., Chen, M., Chen, Y., The oscillatory damped behavior of double wall carbon nanotube oscillators in gaseous environment, Science in China, Series E: Technological Sciences, 52, 916–21, 2009. doi:10.1007/s11431-009-0073-9

[46] Barnard, A.W., Sazonova, V., van der Zande, A.M., McEuen, P.L., Fluctuation broadening in carbon nanotube resonators., Proceedings of the National Academy of Sciences of the United States of America, 109, 19093–6, 2012. doi:10.1073/pnas.1216407109

[47] Hüttel, A.K., Steele, G.A., Witkamp, B., Poot, M., Kouwenhoven, L.P., Van Der Zant, H.S.J., Carbon nanotubes as ultrahigh quality factor mechanical resonators, Nano Letters, 9, 2547–52, 2009. doi:10.1021/nl900612h

[48] Aydogdu, M., Elishakoff, I., On the vibration of nanorods restrained by a linear spring in-span, Mechanics Research Communications, 57, 90–6, 2014. doi:10.1016/j.mechrescom.2014.03.003

International Journal of Engineering & Applied Sciences (IJEAS)
Vol.9, Issue 2 (Special Issue: Composite Structures) (2017) 39-54
http://dx.doi.org/10.24107/ijeas.303299
Int J Eng Appl Sci 9(2) (2017) 39-54

Vibration Characteristics of Axially Moving Titanium- Polymer Nanocomposite Faced Sandwich Plate Under Initial Tension

Ali Ghorbanpour Arani [a], Elham Haghparast [a] and Hassan BabaAkbar Zarei [a]*

[a] *Faculty of Mechanical Engineering, Institute of Nanoscience& Nanotechnology, University of Kashan, Kashan, Iran*
[*] *E-mail address*: aghorban@kashanu.ac.ir

Received date: March 2017

Abstract

In the present research, vibration and instability of axially moving sandwich plate made of soft core and composite face sheets under initial tension is investigated. Single-walled carbon nano-tubes (SWCNTs) are selected as a reinforcement of composite face sheets inside Poly methyl methacrylate (PMMA) matrix. Higher order shear deformation theory (HSDT) is utilized due to its accuracy of polynomial functions than other plate theories. Based on extended rule of mixture, the structural properties of composite face sheets are taken into consideration. Motion equations are obtained by means of Hamilton's principle and solved analytically. Influences of various parameters such as axially moving speed, volume fraction of CNTs, pre-tension, thickness and aspect ratio of sandwich plate on the vibration characteristics of moving system are discussed in details. The results indicated that the critical speed of moving sandwich plate is strongly dependent on the volume fraction of CNTs. Therefore, the critical speed of moving sandwich plate can be improved by adding appropriate values of CNTs. The results of this investigation can be used in design and manufacturing of marine vessels and aircrafts.

Keywords: Vibration analysis; Axially moving; sandwich plate; Nanocomposite face sheets, Initial tension.

1. Introduction

The use of sandwich structures in the world is increasingly growing. In today's modern engineering, sandwich structures are being used successfully for a variety of applications such as aircraft, wind turbine blades, spacecraft, train and car structures, boat/ship hulls boat/ship superstructures and many others. This is due to the excellent mechanical properties of these structures (High strength to weight ratio, high resistance to impact, flexibility and etc.). Most of sandwich structures are composed of three layers: the top layer, middle layer that is called the core and the bottom layer. The core is less stiff compared to other two-layer. Hence, selecting the appropriate material for the core and the other layer is a significant for optimum design of sandwich structures. Carbon nanotube-reinforced composite can be an excellent option for the top and bottom layers due to the high stiffness and the other supreme properties. In this regard, study on vibration and instability of sandwich structures which are reinforced by carbon fibers have been conducted by many researchers that some of them are presented below.

Thostenson and Chou [1] have modelled the elastic properties of carbon nanotube-reinforced composite. Investigation of the structure/size influence of carbon nanotubes on the elastic properties of nanotube-based composites is the main objective of their research. Zhou et al. [2] analyzed the static and free vibration of carbon nanotube-reinforced composite plates using finite element method with first order shear deformation plate theory (FSDT). They have studied on the influences of the volume fractions of carbon nanotubes and the edge-to-thickness ratios on the bending responses, natural frequencies and mode shapes of the plates. Also, Lei et al. [3] have done similar work before, but they used the element free kP-Ritz method in thermal environment. Bending behavior of functionally graded carbon nanotube reinforced composite (FG-CNTRC) plate embedded in thin piezoelectric layers subjected to mechanical uniform load is investigated by Alibeigloo [4]. He applied simply supported boundary conditions on plate and used three-dimensional elasticity theory to analyze bending behavior of composite plate.

In recent years, with the advance of industry, there was a need for structures with multiple capabilities simultaneously. One of the requirements was answered by the discovery of sandwich structures. Thus, researchers have been working in this field. Nayak et al. [5] investigated free vibration analysis of composite sandwich plates based on Reddy's higher-order theory. Using this theory that they have provided, it can be calculated the natural frequencies of isotropic, orthotropic, and layered anisotropic composite and sandwich plates. Utilizing radial basis collocation function, Ferreira et al. [6] analyzed the static, buckling and vibration responses of the plate. Khalili and Mohammadi [7] used improved high-order sandwich plate to analyze the free vibration of sandwich plates with FG face sheets. The material properties of FG face sheets and core are considered to be temperature-dependent by a third-order function of temperature. Recently, Sahoo and Singh [8] proposed a new trigonometric zigzag theory to analyze the static analysis of laminated composite and sandwich plates. They assumed shear strain shape function for non-linear distribution of in-plane displacement across the thickness. Thai et al. [9] presented a new first-order shear deformation theory for functionally graded sandwich plates composed of isotropic core and functionally graded face sheets. They approved that the presented theory is accurate in predicting the bending, buckling and free vibration responses of FG sandwich plates. In another work, Plagianakos and Papadopoulos [10] presented coupled higher-order layerwise piezoelectric laminate mechanics. Their developed model was applicable to predict the static electromechanical response of composite and sandwich composite plates subjected to static mechanical loads and/or electric voltages. Natarajan et al. [11] have attempted to achieve an efficient solution for the bending and free vibration analysis of sandwich plates with CNT reinforced composite face sheets. For this purpose, they have used QUAD-8 shear flexible element developed based on higher-order structural theory. This theory considered the possible discontinuity in slope at the interfaces layers, the realistic variation of the displacements through the thickness, and the thickness stretch effects on the transverse deflection. Kheirikhah et al. [12] carried out biaxial buckling analysis of soft-core composite sandwich plates. In this way, they employed third-order plate theory for face sheets and quadratic and cubic functions for transverse and in-plane displacements of the core, respectively. Moreover, analytical solution has been presented for sandwich plates with simply supported boundary conditions under biaxial in-plane compressive loads using Navier's solution.

Axially moving beams and plates have attracted many authors. The geometrically nonlinear dynamics and stability of an axially moving plate is presented by Ghayesh et al. [13]. In their study, plate is placed under an out-of-plane incitement load and the frequency–response curves of the system are plotted. Also, Dong Yang et al. [14] have been working on the previous thread. To solve the differential equations governing the problem, they have used both the Galerkin method and differential quadrature method. In the case of free vibration analysis of axially moving viscoelastic plates, Hatami et al. [15] and Marynowski [16] have studied. However, each of them has used different models for their work. Marynowski and Grabski [17] have investigated dynamic analysis of an axially moving plate subjected to thermal loading using the extended Galerkin method the. In addition, they have been examined the effects of transport speed, the thermal critical loading and axial tension on dynamic behavior of axially moving aluminum plate.

Despite mentioned researches, vibration and instability analysis of axially moving sandwich plate under initial tension using HSDT is a novel topic that cannot be found in literature. To the best of authors' knowledge, for the first time, analysis of axially moving sandwich plate with CNT face sheets is developed in this paper. Material properties of composite plate are obtained based on extended rule of mixture. Motions equations are obtained based on energy method and solved by means of analytical approach. Influences of various parameters such as moving speed, volume fraction of CNTs, pre-tension load, thickness and aspect ratio on instability and critical speed of moving composite sandwich plate are discussed in details. To verify the presented method, the natural frequencies for stationary sandwich plate have been compared with previous researches. The result of this work can be useful to control and improve the performance of axially moving devices which are employed in military equipment.

2. Potential energies of axially moving sandwich plate

Consider a rectangular sandwich plate with length (*a*), width (*b*) and thickness ($h = h^t + h^c + h^b$) which is shown in Fig.1. The top and bottom layers are made of carbon nanotube-reinforced composite plate. The carbon nanotube is distributed uniformly in the x direction. The Cartesian coordinate system is selected for this problem. *x* and *y* axes are located in the mid-plane and *z* axis located along the thickness direction. Sandwich plate is moving along the *x* direction with the constant velocity *V*.

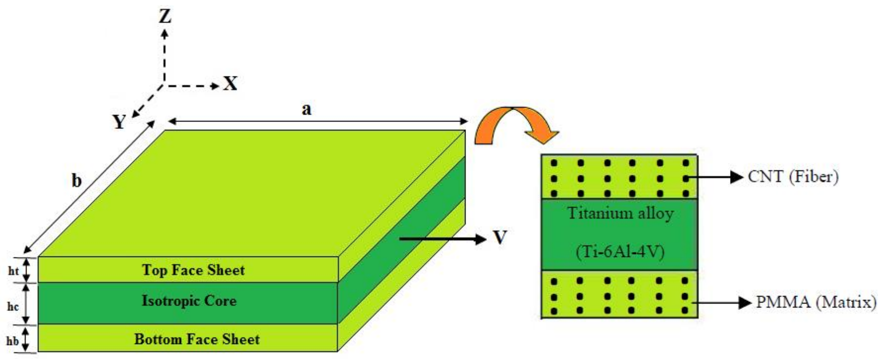

Fig. 1. Schematic figure of axially moving sandwich plate with CNT reinforced face sheets.

The following assumptions have been used to derive motion equations [18 and 19]:

- The core thickness is larger and softer than the top and bottom layer.
- The core is fully bonded with the top and bottom layers. Thus, core and the top layer have the same displacement in ($z = +h^c/2$) as well as the core and the bottom layer in ($z = -h^c/2$),
- No slipping happens at the interfaces between the three layers of the sandwich plate.

Because the core is made of a soft material, to increase the accuracy of results a higher-order theory will be used. According to this theory, the displacement field of the sandwich plate can be expressed as [20]:

$$\begin{aligned}
&u(x, y, z, t) = u_0(x, y, t)+zu_1(x, y, t)+z^2u_2(x, y, t)+z^3u_3(x, y, t),\\
&v(x, y, z, t) = v_0(x, y, t)+zv_1(x, y, t)+z^2v_2(x, y, t)+z^3v_3(x, y, t),\\
&w(x, y, z, t) = w_0(x, y, t)+zw_1(x, y, t)+z^2w_2(x, y, t),
\end{aligned} \tag{1}$$

in which, u_j, v_j and w_k ($j = 0,1,2,3$ and $k = 0,1,2$) are the unknowns of the displacement components of the sandwich plate. In this manner, eleven displacements are unknowns.

The linear von-Karman strain-displacement relations can be defined as:

$$\begin{aligned}
&\varepsilon^{i}_{xx} = u_{,x} = u_{0,x} + zu_{1,x} + z^2u_{2,x} + z^3u_{3,x},\\
&\varepsilon^{i}_{yy} = v_{,y} = v_{0,y} + zv_{1,y} + z^2v_{2,y} + z^3v_{3,y},\\
&\varepsilon^{i}_{zz} = w_{,z} = w_1 + 2zw_2,\\
&\varepsilon^{i}_{xy} = \frac{1}{2}(v_{,x} + u_{,y}) = \frac{1}{2}v_{0,x} + \frac{1}{2}zv_{1,x} + \frac{1}{2}z^{2}v_{2,x} + \frac{1}{2}z^{3}v_{3,x} + \frac{1}{2}u_{0,y} + \frac{1}{2}zu_{1,y} + \frac{1}{2}z^{2}u_{2,y} + \frac{1}{2}z^{3}u_{3,y},\\
&\varepsilon^{i}_{xz} = \frac{1}{2}(w_{,x} + u_{,z}) = \frac{1}{2}w_{0,x} + \frac{1}{2}zw_{1,x} + \frac{1}{2}z^{2}w_{2,x} + \frac{1}{2}u_1 + zu_2 + \frac{3}{2}z^2u_3,\\
&\varepsilon^{i}_{yz} = \frac{1}{2}(w_{,y} + \frac{\partial}{\partial z}v_{,z}) = \frac{1}{2}w_{0,y} + \frac{1}{2}zw_{1,y} + \frac{1}{2}z^{2}w_{2,y} + \frac{1}{2}v_1 + zv_2 + \frac{3}{2}z^2v_3,
\end{aligned} \tag{2}$$

where ε^{i}_{pq} ($p,q = x,y,z$ and $i = t,c,b$) is strain of ith layers. It is obvious that all layers have the same strain due to considering similar displacement field for all of them. The constitutive equations for sandwich plate can be obtained as [12]:

$$\begin{Bmatrix} \sigma^i_{xx} \\ \sigma^i_{yy} \\ \sigma^i_{zz} \\ \sigma^i_{yz} \\ \sigma^i_{xz} \\ \sigma^i_{xy} \end{Bmatrix} = \begin{bmatrix} Q^i_{11} & Q^i_{12} & Q^i_{13} & 0 & 0 & 0 \\ Q^i_{12} & Q^i_{22} & Q^i_{23} & 0 & 0 & 0 \\ Q^i_{13} & Q^i_{23} & Q^i_{33} & 0 & 0 & 0 \\ 0 & 0 & 0 & Q^i_{44} & 0 & 0 \\ 0 & 0 & 0 & 0 & Q^i_{55} & 0 \\ 0 & 0 & 0 & 0 & 0 & Q^i_{66} \end{bmatrix} \begin{Bmatrix} \varepsilon^i_{xx} \\ \varepsilon^i_{yy} \\ \varepsilon^i_{zz} \\ \varepsilon^i_{yz} \\ \varepsilon^i_{xz} \\ \varepsilon^i_{xy} \end{Bmatrix}, \tag{3}$$

where σ^{i}_{pq} and Q^{i}_{rs} ($r,s = 1,2,3$ and $44,55,66$) are stress and the stiffness coefficient matrix of ith layers, respectively. In this paper, the stiffness coefficients is defined for plain strain problems with isotropic core (Q^{c}_{rs}), orthotropic top and bottom layers ($Q^{t,b}_{rs}$). Also, the extended rule of mixture is used to calculate mechanical properties of CNTRC face sheets [12]:

$$\begin{aligned}
&Q^i_{11} = \frac{E^i_{11}}{1-\nu^i_{12}\nu^i_{21}}, \quad Q^i_{12} = \frac{\nu^i_{12}E^i_{11}}{1-\nu^i_{12}\nu^i_{21}}, \quad Q^i_{21} = \frac{\nu^i_{21}E^i_{11}}{1-\nu^i_{12}\nu^i_{21}}, \quad Q^i_{22} = \frac{E^i_{22}}{1-\nu^i_{12}\nu^i_{21}},\\
&Q^i_{44} = G^i_{23}, \quad Q^i_{55} = G^i_{13}, \quad Q^i_{66} = G^i_{12},
\end{aligned} \tag{4}$$

where:

$$E^i_{11} = \eta_1 V^i_f E^i_{11f} + V^i_m E^i_m, \tag{5a}$$

$$\frac{\eta_2}{E_{22}^i} = \frac{V_{cnt}^*}{E_{22f}^i} + \frac{V_m^i}{E_m^i}, \tag{5b}$$

$$\frac{\eta_3}{G_{12}^i} = \frac{V_{cnt}^*}{G_{12f}^i} + \frac{V_m^i}{G_m^i}. \tag{5c}$$

The total potential energy consists of two factors, bending and elongation. Thus, it can be written as:

$$U^i = U_b^i + U_e{}^i, \tag{6}$$

where U_b^i and $U_e{}^i$ represent potential energy due to bending and elongation, respectively, and defined as [21]:

$$U_b^i = \int_{V^i} [\frac{1}{2}(\sigma_{xx}^i \varepsilon_{xx}^i + \sigma_{yy}^i \varepsilon_{yy}^i + \sigma_{zz}^i \varepsilon_{zz}^i) + \sigma_{xy}^i \varepsilon_{xy}^i + \sigma_{xz}^i \varepsilon_{xz}^i + \sigma_{yz}^i \varepsilon_{yz}^i] dV, \tag{7a}$$

$$U_e{}^i = \int_V \frac{1}{2} \sigma_{xx}^0 (w_{,x})^2 dV, \tag{7b}$$

in which, σ_{xx}^0 represent the uniform initial stress along the x direction. Hence, it is neglected the shear stress and the normal stress of the uniform initial stress in the y direction.

3. Kinetic energy

The velocity vector ($\vec{V}$) for axially moving sandwich plate with constant velocity C can be expressed as follows [13]:

$$\vec{V} = (C + u_{,t} + Cu_{,x})\vec{i} + (v_{,t} + Cv_{,x})\vec{j} + (w_{,t} + Cw_{,x})\vec{k}. \tag{8}$$

Thus, the kinetic energy of the sandwich plates is given by:

$$K^i = \frac{1}{2} \rho^i \int_{V^i} [(\mathrm{C} + \mathrm{u}_{,t} + \mathrm{Cu}_{,x})^2 + (\mathrm{v}_{,t} + \mathrm{Cv}_{,x})^2 + (\mathrm{w}_{,t} + \mathrm{Cw}_{,x})^2] dV, \tag{9}$$

where K^i and ρ^i represent kinetic energy and density of ith layers, respectively.

4. Motion equations based on Hamilton's principle

Based on Hamilton's principle, equations of motion for axially moving sandwich plate are derived as [21]:

$$\delta \prod = \delta \int_{t_1}^{t_2} (U^i - K^i) dt = 0. \tag{10}$$

Substituting Eqs. (7a), (7b) and (9) into Eq. (10), the coefficients of $\delta u_0, \delta u_1, \delta u_2, \delta u_3, \delta v_0, \delta v_1, \delta v_2, \delta v_3, \delta w_0, \delta w_1$ and δw_2 can be obtained as follows:

$$\begin{aligned}
&\delta u_0:\\
&h^t\rho^t C^2 u_{0,xx} + 2h^t\rho^t C u_{0,xt} + \rho^t C^2 I_2^t u_{2,xx} + 2\rho^t I_2^t C u_{2,xt} - \frac{1}{2}Q_{66}^t I_2^t v_{2,xy} - Q_{11}^t I_2^t u_{2,xx} - h^t Q_{13}^t w_{1,x} - \frac{1}{2}h^t Q_{66}^t v_{0,xy}\\
&-h^t Q_{12}^t v_{0,xy} + \rho^t I_2^t u_{2,tt} - \frac{1}{2}Q_{66}^t I_2^t u_{2,yy} - Q_{12}^t I_2^t v_{2,xy} + h^t\rho^t u_{0,tt} - \frac{1}{2}h^t Q_{66}^t u_{0,yy} - h^t Q_{11}^t u_{0,xx} + h^c\rho^c C^2 u_{0,xx}\\
&+2h^c\rho^c C u_{0,xt} + \rho^c C^2 I_2^c u_{2,xx} + 2\rho^c I_2^c C u_{2,xt} - \frac{1}{2}Q_{66}^c I_2^c v_{2,xy} - Q_{11}^c I_2^c u_{2,xx} - h^c Q_{13}^c w_{1,x} - \frac{1}{2}h^c Q_{66}^c v_{0,xy} - h^c Q_{12}^c v_{0,xy}\\
&+\rho^c I_2^c u_{2,tt} - \frac{1}{2}Q_{66}^c I_2^c u_{2,yy} - Q_{12}^c I_2^c v_{2,xy} + h^c\rho^c u_{0,tt} - \frac{1}{2}h^c Q_{66}^c u_{0,yy} - h^c Q_{11}^c u_{0,xx} + h^b\rho^b C^2 u_{0,xx} + 2h^b\rho^b C u_{0,xt}\\
&+\rho^b C^2 I_2^b u_{2,xx} + 2\rho^b I_2^b C u_{2,xt} - \frac{1}{2}Q_{66}^b I_2^b v_{2,xy} - Q_{11}^b I_2^b u_{2,xx} - h^b Q_{13}^b w_{1,x} - \frac{1}{2}h^b Q_{66}^b v_{0,xy} - h^b Q_{12}^b v_{0,xy} + \rho^b I_2^b u_{2,tt}\\
&-\frac{1}{2}Q_{66}^b I_2^b u_{2,yy} - Q_{12}^b I_2^b v_{2,xy} + h^b\rho^b u_{0,tt} - \frac{1}{2}h^b Q_{66}^b u_{0,yy} - h^b Q_{11}^b u_{0,xx} = 0,
\end{aligned} \tag{11a}$$

$$\begin{aligned}
&\delta u_1:\\
&\frac{1}{2}h^t Q_{55}^t u_1 + 2\rho^t I_2^t C u_{1,xt} + \rho^t C^2 I_2^t u_{1,xx} + \rho^t C^2 I_4^t u_{3,xx} + 2\rho^t I_4^t C u_{3,xt} - Q_{12}^t I_4^t v_{3,xy} - \frac{1}{2}Q_{66}^t I_4^t u_{3,yy} - \frac{1}{2}Q_{66}^t I_2^t v_{1,xy}\\
&-Q_{12}^t I_2^t v_{1,xy} + \rho^t I_4^t u_{3,tt} + \frac{3}{2}Q_{55}^t I_2^t u_3 - Q_{11}^t I_2^t u_{1,xx} + \rho^t I_2^t u_{1,tt} + \frac{1}{2}h^t Q_{55}^t w_{0,x} - Q_{11}^t I_4^t u_{3,xx} - \frac{1}{2}Q_{66}^t I_4^t v_{3,xy} + \frac{1}{2}Q_{55}^t I_2^t w_{2,x}\\
&-2Q_{13}^t I_2^t w_{2,x} - \frac{1}{2}Q_{66}^t I_2^t u_{1,yy} + \frac{1}{2}h^c Q_{55}^c u_1 + 2\rho^c I_2^c C u_{1,xt} + \rho^c C^2 I_2^c u_{1,xx} + \rho^c C^2 I_4^c u_{3,xx} + 2\rho^c I_4^c C u_{3,xt} - Q_{12}^c I_4^c v_{3,xy}\\
&-\frac{1}{2}Q_{66}^c I_4^c u_{3,yy} - \frac{1}{2}Q_{66}^c I_2^c v_{1,xy} - Q_{12}^c I_2^c v_{1,xy} + \rho^c I_4^c u_{3,tt} + \frac{3}{2}Q_{55}^c I_2^c u_3 - Q_{11}^c I_2^c u_{1,xx} + \rho^c I_2^c u_{1,tt} + \frac{1}{2}h^c Q_{55}^c w_{0,x}\\
&-Q_{11}^c I_4^c u_{3,xx} - \frac{1}{2}Q_{66}^c I_4^c v_{3,xy} + \frac{1}{2}Q_{55}^c I_2^c w_{2,x} - 2Q_{13}^c I_2^c w_{2,x} - \frac{1}{2}Q_{66}^c I_2^c u_{1,yy} + \frac{1}{2}h^b Q_{55}^b u_1 + 2\rho^b I_2^b C u_{1,xt} + \rho^b C^2 I_2^b u_{1,xx}\\
&+\rho^b C^2 I_4^b u_{3,xx} + 2\rho^b I_4^b C u_{3,xt} - Q_{12}^b I_4^b v_{3,xy} - \frac{1}{2}Q_{66}^b I_4^b u_{3,yy} - \frac{1}{2}Q_{66}^b I_2^b v_{1,xy} - Q_{12}^b I_2^b v_{1,xy} + \rho^b I_4^b u_{3,tt} + \frac{3}{2}Q_{55}^b I_2^b u_3\\
&-Q_{11}^b I_2^b u_{1,xx} + \rho^b I_2^b u_{1,tt} + \frac{1}{2}h^b Q_{55}^b w_{0,x} - Q_{11}^b I_4^b u_{3,xx} - \frac{1}{2}Q_{66}^b I_4^b v_{3,xy} + \frac{1}{2}Q_{55}^b I_2^b w_{2,x} - 2Q_{13}^b I_2^b w_{2,x} - \frac{1}{2}Q_{66}^b I_2^b u_{1,yy} = 0,
\end{aligned} \tag{11b}$$

$$\begin{aligned}
&\delta u_2:\\
&\rho^t C^2 I_4^t u_{2,xx} + 2\rho^t I_4^t C u_{2,xt} + \rho^t C^2 I_2^t u_{0,xx} + 2\rho^t I_2^t C u_{0,xt} - \frac{1}{2}Q_{66}^t I_2^t u_{0,yy} - Q_{12}^t I_2^t v_{0,xy} - Q_{12}^t I_4^t v_{2,xy} - \frac{1}{2}Q_{66}^t I_4^t v_{2,xy}\\
&-Q_{11}^t I_2^t u_{0,xx} - Q_{13}^t I_2^t w_{1,x} + Q_{55}^t I_2^t w_{1,x} - \frac{1}{2}Q_{66}^t I_2^t v_{0,xy} + \rho^t I_2^t u_{0,tt} + 2Q_{55}^t I_2^t u_2 - \frac{1}{2}Q_{66}^t I_4^t u_{2,yy} - Q_{11}^t I_4^t u_{2,xx} + \rho^t I_4^t u_{2,tt}\\
&+\rho^c C^2 I_4^c u_{2,xx} + 2\rho^c I_4^c C u_{2,xt} + \rho^c C^2 I_2^c u_{0,xx} + 2\rho^c I_2^c C u_{0,xt} - \frac{1}{2}Q_{66}^c I_2^c u_{0,yy} - Q_{12}^c I_2^c v_{0,xy} - Q_{12}^c I_4^c v_{2,xy} - \frac{1}{2}Q_{66}^c I_4^c v_{2,xy}\\
&-Q_{11}^c I_2^c u_{0,xx} - Q_{13}^c I_2^c w_{1,x} + Q_{55}^c I_2^c w_{1,x} - \frac{1}{2}Q_{66}^c I_2^c v_{0,xy} + \rho^c I_2^c u_{0,tt} + 2Q_{55}^c I_2^c u_2 - \frac{1}{2}Q_{66}^c I_4^c u_{2,yy} - Q_{11}^c I_4^c u_{2,xx} + \rho^c I_4^c u_{2,tt}\\
&+\rho^b C^2 I_4^b u_{2,xx} + 2\rho^b I_4^b C u_{2,xt} + \rho^b C^2 I_2^b u_{0,xx} + 2\rho^b I_2^b C u_{0,xt} - \frac{1}{2}Q_{66}^b I_2^b u_{0,yy} - Q_{12}^b I_2^b v_{0,xy} - Q_{12}^b I_4^b v_{2,xy} - \frac{1}{2}Q_{66}^b I_4^b v_{2,xy}\\
&-Q_{11}^b I_2^b u_{0,xx} - Q_{13}^b I_2^b w_{1,x} + Q_{55}^b I_2^b w_{1,x} - \frac{1}{2}Q_{66}^b I_2^b v_{0,xy} + \rho^b I_2^b u_{0,tt} + 2Q_{55}^b I_2^b u_2 - \frac{1}{2}Q_{66}^b I_4^b u_{2,yy} - Q_{11}^b I_4^b u_{2,xx} + \rho^b I_4^b u_{2,tt} = 0,
\end{aligned} \tag{11c}$$

$$
\begin{aligned}
&\delta u_3:\\
&2\rho^t I_6^t C u_{3,xt}+\rho^t C^2 I_4^t u_{1,xx}+2\rho^t I_4^t C u_{1,xt}-\frac{1}{2}Q_{66}^t I_4^t u_{1,yy}-Q_{12}^t I_4^t v_{1,xy}+\rho^t I_4^t u_{1,tt}+\frac{3}{2}Q_{55}^t I_2^t u_1-\frac{1}{2}Q_{66}^t I_6^t u_{3,yy}-Q_{11}^t I_6^t u_{3,xx}\\
&-2.0Q_{13}^t I_4^t w_{2,x}-\frac{1}{2}Q_{66}^t I_6^t v_{3,xy}-Q_{11}^t I_4^t u_{1,xx}-Q_{12}^t I_6^t v_{3,xy}+\frac{3}{2}Q_{55}^t I_2^t w_{0,x}-\frac{1}{2}Q_{66}^t I_4^t v_{1,xy}+\frac{3}{2}Q_{55}^t I_4^t w_{2,x}+5Q_{55}^t I_4^t u_3\\
&+2\rho^t C^2 I_6^t u_{3,xx}+\rho^t I_6^t u_{3,tt}+2\rho^c I_6^c C u_{3,xt}+\rho^c C^2 I_4^c u_{1,xx}+2\rho^c I_4^c C u_{1,xt}-\frac{1}{2}Q_{66}^c I_4^c u_{1,yy}-Q_{12}^c I_4^c v_{1,xy}+\rho^c I_4^c u_{1,tt}\\
&+\frac{3}{2}Q_{55}^c I_2^c u_1-\frac{1}{2}Q_{66}^c I_6^c u_{3,yy}-Q_{11}^c I_6^c u_{3,xx}-2.0Q_{13}^c I_4^c w_{2,x}-\frac{1}{2}Q_{66}^c I_6^c v_{3,xy}-Q_{11}^c I_4^c u_{1,xx}-Q_{12}^c I_6^c v_{3,xy}+\frac{3}{2}Q_{55}^c I_2^c w_{0,x}\\
&-\frac{1}{2}Q_{66}^c I_4^c v_{1,xy}+\frac{3}{2}Q_{55}^c I_4^c w_{2,x}+5Q_{55}^c I_4^c u_3+2\rho^c C^2 I_6^c u_{3,xx}+\rho^c I_6^c u_{3,tt}+2\rho^b I_6^b C u_{3,xt}+\rho^b C^2 I_4^b u_{1,xx}+2\rho^b I_4^b C u_{1,xt}\\
&-\frac{1}{2}Q_{66}^b I_4^b u_{1,yy}-Q_{12}^b I_4^b v_{1,xy}+\rho^b I_4^b u_{1,tt}+\frac{3}{2}Q_{55}^b I_2^b u_1-\frac{1}{2}Q_{66}^b I_6^b u_{3,yy}-Q_{11}^b I_6^b u_{3,xx}-2.0Q_{13}^b I_4^b w_{2,x}-\frac{1}{2}Q_{66}^b I_6^b v_{3,xy}\\
&-Q_{11}^b I_4^b u_{1,xx}-Q_{12}^b I_6^b v_{3,xy}+\frac{3}{2}Q_{55}^b I_2^b w_{0,x}-\frac{1}{2}Q_{66}^b I_4^b v_{1,xy}+\frac{3}{2}Q_{55}^b I_4^b w_{2,x}+5Q_{55}^b I_4^b u_3+2\rho^b C^2 I_6^b u_{3,xx}+\rho^b I_6^b u_{3,tt}=0,
\end{aligned}
\tag{11d}
$$

$$
\begin{aligned}
&\delta v_0:\\
&h^t\rho^t C^2 v_{0,xx}+2h^t\rho^t C v_{0,xt}+2\rho^t I_2^t C v_{2,xt}+\rho^t C^2 I_2^t v_{2,xx}-Q_{12}^t I_2^t u_{2,xy}+\rho^t I_2^t v_{2,tt}-\frac{1}{2}Q_{66}^t I_2^t v_{2,xx}-h^t Q_{23}^t w_{1,y}-\frac{1}{2}h^t Q_{66}^t u_{0,xy}\\
&-h^t Q_{12}^t u_{0,xy}-\frac{1}{2}Q_{66}^t I_2^t u_{2,xy}-Q_{22}^t I_2^t v_{2,yy}+h^t\rho^t v_{0,tt}-\frac{1}{2}h^t Q_{66}^t v_{0,xx}-h^t Q_{22}^t v_{0,yy}+h^c\rho^c C^2 v_{0,xx}+2h^c\rho^c C v_{0,xt}+2\rho^c I_2^c C v_{2,xt}\\
&+\rho^c C^2 I_2^c v_{2,xx}-Q_{12}^c I_2^c u_{2,xy}+\rho^c I_2^c v_{2,tt}-\frac{1}{2}Q_{66}^c I_2^c v_{2,xx}-h^c Q_{23}^c w_{1,y}-\frac{1}{2}h^c Q_{66}^c u_{0,xy}-h^c Q_{12}^c u_{0,xy}-\frac{1}{2}Q_{66}^c I_2^c u_{2,xy}-Q_{22}^c I_2^c v_{2,yy}\\
&+h^c\rho^c v_{0,tt}-\frac{1}{2}h^c Q_{66}^c v_{0,xx}-h^c Q_{22}^c v_{0,yy}+h^b\rho^b C^2 v_{0,xx}+2h^b\rho^b C v_{0,xt}+2\rho^b I_2^b C v_{2,xt}+\rho^b C^2 I_2^b v_{2,xx}-Q_{12}^b I_2^b u_{2,xy}+\rho^b I_2^b v_{2,tt}\\
&-\frac{1}{2}Q_{66}^b I_2^b v_{2,xx}-h^b Q_{23}^b w_{1,y}-\frac{1}{2}h^b Q_{66}^b u_{0,xy}-h^b Q_{12}^b u_{0,xy}-\frac{1}{2}Q_{66}^b I_2^b u_{2,xy}-Q_{22}^b I_2^b v_{2,yy}+h^b\rho^b v_{0,tt}-\frac{1}{2}h^b Q_{66}^b v_{0,xx}-h^b Q_{22}^b v_{0,yy}=0,
\end{aligned}
\tag{11e}
$$

$$
\begin{aligned}
&\delta v_1:\\
&\frac{1}{2}h^t Q_{44}^t v_1+2\rho^t C^2 I_2^t v_{1,xx}+2\rho^t I_2^t C v_{1,xt}+2\rho^t I_4^t C v_{3,xt}+\rho^t C^2 I_4^t v_{3,xx}-Q_{22}^t I_4^t v_{3,yy}\\
&-Q_{12}^t I_4^t u_{3,xy}-\frac{1}{2}Q_{66}^t I_2^t u_{1,xy}+\rho^t I_4^t v_{3,tt}-Q_{12}^t I_2^t u_{1,xy}+\frac{1}{2}Q_{44}^t I_2^t w_{2,y}+\frac{3}{2}Q_{44}^t I_2^t v_3+\frac{1}{2}h^t Q_{44}^t w_{0,y}\\
&-\frac{1}{2}Q_{66}^t I_4^t v_{3,xx}-\frac{1}{2}Q_{66}^t I_4^t u_{3,xy}-2.0Q_{23}^t I_2^t w_{2,y}+\rho^t I_2^t v_{1,tt}-Q_{22}^t I_2^t v_{1,yy}-\frac{1}{2}Q_{66}^t I_2^t v_{1,xx}+\frac{1}{2}h^c Q_{44}^c v_1\\
&+2\rho^c C^2 I_2^c v_{1,xx}+2\rho^c I_2^c C v_{1,xt}+2\rho^c I_4^c C v_{3,xt}+\rho^c C^2 I_4^c v_{3,xx}-Q_{22}^c I_4^c v_{3,yy}-Q_{12}^c I_4^c u_{3,xy}\\
&-\frac{1}{2}Q_{66}^c I_2^c u_{1,xy}+\rho^c I_4^c v_{3,tt}-Q_{12}^c I_2^c u_{1,xy}+\frac{1}{2}Q_{44}^c I_2^c w_{2,y}+\frac{3}{2}Q_{44}^c I_2^c v_3+\frac{1}{2}h^c Q_{44}^c w_{0,y}-\frac{1}{2}Q_{66}^c I_4^c v_{3,xx}\\
&-\frac{1}{2}Q_{66}^c I_4^c u_{3,xy}-2.0Q_{23}^c I_2^c w_{2,y}+\rho^c I_2^c v_{1,tt}-Q_{22}^c I_2^c v_{1,yy}-\frac{1}{2}Q_{66}^c I_2^c v_{1,xx}+\frac{1}{2}h^b Q_{44}^b v_1+2\rho^b C^2 I_2^b v_{1,xx}\\
&+2\rho^b I_2^b C v_{1,xt}+2\rho^b I_4^b C v_{3,xt}+\rho^b C^2 I_4^b v_{3,xx}-Q_{22}^b I_4^b v_{3,yy}-Q_{12}^b I_4^b u_{3,xy}-\frac{1}{2}Q_{66}^b I_2^b u_{1,xy}+\rho^b I_4^b v_{3,tt}\\
&-Q_{12}^b I_2^b u_{1,xy}+\frac{1}{2}Q_{44}^b I_2^b w_{2,y}+\frac{3}{2}Q_{44}^b I_2^b v_3+\frac{1}{2}h^b Q_{44}^b w_{0,y}-\frac{1}{2}Q_{66}^b I_4^b v_{3,xx}-\frac{1}{2}Q_{66}^b I_4^b u_{3,xy}-2.0Q_{23}^b I_2^b w_{2,y}\\
&+\rho^b I_2^b v_{1,tt}-Q_{22}^b I_2^b v_{1,yy}-\frac{1}{2}Q_{66}^b I_2^b v_{1,xx}=0,
\end{aligned}
\tag{11f}
$$

$\delta v_2:$

$$
\begin{aligned}
&2\rho^t I_4^t C v_{2,xt} + \rho^t C^2 I_4^t v_{2,xx} + 2\rho^t I_2^t C v_{0,xt} + \rho^t C^2 I_2^t v_{0,xx} - Q_{12}^t I_4^t u_{2,xy} - \frac{1}{2} Q_{66}^t I_4^t u_{2,xy} + \rho^t I_2^t v_{0,tt} - \frac{1}{2} Q_{66}^t I_2^t u_{0,xy} \\
&- \frac{1}{2} Q_{66}^t I_2^t v_{0,xx} - Q_{23}^t I_2^t w_{1,y} + \rho^t I_4^t v_{2,tt} + Q_{44}^t I_2^t w_{1,y} - Q_{22}^t I_2^t v_{0,yy} - Q_{12}^t I_2^t u_{0,xy} + 2Q_{44}^t I_2^t v_2 - Q_{22}^t I_4^t v_{2,yy} \\
&- \frac{1}{2} Q_{66}^t I_4^t v_{2,xx} + 2\rho^c I_4^c C v_{2,xt} + \rho^c C^2 I_4^c v_{2,xx} + 2\rho^c I_2^c C v_{0,xt} + \rho^c C^2 I_2^c v_{0,xx} - Q_{12}^c I_4^c u_{2,xy} - \frac{1}{2} Q_{66}^c I_4^c u_{2,xy} \\
&+ \rho^c I_2^c v_{0,tt} - \frac{1}{2} Q_{66}^c I_2^c u_{0,xy} - \frac{1}{2} Q_{66}^c I_2^c v_{0,xx} - Q_{23}^c I_2^c w_{1,y} + \rho^c I_4^c v_{2,tt} + Q_{44}^c I_2^c w_{1,y} - Q_{22}^c I_2^c v_{0,yy} - Q_{12}^c I_2^c u_{0,xy} + 2Q_{44}^c I_2^c v_2 \\
&- Q_{22}^c I_4^c v_{2,yy} - \frac{1}{2} Q_{66}^c I_4^c v_{2,xx} + 2\rho^b I_4^b C v_{2,xt} + \rho^b C^2 I_4^b v_{2,xx} + 2\rho^b I_2^b C v_{0,xt} + \rho^b C^2 I_2^b v_{0,xx} - Q_{12}^b I_4^b u_{2,xy} \\
&- \frac{1}{2} Q_{66}^b I_4^b u_{2,xy} + \rho^b I_2^b v_{0,tt} - \frac{1}{2} Q_{66}^b I_2^b u_{0,xy} - \frac{1}{2} Q_{66}^b I_2^b v_{0,xx} - Q_{23}^b I_2^b w_{1,y} + \rho^b I_4^b v_{2,tt} + Q_{44}^b I_2^b w_{1,y} - Q_{22}^b I_2^b v_{0,yy} \\
&- Q_{12}^b I_2^b u_{0,xy} + 2Q_{44}^b I_2^b v_2 - Q_{22}^b I_4^b v_{2,yy} - \frac{1}{2} Q_{66}^b I_4^b v_{2,xx} = 0,
\end{aligned} \tag{11g}
$$

$\delta v_3:$

$$
\begin{aligned}
&2\rho^t I_6^t C v_{3,xt} + 2\rho^t C^2 I_6^t v_{3,xx} + 2\rho^t I_4^t C v_{1,xt} + \rho^t C^2 I_4^t v_{1,xx} - Q_{12}^t I_4^t u_{1,xy} - Q_{22}^t I_4^t v_{1,yy} + \rho^t I_4^t v_{1,tt} + \frac{3}{2} Q_{44}^t I_4^t w_{2,y} \\
&- 2.0 Q_{23}^t I_4^t w_{2,y} - \frac{1}{2} Q_{66}^t I_6^t v_{3,xx} - \frac{1}{2} Q_{66}^t I_6^t u_{3,xy} - \frac{1}{2} Q_{66}^t I_4^t u_{1,xy} - Q_{12}^t I_6^t u_{3,xy} - \frac{1}{2} Q_{66}^t I_4^t v_{1,xx} + \frac{3}{2} Q_{44}^t I_2^t v_1 + \frac{3}{2} Q_{44}^t I_2^t w_{0,y} \\
&+ 5Q_{44}^t I_4^t v_3 + \rho^t I_6^t v_{3,tt} - Q_{22}^t I_6^t v_{3,yy} + 2\rho^c I_6^c C v_{3,xt} + 2\rho^c C^2 I_6^c v_{3,xx} + 2\rho^c I_4^c C v_{1,xt} + \rho^c C^2 I_4^c v_{1,xx} - Q_{12}^c I_4^c u_{1,xy} \\
&- Q_{22}^c I_4^c v_{1,yy} + \rho^c I_4^c v_{1,tt} + \frac{3}{2} Q_{44}^c I_4^c w_{2,y} - 2.0 Q_{23}^c I_4^c w_{2,y} - \frac{1}{2} Q_{66}^c I_6^c v_{3,xx} - \frac{1}{2} Q_{66}^c I_6^c u_{3,xy} - \frac{1}{2} Q_{66}^c I_4^c u_{1,xy} - Q_{12}^c I_6^c u_{3,xy} \\
&- \frac{1}{2} Q_{66}^c I_4^c v_{1,xx} + \frac{3}{2} Q_{44}^c I_2^c v_1 + \frac{3}{2} Q_{44}^c I_2^c w_{0,y} + 5Q_{44}^c I_4^c v_3 + \rho^c I_6^c v_{3,tt} - Q_{22}^c I_6^c v_{3,yy} + 2\rho^b I_6^b C v_{3,xt} + 2\rho^b C^2 I_6^b v_{3,xx} \\
&+ 2\rho^b I_4^b C v_{1,xt} + \rho^b C^2 I_4^b v_{1,xx} - Q_{12}^b I_4^b u_{1,xy} - Q_{22}^b I_4^b v_{1,yy} + \rho^b I_4^b v_{1,tt} + \frac{3}{2} Q_{44}^b I_4^b w_{2,y} - 2.0 Q_{23}^b I_4^b w_{2,y} - \frac{1}{2} Q_{66}^b I_6^b v_{3,xx} \\
&- \frac{1}{2} Q_{66}^b I_6^b u_{3,xy} - \frac{1}{2} Q_{66}^b I_4^b u_{1,xy} - Q_{12}^b I_6^b u_{3,xy} - \frac{1}{2} Q_{66}^b I_4^b v_{1,xx} + \frac{3}{2} Q_{44}^b I_2^b v_1 + \frac{3}{2} Q_{44}^b I_2^b w_{0,y} + 5Q_{44}^b I_4^b v_3 + \rho^b I_6^b v_{3,tt} \\
&- Q_{22}^b I_6^b v_{3,yy} = 0,
\end{aligned} \tag{11h}
$$

$\delta w_0:$

$$
\begin{aligned}
&h^t \rho^t C^2 w_{0,xx} + 2h^t \rho^t C w_{0,xt} + 2\rho^t I_2^t C w_{2,xt} + \rho^t C^2 I_2^t w_{2,xx} + \rho^t I_2^t w_{2,tt} - \frac{1}{2} Q_{44}^t I_2^t w_{2,yy} - \frac{1}{2} h^t Q_{44}^t v_{1,y} - \frac{1}{2} h^t Q_{55}^t u_{1,x} \\
&- \frac{1}{2} Q_{55}^t I_2^t w_{2,xx} - \frac{3}{2} Q_{55}^t I_2^t u_{3,x} - \frac{3}{2} Q_{44}^t I_2^t v_{3,y} + h^t \rho^t w_{0,tt} - \frac{1}{2} h^t Q_{44}^t w_{0,yy} - \frac{1}{2} h^t Q_{55}^t w_{0,xx} + h^c \rho^c C^2 w_{0,xx} + 2h^c \rho^c C w_{0,xt} \\
&+ 2\rho^c I_2^c C w_{2,xt} + \rho^c C^2 I_2^c w_{2,xx} + \rho^c I_2^c w_{2,tt} - \frac{1}{2} Q_{44}^c I_2^c w_{2,yy} - \frac{1}{2} h^c Q_{44}^c v_{1,y} - \frac{1}{2} h^c Q_{55}^c u_{1,x} - \frac{1}{2} Q_{55}^c I_2^c w_{2,xx} - \frac{3}{2} Q_{55}^c I_2^c u_{3,x} \\
&- \frac{3}{2} Q_{44}^c I_2^c v_{3,y} + h^c \rho^c w_{0,tt} - \frac{1}{2} h^c Q_{44}^c w_{0,yy} - \frac{1}{2} h^c Q_{55}^c w_{0,xx} + h^b \rho^b C^2 w_{0,xx} + 2h^b \rho^b C w_{0,xt} + 2\rho^b I_2^b C w_{2,xt} + \rho^b C^2 I_2^b w_{2,xx} \\
&+ \rho^b I_2^b w_{2,tt} - \frac{1}{2} Q_{44}^b I_2^b w_{2,yy} - \frac{1}{2} h^b Q_{44}^b v_{1,y} - \frac{1}{2} h^b Q_{55}^b u_{1,x} - \frac{1}{2} Q_{55}^b I_2^b w_{2,xx} - \frac{3}{2} Q_{55}^b I_2^b u_{3,x} - \frac{3}{2} Q_{44}^b I_2^b v_{3,y} + h^b \rho^b w_{0,tt} \\
&- \frac{1}{2} h^b Q_{44}^b w_{0,yy} - \frac{1}{2} h^b Q_{55}^b w_{0,xx} - N_x h^t w_{0,xx} - N_x h^b w_{0,xx} - N_x h^c w_{0,xx} = 0,
\end{aligned} \tag{11i}
$$

$\delta w_1:$

$$
\begin{aligned}
&h^t Q_{33}^t w_1 + 2\rho^t I_2^t C w_{1,xt} + Q_{23}^t I_2^t v_{2,y} + Q_{13}^t I_2^t u_{2,x} + \rho^t I_2^t w_{1,tt} - Q_{55}^t I_2^t u_{2,x} + h^t Q_{23}^t v_{0,y} + h^t Q_{13}^t u_{0,x} \\
&- Q_{44}^t I_2^t v_{2,y} + \rho^t C^2 I_2^t w_{1,xx} - \frac{1}{2} Q_{55}^t I_2^t w_{1,xx} - \frac{1}{2} Q_{44}^t I_2^t w_{1,yy} + h^c Q_{33}^c w_1 + 2\rho^c I_2^c C w_{1,xt} + Q_{23}^c I_2^c v_{2,y} \\
&+ Q_{13}^c I_2^c u_{2,x} + \rho^c I_2^c w_{1,tt} - Q_{55}^c I_2^c u_{2,x} + h^c Q_{23}^c v_{0,y} + h^c Q_{13}^c u_{0,x} - Q_{44}^c I_2^c v_{2,y} + \rho^c C^2 I_2^c w_{1,xx} - Q_{55}^b I_2^b u_{2,x} \\
&- \frac{1}{2} Q_{55}^c I_2^c w_{1,xx} - \frac{1}{2} Q_{44}^c I_2^c w_{1,yy} + h^b Q_{33}^b w_1 + 2\rho^b I_2^b C w_{1,xt} + Q_{23}^b I_2^b v_{2,y} + Q_{13}^b I_2^b u_{2,x} + \rho^b I_2^b w_{1,tt} \\
&+ h^b Q_{23}^b v_{0,y} + h^b Q_{13}^b u_{0,x} - Q_{44}^b I_2^b v_{2,y} + \rho^b C^2 I_2^b w_{1,xx} - \frac{1}{2} Q_{55}^b I_2^b w_{1,xx} - \frac{1}{2} Q_{44}^b I_2^b w_{1,yy} = 0,
\end{aligned}
\tag{11j}
$$

$\delta w_2:$

$$
\begin{aligned}
&2\rho^t I_4^t C w_{2,xt} + \rho^t C^2 I_4^t w_{2,xx} + 2\rho^t I_2^t C w_{0,xt} + \rho^t C^2 I_2^t w_{0,xx} + \rho^t I_2^t w_{0,tt} - \frac{1}{2} Q_{44}^t I_2^t w_{0,yy} - \frac{3}{2} Q_{44}^t I_4^t v_{3,y} - \frac{1}{2} Q_{44}^t I_2^t v_{1,y} \\
&+ 2.0 Q_{23}^t I_4^t v_{3,y} + 2.0 Q_{13}^t I_4^t u_{3,x} - \frac{1}{2} Q_{55}^t I_2^t w_{0,xx} - \frac{1}{2} Q_{55}^t I_2^t u_{1,x} + 2.0 Q_{13}^t I_2^t u_{1,x} + 2.0 Q_{23}^t I_2^t v_{1,y} - \frac{3}{2} Q_{55}^t I_4^t u_{3,x} + 4 Q_{33}^t I_2^t w_2 \\
&- \frac{1}{2} Q_{44}^t I_4^t w_{2,yy} + \rho^t I_4^t w_{2,tt} - \frac{1}{2} Q_{55}^t I_4^t w_{2,xx} + 2\rho^c I_4^c C w_{2,xt} + \rho^c C^2 I_4^c w_{2,xx} + 2\rho^c I_2^c C w_{0,xt} + \rho^c C^2 I_2^c w_{0,xx} + \rho^c I_2^c w_{0,tt} \\
&- \frac{1}{2} Q_{44}^c I_2^c w_{0,yy} - \frac{3}{2} Q_{44}^c I_4^c v_{3,y} - \frac{1}{2} Q_{44}^c I_2^c v_{1,y} + 2.0 Q_{23}^c I_4^c v_{3,y} + 2.0 Q_{13}^c I_4^c u_{3,x} - \frac{1}{2} Q_{55}^c I_2^c w_{0,xx} - \frac{1}{2} Q_{55}^c I_2^c u_{1,x} + 2.0 Q_{13}^c I_2^c u_{1,x} \\
&+ 2.0 Q_{23}^c I_2^c v_{1,y} - \frac{3}{2} Q_{55}^c I_4^c u_{3,x} + 4 Q_{33}^c I_2^c w_2 - \frac{1}{2} Q_{44}^c I_4^c w_{2,yy} + \rho^c I_4^c w_{2,tt} - \frac{1}{2} Q_{55}^c I_4^c w_{2,xx} + 2\rho^b I_4^b C w_{2,xt} + \rho^b C^2 I_4^b w_{2,xx} \\
&+ 2\rho^b I_2^b C w_{0,xt} + \rho^b C^2 I_2^b w_{0,xx} + \rho^b I_2^b w_{0,tt} - \frac{1}{2} Q_{44}^b I_2^b w_{0,yy} - \frac{3}{2} Q_{44}^b I_4^b v_{3,y} - \frac{1}{2} Q_{44}^b I_2^b v_{1,y} + 2.0 Q_{23}^b I_4^b v_{3,y} + 2.0 Q_{13}^b I_4^b u_{3,x} \\
&- \frac{1}{2} Q_{55}^b I_2^b w_{0,xx} - \frac{1}{2} Q_{55}^b I_2^b u_{1,x} + 2.0 Q_{13}^b I_2^b u_{1,x} + 2.0 Q_{23}^b I_2^b v_{1,y} - \frac{3}{2} Q_{55}^b I_4^b u_{3,x} + 4 Q_{33}^b I_2^b w_2 - \frac{1}{2} Q_{44}^b I_4^b w_{2,yy} + \rho^b I_4^b w_{2,tt} \\
&- \frac{1}{2} Q_{55}^b I_4^b w_{2,xx} - N_x I_2^t w_{2,xx} - N_x I_2^b w_{2,xx} - N_x I_2^c w_{2,xx} = 0,
\end{aligned}
\tag{11k}
$$

where I_i^t, I_i^c and I_i^b are defined for top, core and bottom layers, respectively, as follows:

$$
I_{2,4,6}^t = \int_{+h^c/2}^{+(\frac{h^c}{2}+h^t)} z^{2,4,6} dz, \qquad I_{2,4,6}^c = \int_{-h^c/2}^{h^c/2} z^{2,4,6} dz, \qquad I_{2,4,6}^b = \int_{-(\frac{h^c}{2}+h^b)}^{-h^c/2} z^{2,4,6} dz. \tag{12}
$$

5. Analytical Solution

The analytical solution of Eqs. (11) exists for the simply-supported axially moving rectangular sandwich plate with composite face sheets. In this approach, the displacements are considered as functions which satisfy at least the various geometric boundary conditions. Based on Navier's procedure, the solution of the displacement variables can be expressed in the following forms [15]:

(13)

$$u_i(x,y,t)=\sum_{n=1}^{N}\sum_{m=1}^{M}U_i^{mn}\cos(\alpha x)\sin(\beta y)e^{i\Omega t},$$
$$v_i(x,y,t)=\sum_{n=1}^{N}\sum_{m=1}^{M}V_i^{mn}\sin(\alpha x)\cos(\beta y)e^{i\Omega t},$$
$$w_i(x,y,t)=\sum_{n=1}^{N}\sum_{m=1}^{M}W_i^{mn}\sin(\alpha x)\sin(\beta y)e^{i\Omega t},$$

Substituting above relations into Eqs. (11) lead to final equations as a matrix form:

$$\left[S_{ij}\right]_{11\times 11}\left[U_0^{mn}\quad U_1^{mn}\quad U_2^{mn}\quad U_3^{mn}\quad V_0^{mn}\quad V_1^{mn}\quad V_2^{mn}\quad V_3^{mn}\quad W_0^{mn}\quad W_1^{mn}\quad W_2^{mn}\right]^T=\left[N_i\right]^T, \tag{14}$$

in which, $N_i\ (i=1,2,3)$ is related to external thermal or mechanical loads. It should be noted that in the case of free vibration $N_i\ (i=1,2,3)$ are assumed to be zero. The arrays of matrix S_{ij} are obtained from Eqs. (11) and (13).

6. Numerical results and discussion

In this section, effects of various parameters such as volume fraction of CNTs, axially moving speed, aspect ratio and thickness on the vibration characteristics of axially moving sandwich plate with composite face sheets are discussed in details. In the present study, Titanium alloy (Ti-6Al-4V) is considered for the homogeneous core. Poly methyl methacrylate, referred to as PMMA, is selected for the matrix of composite face sheets inside CNTs fibers. The effective material properties of CNTs, Ti-6Al-4V and PMMA are presented in Table 1 and 2. It should be noted that $\eta_1=0.137,\eta_2=1.022$ and $\eta_3=0.715$ for the case of $V^*_{CNT}=0.12$, $\eta_1=0.142,\eta_2=1.626$ and $\eta_3=1.138$ for the case of $V^*_{CNT}=0.17$, and $\eta_1=0.141,\eta_2=1.585$ and $\eta_3=1.109$ for the case of $V^*_{CNT}=0.28$. Moreover, it's assumed that $G_{12}=G_{13}$ and $G_{23}=1.2G_{12}$ according to Wang and Shen [22].

Table 1. Mechanical properties of SWCNT with 10 [22].

Temperature (K)	$E_{11}^{CNT}(TPa)$	$E_{22}^{CNT}(TPa)$	$G_{12}^{CNT}(TPa)$	υ^{CNT}	$\rho^{CNT}(Kg/m^3)$
300	5.6466	7.0800	1.9445	0.19	1400
500	5.5308	6.9348	1.9643	0.19	1400
700	5.4744	6.8641	1.9644	0.19	1400

Table 2. Mechanical properties of PMMA and Ti-6Al-4V [22].

Material	$E(GPa)$	$\rho(Kg/m^3)$	υ
PMMA	3.52-0.0034T	1150	0.34
Ti-6Al-4V	$122.56(1-4.586\times10^{-4}T)$	4429	0.29

Dimensionless parameters are defined to obtain dimensionless results:

$$(\zeta,\eta)=\left(\frac{x}{a},\frac{y}{b}\right),\ (U,V,W)=\left(\frac{u}{a},\frac{v}{b},\frac{w}{h}\right),\ (\alpha,\beta,\gamma)=\left(\frac{h}{a},\frac{h}{b},\frac{a}{b}\right),\ C^{*}=C\sqrt{\frac{Q_{11}{}^{c}}{\rho^{c}}}\quad P^{*}=\frac{N_{x}}{Q_{11}{}^{c}a}\quad \Omega=\omega a\sqrt{\frac{\rho^{c}}{Q_{11}{}^{c}}}. \tag{15}$$

Fig. 2 illustrates the influence of volume fractions of CNTs on the dimensionless frequencies of axially moving sandwich plate. This figure shows that increasing volume fractions of CNTs leads to increase stiffness of sandwich plate and consequently the frequencies of moving system increase. In addition, it's evident that increasing V^{*}_{CNT} from 0.17 to 0.28 not considerably affected the natural frequencies of moving system, especially at lower aspect ratios. Moreover, it can be observed that the frequencies moving system increase with increasing aspect ratios of sandwich plate.

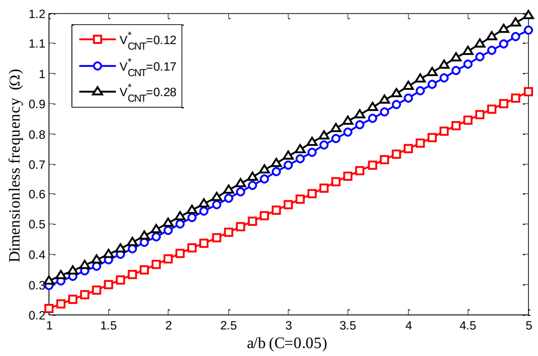

Fig. 2. Dimensionless frequency versus aspect ratio of sandwich plate for different volume fractions of CNTs.

The real part of dimensionless frequency versus dimensionless axially moving speed for different core thickness is depicted in Fig.3. As can be observed, $\mathrm{Im}(\omega)$ diminishes with increasing C. These physically proved that the system is stable and the small moving speed does not result in damping behavior. For zero resonance frequency, axially moving sandwich plate becomes unstable due to the divergence via a pitchfork bifurcation and the corresponding moving speed is called the critical speed. Therefore, with increasing moving speed, system stability decreases and became susceptible to buckling. It is obvious that increasing core thickness causes to increase strength of sandwich plate and consequently the frequencies of system increase.

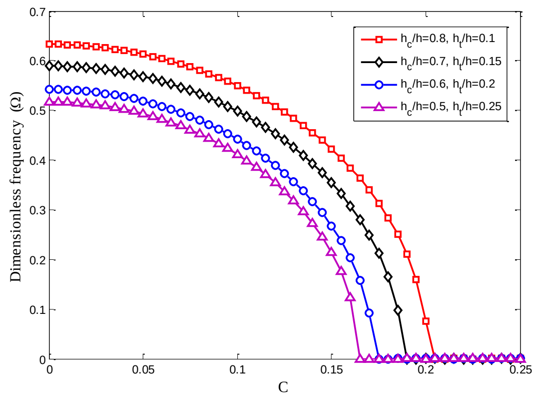

Fig. 3. Dimensionless frequency versus dimensionless moving speed of sandwich plate in different values of core and face sheets thickness.

The influences of volume fractions of sandwich plate on dimensionless frequencies versus dimensionless thickness parameter are demonstrated in Fig.4. This figure approved that increasing thickness of sandwich plate leads to increase frequencies of moving system. In addition, the effect of CNTs reinforcement is more significant at thicker sandwich plate. Also, it can be found that the frequencies of sandwich plate which is reinforced by 0.17 and 0.28 volume fractions of CNTs are similar. So, in this study $V^*_{CNT} = 0.17$ is selected for the face sheets of sandwich plate.

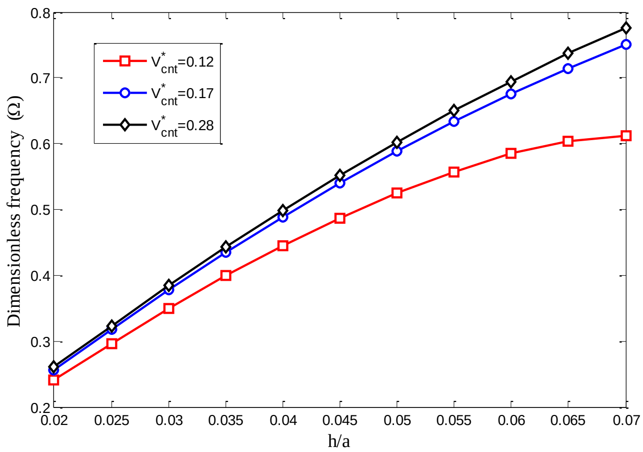

Fig. 4. The influence of CNTs volume fraction on dimensionless frequency versus dimensionless thickness ratio of sandwich plate.

As mentioned ago, SWCNTs is selected as a reinforcement of face sheets of sandwich plate. The mechanical properties of CNTs at different temperatures are adopted from Wang and Shen (2012). Fig. 5 presents the effect of temperature on vibration frequencies of moving sandwich plate. As can be seen, increasing temperature leads to increase the frequencies of moving composite plate, especially at higher thickness of plate.

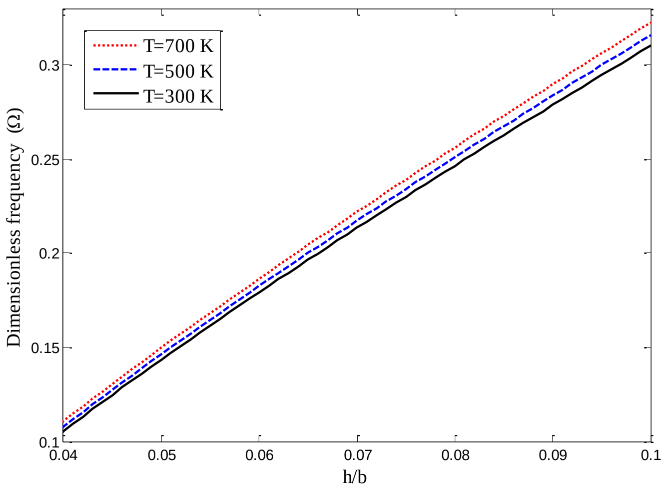

Fig. 5. The effect of temperature on dimensionless frequencies of axially moving sandwich plate versus dimensionless thickness ratio of sandwich plate.

Fig.6 shows the influences of temperature changes and volume fractions on dimensionless frequencies versus dimensionless core thickness parameter, simultaneously. This figure approved that volume fractions of CNTs and temperature changes are a significant parameters which are changed frequencies of moving sandwich plate, considerably.

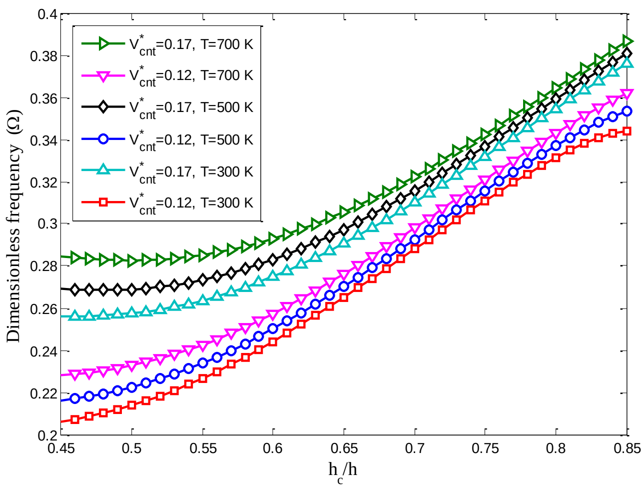

Fig. 6. Dimensionless frequency versus dimensionless core thickness of sandwich plate in different temperature and volume fractions of CNTs.

The effect of moving speed of sandwich plate on dimensionless frequency versus dimensionless aspect ratio is demonstrated in Fig. 7. It can be found from this figure that the values of critical speed in square plate are lower than rectangular plate. Moreover, increasing moving speed leads to increase instability of sandwich plate and consequently the frequencies decrease.

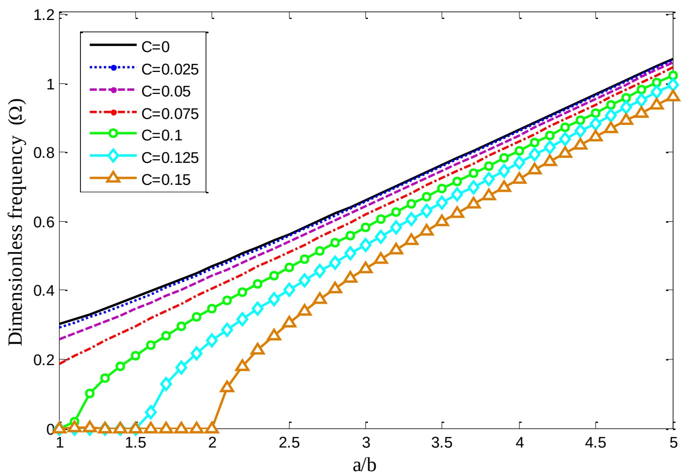

Fig. 7. The effect of moving speed on dimensionless frequency versus aspect ratio of sandwich plate.

Dimensionless frequencies versus dimensionless initial tension in different moving speeds are demonstrated in Fig.8. It's concluded that increasing pre-tension leads to decrease dimensionless frequency of sandwich plate. In addition, the influence of initial tension in axially moving plate with higher moving speeds is more considerable than stationary plates.

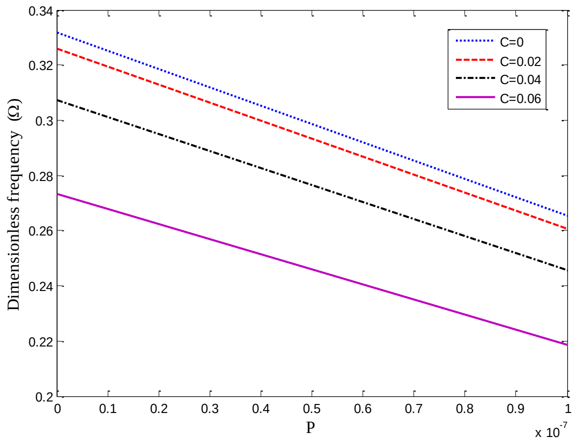

Fig. 8. The effect of moving speed on the dimensionless frequency versus dimensionless initial tension.

Fig.9 illustrates the effect of vibration modes on dimensionless frequencies versus dimensionless moving speed of sandwich plate. It is evident that the critical speed and frequencies of sandwich plate in third mode are higher than the first mode.

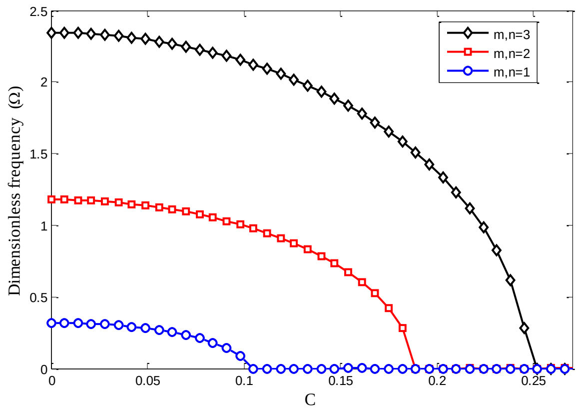

Fig. 9. The effect of vibration modes on the dimensionless frequency versus dimensionless moving speed of sandwich plate.

In order to examine the reliability of the presented method, the results of this method are compared with the work by Wang and Shen (2012). For this purpose, sandwich plate with CNTRC face sheets is considered. Non-dimensional natural frequencies are obtained by $\Omega = \omega a^2 / h\left(\sqrt{\rho^c / E^c}\right)$ where ρ^c and E^c represents mass density and Young's module of core layer at T=300 K. As can be seen, there are good agreement between the results of present study and their approach.

Table 3. Comparison between non-dimensional natural frequencies of sandwich plate with CNTRC face sheets (C=0, a/b=1, b/h=20)

T= 300 K	$\frac{h_c}{h_t}=8$		$\frac{h_c}{h_t}=6$		$\frac{h_c}{h_t}=4$	
V^*_{CNT}	0.17	0.28	0.17	0.28	0.17	0.28
Present	4.5577	4.5673	4.2701	4.2710	3.7173	3.7203
Ref. [22]	4.5887	4.5871	4.2642	4.2939	3.7320	3.7378

7. Conclusion

Based on HSDT, vibration analysis of axially moving sandwich plate with composite face sheets was developed for the first time. PMMA was selected as a matrix composite face sheets inside CNTs fibers. Extended rule of mixture was utilized to obtain structural properties of composite face sheets. Considering simply supported boundary condition, the motion equations were obtained using Hamilton's principle and solved by analytical solution. It was found that vibrating behavior of moving sandwich plate was strongly dependent on moving speed, so that, with increasing moving speed, system stability decreases and became susceptible to buckling. In addition, increasing small amount in volume fraction of fibers led to increase frequencies of sandwich plate, considerably. Comparison between natural frequencies of this study and the work which was done by Wang and Shen [22] confirmed the accuracy of presented results. The results of this study is hoped to be used in optimum design of aircrafts and military equipment.

Acknowledgements

The authors are grateful to University of Kashan for supporting this work by Grant No. 574600/24.

References

[1] Thostenson, E.T., Wei Chou, T., On the elastic properties of carbon nanotube-based composites: modelling and characterization. *Journal of Physics D: Applied Physics*, 36, 573-582, 2003.

[2] Zhu, P., Lei, Z.X., Liew, K.L., Static and free vibration analyses of carbon nanotube-reinforced composite plates using finite element method with first order shear deformation plate theory. *Composite Structures*, 94, 1450-1460, 2012.

[3] Lei, Z.X., Liew, K.M., Yu, J.L., Free vibration analysis of functionally graded carbon nanotube-reinforced composite plates using the element-free kp-Ritz method in thermal environment. *Composite Structures*, 106, 128-138, 2013.

[4] Alibeigloo, A., Static analysis of functionally graded carbon nanotube-reinforced composite plate embedded in piezoelectric layers by using theory of elasticity. *Composite Structures*, 95, 612-622, 2013.

[5] Nayak, A.K., Moy, S.S.J., Shenoi, R.A., Free vibration analysis of composite sandwich plates based on Reddy's higher-order theory, *Composite Part B: Engineering*, 33, 505-519, 2002.

[6] Ferreira, A.J.M., Roque, C.M.C., Jorge, R.M.N., Kansa, E.J., Radial basis functions collocation and a unified formulation for bending, vibration and buckling analysis of laminated plates, according to variation of Murakami's zigzag theory. *European Journal of Mechanics - A/Solids*, 30(4), 559–570, 2011.

[7] Khalili, S.M.R., Mohammadi, Y., Free vibration analysis of sandwich plates with functionally graded face sheets and temperature-dependent material properties: A new approach. *European Journal of Mechanics - A/Solids*, 35, 61-74, 2012.

[8] Sahoo, R., Singh, B.N., A new trigonometric zigzag theory for static analysis of laminated composite and sandwich plates. *Aerospace Science and Technology*, 35, 15-28, 2014.

[9] Thai, H.T., Nguyen, T.K., Vo, T.P., Lee, J., Analysis of functionally graded sandwich plates using a new first-order shear deformation theory. *European Journal of Mechanics - A/Solids*, 45, 211-225, 2014.

[10] Plagianakos, T.S., Papadopoulos, E.G., Higher-order 2-D/3-D layerwise mechanics and finite elements for composite and sandwich composite plates with piezoelectric layers. *Aerospace Science and Technology*, 40, 150-163, 2015.

[11] Natarajan, S., Haboussi, M., Manickam, G., Application of higher-order structural theory to bending and free vibration analysis of sandwich plates with CNT reinforced composite facesheets. *Composite Structures*, 113, 197-207, 2014.

[12] Kheirikhah, M.M., Khalili, S.M.R., Malekzadeh Fard, K., Biaxial buckling analysis of soft-core composite sandwich plates using improved high-order theory. *European Journal of Mechanics - A/Solids*, 31, 54-66, 2012.

[13] Ghayesh, M.H., Amabili, M., Paı¨doussis, M.P., Nonlinear dynamics of axially moving plates. *Journal of Sound and Vibration*, 332, 391-406, 2013.

[14] Dong Yang, X., Qun Chen, L., Zu, J.W., Vibrations and stability of an axially moving rectangular composite plate. *Journal of Applied Mechanics*, 78, 011018-011029, 2010.

[15] Hatami, S., Ronagh, H.R., Azhari, M., Exact free vibration analysis of axially moving viscoelastic plates. *Computers & Structures*, 86, 1738-1746, 2008.

[16] Marynowsky, K., Free vibration analysis of the axially moving Levy-type viscoelastic plate. *European Journal of Mechanics - A/Solids*, 29, 879-886, 2010.

[17] Marynowski, K., Grabski, J., Dynamic analysis of an axially moving plate subjected to thermal loading. *Mechanics Research Communications*, 51, 67-71, 2013.

[18] Marynowski, K., Dynamic analysis of an axially moving sandwich beam with viscoelastic core. *Composite Structures*, 94, 2931-2936, 2012.

[19] Bozhevolnaya, E., Sun, J.Q., Free vibration analysis of curved sandwich beams. *Journal of Sandwich Structures and Materials*, 6, 47-73, 2004.

[20] Reddy, J.N., *Mechanics of Laminated Composite Plates and Shells: Theory and Analysis*, CRC Press, 2004.

[21] Ghorbanpour Arani, A., Haghparast, E., Heidari Rarani, M.H., Khoddami Maraghi, Z., Strain gradient shell model for nonlinear vibration analysis of visco-elastically coupled Boron Nitride nano-tube reinforced composite micro-tubes conveying viscous fluid. *Computational Materials Science*, 96, 448-458, 2015.

[22] Wang, X.Z., Shen, S.H., Nonlinear vibration and bending of sandwich plates with nanotube-reinforced composite face sheets. *Composite Part B: Engineering*, 43, 411–421, 2012.

International Journal of Engineering & Applied Sciences (IJEAS)
Vol.9, Issue 2 (Special Issue: Composite Structures) (2017) 55-65
http://dx.doi.org/10.24107/ijeas.309060
Int J Eng Appl Sci 9(2) (2017) 55-65

Frequencies Values of Orthotropic Composite Circular and Annular Plates

*Kadir Mercan, Bekir Akgöz, Ciğdem Demir, Ömer Civalek**

Akdeniz University, Engineering Faculty, Civil Engineering Dept., Division of Mechanics
07058, Antalya-TURKIYE
E-mail address: civalek@yahoo.com

Received date: April 2017

Abstract

Free vibration analysis of orthotropic composite annular plate is investigated. First-order shear deformation theory (FSDT) is used for equation of motion. Two different kernels such as Regularized Shannon delta (RSD) kernel and Lagrange delta sequence (LDS) kernel are used. The method of discrete singular convolution (DSC) is used for numerical simulation of governing equations to obtain the frequency values. It is shown that the convergence and accuracy of the DSC method is very good for vibration problem of orthotropic annular plate.

Keywords: *Frequency, annular plate, discrete singular convolution, composite laminated.*

1. Introduction

Free vibration analyses of shells and plates have widely studied by this time. Frequencies values of shell structures have major importance for their design in different fields. In literature, it is possible to find a few books on analysis and design of these structures [1-11]. Some important studies have been listed in references [9-42].

This paper is summarized in a few sections. In section 2, just main formulations for truncated conical shells and annular plates are given via Tong's [43] paper. The method of discrete singular convolution (DSC) is given in section 3. DSC solution for free vibration of orthotropic annular plates with is briefly defined in section 4. Results are listed in Section 5. Finally, a conclusion is located at the end of the paper.

2. Fundamental Equations

Geometry and parameters of conical shells and annular plates are depicted in Fig. 1.

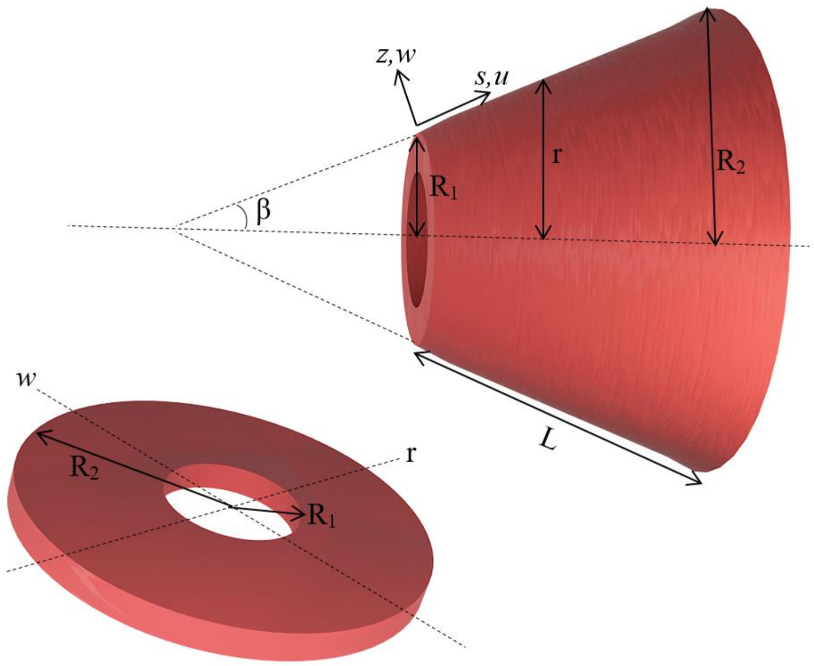

Fig. 1. Demonstration and notation of conical shell and annular plate

The equations of motion are [43]

$$\frac{\partial N_x}{\partial x}+\frac{1}{R(x)}\frac{\partial N_{xs}}{\partial s}+\frac{\sin\alpha}{R(x)}(N_x-N_s)=\rho h\frac{\partial^2 u}{\partial t^2} \tag{1}$$

$$\frac{\partial N_{xs}}{\partial x}+\frac{1}{R(x)}\frac{\partial N_s}{\partial s}+\frac{\cos\alpha}{R(x)}V_s+2\frac{\sin\alpha}{R(x)}N_{xs}=\rho h\frac{\partial^2 v}{\partial t^2} \tag{2}$$

$$\frac{\partial V_x}{\partial x}+\frac{\sin\alpha}{R(x)}V_x+\frac{1}{R(x)}\frac{\partial V_s}{\partial s}-\frac{\cos\alpha}{R(x)}N_s=\rho h\frac{\partial^2 w}{\partial t^2} \tag{3}$$

$$\frac{\partial V_x}{\partial x}+\frac{1}{R(x)}\frac{\partial V_s}{\partial s}-\frac{\cos\alpha}{R(x)}N_s+\frac{\sin\alpha}{R(x)}V_x=\frac{\rho h^3}{12}\frac{\partial^2 \varphi_x}{\partial t^2} \tag{4}$$

$$\frac{\partial M_{xs}}{\partial x}+2M_{xs}\frac{\sin\alpha}{R(x)}+\frac{1}{R(x)}\frac{\partial M_s}{\partial s}-V_s=\frac{\rho h^3}{12}\frac{\partial^2 \varphi_s}{\partial t^2} \tag{5}$$

Moment and forces components can be defined as:

$$\tilde{N}=\begin{Bmatrix}N_x\\N_s\\N_{xs}\end{Bmatrix}=\int_{-h/2}^{h/2}\begin{Bmatrix}\sigma_x\\\sigma_s\\\tau_{xs}\end{Bmatrix}dz \tag{6}$$

$$\tilde{M}=\begin{Bmatrix}M_x\\M_s\\M_{xs}\end{Bmatrix}=\int_{-h/2}^{h/2}\begin{Bmatrix}\sigma_x\\\sigma_s\\\tau_{xs}\end{Bmatrix}zdz \tag{7}$$

$$\tilde{V} = \begin{Bmatrix} V_s \\ V_x \end{Bmatrix} = \int_{-h/2}^{h/2} \begin{Bmatrix} \tau_{sz} \\ \tau_{xz} \end{Bmatrix} dz \tag{8}$$

For annular plates (α=90; φ=360) based on the FSDT the differential equations of motion can be defined in each direction:

$$\begin{aligned}
&A_{11}\frac{\partial^2 u}{\partial x^2}+\frac{A_{11}}{R(x)}\sin\alpha\frac{\partial u}{\partial x}-\frac{A_{22}}{R^2(x)}\sin^2\alpha\cdot u+\frac{A_{33}}{R^2(x)}\frac{\partial^2 u}{\partial s^2}+\frac{(A_{12}+A_{33})}{R(x)}\frac{\partial^2 v}{\partial x\partial s}\\
&-\frac{(A_{22}+A_{33})}{R^2(x)}\sin\alpha\frac{\partial v}{\partial s}+\frac{A_{12}}{R(x)}\cos\alpha\frac{\partial w}{\partial x}-\frac{A_{22}}{R^2(x)}\sin\alpha\cdot\cos\alpha\cdot w-B_{11}\frac{\partial^2\varphi_x}{\partial x^2}\\
&+\frac{B_{11}}{R(x)}\sin\alpha\frac{\partial\varphi_x}{\partial x}-\frac{B_{22}}{R^2(x)}\sin^2\alpha\cdot\varphi_x+\frac{B_{33}}{R^2(x)}\frac{\partial^2\varphi_x}{\partial s^2}\\
&+\frac{(B_{12}+B_{33})}{R(x)}\frac{\partial^2\varphi_s}{\partial x\partial s}-\frac{(B_{22}+B_{33})}{R^2(x)}\frac{\partial\varphi_s}{\partial s}\sin\alpha=\rho h\frac{\partial^2 u}{\partial t^2}
\end{aligned}\tag{9}$$

$$\begin{aligned}
&\frac{(A_{12}+A_{33})}{R(x)}\frac{\partial^2 u}{\partial x\partial s}+\frac{(A_{22}+A_{33})}{R^2(x)}\sin\alpha\frac{\partial u}{\partial s}+A_{33}\frac{\partial^2 v}{\partial x^2}+A_{33}\frac{\sin\alpha}{R(x)}\frac{\partial v}{\partial x}\\
&-\frac{A_{33}}{R^2(x)}\sin^2\alpha\cdot v+\frac{A_{22}}{R^2(x)}\frac{\partial^2 v}{\partial s^2}-\frac{A_{44}}{R^2(x)}\cos^2\alpha\cdot v+\frac{(A_{22}+A_{44})}{R^2(x)}\cos\alpha\frac{\partial w}{\partial s}\\
&+\frac{(B_{12}+B_{33})}{R(x)}\frac{\partial^2\varphi_x}{\partial x\partial s}+\frac{(B_{22}+B_{33})}{R^2(x)}\sin\alpha\frac{\partial\varphi_x}{\partial s}+B_{33}\frac{\partial^2\varphi_s}{\partial x^2}+B_{33}\frac{\sin\alpha}{R(x)}\frac{\partial\varphi_s}{\partial x}\\
&-\frac{B_{33}}{R^2(x)}\sin^2\alpha\cdot\varphi_s+\frac{B_{22}}{R^2(x)}\frac{\partial^2\varphi_s}{\partial s^2}+A_{44}\frac{\cos\alpha}{R(x)}\cdot\varphi_s=\rho h\frac{\partial^2 v}{\partial t^2}
\end{aligned}\tag{10}$$

$$\begin{aligned}
&-\frac{A_{12}}{R(x)}\cos\alpha\frac{\partial u}{\partial x}-\frac{A_{22}}{R^2(x)}\cdot u\cdot\sin\alpha\cdot\cos\alpha-\frac{(A_{22}+A_{44})}{R^2(x)}\cdot\cos\alpha\frac{\partial v}{\partial s}+A_{55}\frac{\partial^2 w}{\partial x^2}\\
&+\frac{A_{55}}{R(x)}\sin\alpha\cdot\frac{\partial w}{\partial s}+\frac{A_{44}}{R^2(x)}\frac{\partial^2 w}{\partial s^2}-\frac{A_{22}}{R^2(x)}\cdot w\cdot\cos^2\alpha+A_{55}\frac{\partial\varphi_x}{\partial x}-\frac{B_{12}}{R(x)}\cos\alpha\cdot\frac{\partial\varphi_x}{\partial x}\\
&+\frac{A_{55}}{R(x)}\sin\alpha\cdot\varphi_x-\frac{B_{22}}{R^2(x)}\sin\alpha\cdot\cos\alpha\cdot\varphi_x+\frac{A_{44}}{R(x)}\cdot\frac{\partial\varphi_s}{\partial s}\\
&-\frac{B_{22}}{R^2(x)}\cdot\cos\alpha\frac{\partial\varphi_s}{\partial s}=\rho h\frac{\partial^2 w}{\partial t^2}
\end{aligned}\tag{11}$$

$$\begin{aligned}
&B_{11}\frac{\partial^2 u}{\partial x^2}+\frac{B_{11}}{R(x)}\sin\alpha\frac{\partial u}{\partial x}-\frac{B_{22}}{R^2(x)}\cdot u\cdot\sin^2\alpha+\frac{B_{33}}{R^2(x)}\frac{\partial^2 u}{\partial s^2}+\frac{(B_{12}+B_{33})}{R(x)}\frac{\partial^2 v}{\partial x\partial s}\\
&-\frac{(B_{22}+B_{33})}{R^2(x)}\sin\alpha\frac{\partial v}{\partial s}-A_{55}\frac{\partial w}{\partial x}+B_{12}\frac{\cos\alpha}{R(x)}\frac{\partial w}{\partial x}-\frac{B_{22}}{R^2(x)}\cdot w\cdot\sin\alpha\cos\alpha\\
&+D_{11}\frac{\partial^2\varphi_x}{\partial x^2}+D_{11}\frac{\sin\alpha}{R(x)}\frac{\partial\varphi_x}{\partial x}-\frac{D_{22}}{R^2(x)}\varphi_x\sin^2\alpha+\frac{D_{33}}{R^2(x)}\frac{\partial^2\varphi_x}{\partial s^2}-A_{55}\varphi_x\\
&+\frac{(D_{12}+D_{33})}{R(x)}\frac{\partial^2\varphi_s}{\partial x\partial s}-\frac{(D_{22}+D_{33})}{R^2(x)}\frac{\partial\varphi_s}{\partial s}\sin\alpha=\rho h\frac{\partial^2\varphi_x}{\partial t^2}
\end{aligned}\tag{12}$$

$$\frac{(B_{12}+B_{33})}{R(x)}\frac{\partial^2 u}{\partial x\partial s}+\frac{(B_{22}+B_{33})}{R^2(x)}\frac{\partial u}{\partial s}\sin\alpha+B_{33}\frac{\partial^2 v}{\partial x^2}+B_{33}\frac{\sin\alpha}{R(x)}\frac{\partial v}{\partial x}$$
$$-B_{33}\frac{\sin^2\alpha}{R^2(x)}\cdot v+\frac{B_{22}}{R^2(x)}\frac{\partial^2 v}{\partial s^2}+\frac{A_{44}}{R(x)}\cdot v\cdot\cos\alpha-\frac{A_{44}}{R(x)}\frac{\partial w}{\partial s}+\frac{B_{22}}{R^2(x)}\cos\alpha\frac{\partial w}{\partial s}$$
$$+\frac{(D_{12}+D_{33})}{R(x)}\frac{\partial^2\varphi_x}{\partial x\partial s}+\frac{(D_{22}+D_{33})}{R^2(x)}\sin\alpha\frac{\partial\varphi_x}{\partial s}-D_{33}\frac{\partial^2\varphi_s}{\partial x^2}$$
$$+D_{33}\frac{\sin\alpha}{R(x)}\frac{\partial\varphi_s}{\partial x}-\frac{D_{33}}{R^2(x)}\sin^2\alpha\cdot\varphi_s+\frac{D_{22}}{R^2(x)}\frac{\partial^2\varphi_s}{\partial s^2}-A_{44}\cdot\varphi_s=\rho h\frac{\partial^2\varphi_s}{\partial t^2} \tag{13}$$

3. Discrete Singular Convolution (DSC)

The method is originally introduced by Wei [44-47]. After the Wei's paper, the method of DSC have been used in many problems related to static, dynamic, free vibration and buckling analysis of structures [48-74]. A singular convolution F can be formulated as [44]

$$F(t)=(T*\eta)(t)=\int_{-\infty}^{\infty}T(t-x)\eta(x)dx \tag{14}$$

In the study, regularized Shannon kernel (RSK) and Lagrange kernels are used.
Regularized Shannon kernel (RSK)
RSK kernel can be listed below [45-47]

$$\delta_{\Delta,\sigma}(x-x_k)=\frac{\sin[(\pi/\Delta)(x-x_k)]}{(\pi/\Delta)(x-x_k)}\exp\left[-\frac{(x-x_k)^2}{2\sigma^2}\right];\ \sigma>0 \tag{15}$$

Gaussian envelope is showed by symbol σ. In discrete form, any derivation can be written as

$$\left.\frac{d^n f(x)}{d x^n}\right|_{x=x_i}=f^{(n)}(x)\approx\sum_{k=-M}^{M}\delta_{\Delta,\sigma}^{(n)}(x_i-x_k)f(x_k)\quad;\ (n=0,1,2,...,) \tag{16}$$

Lagrange delta sequence (LDS) kernel
LDS kernel is defined for i = 0,1,…, N-1 and j = -M,…,M is given by [44-50]

$$\Re_{i,j}(x)=\begin{cases}\displaystyle\prod_{k=i-M,k\neq i+j}^{i+M}\frac{x-x_k}{x_{i+j}-x_k}, & x_{i-M}\le x\le x_{i+M},\\ 0 & \text{otherwise.}\end{cases} \tag{17}$$

In this case, the first and second order derivatives are given as

$$\delta^{(1)}_{\Delta,\sigma}(x)=\sum_{i=-M;i\neq k}^{M}\left(\frac{1}{x_k-x_i}\right)\prod_{i=-M,k\neq i}^{i+M}\frac{x-x_i}{x_k-x_i} \tag{18}$$

$$\delta^{(2)}_{\Delta,\sigma}(x)=\sum_{\substack{i,m=-M;i\neq k\\ m\neq k,i\neq m}}^{M}\left(\frac{1}{(x-x_i)(x-x_m)}\right)\prod_{i=-M,k\neq i}^{i+M}\frac{x-x_i}{x_k-x_i} \tag{19}$$

4. Results

In this section, two examples are solved via two different kernels such as Regularized Shannon delta (RSD) kernel and Lagrange delta sequence (LDS). Frequency values for annular and circular plates have been obtained and results are listed in Tables 1-2 for orthotropic case. Results are obtained for clamped cases for annular and circular plates. Both kernels are useful for numerical discretization via DSC. It is shown that the 9*7 grids are efficient for best convergence.

Table 1. Frequency values $(\Omega=\omega R_1\sqrt{\rho(1-\upsilon_r\upsilon_\theta)/E_r}$) for orthotropic annular plate with C-C edges (R_1/R_2=2; R_1/h=1000; E_θ=70 GPa, υ_c=0.3, ρ_c=5700 kg/m^3, E_r=1400 GPa, υ_r=0.3, ρ =7850 kg/m^3)

Modes	Present DSC Results- RSD kernel			
(σ=2.8)	7×*7(M=14)*	9×*7(M=14)*	9×*9(M=14)*	11×*9(M=14)*
1	4.52420	4.52413	4.52413	4.52413
2	4.74045	4.74038	4.74038	4.74038
3	5.31453	5.31449	5.31442	5.31442
4	6.10096	6.10090	6.10085	6.10085
5	7.04989	7.04978	7.04976	7.04976
	Present DSC Results- LDS kernel			
(σ=2.8)	7×*7(M=14)*	9×*7(M=14)*	9×*9(M=14)*	11×*9(M=14)*
1	4.52443	4.52438	4.52438	4.52438
2	4.74059	4.74053	4.74051	4.74051
3	5.31504	5.31493	5.31493	5.31493
4	6.10103	6.10098	6.10094	6.10094
5	7.05068	7.05016	7.05003	7.05003

Table 2. Frequency values ($\Omega = \omega R_1 \sqrt{\rho(1-\upsilon_r \upsilon_\theta)/E_r}$) for orthotropic circular plate with clamped edges (R_1/h=1000; E_θ=70 GPa, υ_c=0.3, ρ_c=5700 kg/m^3, E_r=2800 GPa, υ_r=0.3, ρ =7850 kg/m^3)

Modes	Present DSC Results- RSD kernel			
(σ=2.8)	9×*9(M=14)*	9×*7(M=14)*	11×*9(M=14)*	11×*11(M=14)*
1	2.72081	2.72081	2.72081	2.72081
2	3.37236	3.37236	3.37236	3.37236
3	4.50756	4.50753	4.50753	4.50753
4	4.98188	4.98182	4.98182	4.98182
5	5.60235	5.60227	5.60227	5.60227
	Present DSC Results- LDS kernel			
(σ=2.8)	9×*9(M=14)*	9×*7(M=14)*	11×*9(M=14)*	11×*11(M=14)*
1	2.72086	2.72086	2.72086	2.72086
2	3.37244	3.37240	3.37240	3.37240
3	4.50767	4.50760	4.50760	4.50760
4	4.98195	4.98190	4.98188	4.98188
5	5.60242	5.60236	5.60234	5.60234

5. Discussions

In this paper discrete singular convolution method via FSDT shell theory is used for free vibration of annular and circular plates with orthotropic case. Two kernels namely Regularized Shannon delta (RSD) kernel and Lagrange delta sequence (LDS) kernel are used. The effects of grid numbers and kernel types on results have been investigated.

Acknowledgements

The financial support of the Scientific Research Projects Unit of Akdeniz University is gratefully acknowledged.

References

[1] Leissa, A.W., *Vibration of plates,* Acoustical Society of America, USA,1993.

[2] Reddy, J.N., *Mechanics of laminated composite plates and shells: theory and analysis.* (2nd ed.) New York: CRC Press, 2003.

[3] Qatu, M., *Vibration of Laminated Shells and Plates*, Academic Press, U.K., 2004.

[4] Soedel, W., *Vibrations of shells and plates,* Third Edition, CRC Press, 2004.

[5] Shen, H.S., *Functionally Graded Materials: Nonlinear Analysis of Plates and Shells,* CRC Press, USA, 2009.

[6] Elishakoff, I., Demetris, P.D., Gentilini, C., *Mechanics of Functionally Graded Material Structures,* World Scientific, USA, 2016.

[7] Ugural, A.C., *Stresses in Beams, Plates, and Shells, Third Edition,* CRC Press, 2010.

[8] Ye, J., *Laminated Composite Plates and Shells: 3D Modelling,* Springer, 2003.

[9] Jin, G., Ye, T., Su, Z., *Structural Vibration: A Uniform Accurate Solution for Laminated Beams, Plates and shells with general boundary conditions*, Springer, 2015.

[10] Civalek, O., Finite Element analyses of plates and shells, Elazığ: Fırat University, (in Turkish), 1998.

[11] Nie, G.J., Zhong, Z., Semi-analytical solution for three-dimensional vibration of functionally graded circular plates. *Comput Methods Appl Mech Eng,* 196, 4901-4910, 2007.

[12] Nie, G.J., Zhong, Z., Dynamic analysis of multidirectional functionally graded annular plates. *Appl Math Model,* 34, 608-616, 2010.

[13] Civalek, O., Gürses, M., Free vibration analysis of rotating cylindrical shells using discrete singular convolution technique. *Int J Pres Ves Pip,* 86(10), 677-683, 2009.

[14] Zhou, D., Lo, S.H., Cheung, Y.K., 3-D vibration analysis of annular sector plates using the Chebyshev-Ritz method. *J Sound Vib,* 320, 421 – 437, 2009.

[15] Civalek, O., Vibration analysis of laminated composite conical shells by the method of discrete singular convolution based on the shear deformation theory. *Compos Part B Eng,* 45(1), 1001-1009, 2013.

[16] Civalek, O., Free vibration analysis of composite conical shells using the discrete singular convolution algorithm. *Steel Compos Struct,* 6(4), 353-366, 2006.

[17] Civalek, O., The determination of frequencies of laminated conical shells via the discrete singular convolution method. *J Mech Mater Struct,* 1(1), 163-182, 2006.

[18] Zhao, X., Liew, K.M., Free vibration analysis of functionally graded conical shell panels by a meshless method, *Compos Struct,* 93, 649-664, 2011.

[19] Liew, K.M., Feng, Z.C., Vibration characteristics of conical shell panels with three-dimensional flexibility. *J Appl Mech,* 67(2), 314–320, 2000.

[20] Liew, K.M., Ng, T.Y., Zhao, X., Free vibration analysis of conical shells via the element-free kp-Ritz method. *J Sound Vib,* 281, 627-645, 2005.

[21] Demir, Ç., Mercan, K., Civalek, O., Determination of critical buckling loads of isotropic, FGM and laminated truncated conical panel. *Compos Part B: Eng,* 94, 1-10, 2016.

[22] Tornabene, F., Fantuzzi, N., Viola, E., Ferreira, A.J.M., Radial basis function method applied to doubly-curved laminated composite shells and panels with a General Higher-order Equivalent Single Layer formulation. *Compos Part B: Eng,* 55, 642–659, 2013.

[23] Liu, B., Ferreira, A.J.M., Xing, Y.P., Neves, A.M.A., Analysis of functionally graded sandwich and laminated shells using a layerwise theory and a differential quadrature finite element method. *Compos Struct,* 136, 546-553, 2016.

[24] Ferreira, A.J.M., Jorge, R.M.N., Roque, C.M.C., Free vibration analysis of symmetric laminated composite plates by FSDT and radial basis functions. *Comput Method Appl Mech Eng,* 194, 4265–4278, 2005.

[25] Ferreira, A.J.M., Roque, C.M.C., Neves, A.M.A., Jorge, R.M.N., Soares, C.M.M., Reddy, J.N., Buckling analysis of isotropic and laminated plates by radial basis functions according to a higher-order shear deformation theory. *Thin-Wall Struct,* 49(7), 804-811, 2011.

[26] Fantuzzi, N., Tornabene, F., Bacciocchi, M., Dimitri, R., Free vibration analysis of arbitrarily shaped Functionally Graded Carbon Nanotube-reinforced plates, *Compos Part B: Eng* doi.org/10.1016/j.compositesb.2016.09.021.

[27] Jin, G., Ma, X., Shi, S., Ye, T., Liu, Z., A modified Fourier series solution for vibration analysis of truncated conical shells with general boundary conditions. *Appl Acoustics,* 85, 82-96, 2014.

[28] Xie, X., Jin, G., Ye, T., Liu, Z., Free vibration analysis of functionally graded conical shells and annular plates using the Haar wavelet method. *Appl Acoustics,* 85, 130-142, 2014.

[29] Su, Z., Jin, G., Shi, S., Ye, T., Jia, Z., A unified solution for vibration analysis of functionally graded cylindrical, conical shells and annular plates with general boundary conditions. *Int J Mech Sci,* 80, 62-80, 2014.

[30] Jooybar, N., Malekzadeh, P., Fious, A., Vaghefi, M., Thermal effect on free vibration of functionally graded truncated conical shell panels. *Thin Wall Struct,* 103, 45-61, 2016.

[31] Malekzadeh, P., Heydarpour, Y., Free vibration analysis of rotating functionally graded cylindrical shells in thermal environment. *Compos Struct,* 94, 2971–81, 2012.

[32] Su, Z., Jin, G., Ye, T., Three-dimensional vibration analysis of thick functionally graded conical, cylindrical shell and annular plate structures with arbitrary elastic restraints. *Compos Struct,* 118, 432-447, 2014.

[33] Akgöz, B., Civalek O., Nonlinear vibration analysis of laminated plates resting on nonlinear two-parameters elastic foundations. *Steel Compos Struct,* 11(5), 403-421, 2011.

[34] Saidi, A.R., Baferani, A.H., Jomehzadeh, E., Benchmark solution for free vibration of functionally graded moderately thick annular sector plates. *Acta Mech,* 219, 309-335, 2011.

[35] Civalek, O., Ersoy, H., Free vibration and bending analysis of circular Mindlin plates using singular convolution method. *Int J Num Method Biomed Eng,* 25(8),907-922, 2009.

[36] Lin, C.C., Teng, C.S., Free vibration of polar orthotropic laminated circular and annular plates. *J Sound Vib,* 209, 797-810, 1988.

[37] Civalek, O., Dairesel Plakların Nöro-Fuzzy Tekniği ile Analizi. *Dokuz Eylül Üniversitesi Mühendislik Fakültesi,* 1(2), 13-31, 1999.

[38] Wang, Q., Shi, D., Liang, Q., Ahad, F., An improved Fourier series solution for the dynamic analysis of laminated composite annular, circular, and sector plate with general boundary conditions. *J Comp Mater,* 50, 4199-4233, 2016.

[39] Civalek, O., Çatal, H.H., Linear static and vibration analysis of circular and annular plates by the harmonic differential quadrature (HDQ) method. *Osmangazi Üniversitesi, Mühendislik ve Mimarlık Fakültesi Dergisi,* 16(1), 43-71, 2003.

[40] Jin, G., Ma, X., Shi, S., Ye, T., Liu, Z., A modified Fourier series solution for vibration analysis of truncated conical shells with general boundary conditions. *Appl Acoustics,* 85, 82-96, 2014.

[41] Civalek, O., Çatal, H.H., Plakların Diferansiyel Quadrature Metodu ile Stabilite ve Titreşim Analizi, *Teknik Dergi,* 14(1), 2835-2852, 2003.

[42] Su, Z., Jin, G., Shi, S., Ye, T., Jia, X., A unified solution for vibration analysis *Int J Mech Sci,* 80, 62-80, 2014.

[43] Tong, L., Free vibration of laminated conical shells including transverse shear deformation. *Int J Solids Struct,* 31, 443–456, 1994.

[44] Wei, G.W., Solving quantum eigenvalue problems by discrete singular convolution. *J Phys B*, 20, 343-352, 2000.

[45] Wei, G.W., A new algorithm for solving some mechanical problems. *Comput Meth Appl Mech Eng,* 190, 2017-2030, 2001.

[46] Wei, G.W., Vibration analysis by discrete singular convolution. *J Sound Vib,* 244, 535-553, 2001.

[47] Wei, G.W., Discrete singular convolution for beam analysis. Eng Struct, 23, 1045-1053, 2001.

[48] Hoffman, D.K., Wei, G.W., Zhang, D.S., Kouri, D.J., Shannon–Gabor wavelet distributed approximating functional, *Chem Phys Letter,* 287, 119-124, 1998.

[49] Shao, Z., Wei, G.W., Zhao, S., DSC time-domain solution of Maxwell's equations, *J Comput Phys,* 189, 427-453, 2003.

[50] Wei, G.W., Zhao, Y.B., Xiang, Y., A novel approach for the analysis of high-frequency vibrations. *J Sound Vib,* 257, 207-246, 2002.

[51] Wei, G.W., Zhao, Y.B., Xiang, Y., Discrete singular convolution and its application to the analysis of plates with internal supports. Part 1: Theory and algorithm. *Int J Num Meth Eng,* 55, 913-946, 2002.

[52] Ng, C.H.W., Zhao, Y.B., Wei, G.W., Comparison of discrete singular convolution and generalized differential quadrature for the vibration analysis of rectangular plates. *Comput Method Appl Mech Eng,* 193, 2483-2506, 2004.

[53] Hou, Y., Wei, G.W., Xiang, Y., DSC-Ritz method for the free vibration analysis of Mindlin plates. *Int J Num Meth Eng,* 62, 262-288, 2005.

[54] Civalek, O., Numerical analysis of free vibrations of laminated composite conical and cylindrical shells: discrete singular convolution (DSC) approach. *J Comput Appl Math*, 205, 251- 271, 2007.

[55] Civalek, O., Korkmaz, A., Demir, Ç., Discrete singular convolution approach for buckling analysis of rectangular Kirchhoff plates subjected to compressive loads on two opposite edges. *Adv Eng Softw*, 41, 557-560, 2010.

[56] Civalek, O., Analysis of thick rectangular plates with symmetric cross-ply laminates based on first-order shear deformation theory. *J Compos Mater*, 42, 2853–2867, 2008.

[57] Xin, L., Hu, Z., Free vibration of layered magneto-electro-elastic beams by SSDSC approach. *Compos Struct*, 125, 96-103, 2015.

[58] Xin, L., Hu, Z., Free vibration of simply supported and multilayered magnetoelectro-elastic plates. *Compos Struct*, 121, 344-350, 2015.

[59] Baltacıoğlu, A.K., Civalek, Ö., Akgöz, B., Demir, F., Large deflection analysis of laminated composite plates resting on nonlinear elastic foundations by the method of discrete singular convolution. *Int J Pres Ves Pip*, 88, 290-300, 2011.

[60] Civalek, Ö., Akgöz, B., Vibration analysis of micro-scaled sector shaped graphene surrounded by an elastic matrix. *Comp Mater Sci*, 77, 295-303, 2013.

[61] Gürses, M., Civalek, Ö., Korkmaz, A., Ersoy, H., Free vibration analysis of symmetric laminated skew plates by discrete singular convolution technique based on first-order shear deformation theory. *Int J Numer Methods Eng*, 79, 290-313, 2009.

[62] Baltacıoglu, A.K., Akgöz, B., Civalek, Ö., Nonlinear static response of laminated composite plates by discrete singular convolution method. *Compos Struct*, 93, 153-161, 2010.

[63] Gürses, M., Akgöz, B., Civalek, Ö., Mathematical modeling of vibration problem of nano-sized annular sector plates using the nonlocal continuum theory via eight-node discrete singular convolution transformation. *Appl Math Comput*, 219, 3226–3240, 2012.

[64] Mercan, K., Civalek, Ö., DSC method for buckling analysis of boron nitride nanotube (BNNT) surrounded by an elastic matrix. *Compos Struct*, 143, 300-309, 2016.

[65] Xin, L., Hu, Z., Free vibration analysis of laminated cylindrical panels using discrete singular convolution. *Compos Struct*, 149, 362-368, 2016.

[66] Civalek, O., Mercan, K., Demir, C., Vibration analysis of FG cylindrical shells with power-law index using discrete singular convolution technique. *Curved and Layer Struct*, 3, 82-90, 2016.

[67] Civalek, O., Ulker, M., HDQ-FD integrated methodology for nonlinear static and dynamic response of doubly curved shallow shells. *Struct Eng Mech*, 19, 535-550, 2005.

[68] Yang, S.Y., Zhou, Y.C., Wei, G.W., Comparison of the discrete singular convolution algorithm and the Fourier pseudospectral method for solving partial differential equations. *Comp Phys Commun*, 143, 113-135, 2002.

[69] Civalek, O. Nonlinear dynamic response of laminated plates resting on nonlinear elastic foundations by the discrete singular convolution-differential quadrature coupled approaches. *Compos Part B: Eng,* 50, 171-179, 2013.

[70] Mercan, K., Civalek, Ö., Buckling Analysis of Silicon Carbide Nanotubes (SiCNTs). *Int J Eng Appl Sci*, 8(2), 101-108, 2016.

[71] Mercan, K., Demir, Ç., Akgöz, B., Civalek, Ö., Coordinate Transformation for Sector and Annular Sector Shaped Graphene Sheets on Silicone Matrix. *Int J Eng Appl Sci*, 7(2), 56-73, 2015.

[72] Wang, X., Xu, S., Free vibration analysis of beams and rectangular plates with free edges by the discrete singular convolution. *J Sound Vib*, 329, 1780-1792, 2010.

[73] Wang, X., Wang, Y., Xu, S., DSC analysis of a simply supported anisotropic rectangular plate. *Compos Struct,* 94, 2576-2584, 2012.

[74] Duan, G., Wang, X., Jin, C., Free vibration analysis of circular thin plates with stepped thickness by the DSC element method. *Thin Wall Struct*, 85, 25-33, 2014.

International Journal of Engineering & Applied Sciences (IJEAS)
Vol.9, Issue 2 (Special Issue: Composite Structures) (2017) 66-87
http://dx.doi.org/10.24107/ijeas.309786
Int J Eng Appl Sci 9(2) (2017) 66-87

Heat-Induced, Pressure-Induced and Centrifugal-Force-Induced Exact Axisymmetric Thermo-Mechanical Analyses in a Thick-Walled Spherical Vessel, an Infinite Cylindrical Vessel, and a Uniform Disc Made of an Isotropic and Homogeneous Material

Vebil Yıldırım

University of Çukurova, Department of Mechanical Engineering, 01330, Adana, TURKEY
E-mail address: vebil@cu.edu.tr

Received date: April 2017
Accepted Date: May 2017

Abstract

Heat-induced, pressure-induced, and centrifugal force-induced axisymmetric exact deformation and stresses in a thick-walled spherical vessel, a cylindrical vessel, and a uniform disc are all determined analytically at a specified constant surface temperature and at a constant angular velocity. The inner and outer pressures are both included in the formulation of annular structures made of an isotropic and homogeneous linear elastic material. Governing equations in the form of Euler-Cauchy differential equation with constant coefficients are solved and results are presented in compact forms. For discs, three different boundary conditions are taken into account to consider mechanical engineering applications. The present study is also peppered with numerical results in graphical forms.

Keywords: Thermo-Mechanical, Elasticity solution, Exact solution, Rotating disc, Pressure vessel, Linear elastic

1. Introduction

Annular structures such as cylindrical or spherical vessels including discs are essential structural elements mainly made of an isotropic and homogeneous material. (Fig. 1). From those vessels may store gases, vapors, and liquids at various pressures and temperatures. The pressure is obtained from an external source, or by the application of heat from an indirect or direct source. That is a pressure vessel is mostly subjected simultaneously to both the mechanical and thermal loads. In a pressure vessel design determination of both the displacements and stresses is of great importance. If the material of the vessel is isotropic and homogeneous then those may be calculated analytically. By choosing appropriate parameters, an analytical solution also allows the optimization of the design parameters of a vessel structure.

Apart from vessels, a rotating disc is also one of the essential annular structural component. They are commonly used in a wide variety of engineering applications including space structures, electronic components and rotating machinery. Axisymmetric elasticity solutions to the both mechanical and thermal stress analysis of rotating discs have long been studied in the available literature. However, most of those studies modelled the thermo-elastic behavior of a disc with boundary condition which commonly proper for the cylindrical vessel having stress-free surfaces (Fig. 1c). But, in mechanical engineering applications rotating discs are commonly attached a rigid shaft at the center (Figs. 1d-e).

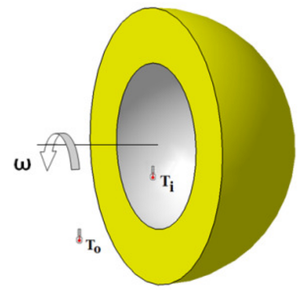

(a) Sphere

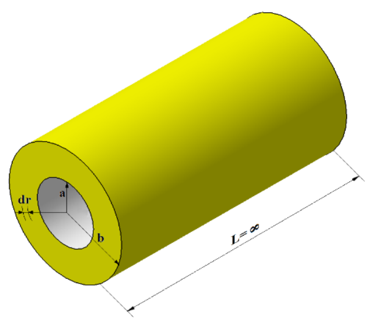

b) Infinite cylinder

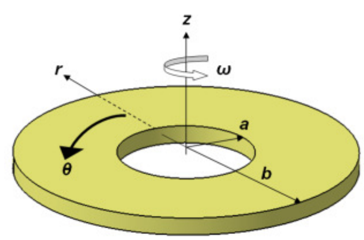

c) Disc / Circular annulus

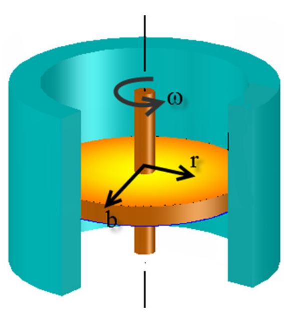

d) Disc having rigid case at the outer surface

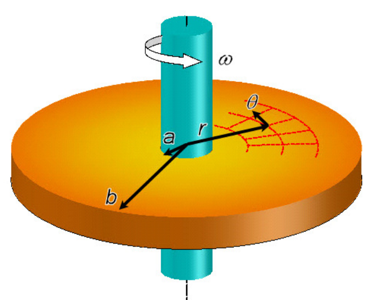

e) Disc mounted a shaft at its center

Fig. 1. Rotating annular structural geometries

As is well known in the thin-walled structure analysis the uniform stress distribution along the thickness is taken for granted. Apart from this, the effect of the radial stress on the equivalent stress is neglected. That is the radial stress due to either/both inner or/and outer pressures are assumed to be virtually zero.

However, in thick-walled structures, both the radial and hoop stresses play a role in the vessel design. It is obvious that the distribution of the stresses along the radial coordinate are no further uniform in thick-walled annular structures.

In the literature, the most number of studies are conducted with such structures subjected to just internal pressure. However, there are some types of structures such as submarine structures and vacuum tanks for which the predominant pressure is assumed to be the outer pressure and just the effect of this external pressure is considered in their analysis. In the present study effects of both the inner and the outer pressures are formulated analytically for each type of annular structures.

In some thermal studies, for the aim of simplicity, the distribution of the temperature along the radial coordinate is assumed to be linear without solving related Fourier heat conduction differential equation in thick-walled annular structures. As might be expected, this not reflects the true thermal behavior of such structures. The appropriate temperature distribution, which is obtained in terms of a logarithmic function, is identically the same but not linear for discs and cylindrical structures (Fig. 2). The temperature distribution in spheres shows a hyperbolic variation. In the present study, the exact temperature distributions obtained by the solution of Fourier heat conduction differential equation are used to study the thermo-elastic behaviors of such structures.

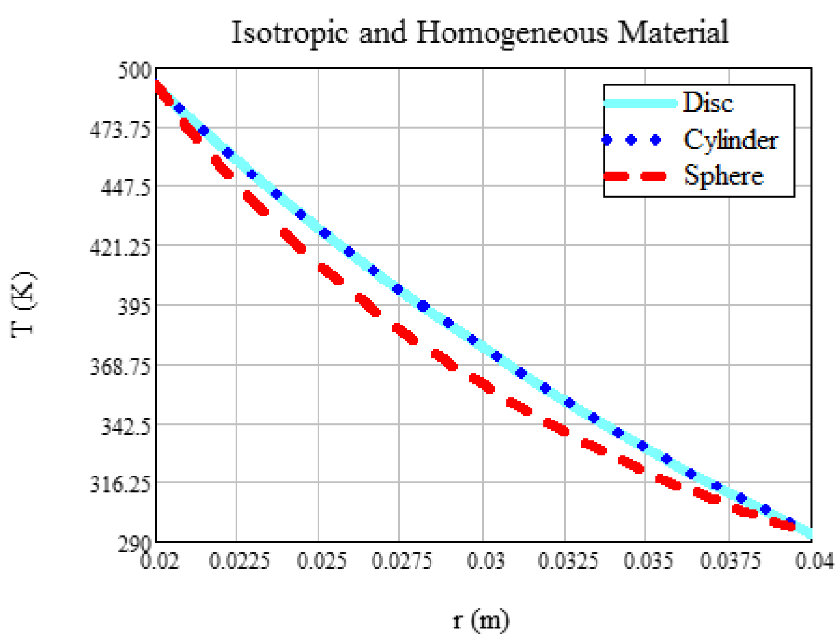

Fig. 2. Temperature distribution in thick-walled annular structures

Apart from the above, one may also be confused undoubtedly when studying the disc and cylindrical geometries. Discs are modeled in the case of plane stress assumption while the cylinders are modeled under plane-strain assumptions. The strain-displacement relations together with the equilibrium equation are identically the same under axisymmetric conditions for two annular structural types. As stated above, the temperature distribution of two types of structures are also one and the same. In spite of those, there are differences in their stress-strain relations that is in Hooke's law. This, sometimes, may cause some misperceptions in the formulation. In the present study the main differences in the formulation are demonstrated clearly.

Finally, one may spend relatively much time to obtain formulas with the same notation for thermo-mechanical behavior of such structures. In this respect, this study offers a concise and a complete study.

The subject of the present work is to form an infallible all-in-one source for the linear elastic behavior of such structures made of an isotropic and homogeneous material under thermal and mechanical loads (Fig. 1). Centrifugal forces, internal and external pressure forces are all classified as mechanical loads. To do so, governing equations which are second degree order non-homogeneous differential equations of constant coefficients are first derived from the elasticity field equations, and then they are solved analytically to obtain thermal and mechanical deformation and stresses. In this study exact thermo-mechanical analysis of this types of structures are carried out according to the superposition principle since small displacements are assumed. That is, each elastic quantity, either displacement or stress, is first determined separately for the related loading type. The resultant elastic quantity is then determined as a sum of each contributions.

$$
\begin{aligned}
(\sigma_\theta)_{THERMO-MECHANICAL} &= (\sigma_\theta)_{Pressure} + (\sigma_\theta)_{Rotation} + (\sigma_\theta)_{Thermal} \\
(u_r)_{THERMO-MECHANICAL} &= (u_r)_{Pressure} + (u_r)_{Rotation} + (u_r)_{Thermal} \\
(\sigma_r)_{THERMO-MECHANICAL} &= (\sigma_r)_{Pressure} + (\sigma_r)_{Rotation} + (\sigma_r)_{Thermal}
\end{aligned}
\tag{1}
$$

2. Spherical Vessels

In a spherical coordinate system, $(r, \theta, \emptyset)$, relations between the strain and displacement components for spherically symmetric case are as follows (see Notations)

$$
\begin{aligned}
\varepsilon_r(r) &= u_r'(r) \\
\varepsilon_\theta(r) = \varepsilon_\phi(r) &= \frac{u_r(r)}{r}
\end{aligned}
\tag{2}
$$

$$\gamma_{r\theta}(r) = \gamma_{r\phi}(r) = \gamma_{\theta\phi}(r) = 0$$

where prime symbol denotes the first derivative of the quantity with respect to the radial coordinate. It may be noted that the properties in θ and $\emptyset$ directions are identical for axisymmetric hollow spheres. Denoting the rise in temperature with respect to the temperature where stress value in the material is zero by $\Delta T(r) = T - T_\infty$, Hooke's law for a sphere made of an isotropic and homogeneous material is given by

$$\begin{aligned}\sigma_r(r) &= C_{11}\,\varepsilon_r(r) + C_{12}\varepsilon_\theta(r) + C_{12}\varepsilon_\phi(r) - (C_{11} + 2C_{12})\alpha\Delta T(r)\\ &= C_{11}\,\varepsilon_r(r) + 2C_{12}\varepsilon_\theta(r) - \frac{E}{1-2\nu}\alpha\Delta T(r)\\ &= C_{11}\,\varepsilon_r(r) + 2\lambda C_{11}\varepsilon_\theta(r) - (1+2\lambda)C_{11}\alpha\Delta T(r)\end{aligned} \tag{3}$$

$$\begin{aligned}\sigma_\theta(r) = \sigma_\phi(r) &= C_{12}\varepsilon_r(r) + (C_{11} + C_{12})\varepsilon_\theta(r) - (C_{11} + 2C_{12})\alpha\Delta T(r)\\ &= C_{12}\varepsilon_r(r) + (C_{11} + C_{12})\varepsilon_\theta(r) - \frac{E}{1-2\nu}\alpha\Delta T(r)\\ &= \lambda C_{11}\varepsilon_r(r) + (1+\lambda)C_{11}\varepsilon_\theta(r) - (1+2\lambda)C_{11}\alpha\Delta T(r)\end{aligned}$$

Where

$$C_{11} = \frac{(1-\nu)E}{(1-2\nu)(1+\nu)} \;;\quad C_{12} = \frac{\nu E}{(1-2\nu)(1+\nu)} = \frac{\nu}{1-\nu}C_{11} = \lambda C_{11} \tag{4}$$

Equilibrium equation for a spherical vessel rotating at a constant angular velocity is

$$\sigma_r'(r) + \frac{2}{r}(\sigma_r - \sigma_\theta) = -\rho\omega^2 r \tag{5}$$

Eqs. (2), (3), and (5) are referred to as the field equations of the elasticity. Substituting Eq. (2) into Eq. (3), and then successive substitution of Eq. (3) together with the first derivative of the radial stress into the equilibrium equation (5), the governing equation called Navier equation in terms of radial displacement is obtained as follow

$$u_r''(r) + \frac{2}{r}u_r'(r) - \frac{2}{r^2}u_r(r) = -\frac{\rho\omega^2 r}{C_{11}} + (1+2\lambda)\alpha T'(r) = -\frac{\rho\omega^2 r}{C_{11}} + \frac{(1+\nu)}{(1-\nu)}\alpha T'(r) \tag{6}$$

This is a second order non-homogeneous Euler-Cauchy type differential equation with constant coefficient. Its solution consists of the sum of its homogeneous and particular solutions. Since small displacements are assumed, the superposition principle holds.

To consider just mechanical loads due to either internal or external pressures, the following ($\omega = \Delta T = 0$) is solved with the boundary conditions [1]: $\sigma_r(a) = -p_a$, and $\sigma_r(b) = -p_b$.

$$u_r''(r) + \frac{2}{r}u_r'(r) - \frac{2}{r^2}u_r(r) = 0 \tag{7}$$

In order to account for just the rotation as a mechanical load ($p_a = p_b = 0;\ \Delta T = 0$) , Eq. (8) is solved under the boundary conditions: $\sigma_r(a) = 0$ and $\sigma_r(b) = 0$.

$$u_r''(\mathrm{r}) + \frac{2}{r}u_r'(r) - \frac{2}{r^2}u_r(r) = -\frac{\rho\omega^2 r}{C_{11}} \tag{8}$$

After determination of the temperature distribution along the thickness of the sphere, the thermo-elastic analysis is merely taken into consideration by the following [2-6] under the boundary conditions: $\sigma_r(a) = 0$; $\sigma_r(b) = 0$.

$$u_r''(r) + \frac{2}{r}u_r'(r) - \frac{2}{r^2}u_r(r) = \frac{(1+\nu)}{(1-\nu)}\alpha T'(r) \tag{9}$$

As stated above, before conducting the thermo-elastic analysis, a thermal analysis which defines the distribution of the temperature along the radial coordinate is required. Under the steady-state condition, in the absence of heat generation, temperature distribution along the thickness of the spherical vessel is found from the solution of the following heat conduction equation (Fourier's equation) with the first kind boundary conditions (Dirichlet): $T(a)=T_a$ and $T(b)=T_b$.

$$T''(r) + \frac{2}{r}T'(r) = 0 \tag{10}$$

Solution of the above is found as

$$T(r) = -\frac{D_1}{r} + D_2$$

$$D_1 = \frac{ab(T_a - T_b)}{a-b} = \frac{b(T_a - T_b)}{1-\frac{b}{a}}; \qquad D_2 = \frac{aT_a - bT_b}{a-b} = \frac{T_a - \frac{b}{a}T_b}{1-\frac{b}{a}} \tag{11}$$

$$T(r) = \frac{-brT_b + a(rT_a + b(T_b - T_a))}{(a-b)r} = \frac{a(r-b)T_a + b(a-r)T_b}{(a-b)r} = -\frac{ab(T_a - T_b)}{(a-b)r} + \frac{aT_a - bT_b}{a-b}$$

Eq. (9), now, takes the following form with Eq. (11)

$$u_r''(r) + \frac{2}{r}u_r'(r) - \frac{2}{r^2}u_r(r) = \frac{ab(T_a - T_b)\alpha(1+\nu)}{(a-b)r^2(1-\nu)} = \frac{\Psi}{r^2} \tag{12}$$

Solution of the above inhomogeneous equation with the boundary conditions, $\sigma_r(a) = 0$, and $\sigma_r(b) = 0$, gives the following

$$u_r(r) = \frac{B_2}{r^2} + B_1 r - \frac{\Psi}{2} \tag{13a}$$

$$B_1 = \frac{\lambda(\nu-1)\Psi(a-b)(a+b) - \alpha(\nu+1)(a^3T_a - b^3T_b)}{(2\lambda+1)(\nu-1)(a^3-b^3)} \tag{13b}$$

$$B_2 = \frac{a^2b^2(\lambda(\nu-1)\Psi(a-b)+ab\alpha(\nu+1)(T_a-T_b))}{2(\lambda-1)(\nu-1)(a^3-b^3)} \tag{13c}$$

Compact forms of the thermo-elastic radial displacement, radial and hoop stresses are

$$u_r(r) = \frac{K}{2(\nu-1)r^2(a^3-b^3)}$$

$$\begin{aligned} K = \alpha\big(a^3\big(b^3(\nu+1)\big(-(T_a-T_b)\big) + b(\nu+1)r^2(T_a-T_b) + 2(\nu-1)r^3T_a\big) \\ + a^2br^2(T_a-T_b)(b\nu+b-2\nu r) + ab^2r^2(T_a-T_b)(b\nu+b-2\nu r) \\ - 2b^3(\nu-1)r^3T_b\big) \end{aligned}$$

$$\sigma_r(r) = \frac{ab\alpha E(a-r)(b-r)(T_a-T_b)(a(b+r)+br)}{(\nu-1)r^3(a^3-b^3)} \tag{14}$$

$$\sigma_\theta(r) = -\frac{ab\alpha E(T_a-T_b)(r^2(a^2+ab+b^2)+a^2b^2-2r^3(a+b))}{2(\nu-1)r^3(a^3-b^3)}$$

Nayak et al. [4] offered the following thermal stresses for hollow spheres.

$$\sigma_r(r) = \frac{-\alpha E(T_a-T_b)}{(1-\nu)}\left\{\frac{\frac{b}{r}-1}{\frac{b}{a}-1} - \frac{\frac{b^3}{r^3}-1}{\frac{b^3}{a^3}-1}\right\} = \sigma_{r-Present\ (Eq.14)}$$

$$\sigma_\theta(r) = \frac{-\alpha E(T_a-T_b)}{(1-\nu)}\left\{\frac{\frac{b}{2r}-1}{\frac{b}{a}-1} + \frac{\frac{b^3}{2r^3}+1}{\frac{b^3}{a^3}-1}\right\} = \sigma_{\theta-Present\ (Eq.14)} \tag{15}$$

Nayak et al. [4] stated that from References [5-6] one can easily verify that Eq. (15) is indeed the expression for radial and tangential stresses for an isotropic and homogeneous thick spherical vessel. It is also readily verified that Nayak et al.'s [4] equations in (15) and present equations in (14) are identical. For the mechanical load due to internal and external pressures, analytical solution is found as

$$u_r(r) = \frac{C_2}{r^2} + C_1 r$$

$$\sigma_r = \frac{C_{11}(2C_2(-1+\lambda) + C_1r^3(1+2\lambda))}{r^3}$$

$$\sigma_\theta = \frac{C_{11}(C_2 - C_2\lambda + C_1r^3(1+2\lambda))}{r^3} \tag{16}$$

$$C_1 = -\frac{(2\nu^2+\nu-1)(a^3p_a-b^3p_b)}{E(2\lambda+1)(\nu-1)(a^3-b^3)}\,;\; C_2 = \frac{a^3b^3(2\nu^2+\nu-1)(p_a-p_b)}{2E(\lambda-1)(\nu-1)(a^3-b^3)}$$

Compact forms of the above in which radial and hoop stresses coincide with Roark's formulas [2] are.

$$
\begin{aligned}
u_r(r) &= -\frac{a^3 p_a\left(b^3(\nu+1)+2(1-2\nu)r^3\right)}{2r^2(a^3-b^3)E}+\frac{b^3 p_b\left(a^3(\nu+1)+2(1-2\nu)r^3\right)}{2r^2(a^3-b^3)E} \\
\sigma_r(r) &= \frac{a^3 p_a\left(b^3-r^3\right)}{\left(a^3-b^3\right)r^3}+\frac{b^3 p_b\left(r^3-a^3\right)}{\left(a^3-b^3\right)r^3} \\
\sigma_\theta(r) &= -\frac{a^3 p_a\left(b^3+2r^3\right)}{2\left(a^3-b^3\right)r^3}+\frac{b^3 p_b\left(a^3+2r^3\right)}{2\left(a^3-b^3\right)r^3}
\end{aligned} \tag{17}
$$

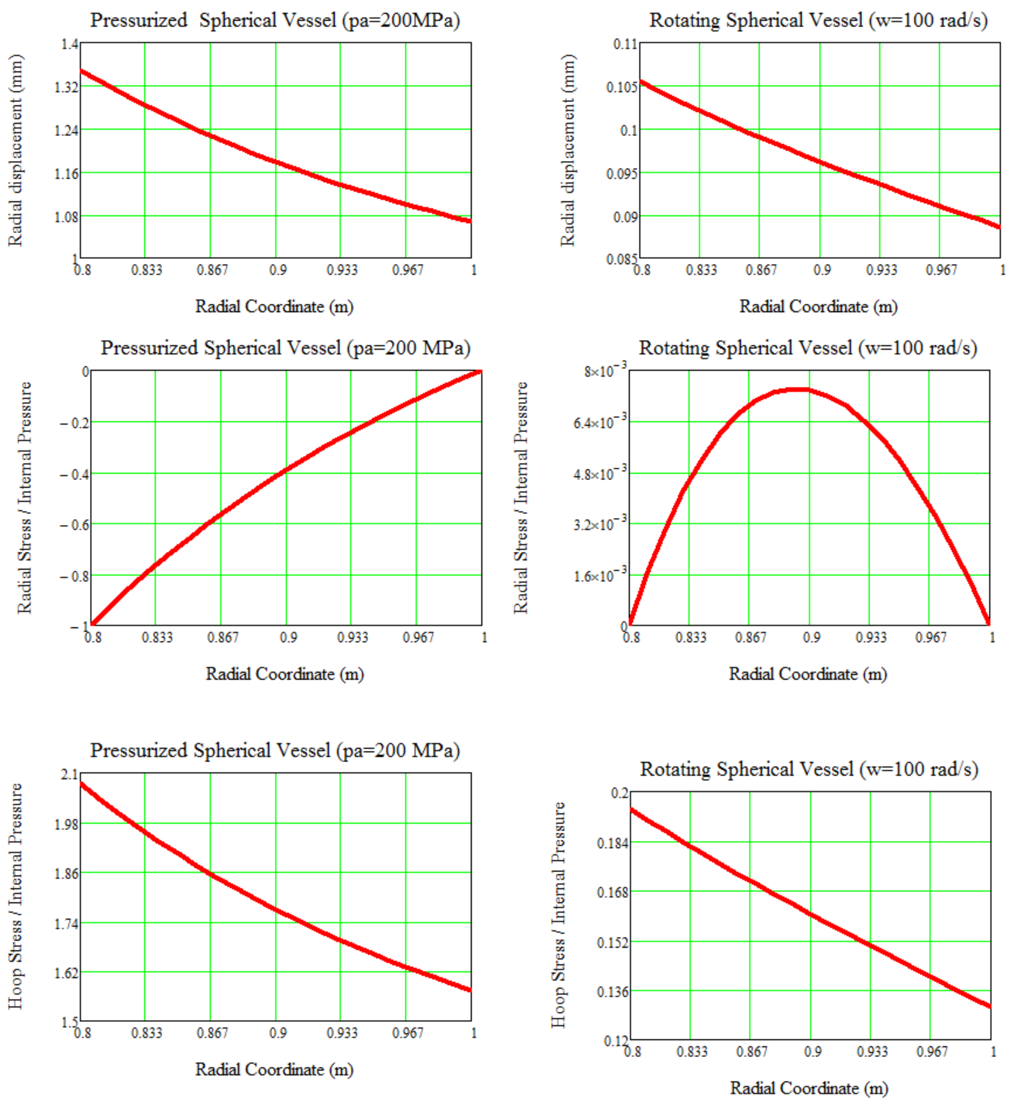

Fig. 3. Displacements and stresses induced by mechanical loads

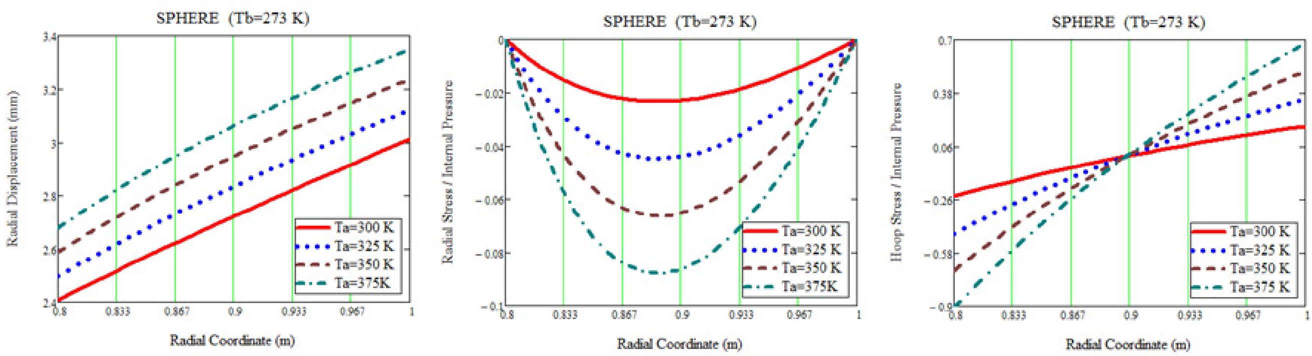

Fig. 4. Displacements and stresses induced by thermal loads

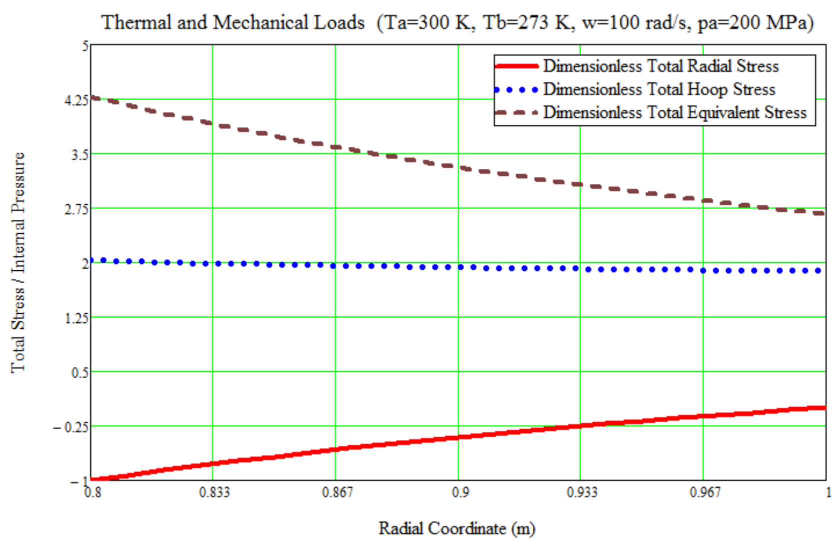

(a)

Fig. 5. Total and equivalent stresses for thermo-mechanical loads

Analytical solutions for mechanical load due to just rotation at a constant angular velocity is

$$u_r(r) = \frac{A_2}{r^2} + A_1 r - r^3 \Omega$$
$$\sigma_r(r) = \frac{2C_{11}A_2(-1+\lambda)}{r^3} + A_1 C_{11}(1+2\lambda) - C_{11} r^2 (3+2\lambda)\Omega \qquad (18a)$$
$$\sigma_\theta(r) = -\frac{C_{11}A_2(-1+\lambda)}{r^3} + A_1 C_{11}(1+2\lambda) - C_{11} r^2 (1+4\lambda)\Omega$$

$$\Omega = \frac{(2\nu^2 + \nu - 1)\,\rho\omega^2}{10\; E\;(\nu - 1)}$$
$$(18b)$$
$$A_1 = \frac{(a^4 + ba^3 + b^2a^2 + b^3a + b^4)(2\lambda+3)\,\Omega}{(a^2+ba+b^2)\;(2\lambda+1)} \qquad A_2 = -\frac{a^3b^3(a+b)(2\lambda+3)\,\Omega}{2(a^2+ba+b^2)\;(\lambda-1)}$$

For a numerical example, geometrical and material properties together with boundary conditions of the sphere are assumed to be [4]:

$$E = 209.2GPa \ ; \quad \nu = 0.29 \ ; \quad \sigma_{yield} = 700MPa \ ; \ \alpha = 10.58\,10^{-6}\,1/^{o}C$$
$$T_a = 27^{o}C \ ; \ T_b = 0^{o}C \ ; \ p_a = 200MPa \ ; \ p_b = 0 \ ; \ \omega = 100\,rad/s \ ; \ a = 0.8m \ ; b = 1.0m$$

Variation of the displacements and stresses induced by separate mechanical and thermal loads are illustrated in Figs. 3-4. From these figures it is observed that the radial displacement and hoop stresses which are tension in nature decrease with increasing b/a ratios for each individual mechanical loads. The maximum radial stress which is compression in nature is observed at the inner surface for mechanical pressure loads, and at the vicinity of the middle surface as being tension in nature for mechanical rotational loads. Variation of the displacements and stresses induced by thermal loads is illustrated in Fig. 4 at different temperatures of the inner surface. From the figure it is observed that the radial displacement increases with increasing b/a ratios and with increasing inner surface temperature. The maximum radial stress in compression is observed at the vicinity of the middle surface and increases with increasing surface temperature differences. Tangential stress varies from compressive to tensile for thermal load, from inside surface to outside. Considering superposition principle, variation of the thermo-mechanical stresses and equivalent stress in Eq. (19) which is given by [4] based on the Von-Mises criteria is illustrated in Fig. 5. It is observed that the equivalent stress gradually decreases in the radial direction, from inside surface to outside for thermo- mechanical loads and sets up tensile stresses. From this figure it is also observed that the equivalent stress exceeds the yield strength at the inner surface, $\sigma_{yield}/p_a = 3.5$.

$$\sigma_{eq} = \sqrt{2}(\sigma_\theta - \sigma_r) \tag{19}$$

3. Cylindrical Vessels

In a polar coordinate system, (r, θ), axisymmetric relations between the strain and displacement components are as follows (Fig. 1)

$$\varepsilon_r(r) = u_r'(r) \ ; \qquad \varepsilon_\theta(r) = \frac{u_r(r)}{r} \quad ; \qquad \gamma_{r\theta}(r) = 0 \tag{20}$$

Stress-strain relations for a cylindrical structure are given in the form of

$$\sigma_r(r) = C_{11}\,\varepsilon_r(r) + C_{12}\varepsilon_\theta(r) - (C_{11} + 2C_{12})\alpha\Delta T(r) = C_{11}\,\varepsilon_r(r) + \lambda C_{11}\varepsilon_\theta(r) - (1+2\lambda)C_{11}\alpha\Delta T(r)$$

$$\sigma_\theta(r) = C_{12}\varepsilon_r(r) + C_{11}\varepsilon_\theta(r) - (C_{11} + 2C_{12})\alpha\Delta T(r) = \lambda C_{11}\varepsilon_r(r) + C_{11}\varepsilon_\theta(r) - (1+2\lambda)C_{11}\alpha\Delta T(r) \tag{21}$$

$$C_{11} = \frac{(1-\nu)E}{(1-2\nu)(1+\nu)} \quad ; \quad C_{12} = \frac{\nu E}{(1-2\nu)(1+\nu)} = \frac{\nu}{1-\nu}C_{11} = \lambda C_{11}$$

Equilibrium equation for a cylindrical vessel or a disc rotating at a constant angular velocity, is

$$\sigma_r'(r)+\frac{1}{r}(\sigma_r-\sigma_\theta)=-\rho\omega^2 r \tag{22}$$

Substituting Eqs. (20) into Eqs. (21), and then successive substitution of Eqs. (21) with the first derivative of radial stress into the equilibrium equation in (22), a second order non-homogeneous Navier differential equation which governs the thermo-mechanical behavior of a cylindrical vessel is obtained as follows

$$u_r''(r)+\frac{1}{r}u_r'(r)-\frac{1}{r^2}u_r(r)=-\frac{\rho\omega^2 r}{C_{11}}+(1+2\lambda)\alpha T'(r) \tag{23}$$

In order to study thermo-elastic analysis alone of such structures, let's neglect the rotation together with inner/outer pressures

$$u_r''(r)+\frac{1}{r}u_r'(r)-\frac{1}{r^2}u_r(r)=(1+2\lambda)\alpha T'(r) \tag{24}$$

Solution of the above equation consists of the sum of its homogeneous and particular solutions. To get the particular solution, first, the temperature distribution due to the temperature difference between the cylinder surfaces at specific temperatures is required. Let's consider the Fourier heat conduction equation in polar coordinates for cylinders or discs

$$\frac{1}{r}\frac{d}{dr}\left(\frac{dT(r)}{dr}\right)=T''(r)+\frac{1}{r}T'(r)=0 \tag{25}$$

Temperature distribution along the thickness of a cylinder or a disc is found from the solution of the above equation with the first kind boundary conditions: $T(a)=T_a$ and $T(b)=T_b$.

$$T_{Cylinder}(r)=T_{Disk}(r)=lnr\Theta_1+\Theta_2$$
$$\Theta_1=\frac{T_a-T_b}{\ln a-\ln b} \quad ; \quad \Theta_2=\frac{-\ln bT_a+\ln aT_b}{\ln a-\ln b} \tag{26}$$

It may be noted that the temperature distribution in both cylinder and disc is govern by the same differential equation under the same boundary conditions. Considering the temperature distribution in Eq. (26) and its derivative, Navier equation for the thermo-elastic analysis of a cylindrical vessel made of a homogeneous and isotropic material is achieved as follows

$$u_r''(r)+\frac{1}{r}u_r'(r)-\frac{1}{r^2}u_r(r)=(1+2\lambda)\alpha T'(r)=(1+2\lambda)\frac{\alpha}{r}\left(\frac{T_a-T_b}{\ln a-\ln b}\right) \tag{27}$$

In the present work, the above differential equation is solved for the boundary conditions: $\sigma_r(a)=0$ and $\sigma_r(b)=0$. Solution of Eq. (27) is obtained as follows

$$u_r(r) = -\frac{H}{2(\nu-1)r(a-b)(a+b)(log(a)-log(b))}$$

$$\begin{aligned} H = \Big\{(\nu+1)\alpha\Big(&T_a(a^2\log(a)\,(b^2-2\nu r^2+r^2)-b^2\log(b)\,(a^2-2\nu r^2+r^2)\\ &+(\nu-1)r^2(a-b)(a+b)+2(\nu-1)r^2(a-b)(a+b)\log(b)\\ &+r^2(a-b)(a+b)\log(r))\\ &+T_b\big(a^2\log(a)\left(-(b^2-2\nu r^2+r^2)\right)+b^2\log(b)\,(a^2-2\nu r^2+r^2)\\ &+r^2(b^2-a^2)\log(r)-(\nu-1)r^2(a-b)(a+b)\\ &-2(\nu-1)r^2(a-b)(a+b)\log(a)\big)\Big)\Big\} \end{aligned} \tag{28}$$

$$\sigma_r(r) = \frac{(T_a-T_b)\alpha E(b^2(r^2-a^2)\ln b + a^2\ln a(b-r)(b+r)+r^2(a-b)(a+b)\ln r)}{2(\nu-1)r^2(a-b)(a+b)(\ln a-\ln b)}$$

$$\sigma_\theta(r) = \frac{(T_a-T_b)\alpha E(a^2\ln a(-(b^2+r^2))+b^2(a^2+r^2)\ln b + r^2(a-b)(a+b)(\ln r+1))}{2(\nu-1)r^2(a-b)(a+b)(\ln a-\ln b)}$$

In equations (28) stress formulas coincides with the literature [7]. However an error is found in the definitions of those stresses in Reference [8]. Solutions in Reference [8] is unfortunately employed in Reference [9]. The analytical formulas, again derived in the present study, for the radial displacements and stresses due to mechanical loads such as internal/external pressure and rotation at a constant angular velocity are presented below for the sake of the completeness of the study.

$$\begin{aligned} u_r(r) &= \left\{-\frac{a^2(\nu+1)p_a(b^2-2\nu r^2+r^2)}{r(a^2-b^2)E}\right\}+\left\{\frac{b^2(\nu+1)p_b(a^2-2\nu r^2+r^2)}{r(a^2-b^2)E}\right\}\\ \sigma_r(r) &= \left\{\frac{a^2p_a(b^2-r^2)}{r^2(a^2-b^2)}\right\}+\left\{\frac{b^2(a-r)(a+r)p_b}{r^2(b^2-a^2)}\right\}\\ \sigma_\theta(r) &= \left\{-\frac{a^2p_a(b^2+r^2)}{r^2(a^2-b^2)}\right\}+\left\{\frac{b^2(a^2+r^2)p_b}{r^2(a^2-b^2)}\right\} \end{aligned} \tag{29}$$

$$\begin{aligned} u_r(r) &= \left\{\frac{(\nu+1)\omega^2\rho\left(a^2(2\nu-3)(b^2+(1-2\nu)r^2)-(2\nu-1)r^2(b^2(2\nu-3)+r^2)\right)}{8(\nu-1)rE}\right\}\\ \sigma_r(r) &= \left\{\frac{(2\nu-3)\omega^2(a-r)(a+r)(r^2-b^2)\rho}{8(\nu-1)r^2}\right\}\\ \sigma_\theta(r) &= \left\{\frac{\omega^2\rho\left(a^2(2\nu-3)(b^2+r^2)+r^2(b^2(2\nu-3)+(2\nu+1)r^2)\right)}{8(\nu-1)r^2}\right\} \end{aligned} \tag{30}$$

Table 1. Material properties for cylinders

	METALS	E (GPa)	$\rho(kg/m^3)$	ν	k (W/mK)	α (1/K)
Metals	Titanium (Ti-6Al-4V)	122.557	2370	0.29	13.723	$7.579\text{x}10^{-6}$
	Aluminum (Al)	70	2700	0.3	204	$23\text{x}10^{-6}$
	Nickel (Ni)	199.5	8900	0.3	90.7	$13.3\text{x}10^{-6}$
	Stainless-Steel (SUS304)	201.04	7800	0.3262	15.379	$12.33\text{x}10^{-6}$
Ceramics	Silicon-Nitride (Si_3N_4)	348.43	4429	0.24	1.209	$5.8723\text{x}10^{-6}$
	Zirconium-Oxide (ZrO_2)	116.4	3657	0.3	1.78	$8.7\text{x}10^{-6}$
	Aluminum-Oxide (Al_2O_3)	393	3970	0.3	30.1	$8.8\text{x}10^{-6}$

For numerical example, geometrical and material properties of the cylindrical vessel are assumed to be: $a = 0.8m$; $b = 1.0m$. Variation of the displacements and stresses induced by thermal loads at different temperature differences is illustrated in Figs. 6-7 for both ceramics and metallic materials whose properties are given in Table 1. From these figures it is observed that the characteristics of the curves of the elastic quantities are similar for both ceramics and metals since they are both isotropic and homogeneous: The radial displacement gradually increases with increasing radial coordinate. The maximum thermo-elastic radial displacement is observed at the vicinity of the middle surface. The thermo-elastic radial stresses are compression in nature. The maximum hoop stresses are observed at the inner surface of the cylindrical vessel. The thermo-elastic hoop stresses are gradually changed their signs from inside surface to the outer surface. The numerical values of the hoop stresses are 10-times more than radial stresses. So the hoop stresses become leading in the thermo-elastic analysis.

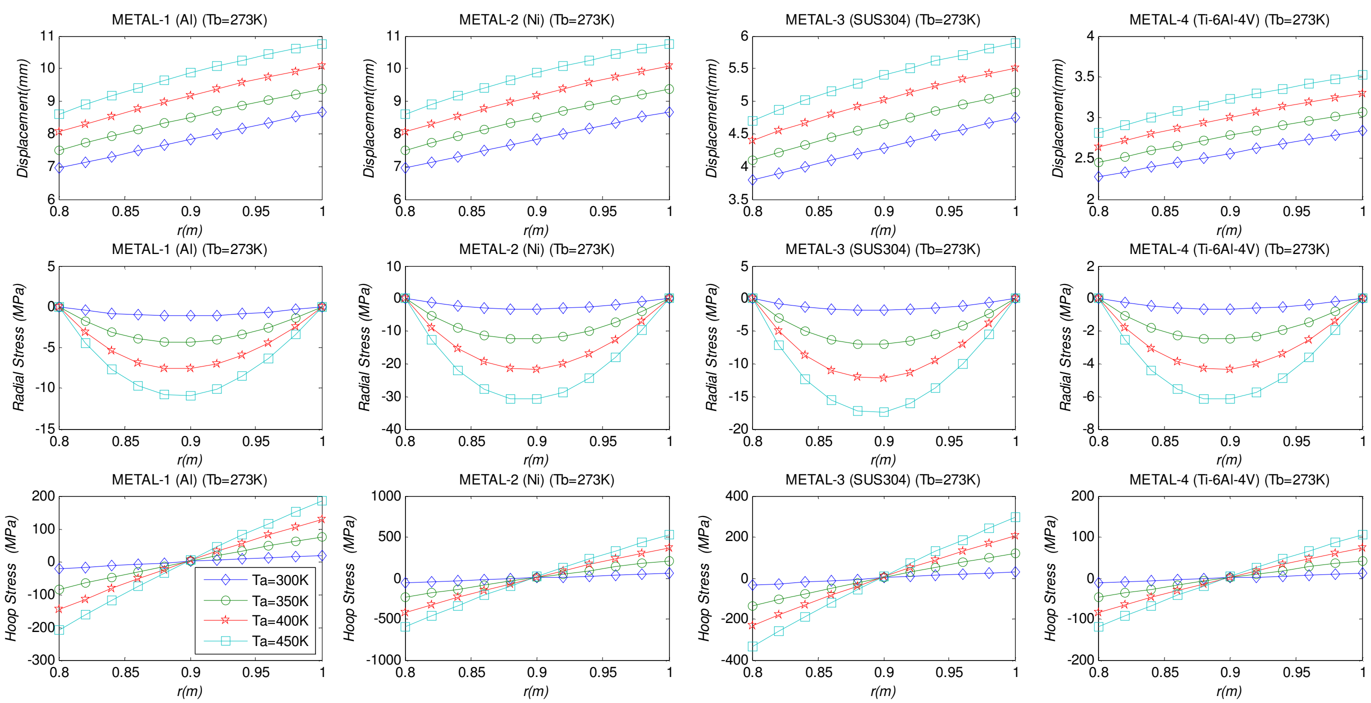

Fig. 6. Thermo-elastic radial displacement and the radial and hoop stresses for cylindrical vessels made of different metallic materials

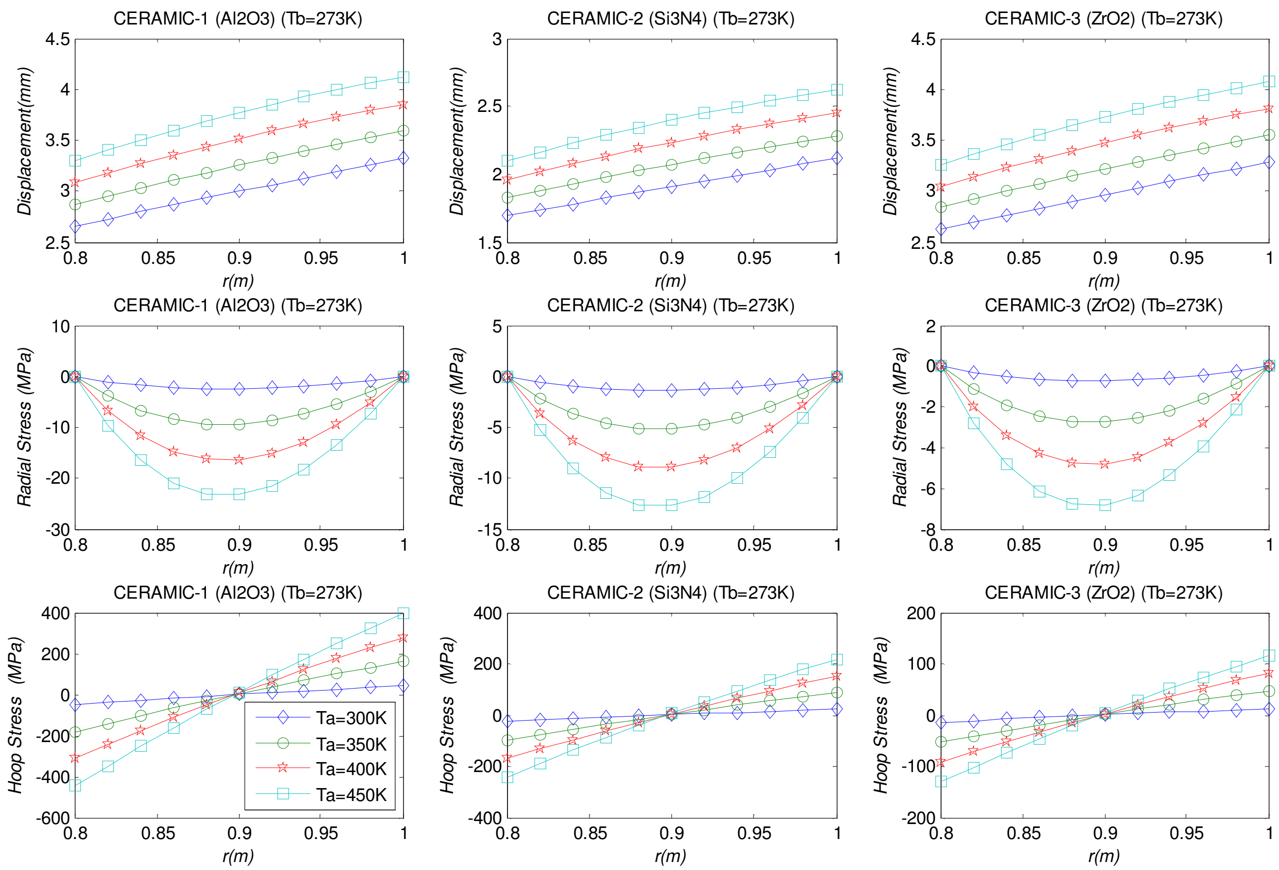

Fig. 7. Thermo-elastic radial displacement and the radial and hoop stresses for cylindrical vessels made of different ceramic materials

As expected, in a thermo-elastic analysis, the ceramic materials are more strength to the metallic materials. However, thermo-elastic behavior of a titanium-alloy is very similar to a zirconia. The titanium-alloy offers smaller displacements than the zirconia.

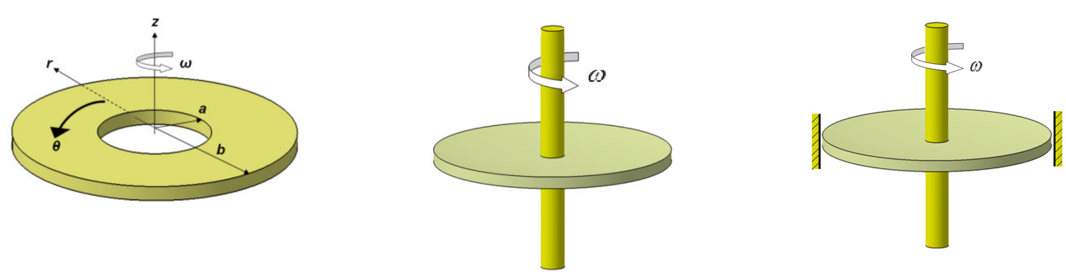

BC=1 $\{\sigma_r(a)=0 \text{ and } \sigma_r(b)=0\}$

BC=2 $\{u_r(a)=0 \text{ and } \sigma_r(b)=0\}$

BC=3 $\{u_r(a)=0 \text{ and } u_r(b)=0\}$

Fig. 8. Boundary conditions considered for discs

4. Discs at Different Boundary Conditions

In a polar coordinate system, (r,θ), axisymmetric field equations are as follows

$$
\begin{gathered}
\varepsilon_r(r)=u_r'(r)\ ; \qquad \varepsilon_\theta(r)=\frac{u_r(r)}{r}\ ; \qquad \gamma_{r\theta}(r)=0 \\
\sigma_r(r)=C_{11}\,\varepsilon_r(r)+C_{12}\varepsilon_\theta(r)-(C_{11}+C_{12})\alpha\Delta T(r)=C_{11}\,\varepsilon_r(r)+\lambda C_{11}\varepsilon_\theta(r)-(1+\lambda)C_{11}\alpha\Delta T(r) \\
\sigma_\theta(r)=C_{12}\varepsilon_r(r)+C_{11}\varepsilon_\theta(r)-(C_{11}+C_{12})\alpha\Delta T(r)=\lambda C_{11}\varepsilon_r(r)+C_{11}\varepsilon_\theta(r)-(1+\lambda)C_{11}\alpha\Delta T(r) \\
C_{11}=\frac{E}{(1-\nu)^2}\ ; \qquad C_{12}=\nu\,C_{11}=\lambda C_{11}
\end{gathered} \tag{31}
$$

From the above field equations, the following Navier differential equation which governs the thermo-mechanical behavior of the uniform disc is obtained.

$$u_r''(r)+\frac{1}{r}u_r'(r)-\frac{1}{r^2}u_r(r)=-\frac{\rho\omega^2 r}{C_{11}}+(1+\lambda)\alpha T'(r) \tag{32}$$

As stated above, temperature distribution for both discs and cylindrical vessels obey the same differential equations. So, from Eq. (26) the following is rewritten under the first kind boundary conditions

$$T(r)_{Cylinder\ and\ Disc}=lnr\Theta_1+\Theta_2=lnr\frac{T_a-T_b}{\ln a-\ln b}+\frac{-\ln bT_a+\ln aT_b}{\ln a-\ln b} \tag{33}$$

In order to study thermo-elastic analysis alone of such structures, the rotation is omitted in Eq. (32).

$$u_r''(r)+\frac{1}{r}u_r'(r)-\frac{1}{r^2}u_r(r)=(1+\nu)\alpha\frac{\Theta_1}{r}=(1+\nu)\frac{\alpha}{r}\left(\frac{T_a-T_b}{\ln a-\ln b}\right) \tag{34}$$

In the present work, the above differential equation is solved for each boundary condition given in Fig. 8 and the results are presented in Table 2. As ease of reference, the analytical formulas in Reference [10] for the uniform discs subjected to the mechanical loads are presented for different boundary conditions in the Appendix.

For a numerical study, geometrical and material properties of the disc are assumed to be: $a=0.1m$; $b=1.0m$, $E=209.2GPa$; $\nu=0.29$; $\sigma_{yield}=700MPa$; $\alpha=10.58\,10^{-6}\,1/^oC$. Variation of the displacements and stresses induced by thermal loads is illustrated in Fig. 9 under different boundary conditions and for different temperature differences. From Fig. 9 it is observed that the radial displacement gradually increases with increasing b/a ratios for *BC=1* and *BC=2*. The maximum radial displacement is observed at the outer surface for both *BC=1* and *BC=2* while it is at the vicinity of the middle surface for *BC=3*. *BC=1* and *BC=3* present radial stress as compression in nature while *BC=2* offers radial stress in tension. The maximum radial stress is observed at the inner surface for *BC=2*, at the close to the inner surface for the others. From Fig. 9, for all types of boundary conditions, maximum hoop stress is observed at the inner surface of the disc. Hoop stresses are gradually changed their signs from inside surface to the outer surface.

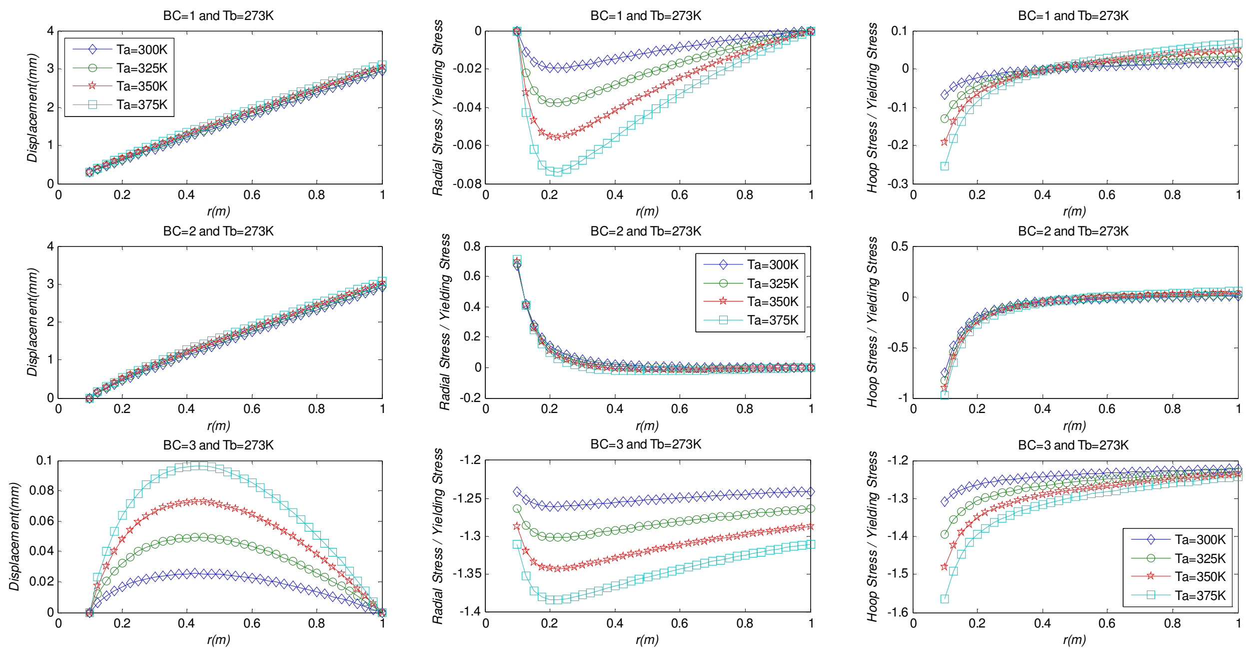

Fig. 9. Thermo-elastic behavior of a rotating disc at different boundary conditions

As stated above, some existing formulas in the literature contain some errors. Poworoznek [8] conducted an analytical study for cylindrical pressure vessels based on the theory proposed by Timoshenko [11]. He suggested some analytical formulas for both hollow cylinders (plain strain) and hollow discs (plain stress) for *BC=1*.

$$
\begin{aligned}
(\sigma_r)_{Poworoznek/DISC} &= \frac{E\alpha T_a}{2(1-\nu)\,ln\left(\frac{b}{a}\right)}\left(-\,ln\left(\frac{b}{r}\right) - \frac{a^2}{b^2-a^2}\left(1-\frac{b^2}{r^2}\right) ln\left(\frac{b}{a}\right)\right)\\
(\sigma_\theta)_{Poworoznek/DISC+CYLINDER} &= \frac{E\alpha T_a}{2\,ln\left(\frac{b}{a}\right)}\left(1 - ln\left(\frac{b}{r}\right) - \frac{a^2}{b^2-a^2}\left(1+\frac{b^2}{r^2}\right) ln\left(\frac{b}{a}\right)\right)\\
(\sigma_r)_{Poworoznek/CYLINDER} &= \frac{E\alpha T_a}{2\,ln\left(\frac{b}{a}\right)}\left(-\,ln\left(\frac{b}{r}\right) - \frac{a^2}{b^2-a^2}\left(1-\frac{b^2}{r^2}\right) ln\left(\frac{b}{a}\right)\right)
\end{aligned}
\tag{35}
$$

Let's re-consider analytical formulas derived in this study for the radial and hoop stresses for discs (Table 2) and cylinders (Eq. (28)) under *BC=1*. Comparison shows that there are some syntax errors in those formulas suggested by Poworoznek [8] as follows

$$
\begin{aligned}
(\sigma_r)_{Present/DISC} &= (1-\nu)(\sigma_r)_{Poworoznek/DISC}\\
(\sigma_\theta)_{Present/DISC} &= (\sigma_\theta)_{Poworoznek/DISC}\\
(\sigma_r)_{Present/CYLINDER} &= \frac{1}{(1-\nu)}(\sigma_r)_{Poworoznek/CYLINDER}\\
(\sigma_\theta)_{Present/CYLINDER} &= \frac{1}{(1-\nu)}(\sigma_\theta)_{Poworoznek/CYLINDER}
\end{aligned}
\tag{36}
$$

Table 2. Thermo-elastic formulas derived in this study for uniform discs ($\Theta_1 = \frac{T_a - T_b}{\ln a - \ln b}$; $\Theta_2 = \frac{-\ln b T_a + \ln a T_b}{\ln a - \ln b}$)

BC = 1 ⟹ $\sigma_r(a) = 0$; $\sigma_r(b) = 0$

$$u_r = \frac{\alpha(\Theta_1(a^2 \ln a(b^2(\nu+1) - (\nu-1)r^2) - b^2 \ln b(a^2(\nu+1) - (\nu-1)r^2) + r^2(a-b)(a+b)((\nu+1)\ln r - 1)) + 2\Theta_2 r^2(a-b)(a+b))}{2r(a-b)(a+b)}$$

$$\sigma_r = -\frac{\alpha E(T_a - T_b)(b^2(r^2 - a^2)\ln b + a^2 \ln a(b-r)(b+r) + r^2(a-b)(a+b)\ln r)}{2r^2(a-b)(a+b)(\ln a - \ln b)}$$

$$\sigma_\theta = \frac{\alpha E(T_a - T_b)(a^2 \ln a(b^2 + r^2) - b^2(a^2 + r^2)\ln b - r^2(a-b)(a+b)(\ln r + 1))}{2r^2(a-b)(a+b)(\ln a - \ln b)}$$

BC = 2 ⟹ $u_r(a) = 0$; $\sigma_r(b) = 0$

$$u_r = \frac{(\nu+1)\alpha(\Theta_1(a^2 \ln a(b^2(\nu+1) - (\nu-1)r^2) - r^2 \ln r(b^2(\nu+1) - a^2(\nu-1)) - b^2(a-r)(a+r)((\nu-1)\ln b + 1)) + 2b^2\Theta_2(a-r)(a+r))}{2a^2(\nu-1)r - 2b^2(\nu+1)r}$$

$$\sigma_r = \frac{\alpha E(\Theta_1(b^2 \ln b(a^2(\nu-1) - (\nu+1)r^2) + r^2 \ln r(b^2(\nu+1) - a^2(\nu-1)) - a^2(\nu+1)\ln a(b-r)(b+r) + a^2(b-r)(b+r)) + 2a^2\Theta_2(r^2 - b^2))}{2r^2(a^2(\nu-1) - b^2(\nu+1))}$$

$$\sigma_\theta = \frac{\alpha E(\Theta_1(a^2(-(b^2 + \nu r^2)) + a^2(\nu+1)\ln a(b^2 + r^2) - b^2 \ln b(a^2(\nu-1) + (\nu+1)r^2) + r^2 \ln r(b^2(\nu+1) - a^2(\nu-1)) + b^2(\nu+1)r^2) + 2a^2\Theta_2(b^2 + r^2))}{2r^2(a^2(\nu-1) - b^2(\nu+1))}$$

BC = 3 ⟹ $u_r(a) = 0$; $u_r(b) = 0$

$$u_r = \frac{(\nu+1)\alpha(T_a - T_b)(b^2(r^2 - a^2)\ln b + a^2 \ln a(b-r)(b+r) + r^2(a-b)(a+b)\ln r)}{2r(a-b)(a+b)(\ln a - \ln b)}$$

$$\sigma_r = \frac{\alpha E\left(\Theta_1\left(a^2 \ln a\left((\nu+1)r^2 - b^2(\nu-1)\right) + b^2 \ln b(a^2(\nu-1) - (\nu+1)r^2) + r^2(a-b)(a+b)(-\nu \ln r + \ln r - 1)\right) + 2\Theta_2 r^2(a-b)(a+b)\right)}{2(\nu-1)r^2(a-b)(a+b)}$$

$$\sigma_\theta = \frac{\alpha E(\Theta_1(a^2 \ln a(b^2(\nu-1) + (\nu+1)r^2) - b^2 \ln b(a^2(\nu-1) + (\nu+1)r^2) - r^2(a-b)(a+b)(\nu + (\nu-1)\ln r)) + 2\Theta_2 r^2(a-b)(a+b))}{2(\nu-1)r^2(a-b)(a+b)}$$

Before anything else, it is not proper to get the identical result for the hoop stresses in both plane strain and plane stress conditions as in Reference [8] while the radial stresses are found somewhat different for cylinders and discs. The author thinks that there must be some typing errors or some confusion between the elastic constants of plane stress and plain stress cases in those formulas in Reference [8].

To study the thermo-elastic behavior of the uniform discs under plane stress assumption the following differential equation should be used (See Eq. (32)).

$$u_r''(r) + \frac{1}{r}u_r'(r) - \frac{1}{r^2}u_r(r) = (1 + \lambda_{Plane-Stress})\alpha T'(r)$$
$$\lambda_{Plane-Stress} = \nu \tag{37}$$

Under plane strain assumption, the following differential equation governing the thermo-elastic behavior of the cylindrical structures should be used.

$$u_r''(r) + \frac{1}{r}u_r'(r) - \frac{1}{r^2}u_r(r) = (1 + 2\lambda_{Plane-Strain})\alpha T'(r)$$
$$\lambda_{Plane-Strain} = \frac{\nu}{1-\nu} \tag{38}$$

Temperature distributions along the radial direction for both cylinders and uniform discs are identical.

$$T(r)_{Cylinder\ and\ Disc} = lnr\Theta_1 + \Theta_2 \tag{39}$$

From the above it is revealed that it is possible to confuse easily with the elasticity constants in the formulation. The present results for cylinders exactly coincides with the literature [7].

To gain insight into the issue in question, an additional numerical example is performed for both the discs and cylindrical vessels having the same inner and outer radii *(a=0.5m, b=1m*) for *BC=1*. The results are shown in Fig. 10 in a comparative manner by using the same axis-scales. From the overall picture the characteristics of the curves are similar to each other. However numerical values of the quantities are not the same. For example, the same temperature difference results in higher stresses in cylinders than discs.

Finally, it is possible to obtain plane-stress formulas from the plane strain formulas by using appropriate coefficients. The converse is also true. In the elementary elasticity theory those coefficients are given for mechanical loads such as rotation and internal/external pressures. For instance, if one replace formally ν with $\frac{\nu}{1-\nu}$, and E with $\frac{E}{1-\nu^2}$ he may get the results for the plain-strain case from the plane stress solutions. As it is known ν should be replaced formally with $\frac{\nu}{1+\nu}$, and E is to be replaced with $\frac{E(1+2\nu)}{(1+\nu)^2}$ to get the plane stress results from the plain strain solutions. However this does not work alone for thermo-elastic analysis.

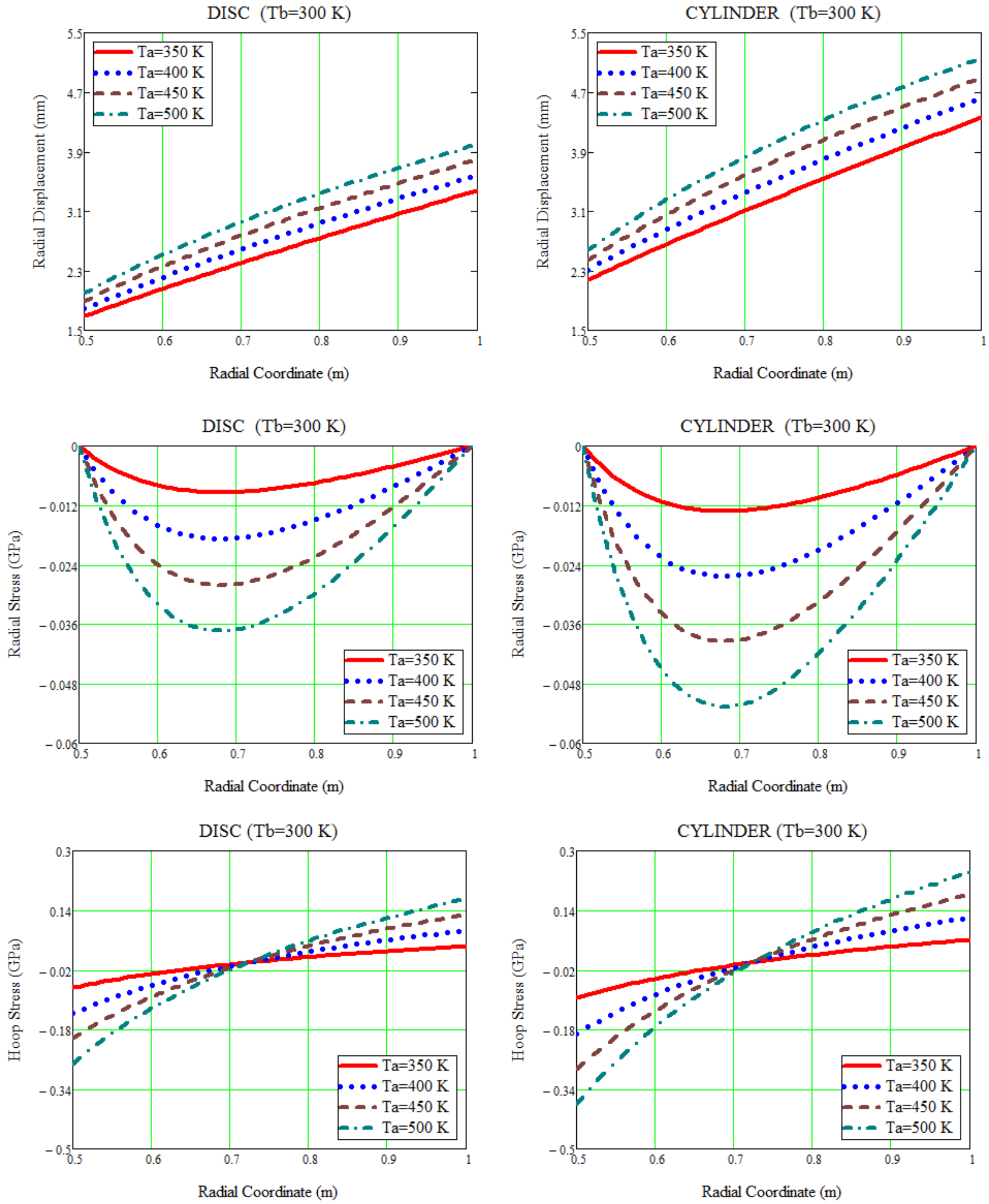

Fig. 10. Comparison of results for discs and cylinders (*a=0.5m, b=1m*) under BC=1

5. Conclusions

In this study thermo-mechanical analysis of annular structures made of a homogeneous and isotropic linear elastic material is handled analytically under different boundary conditions. The closed form formulas for the radial stress, hoop stress and the radial displacement are derived for each boundary condition and for each structural type. Apart from those, some muddles in the formulation of both cylinders and discs are clarified.

For the spherical rotating vessel with $p_a = 200\ MPa, \omega = 100\frac{rad}{s},\ T_a = 300K, T_b = 273K$, it is observed from Figs. 3-5 that

- Maximum radial displacement occurs at the inner surface for both pressure and centrifugal loads while it is located at the outer surface for thermal loads. For the given problem, thermal radial displacement are much excessive than mechanical load induced radial displacements.

- If radial stresses are considered, its maximum value is at the inner surface as in compression under pressure loading, at the mid-surface for both centrifugal force and thermal loads.

- As to the hoop stress, it reaches its maximum value at the inner surface as in tension for mechanical loads and it is also maximum at the inner surface as in compression for thermal loads. This contributes the almost uniform distribution of the total hoop stress along the thickness.

- The equivalent maximum stress is located at the inner surface due to all loadings, namely pressure, centrifugal force and thermal loads.

For the cylinders it is observed from Fig. 6 that the radial displacement progressively increases with increasing radial coordinate. The maximum thermo-elastic compressional radial displacement is examined at the vicinity of the middle surface. The maximum hoop stresses are watched at the inner surface of the cylindrical vessel. The thermo-elastic hoop stresses are in compression at the inner surface while they are in tension at the outer surface. The numerical values of the hoop stresses are nearly 10-times more than radial stresses. So the hoop stresses are guiding stresses in the thermo-elastic analysis.

The thermo-elastic behavior of stress-free discs is very similar to cylindrical vessels. However the same inner and outer radius together with the same temperature difference yield higher stresses in cylinders than stress-free discs. For other types of discs attached a shaft at its center (for BC=2 and BC=3) have much higher hoop stresses at the inner surface as in compression due to thermal loads.

By using the closed-form formulas offered in the present study, such structures may be tailored to the user’s need. The author also hopes that this study may form an infallible all-in-one source for the readers studying the linear elastic behavior of such structures made of an isotropic and homogeneous material under thermal and mechanical loads.

APPENDIX: Displacement and stresses of uniform isotropic and homogeneous discs subjected to mechanical loads [10] ($p_a = Inner\ pressure,\ \ p_b = Outer\ pressure$)

$\sigma_r(a) = -p_a$
$\sigma_r(b) = -p_b$

$$u_r = -\frac{a^2 p_a (b^2(\nu+1) - (\nu-1)r^2)}{Er(a^2-b^2)} + \frac{b^2 p_b (a^2(\nu+1) - (\nu-1)r^2)}{Er(a^2-b^2)}$$

$$\sigma_r = \frac{a^2 p_a (b^2 - r^2)}{r^2(a^2-b^2)} + \frac{b^2 p_b (a-r)(a+r)}{r^2(b^2-a^2)}$$

$$\sigma_\theta = -\frac{a^2 p_a (b^2 + r^2)}{r^2(a^2-b^2)} + \frac{b^2 p_b (a^2 + r^2)}{r^2(a^2-b^2)}$$

$\sigma_r(a) = 0$
$\sigma_r(b) = 0$

$$u_r = \frac{\rho\omega^2(a^2(\nu+3)(b^2(\nu+1) - (\nu-1)r^2) - (\nu-1)r^2(b^2(\nu+3) - (\nu+1)r^2))}{8Er}$$

$$\sigma_r = \frac{\rho\omega^2(\nu+3)(a^2-r^2)(r^2-b^2)}{8r^2}$$

$$\sigma_\theta = \frac{\rho\omega^2(a^2(\nu+3)(b^2+r^2) + r^2(b^2(\nu+3) - (3\nu+1)r^2))}{8r^2}$$

$u_r(a) = 0$
$\sigma_r(b) = 0$

$$u_r = \frac{\omega^2\rho\left(a^2(\nu+3)(b^2(\nu+1) - (\nu-1)r^2) - (\nu-1)r^2(b^2(\nu+3) - (\nu+1)r^2)\right)}{8rE}$$

$$\sigma_r = \frac{(\nu+3)\omega^2(a-r)(a+r)(r^2-b^2)\rho}{8r^2}$$

$$\sigma_\theta = \frac{\omega^2\rho\left(a^2(\nu+3)(b^2+r^2) + r^2(b^2(\nu+3) - (3\nu+1)r^2)\right)}{8r^2}$$

$u_r(a) = 0$
$u_r(b) = 0$

$$u_r = \frac{(\nu^2-1)\omega^2(r^2-a^2)(r^2-b^2)\rho}{8rE}$$

$$\sigma_r = \frac{\omega^2\rho\left(a^2\left((\nu+1)r^2 - b^2(\nu-1)\right) + r^2(b^2(\nu+1) - (\nu+3)r^2)\right)}{8r^2}$$

$$\sigma_\theta = \frac{\omega^2\rho\left(a^2(b^2(\nu-1) + (\nu+1)r^2) + r^2(b^2(\nu+1) - (3\nu+1)r^2)\right)}{8r^2}$$

Notations

a, b	Inner radius and outer radius, respectively
C_1, C_2	Integration constants
C_{ij}	elastic constants in Hooke's law
E	Young's modulus
p_a, p_b	Pressures at inner and outer surfaces, respectively
r	radial coordinate
T_a, T_b	temperature at the inner and outer surfaces, respectively
u_r	radial displacement
ε_r	radial strain
ε_θ	tangential strain
α	thermal expansion coefficient
$\gamma_{r\theta}, \gamma_{r\phi}, \gamma_{\theta\phi}$	engineering shear strain components
$\emptyset$	Azimuthal coordinate
ν	Poisson's ratio
ρ	density of the vessel material
σ_r	radial stress
σ_θ	hoop stress
θ	tangential coordinate
ω	constant angular velocity *(rad/s)*

References

[1] Bower, A. F., *Applied Mechanics of Solids;* Taylor and Francis, 2012.

[2] Young, W.C., Budynas, R.G., *Roark's Formulas for Stress and Strain*; McGraw-Hill, Seventh Edition, New York. 2002.

[3] Hetnarski, B., Eslami, M.R., *Thermal Stresses-Advanced Theory and Applications*; Springer, 2009.

[4] Nayak, P., Mondal, S.C., Nandi, A., Stress, strain and displacement of a functionally graded thick spherical vessel. *International Journal of Engineering Science and Technology (IJEST)*, 3/4, 2659-2671, 2011.

[5] Chakrabarty, J., *Theory of Plasticity*; McGraw Hill, New York, 1998.

[6] Noda, N., Hetnarski, R.B., Tanigawa , Y., *Thermal Stresses*; Taylor and Francis, New York, 2003.

[7] *Heat Transfer Problems and Thermal Stresses*, FEM II. Comp. Lab, www.meil.pw.edu.pl/sms/content/download/24488/.../FEMII_LAB_THERM_v2.pdf

[8] Poworoznek, P.P., Elastic-Plastic Behavior of a Cylinder Subject to Mechanical and Thermal Loads; *Rensselaer Polytechnic Institute, Master Thesis*, Hartford, CT. 2008.

[9] Kanlıkama, B., Abuşoğlu, A., Güzelbey, İ.H. Coupled thermoelastic analysis of thick-walled pressurized cylinders. *International Journal of Energy and Power Engineering,* 2/2, 60-68. 2013.

[10] Yıldırım, V., Analytic solutions to power-law graded hyperbolic rotating discs subjected to different boundary conditions. *International Journal of Engineering & Applied Sciences (IJEAS)*, 8/1, 38-52, 2016.

[11] Timoshenko, S., Strength of Material Part II, Advanced Theory and Problems, 3rd Edition, D. Van Nostrand Company Inc., Princeton, NJ, 1956.

International Journal of Engineering & Applied Sciences (IJEAS)
Vol.9, Issue 2 (Special Issue: Composite Structures) (2017) 88-102
http://dx.doi.org/10.24107/ijeas.309818
Int J Eng Appl Sci 9(2) (2017) 88-102

A Nonlocal Strain Gradient Shell Model for Free Vibration Analysis of Functionally Graded Shear Deformable Nanotubes

Fahimeh Mehralian[a] and Yaghoub Tadi Beni [b]*

[a]Mechanical Engineering Depratment, Shahrekord University, Shahrekord, Iran
[b]Faculty of Engineering, Shahrekord University, Shahrekord, Iran
[*]E-mail address: tadi@eng.sku.ac.ir

Received date: April 2017
Accepted Date: May 2017

Abstract

In the current study, the size dependent free vibration of shear deformable functionally graded (FG) nanotubes is investigated. The nanotube is modeled as cylindrical shell which contains small scale effects by using the nonlocal strain gradient theory. Material properties of the FG nanotube are assumed to be variable along thickness direction according to power law distribution. The Hamilton's principle is implemented to derive the governing equations and boundary conditions. The numerical results are presented for simply supported FG nanotube and the influence of different parameters, such as nonlocal parameter, length scale parameter, length, thickness and power law index on frequency of FG nanotube are extensively studied. The results reveal that the frequency is significantly size dependent.

Keywords: Nonlocal strain gradient theory, Nanotube, Vibration, Size-dependent, first order shear deformation theory.

1. Introduction

Offering unique benefits compared to conventional materials, functionally graded materials have been found tremendous amount of interest among researchers. The material properties of FG materials are changed smoothly in one or more directions to overcome stress concentration, as a common problem in usual composite materials [1]. Since they include two different components, FG materials are able to utilize the desirable properties of each constituent and as a result they can be designed for specific functions and applications. The static and dynamic behavior of FG beams, plats and shells are studied by many researchers. For example, Tadi et al. studied the free vibration of FG nanoshells and the effects of different parameters on frequency was shown as well [2]. The bending, buckling and vibration behaviors of axially FG nanobeams were investigated by Li et al and the critical buckling force and natural frequency were shown size dependent [3]. Ebrahimi et al. examined the wave propagation of FG nanoplate under nonlinear thermal loading and the influence of different parameters such as gradient index, temperature distribution and length scale parameter on the wave dispersion was presented [4]. The buckling of cylindrical and conical panels and shells of laminated composite, FGM and carbon nanotube reinforced functionally graded cases were examined by Civalek and the effects of material and geometrical parameters on buckling response were shown [5]. Akgöz et al. studied the longitudinal free vibration of axially FG microbars for different boundary conditions and the effect of material and geometrical parameters on natural frequency was shown [6].

In recent years, the increasing growth of nanotechnology leads to inspiring innovations in electrical, magnetic, and optical devices at the nanoscale and nanotubes are surely the most exciting nanostructure playing an important role in nanotechnology today [7]. The research on nanotubes has illustrated their prominent mechanical and electronic properties which are expected to result in revolutionary new devices. The more accurate realization of nanotubes behavior, however has so far been limited because of their dimensions, which are often equal or smaller than the characteristics length scales [8]. Modified continuum theories, which are developed as analytical methods producing more accurate results as such being comparable to those of atomistic models, are utilized in many studies. For example, Mehralian et al. studied the buckling of FG piezoelectric nanoshell under pressure based on the new modified couple stress theory and the critical buckling pressure was shown significantly size dependent by increase in thickness and decrease in length [9]. Size-dependent first order shear deformable shell model on the basis of modified strain gradient theory was utilized by Gholami et al. to study the axial buckling of functionally graded cylindrical shell [10]. The effect of material property gradient index was illustrated significant on the buckling load. Mehralian et al. studied the free vibration of FG truncated conical shell in thermal environment based on the modified couple stress theory and natural frequency was shown significantly size dependent particularly by decreasing apex angle and increasing gradient index [11]. The size dependent buckling behavior of silicon carbide nanotubes were investigated by Mercan et al. on the basis of Eringen's nonlocal elasticity and surface elasticity and the influence of geometrical parameters on critical buckling load was indicated [12]. Akgöz et al. studied the buckling of single walled carbon nanotubes using modified couple stress theory and strain gradient theory [13].

Nonlocal strain gradient theory, as higher order continuum theory, which is able to predict the stiffens-hardening effects besides stiffness-softening ones, is introduced by Lim et al. [14]. In this theory, the stress field accounts nonlocal stress field besides strain gradients stress filed and two material length scale parameters beside two Lame constants are introduced [14]. There are many studies in which the static and dynamic behaviors of nanobeams and nanoplates are investigated based on this theory. For example, Ebrahimi et al. examined the buckling of curved FG nanobeam based on the nonlocal strain gradient theory for simply supported and clamped boundary conditions and the effect of different parameters such as length scale parameters, power law exponent and boundary conditions were indicated [15]. The wave propagation in a viscoelastic SWCNT are studied based on the nonlocal strain gradient theory using Timoshenko beam model by Tang et al. and the effects of tube size on the wave dispersion was shown [16].

Motivated by the mentioned discussion, this paper examines the vibration of FG nanotube based on the nonlocal strain gradient theory using the first order shear deformation shell model. The governing equations and boundary conditions are derived using Hamilton's principle. The free vibration of simply supported cylindrical shell, as a case study, is investigated. The effects of different parameters such as material length scale parameters, thickness ratio and length ratio are illustrated on the frequency.

2. Theoretical development

Consider a FG nanotube modeled as cylindrical shell in Fig. 1, in which geometrical parameters of length, L, radius, R and thickness h are also indicated. FGM is usually made by the combination of two components (e.g. ceramics and metal) and the material properties of FG cylindrical shell varies continuously and consistently from the material properties of ceramics on the inner surface of the cylindrical shell to the properties of the metal on the outer surface as a function of constituent's volume fraction. Variation in volume fraction of metal and ceramic according to power law distribution along cylindrical shell thickness is expressed in the following equations:

$$V_m = \left(\frac{\hat{z}}{h}\right)^{\beta} \qquad V_c = 1 - V_m \tag{1}$$

In the above equation, β stands for power index which varies in the $0 \le \beta \le \infty$ interval, and as illustrated by Fig. 1, $\hat{z}$ stands for the arbitrary surface distance from the inner ones of the cylindrical shell. Therefore, the material properties of this cylindrical shell are expressed as:

$$\begin{aligned} E(\hat{z}) &= (E_m - E_c)\left(\frac{\hat{z}}{h}\right)^{\beta} + E_c \\ \rho(\hat{z}) &= (\rho_m - \rho_c)\left(\frac{\hat{z}}{h}\right)^{\beta} + \rho_c \\ \nu(\hat{z}) &= (\nu_m - \nu_c)\left(\frac{\hat{z}}{h}\right)^{\beta} + \nu_c \end{aligned} \tag{2}$$

where E_c , ρ_c and ν_c are obtained in $\hat{z}=0$, and E_m , ρ_m and ν_m are obtained in $\hat{z}=h$, which respectively represent Young's modulus, density and Poisson's ratio of ceramics and metal. As displayed by Fig. 1, the displacement field of cylindrical shell based on first order shear deformation theory along the three directions of x, θ and z is expressed as:

$$\begin{aligned} U(x,\theta,z,t) &= u(x,\theta,t) + z\psi_x(x,\theta,t) \\ V(x,\theta,z,t) &= v(x,\theta,t) + z\psi_\theta(x,\theta,t) \\ W(x,\theta,z,t) &= w(x,\theta,t) \end{aligned} \tag{3}$$

In the above equation, $u(x,\theta,t)$, $v(x,\theta,t)$ and $w(x,\theta,t)$ are considered as neutral axis displacement, and $\psi_x(x,\theta,t)$ and $\psi_\theta(x,\theta,t)$ as rotation of a transverse normal about the circumferential and axial directions. Besides, the position of the neutral axis is expressed as follows [2]:

$$\hat{z}_c = \frac{\int_A \frac{E(\hat{z})}{1-\nu^2(\hat{z})}\hat{z}\,dA}{\int_A \frac{E(\hat{z})}{1-\nu^2(\hat{z})}dA} \tag{4}$$

To extract the governing equations of FG nanotubes, Hamilton's principle is utilized as below:

$$\int_{\Delta t}(\delta U_s - \delta T + \delta W_e)dt = 0 \tag{5}$$

where δT represents kinetic energy variation, δU_s stands for strain energy variation, and δW_e is variation in the work of external loads acting on the cylindrical shell, which is neglected in this study .
The kinetic energy is obtained from time derivation on the displacement variables, as follows:

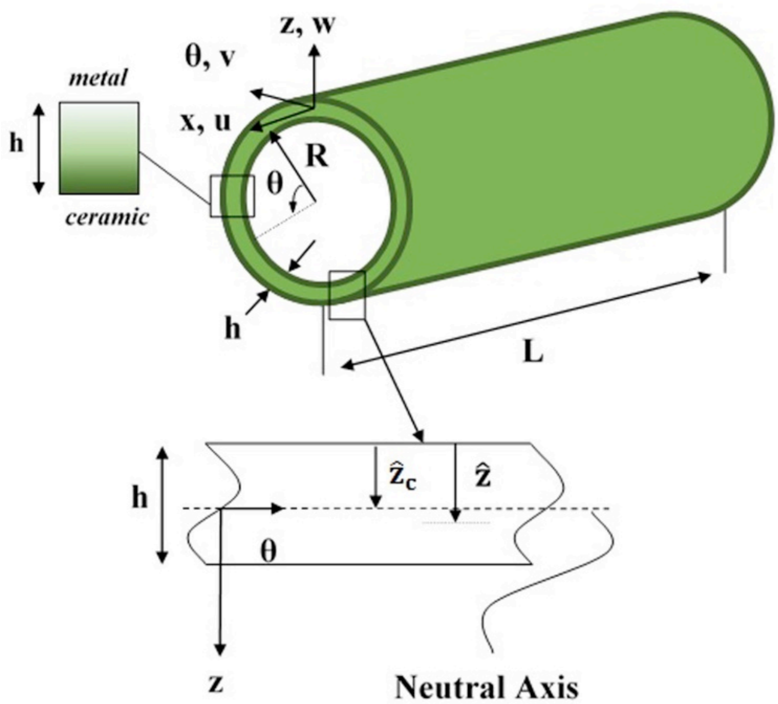

Fig. 1. Coordinate system and geometry of the FG nanotube.

$$T = \frac{\rho(\hat{z})}{2}\iiint_V \left[U^2 + V^2 + W^2\right] dV \tag{6}$$

and the variation of kinetic energy is obtained as:

$$\delta T = \frac{1}{2}\int_V \rho(\hat{z})\left[\left(\frac{\partial \delta u}{\partial t} + z\frac{\partial \delta \psi_x}{\partial t}\right)^2 + \left(\frac{\partial \delta v}{\partial t} + z\frac{\partial \delta\delta \psi_\theta}{\partial t}\right)^2 + \left(\frac{\partial \delta w}{\partial t}\right)^2\right] R\,dx\,d\theta\,dz \tag{7}$$

Based on the nonlocal strain gradient theory proposed by Lim et al. the strain energy is given by [9]:

$$U_s = \frac{1}{2}\iiint_V \left(\sigma_{ij}\varepsilon_{ij} + \sigma^{(1)}{}_{ij}\nabla\varepsilon_{ij}\right) dV \tag{8}$$

where

$$\varepsilon_{ij} = \frac{1}{2}\left(u_{i,j} + u_{j,i}\right) \tag{9}$$

$$\sigma_{ij} = C_{ijkl}\,\varepsilon_{kl} \tag{10}$$

which, ε_{ij}, σ_{ij} are the components of strain and stress tensor respectively and C_{ijkl} represents the elasticity tensor for cylindrical shell. Also, the non-zero components of strain field are obtained by substituting Eq. (3) into (9) and using the assumption $(1+z/R)\approx 1$.

$$\begin{aligned}
\varepsilon_{xx} &= \frac{\partial u}{\partial x} + z\frac{\partial \psi_x}{\partial x} \\
\varepsilon_{\theta\theta} &= \frac{1}{R}\left(\frac{\partial v}{\partial \theta} + w + z\frac{\partial \psi_\theta}{\partial \theta}\right) \\
\varepsilon_{x\theta} &= \frac{1}{2}\left(\frac{1}{R}\frac{\partial u}{\partial \theta} + \frac{\partial v}{\partial x} + \frac{z}{R}\frac{\partial \psi_x}{\partial \theta} + z\frac{\partial \psi_\theta}{\partial x}\right) \\
\varepsilon_{zx} &= \frac{1}{2}\left(\psi_x + \frac{\partial w}{\partial x}\right) \\
\varepsilon_{z\theta} &= \frac{1}{2}\left(\psi_\theta + \frac{1}{R}\frac{\partial w}{\partial \theta} - \frac{v}{R}\right)
\end{aligned} \tag{11}$$

Given the assumption of plane stress in the shear deformation shell theory, the stress tensor can be defined as:

$$\begin{aligned}
\begin{Bmatrix} \sigma_{xx} \\ \sigma_{\theta\theta} \\ \sigma_{x\theta} \end{Bmatrix} &= \begin{bmatrix} C_{11} & C_{12} & 0 \\ C_{12} & C_{22} & 0 \\ 0 & 0 & C_{66} \end{bmatrix} \begin{Bmatrix} \varepsilon_{xx} \\ \varepsilon_{\theta\theta} \\ 2\varepsilon_{x\theta} \end{Bmatrix} \\
\begin{Bmatrix} \sigma_{xz} \\ \sigma_{\theta z} \end{Bmatrix} &= \begin{bmatrix} C_{44} & 0 \\ 0 & C_{55} \end{bmatrix} \begin{Bmatrix} 2\varepsilon_{xz} \\ 2\varepsilon_{\theta z} \end{Bmatrix}
\end{aligned} \tag{12}$$

In Eq. (12), elastic constants are defined as:

$$C_{11} = C_{22} = \frac{E(\hat{z})}{1-\nu(\hat{z})^2}, \quad C_{12} = \frac{E(\hat{z})\nu(\hat{z})}{1-\nu(\hat{z})^2}, \quad C_{33} = C_{44} = C_{55} = \mu(\hat{z}) \tag{13}$$

In the above equation, $E(\hat{z})$ and $\nu(\hat{z})$ respectively represent Young's modulus and Poisson's ratio for FG cylindrical shell. Also, by substituting Eqs. (11) and (12) into Eq. (8), the variation of strain energy is obtained:

$$\int_{dV} \delta U_s dV = \int_{dV} \left[t_{ij}\right]\delta\varepsilon_{ij} dV + \int_{dA} \left[\sigma^{(1)}{}_{ij}\right]\delta\varepsilon_{ij}\Big|_0^L dA \tag{14}$$

where

$$t_{ij} = \sigma_{ij} - \nabla\sigma^{(1)}{}_{ij} \tag{15}$$

According to nonlocal strain gradient theory, its constitutive equation is as follows:

$$\left[1-\mu\nabla^2\right]t_{ij}=C_{ijkl}\varepsilon_{kl}-\eta C_{ijkl}\nabla^2\varepsilon_{kl} \tag{16}$$

In the above equation, μ is equal to square of nonlocal scale parameter (e_0a). Furthermore, η is equal to square of material length scale parameter (l).
Consequently, by substituting Eqs. (7,14) into Eq. (5) and calculating multiple integral by parts, the governing equations of FG nanotube are extracted as:

$$\begin{aligned}\delta U:&\left(1-\eta\nabla^2\right)\left[A_1\frac{\partial^2}{\partial x^2}u(x,\theta,t)+A_2\frac{\partial^2}{\partial x^2}\psi_x(x,\theta,t)+A_3\frac{\partial^2}{\partial x\partial\theta}v(x,\theta,t)\right.\\&\left.+A_4\frac{\partial}{\partial x}w(x,\theta,t)+A_5\frac{\partial^2}{\partial x\partial\theta}\psi_\theta(x,\theta,t)+A_6\frac{\partial^2}{\partial\theta^2}u(x,\theta,t)+A_7\frac{\partial^2}{\partial\theta^2}\psi_x(x,\theta,t)\right]\\&-\left(1-\mu\nabla^2\right)\left[A_8\frac{\partial^2}{\partial t^2}u(x,\theta,t)+A_9\frac{\partial^2}{\partial t^2}\psi_x(x,\theta,t)\right]=0\end{aligned} \tag{17}$$

$$\begin{aligned}\delta V:&\left(1-\eta\nabla^2\right)\left[B_1\frac{\partial^2}{\partial x\partial\theta}u(x,\theta,t)+B_2\frac{\partial^2}{\partial x^2}v(x,\theta,t)+B_3\frac{\partial^2}{\partial x\partial\theta}\psi_x(x,\theta,t)\right.\\&+B_4\frac{\partial^2}{\partial x^2}\psi_\theta(x,\theta,t)+B_5\frac{\partial^2}{\partial\theta^2}v(x,\theta,t)+B_6\frac{\partial}{\partial\theta}w(x,\theta,t)\\&\left.+B_7\frac{\partial^2}{\partial\theta^2}\psi_\theta(x,\theta,t)+B_8\psi_\theta(x,\theta,t)+B_9v(x,\theta,t)\right]\\&-\left(1-\mu\nabla^2\right)\left[B_{10}\frac{\partial^2}{\partial t^2}v(x,\theta,t)+B_{11}\frac{\partial^2}{\partial t^2}\psi_\theta(x,\theta,t)\right]=0\end{aligned} \tag{18}$$

$$\begin{aligned}\delta W:&\left(1-\eta\nabla^2\right)\left[C_1\frac{\partial}{\partial x}\psi_x(x,\theta,t)+C_2\frac{\partial^2}{\partial x^2}w(x,\theta,t)+C_3\frac{\partial}{\partial\theta}\psi_\theta(x,\theta,t)\right.\\&\left.+C_4\frac{\partial^2}{\partial\theta^2}w(x,\theta,t)+C_5\frac{\partial}{\partial\theta}v(x,\theta,t)+C_6w(x,\theta,t)+C_7\frac{\partial}{\partial x}u(x,\theta,t)\right]\\&-\left(1-\mu\nabla^2\right)\left[C_8\frac{\partial^2}{\partial t^2}w(x,\theta,t)\right]=0\end{aligned} \tag{19}$$

$$\begin{aligned}\delta\psi_x:&\left(1-\eta\nabla^2\right)\left[D_1\frac{\partial^2}{\partial x^2}u(x,\theta,t)+D_2\frac{\partial^2}{\partial x^2}\psi_x(x,\theta,t)+D_3\frac{\partial^2}{\partial x\partial\theta}v(x,\theta,t)\right.\\&+D_4\frac{\partial}{\partial x}w(x,\theta,t)+D_5\frac{\partial^2}{\partial x\partial\theta}\psi_\theta(x,\theta,t)+D_6\frac{\partial^2}{\partial\theta^2}u(x,\theta,t)+D_7\frac{\partial^2}{\partial\theta^2}\psi_x(x,\theta,t)\\&\left.+D_8\psi_x(x,\theta,t)\right]-\left(1-\mu\nabla^2\right)\left[D_9\frac{\partial^2}{\partial t^2}\psi_x(x,\theta,t)+D_{10}\frac{\partial^2}{\partial t^2}u(x,\theta,t)\right]=0\end{aligned} \tag{20}$$

$$\delta\psi_\theta : \left[E_1 \frac{\partial^2}{\partial x \partial \theta} u(x,\theta,t) + E_2 \frac{\partial^2}{\partial x^2} v(x,\theta,t) + E_3 \frac{\partial^2}{\partial x \partial \theta} \psi_x(x,\theta,t) + E_4 \frac{\partial^2}{\partial x^2} \psi_\theta(x,\theta,t) \right.$$
$$+ E_5 \frac{\partial^2}{\partial \theta^2} v(x,\theta,t) + E_6 \frac{\partial}{\partial \theta} w(x,\theta,t) + E_7 \frac{\partial^2}{\partial \theta^2} \psi_\theta(x,\theta,t) + E_8 \psi_\theta(x,\theta,t) \tag{21}$$
$$\left. + E_9 v(x,\theta,t) \right] - \left(1 - \mu\nabla^2\right) \left[E_{10} \frac{\partial^2}{\partial t^2} \psi_\theta(x,\theta,t) + E_{11} \frac{\partial^2}{\partial t^2} v(x,\theta,t) \right] = 0$$

where

$$A_1 = Y_1, A_2 = Y_2, A_3 = Y_4/R + Y_7/R, A_4 = Y_4/R, A_5 = Y_5/R + Y_8/R,$$
$$A_6 = Y_7/R^2, A_7 = Y_8/R^2, A_8 = Y_{10}, A_9 = Y_{11}$$
$$B_1 = Y_7/R + Y_4/R, B_2 = Y_7, B_3 = Y_8/R + Y_5/R, B_4 = Y_8, B_5 = Y_1/R^2,$$
$$B_6 = Y_1/R^2 + k\,Y_7/R^2, B_7 = Y_2/R^2, B_8 = kY_7/R, B_9 = -kY_7/R^2, B_{10} = Y_{10}, B_{11} = Y_{11}$$
$$C_1 = kY7 - Y5/R, C_2 = kY_7, C_3 = kY_7/R - Y_2/R^2, C_4 = kY_7/R^2, C_5 = -kY_7/R^2 - Y_1/R^2,$$
$$C_6 = -Y_1/R^2, C_7 = -Y_4/R, C_8 = Y_{10}$$
$$D_1 = Y_2, D_2 = Y_3, D_3 = Y_5/R + Y_8/R, D_4 = Y_5/R - kY_7, D_5 = Y_6/R + Y_9/R, D_6 = Y_8/R^2,$$
$$D_7 = Y_9/R^2, D_8 = -kY_7, D_9 = Y_{12}, D_{10} = Y_{11}$$
$$E_1 = Y_8/R + Y_5/R, E_2 = Y_8, E_3 = Y_9/R + Y_6/R, E_4 = Y_9, E_5 = Y_2/R^2, E_6 = Y_2/R^2 - k\,Y_7/R,$$
$$E_7 = Y_3/R^2, E_8 = -kY_7, E_9 = k\,Y_7/R, E_{10} = Y_{12}, E_{11} = Y_{11}$$

and

$$Y_i = \int_{-\hat{z}_c}^{h-\hat{z}_c} \frac{E(\hat{z})}{1-\nu^2(\hat{z})} \left(z^i\right) dz,\ (i = 1,2,3), Y_i = \int_{-\hat{z}_c}^{h-\hat{z}_c} \frac{E(\hat{z})\nu(\hat{z})}{1-\nu^2(\hat{z})} \left(z^i\right) dz,\ (i = 4,5,6),$$
$$Y_i = \int_{-\hat{z}_c}^{h-\hat{z}_c} \mu(\hat{z})\left(z^i\right) dz,\ (i = 7,8,9), Y_i = \int_{-\hat{z}_c}^{h-\hat{z}_c} \rho(\hat{z})\left(z^i\right) dz,\ (i = 10,11,12)$$

The boundary conditions are given in Appendix A.
In order to solve the governing equations, the following approximate solutions, satisfied differential equations and boundary conditions, are utilized:

$$\begin{aligned} u(x,\theta,\mathrm{t}) &= \sum_n \sum_m U_{mn}(t) \cos\left(\frac{m\pi x}{L}\right) \cos(n\theta) \\ v(x,\theta,\mathrm{t}) &= \sum_n \sum_m V_{mn}(t) \sin\left(\frac{m\pi x}{L}\right) \sin(n\theta) \\ w(x,\theta,\mathrm{t}) &= \sum_n \sum_m W_{mn}(t) \sin\left(\frac{m\pi x}{L}\right) \cos(n\theta) \\ \psi_x(x,\theta,\mathrm{t}) &= \sum_n \sum_m \psi_{xmn}(t) \cos\left(\frac{m\pi x}{L}\right) \cos(n\theta) \end{aligned} \tag{22}$$

$$\psi_\theta\left(x,\theta,\mathrm{t}\right)=\sum_n\sum_m\psi_{\theta mn}\left(t\right)\sin\left(\frac{m\pi x}{L}\right)\sin\left(n\theta\right)$$

where *m, n* stand for axial and circumferential wave numbers.
Therefore, by substituting Eq. (22) into the equations of motion, the equations are written in the matrix form as follows:

$$\left[k\right]\left\{d\right\}+\left[M\right]\left\{\ddot{d}\right\}=0 \tag{23}$$

where

$$\left\{d\right\}=\left\{d_0\right\}e^{i\omega t} \tag{24}$$

Now, by substituting Eq. (24) into (23), we have

$$\left(\left[k\right]-\omega^2\left[M\right]\right)\left\{d_0\right\}=0 \tag{25}$$

where ω stands for natural frequency, $\left\{d_0\right\}=\left\{U_{mn}\,V_{mn}\,W_{mn}\,\psi_{xmn}\,\psi_{\theta mn}\right\}^T$ is displacement amplitude vector. To obtain the non-trivial solution to Eq. (25), one must consider the determinant of coefficients equivalent to zero from which the shell frequency equation is derived and solved.

3. Results

For the sake of predicting the vibration behavior of nanotubes more accurately using nonlocal strain gradient theory, since the efficiency of the nonlocal strain gradient shell model is strongly dependent on the recognition of the proper values of small length scale parameters, $\mu = (e_0a)^2$ and $\eta = l^2$ are also calibrated using MD results of a (5,5) armchair CNT, due to lacking of the values of small length scale parameters of FG nanotubes. Also the values of μ and η are considered to be $(3.3)^2$ to $(3.5)^2$ nm^2 and $(0.1)^2$ to $(0.4)^2$ nm^2, respectively, for different length ratios. The following material parameters are considered for FG nanotube [17]:

Table 1. Material properties of FG cylindrical shell.

	E (GPa)	υ	ρ (kg/m^3)
Aluminum	70	0.3	2702
Ceramics	427	0.17	3100

In the following, the vibration response of nanotubes under different material and geometrical parameters is indicated to illustrate the applications of nonlocal strain gradient theory.
In order to show the influences of small length scale parameters on frequency of nanotubes, Figs. 2 and 3 are presented. It is seen that increasing nonlocal parameter (μ) at a certain scale factor (η) decreases frequency which reveals the softening effect of nonlocal parameter (see Fig. 2); while, increasing scale factor in the case of certain nonlocal parameter increases frequency and it means that the effective stiffness of nanotube becomes larger with increasing scale factor (see Fig. 3). These phenomena illustrate that by using nonlocal strain gradient theory, the nanotube exerts the softening and stiffening behavior by increasing the nonlocal

parameter and scale factor, respectively. Besides, due to the higher elastic modulus of ceramics compared to aluminum, with the increase in the gradient index in the shell, where β = 0 is for the aluminum shell and β = ∞ for the ceramic shell, the frequency increases as well.

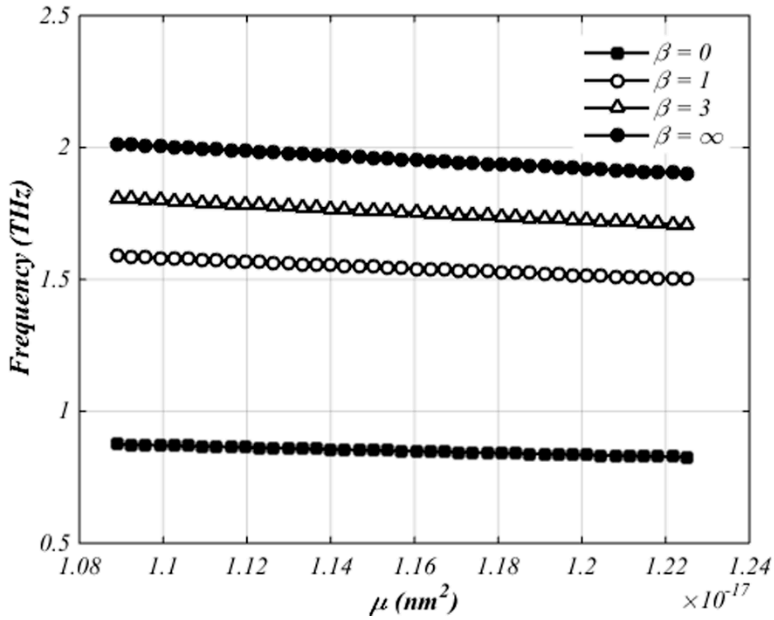

Fig. 2. Effect of nonlocal parameter on frequency for different power law index.

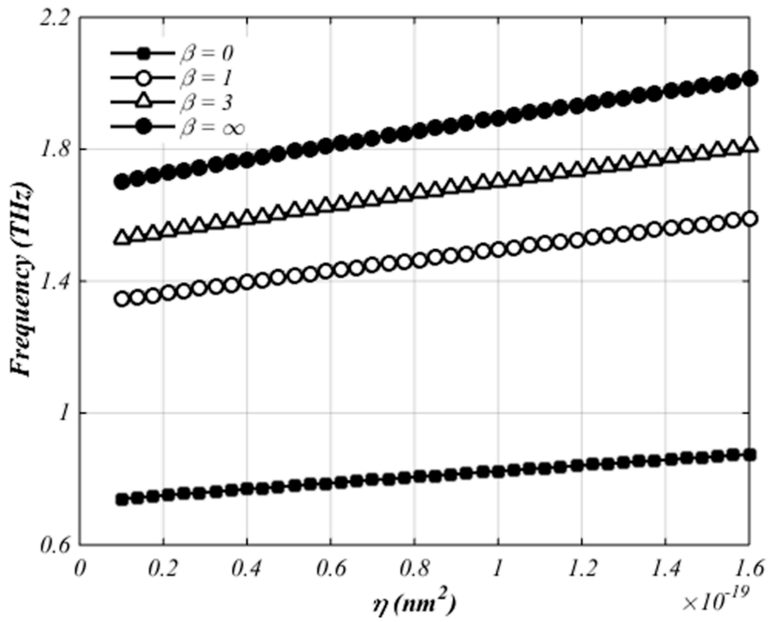

Fig. 3. Effect of scale factor on frequency for different power law index.

Fig. 4 is indicated the influences of thickness ratio on frequency of nanotubes. Regarding Fig. 4, it is witnessed that the increase in thickness ratio contributes to the higher frequency for various values of power law index because of ascending the stiffness of nanotube; besides, the more increase in the frequency is occurred when the power law index goes up. Also, it is found that the higher frequency takes place at high power law index and thickness ratio. This is regarded as evidence that the power law index makes nanotube stiffer.

In order to see the effects of thickness ratio more clearly, Figs. 5 and 6 illustrate the effects of thickness ratio on frequency of nanotubes, particularly on different scale factors and nonlocal parameters. It is shown that, the high frequency appears at high scale factor and low nonlocal parameter. It is clear that the trends of the frequency variation versus thickness ratio for various scale factors and nonlocal parameters are similar to Fig. 4 and similar conclusion can be drawn. It should be noted that, the influence of the transverse shear deformation is significant when thick and short nanotubes are investigated and since the first order shear deformation theory is used in this study, there is no limitation on choosing the values of thickness parameter.

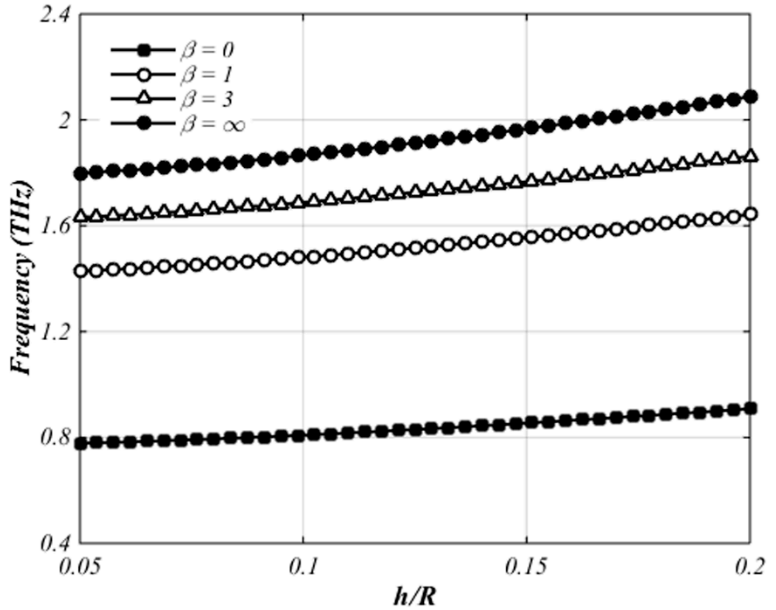

Fig. 4. Effect of thickness ratio on the frequency for different power law index ($\mu = (3.3e\text{-}9)^2$, $\eta = (0.4e\text{-}9)^2$).

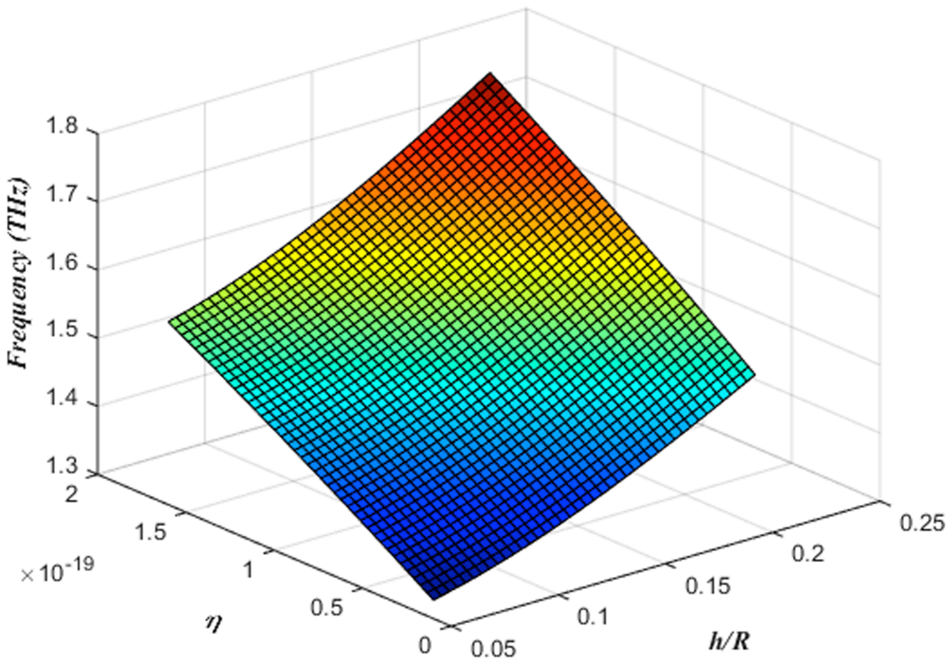

Fig. 5. Effect of thickness ratio on the frequency for different scale factors ($\beta = 2$, $\mu = (3.3e\text{-}9)^2$).

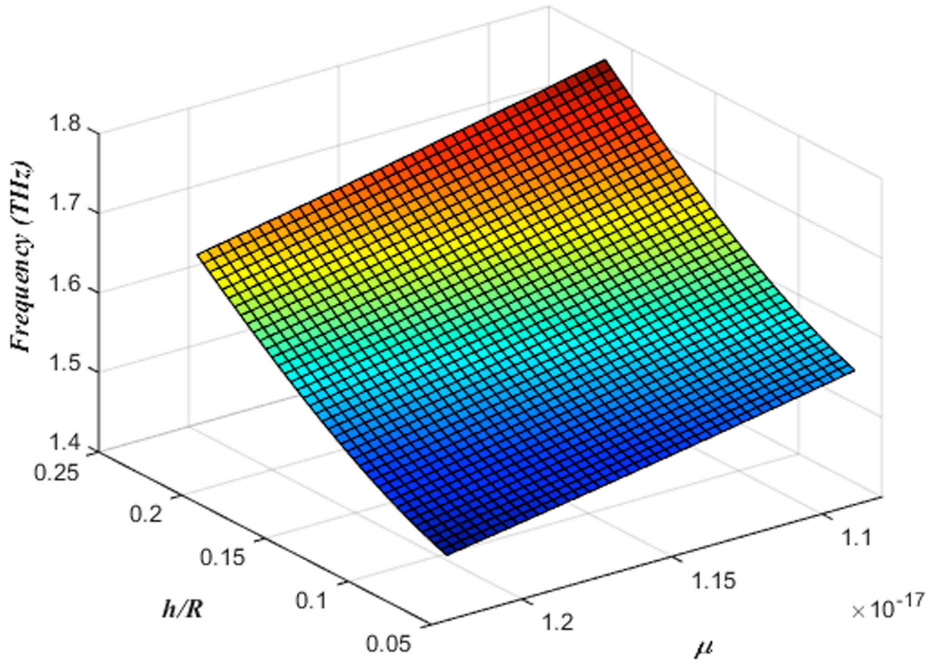

Fig. 6. Effect of thickness ratio on the frequency for different nonlocal parameters ($\beta = 2$, $\eta = (0.4e\text{-}9)^2$).

Variation of frequency versus length ratio for different power law index is illustrated in Fig. 7. As is evident from Fig. 7, the frequency is shown to be decreasing with increasing length ratio and this effect is more significant by increasing power law index which depicting stiffer nanotubes. In other words, the effects of length ratio on the frequency with greater power law index are relatively more than those of ones with small power law index.

In order to have a deeper insight into the influence of length ratio, Figs. 8 and 9 are also illustrated for various scale factors and nonlocal parameters. According to these figures, the decreasing procedure of frequency with respect to the increase in length ratio for various scale factors and nonlocal parameters is the same as Fig. 7. Moreover, from these figures it can be seen that the influence of scale factor and nonlocal parameter is more evident when length ratio is small. Also, according to Figs. 8 and 9, at high length ratio the results of the present model approach to those of classical ones which shows the capability of classical model to predict the vibration response of large-scale structures.

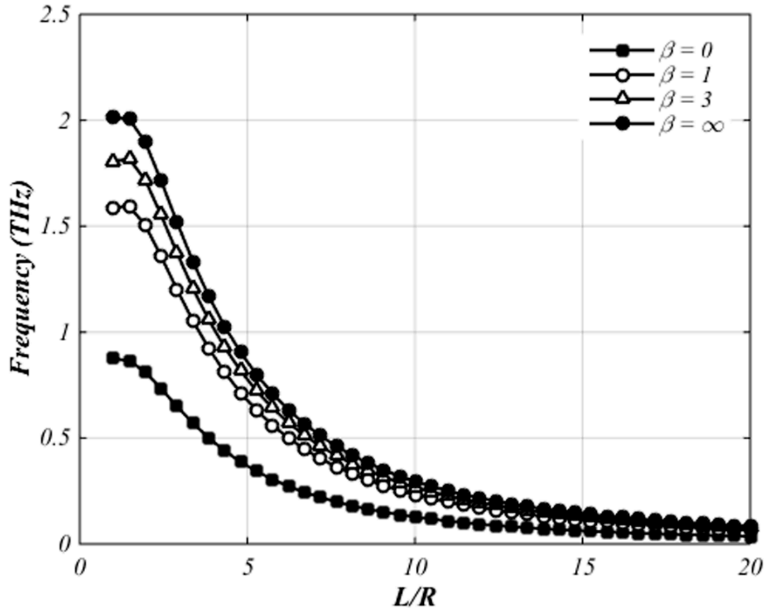

Fig. 7. Effect of length ratio on frequency for different power law index (μ = (3.3e-9)^2, η = (0.4e-9)^2).

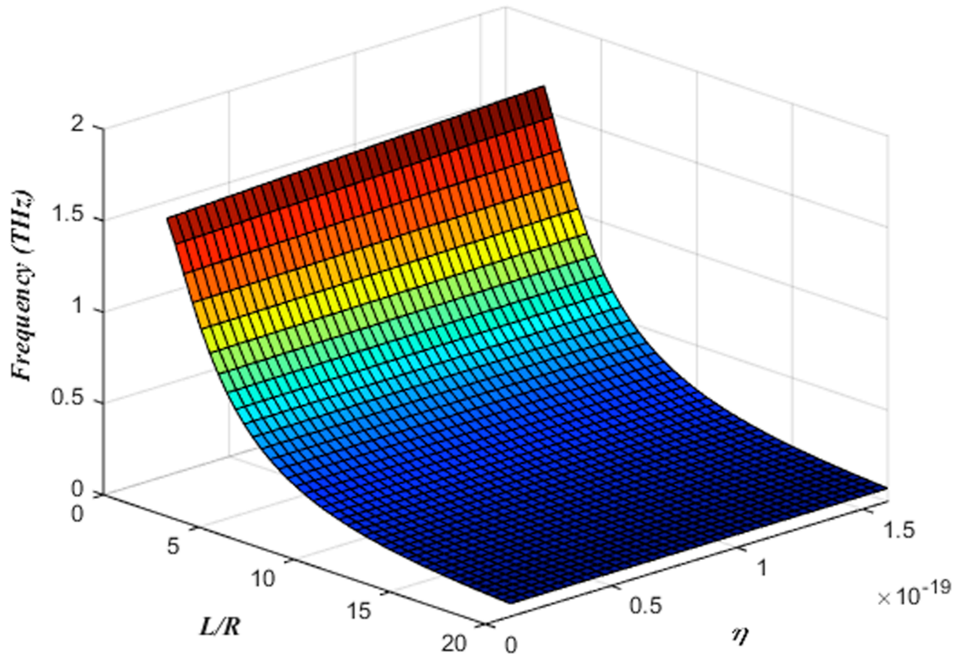

Fig. 8. Effect of length ratio on frequency for different scale factors (β = 2, μ = (3.3e-9)^2).

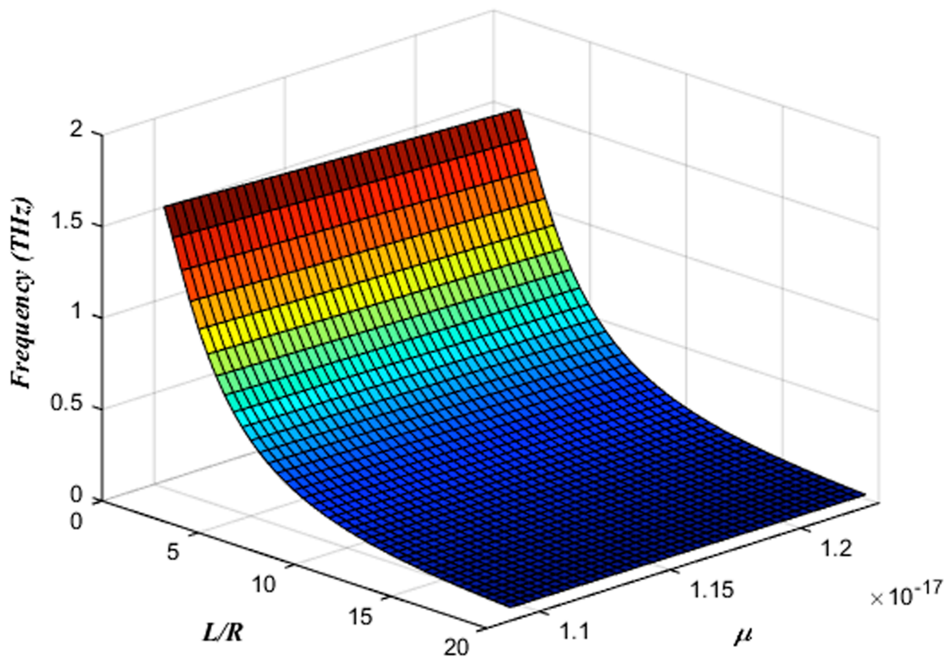

Fig. 9. Effect of length ratio on frequency for different nonlocal parameters ($\beta = 2$, $\eta = (0.4e\text{-}9)^2$).

4. Conclusion

In this study, the free vibration of FG nanotube is studied based on the nonlocal strain gradient theory and first order shear deformable theory. The material properties are considered to be variable through thickness direction according to power law distribution. The governing equations and boundary conditions are derived based on the Hamilton's principle and the free vibration of simply supported FG nanotube is studied as well. The effects of various parameters such as material length scale parameters, thickness, length and power law index are investigated on the frequency. It was revealed that increase in power law index intensifies the influence of nonlocal parameter and scale factors on the FG nanotube frequency. Moreover, the higher frequency appears at higher thickness ratios and lower length ratios. Furthermore, the effects of length ratio and thickness ratio are relatively intense for greater scale factors and lower nonlocal parameters.

References

[1] Tadi Beni, Y., Mehralian, F., Zeighampour, H., The modified couple stress functionally graded cylindrical thin shell formulation. *Mechanics of Advanced Materials and Structures*, 23(7), 791-801, 2016.

[2] Tadi Beni, Y., Mehralian, F., Razavi, H., Free vibration analysis of size-dependent shear deformable functionally graded cylindrical shell on the basis of modified couple stress theory. *Composite Structures*, 120, 65-78, 2015.

[3] Li, X., Li, L., Hu, Y., Ding, Z., Deng, W., Bending, buckling and vibration of axially functionally graded beams based on nonlocal strain gradient theory. *Composite Structures*, 165, 250-265, 2017.

[4] Ebrahimi, F., Barati, M.R., Dabbagh, A., A nonlocal strain gradient theory for wave propagation analysis in temperature-dependent inhomogeneous nanoplates. *International Journal of Engineering Science*, 107, 169-182, 2016.

[5] Civalek, Ö., Buckling analysis of composite panels and shells with different material properties by discrete singular convolution (DSC) method. *Composite Structures*, 161, 93-110, 2017.

[6] Akgöz, B., and Civalek, Ö., Longitudinal vibration analysis of strain gradient bars made of functionally graded materials (FGM). *Composites Part B: Engineering*, 55, 263-268, 2013.

[7] Dzenis, Y., Spinning continuous fibers for nanotechnology. Science, 304 (5679), 1917-1919, 2004.

[8] Love, J.C., Estroff, L.A., Kriebel, J.K., Nuzzo, R.G., Whitesides, G.M., Self-assembled monolayers of thiolates on metals as a form of nanotechnology. *Chemical reviews*, 105(4), 1103-1170, 2005.

[9] Mehralian, F., Tadi Beni, Y., Ansari, R. Size dependent buckling analysis of functionally graded piezoelectric cylindrical nanoshell. *Composite Structures*, 152, 45-61, 2016.

[10] Gholami, R., Darvizeh, A., Ansari, R., Hosseinzadeh, M., Size-dependent axial buckling analysis of functionally graded circular cylindrical microshells based on the modified strain gradient elasticity theory. *Meccanica* 49(7), 1679-1695, 2014.

[11] Mehralian, F., Tadi Beni, Y., Thermo-Mechanical vibration of size dependent shear deformable functionally graded conical nanoshell resting on elastic foundation. *International Journal of Engineering & Applied* Sciences, 8(2), 68-86, 2016.

[12] Mercan, K., Civalek, Ö., Buckling analysis of Silicon carbide nanotubes (SiCNTs) with surface effect and nonlocal elasticity using the method of HDQ. *Composites Part B: Engineering*, 114, 34-45, 2017.

[13] Akgöz, B., Civalek, Ö., Buckling analysis of cantilever carbon nanotubes using the strain gradient elasticity and modified couple stress theories. *Journal of Computational and Theoretical Nanoscience*, 8(9), 1821-1827, 2011.

[14] Lim, C.W., Zhang, G., Reddy, J.N., A higher-order nonlocal elasticity and strain gradient theory and its applications in wave propagation. *Journal of the Mechanics and Physics of Solids*, 78, 298-313, 2015.

[15] Ebrahimi, F., Barati, M.R., A nonlocal strain gradient refined beam model for buckling analysis of size-dependent shear-deformable curved FG nanobeams. *Composite Structures*, 159, 174-182, 2017.

[16] Tang, Y., Liu, Y., Zhao, D., Wave dispersion in viscoelastic single walled carbon nanotubes based on the nonlocal strain gradient Timoshenko beam model. *Physica E: Low-dimensional Systems and Nanostructures*, 87, 301-307, 2017.

[17] Sahmani, S., Ansari, R., Gholami, R., Darvizeh, A., Dynamic stability analysis of functionally graded higher-order shear deformable microshells based on the modified couple stress elasticity theory. *Composite Part B*, 51, 44–53, 2013.

Appendix A

$$\delta U = 0 \qquad or \qquad N_{xx} - \frac{1}{R}\frac{\partial N^{(1)}_{x\theta}}{\partial \theta} = 0 \tag{A-1}$$

$$\frac{\partial \delta U}{\partial x} = 0 \qquad or \qquad N^{(1)}_{xx} = 0 \tag{A-2}$$

$$\delta V = 0 \qquad or \qquad N_{x\theta} - \frac{1}{R}\frac{\partial N^{(1)}_{\theta\theta}}{\partial \theta} - \frac{Q^{(1)}_{\theta z}}{R} = 0 \tag{A-3}$$

$$\frac{\partial \delta V}{\partial x} = 0 \qquad or \qquad N^{(1)}_{x\theta} = 0 \tag{A-4}$$

$$\delta W = 0 \qquad or \qquad Q_{xz} + \frac{N^{(1)}_{\theta\theta}}{R} - \frac{1}{R}\frac{\partial Q^{(1)}_{\theta z}}{\partial \theta} = 0 \tag{A-5}$$

$$\frac{\partial \delta W}{\partial x} = 0 \qquad or \qquad Q^{(1)}_{xz} = 0 \tag{A-6}$$

$$\delta \psi_x = 0 \qquad or \qquad M_{xx} - \frac{1}{R}\frac{\partial M^{(1)}_{x\theta}}{\partial \theta} + Q^{(1)}_{xz} = 0 \tag{A-7}$$

$$\frac{\partial \delta \psi_x}{\partial x} = 0 \qquad or \qquad M^{(1)}_{xx} = 0 \tag{A-8}$$

$$\delta \psi_\theta = 0 \qquad or \qquad M_{x\theta} - \frac{1}{R}\frac{\partial M^{(1)}_{\theta\theta}}{\partial \theta} + Q^{(1)}_{\theta z} = 0 \tag{A-9}$$

$$\frac{\partial \delta \psi_\theta}{\partial x} = 0 \qquad or \qquad M^{(1)}_{x\theta} = 0 \tag{A-10}$$

Due to the stress distribution along thickness of the shell, stress resultants are introduced as follows:

$$\begin{bmatrix} N_{xx}, N^{(1)}{}_{xx} \\ N_{x\theta}, N^{(1)}{}_{x\theta} \\ N_{\theta\theta}, N^{(1)}{}_{\theta\theta} \end{bmatrix} = \int_{-\hat{z}_c}^{h-\hat{z}_c} \begin{Bmatrix} t_{xx}, \sigma^{(1)}{}_{xx} \\ t_{x\theta}, \sigma^{(1)}{}_{x\theta} \\ t_{\theta\theta}, \sigma^{(1)}{}_{\theta\theta} \end{Bmatrix} dz \tag{A-11}$$

$$\begin{bmatrix} Q_{zx}, Q^{(1)}{}_{zx} \\ Q_{z\theta}, Q^{(1)}{}_{z\theta} \end{bmatrix} = \int_{-\hat{z}_c}^{h-\hat{z}_c} \begin{Bmatrix} t_{zx}, \sigma^{(1)}{}_{zx} \\ t_{z\theta}, \sigma^{(1)}{}_{z\theta} \end{Bmatrix} dz \tag{A-12}$$

$$\begin{bmatrix} M_{xx}, M^{(1)}{}_{xx} \\ M_{\theta\theta}, M^{(1)}{}_{\theta\theta} \end{bmatrix} = \int_{-\hat{z}_c}^{h-\hat{z}_c} \begin{Bmatrix} t_{xx}, \sigma^{(1)}{}_{xx} \\ t_{\theta\theta}, \sigma^{(1)}{}_{\theta\theta} \end{Bmatrix} zdz \tag{A-13}$$

International Journal of Engineering & Applied Sciences (IJEAS)
Vol.9, Issue 2 (Special Issue: Composite Structures) (2017) 103-111
http://dx.doi.org/10.24107/ijeas.314635
Int J Eng Appl Sci 9(2) (2017) 103-111

Bending Analysis of a Cantilever Nanobeam With End Forces by Laplace Transform

Mustafa Özgür Yayli [a,], Suheyla Yerel Kandemir [b]

[a,] Uludağ University Engineering Faculty Department of Civil Engineering, Bursa,Turkey
[a,] Bilecik SE University Engineering Faculty Department of Civil Engineering, Bilecik,Turkey
[*] E-mail address: ozguryayli@uludag.edu.tr

Received date: May 2017
Accepted date: June 2017

Abstract

In this study, the static behavior of nanobeams subjected to end concentrated loads is theoretically investigated in the Laplace domain. A closed form of solution for the title problem is presented using Euler-Bernoulli beam theory. Nonlocal elasticity theory proposed by Eringen is used to represent small scale effect. A system of differential equations containing a small scale parameter is derived for nanobeams. Laplace transformation is applied to ***this system*** *of differential equations containing a small scale parameter. The exact static response of the nanobeam with end concentrated loads is obtained by applying inverse Laplace transform. The calculate results are plotted in a series of figures for various combinations of concentrated loads.*

Keywords: Nonlocal elasticity theory, nanobeam, Laplace transform, static response.

1. Introduction

Single walled carbon nanotubes (nanobeams) are non-classical nanomaterials of current interest in several applicative sectors, such as electronics, medicine and engineering. They have superior mechanical and electrical properties and their potential applications in optics, electronics and other fields of nanotechnology. Classical continuum theory is size-free theory and this theory lacks the accountability of the size effects arising from the small-size. There have been different non classical continuum theories used to overcome small size effects. Integral type, differential equation type or gradient nonlocal elasticity type models abandon the classical elasticity assumption of local model, and stated that stress depends not only on the strain at that point.

Eringen [1] proposed the new higher order continuum theory known as "nonlocal elasticity theory" in 1970s. In this theory small size effect can be considered in the constitutive equations simply as a material scale parameter. Nonlocal elasticity theory based nano sized structures are new materials (nanomaterials) which are designed to achieve a higher performance in physical and mechanical properties. The nonlocal continuum theory has been widely applied to many mechanical problems of a wide range of interest, including the bending, buckling, and vibration of beam-like structures [2-4] and plate-like structures [5-7] and elements in nano and micro sized structures. Many research papers correlated to nonlocal continuum theories have been addressed the small scale effects in nanostructures and apply these higher order elasticity theories to determine the mechanical behavior of nanostructures, see Refs. [8-25].

In this work, a Laplace transformation is introduced for the bending analysis of the cantilever nanobeams with end concentrated loads (initial value problems). A systems of differential equations is derived with initial and boundary conditions. Laplace transformation is applied to this systems of differential equations containing nonlocal elasticity parameter with known initial conditions. The closed form of solutions of the nanobeam with end concentrated loads is derived by applying inverse Laplace transform.

2. Formulation of the problem

The constitutive relation, the equations of equilibrium and geometrical compatibility condition of a nanobeam in the two dimensional plane are [26].

$$\frac{dw}{dx}=\varphi, \tag{1}$$

$$\frac{d\varphi}{dx}=\frac{-M}{EI}, \tag{2}$$

$$\frac{dM}{dx}=P_1\varphi+T, \tag{3}$$

$$\frac{dT}{dz}=0, \tag{4}$$

where M and T are the bending moment and the shear force, w and φ are the lateral displacement and the slope of the beam. On the other hand, Eq. (2) takes a different form in nonlocal elasticity [27].

$$M-(e_0a)^2\frac{d^2M}{dx^2}=-EI\frac{d^2w}{dx^2}, \tag{5}$$

where a is the internal characteristic length, is a constant ($e_0=0.39$, $a=4\times10^{-8}$ cm). Using Eq. (2), above relation takes the following form

$$\frac{M}{EI}=(1-\frac{(e_0a)^2P_1}{EI})\frac{d\varphi}{dx}, \tag{6}$$

then according to nonlocal elasticity theory, the system of differential equations **is** given by [26].

$$\frac{d}{dx}\begin{bmatrix} w \\ \varphi \\ M \\ T \end{bmatrix}=\begin{bmatrix} 0 & 1 & 0 & 0 \\ 0 & 0 & \dfrac{-1}{EI(1-(e_0a)^2\dfrac{P_1}{EI})} & 0 \\ 0 & P_1 & 0 & 1 \\ 0 & 0 & 0 & 0 \end{bmatrix}\begin{bmatrix} w \\ \varphi \\ M \\ T \end{bmatrix}, \tag{7}$$

where EI is the flexural rigidity of the nanobeam, E is Young's modulus, I is the moment of inertia of the cross-sectional area A, P_1 the axial concentrated force, P_2 the lateral concentrated force, a the internal characteristic length and e_0 is a constant. The initial conditions can be calculated as follows;

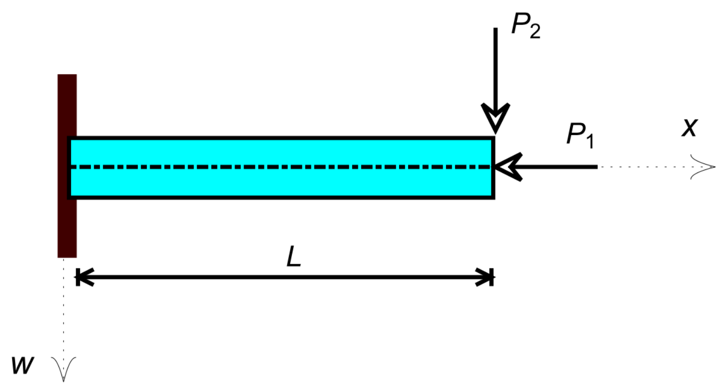

Fig. 1. A cantilever nanobeam with end concentrated forces

$$w(0)=0, \tag{8}$$

$$\varphi(0)=0, \tag{9}$$

$$M(0)=-P_2 L, \tag{10}$$

$$T(0)=P_2. \tag{11}$$

The following systems of differential equations can be derived from the Eq. (7):

$$\frac{dw}{dx}=\varphi, \tag{12}$$

$$\frac{d\varphi}{dx}=\frac{-1}{EI(1-(e_0 a)^2\frac{P_1}{EI})}M, \tag{13}$$

$$\frac{dM}{dx}=P_1\varphi+T, \tag{14}$$

$$\frac{dT}{dz}=0. \tag{15}$$

3. Closed form of solutions

By applying Laplace transform to these equations:

$$sw(S)-w(0)=\varphi(S), \tag{16}$$

$$s\varphi(S)-\varphi(0)=\frac{-1}{EI(1-(e_0a)^2\frac{P_1}{EI})}M(S), \tag{17}$$

$$sM(S)+M(0)=P_1\varphi(S)+T(S), \tag{18}$$

$$sT(S)-T(0)=0, \tag{19}$$

then using the initial conditions given in Eqs. (8-11), following equations are derived in Laplace domain:

$$w(S)=-\frac{-P_2+LP_2s}{s^2(-P_1-EIs^2+P_1s^2(e_0a)^2)}, \tag{20}$$

$$\varphi(S)=-\frac{-P_2-LP_2s}{s^2(P_1+EIs^2-P_1s^2(e_0a)^2)}, \tag{21}$$

$$M(S)=-\frac{EIP_2-EILP_2s-P_1P_2(e_0a)^2+LP_1P_2s(e_0a)^2}{-P_1-EIs^2+P_1s^2(e_0a)^2)}, \tag{22}$$

$$T(S)=\frac{P_2}{s}. \tag{23}$$

Inverse Laplace transforms of above equations give the closed form of solutions:

$$w[x]=\frac{P_2(L-x)}{P_1}-\frac{LP_2\cosh\left[\frac{\sqrt{P_1}x}{\sqrt{-EI+P_1(e_oa)^2}}\right]}{P_1}+\frac{P_2\sqrt{-EI+P_1(e_oa)^2}\sinh\left[\frac{\sqrt{P_1}x}{\sqrt{-EI+P_1(e_oa)^2}}\right]}{P_1^{\frac{3}{2}}}, \tag{24}$$

$$\varphi[x]=\frac{P_2(-1+\cosh\left[\frac{\sqrt{P_1}x}{\sqrt{-EI+P_1(e_oa)^2}}\right]-\frac{L\sqrt{P_1}\sinh\left[\frac{\sqrt{P_1}x}{\sqrt{-EI+P_1(e_oa)^2}}\right]}{\sqrt{-EI+P_1(e_oa)^2}})}{P_1}, \tag{25}$$

$$M[x]=LP_2\cosh\left[\frac{\sqrt{P_1}x}{\sqrt{-EI+P_1(e_oa)^2}}\right]+\frac{P_2\sqrt{-EI+P_1(e_oa)^2}\sinh\left[\frac{\sqrt{P_1}x}{\sqrt{-EI+P_1(e_oa)^2}}\right]}{\sqrt{P_1}}, \tag{26}$$

$$T[x]=P_2. \tag{27}$$

4. Numerical results

To evaluate the significance of end loads on the static analysis of nonlocal beams, this section considers a nano-sized beam with the end concentrated forces. Here we assume E*I = 1 nN.m^2, e_0a=1 nm. In order to investigate the significances of end axial concentrated forces on the mechanical behaviors of the nanobeam, its bending behaviors are compared. The significances of the end axial and lateral forces on the linear bending deflection of the cantilever nanobeam are investigated by using the nonlocal elastic Euler-Bernoulli beam model. Figs. 2 and 3 reveal the effect of the end concentrated forces on the deflection with end lateral force and the deflection with end axial force of a cantilever nanobeam, respectively.

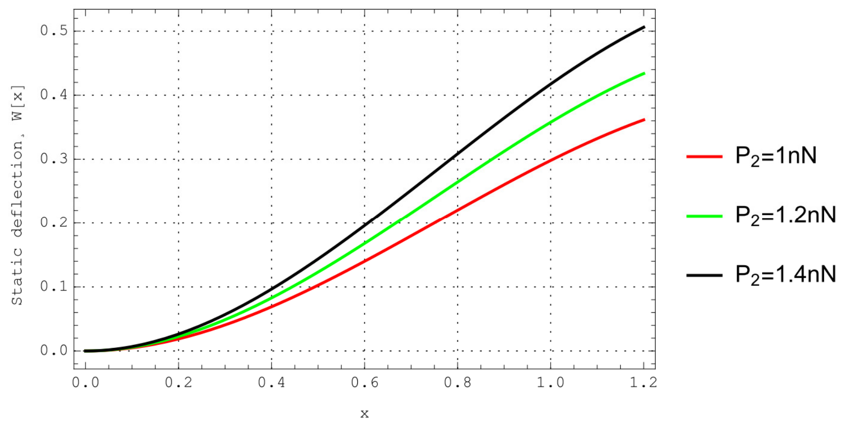

Fig. 2. Static deflection for different concentrated forces (P_1 =1.2 nN).

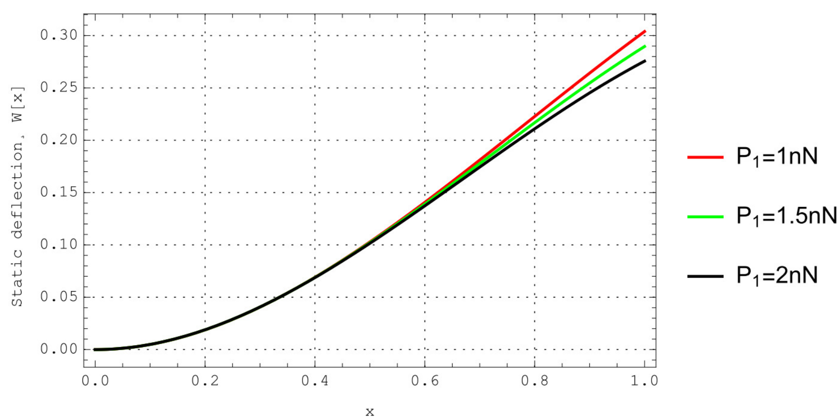

Fig. 3. Static deflection for different axial forces (P_2 =1.0 nN).

The effects of end forces on the slope of cantilever nanobeams are presented in Figs. 4 and 5. The figures show increase and decrease in the slope with increase in distance from fixed end which highlights the significance of end concentrated forces. So, it can be concluded that the lateral deflection is highly increased with higher values of the end lateral concentrated forces.

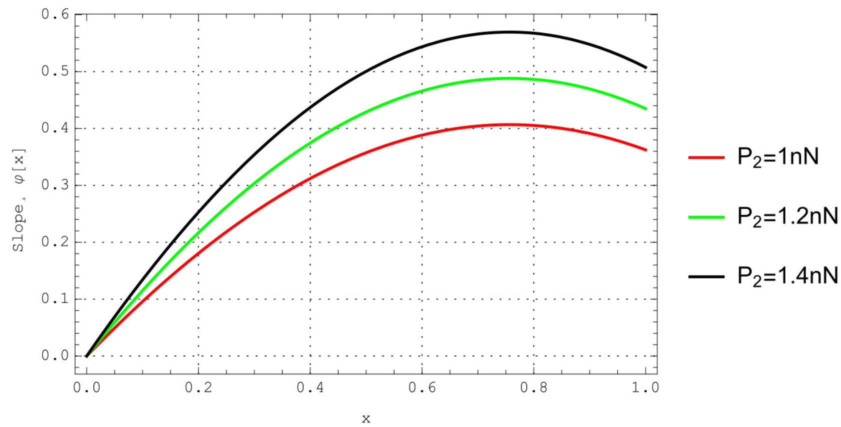

Fig. 4. Slope for different concentrated forces (P_1 =1.2 nN).

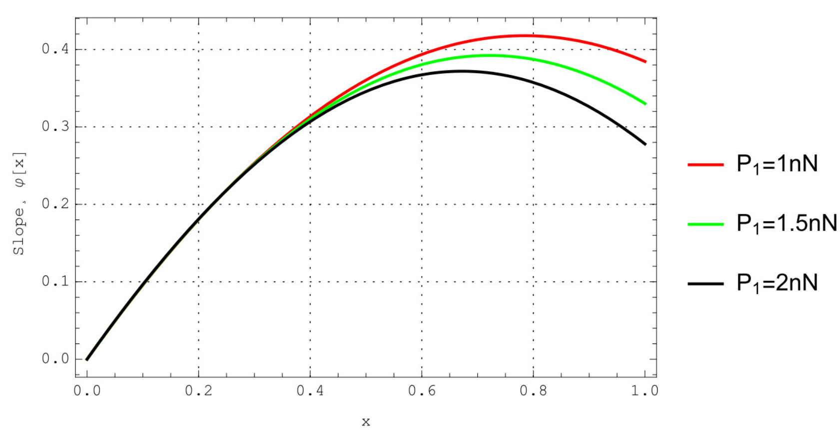

Fig. 5. Slope for different axial forces (P_2 =1.0 nN).

The effects of end forces on the bending of cantilever nanobeams are presented in Figs. 6 and 7. Again the influences of the axial force and the lateral force on the bending moment are quite obvious.

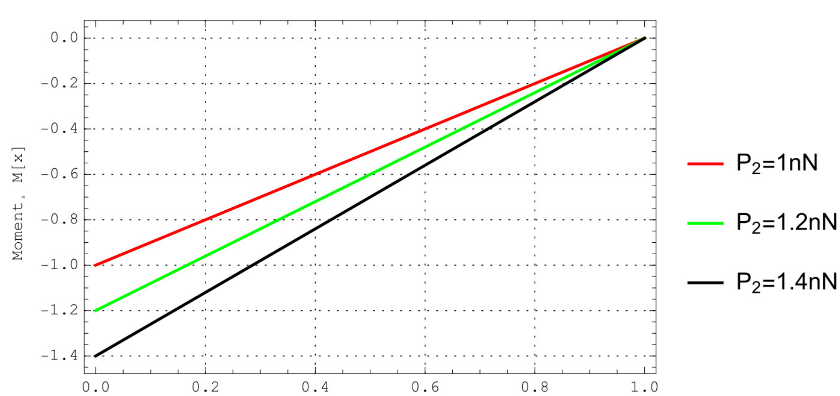

Fig. 6. Moment diagram for zero axial force (P_1 =0.0 nN).

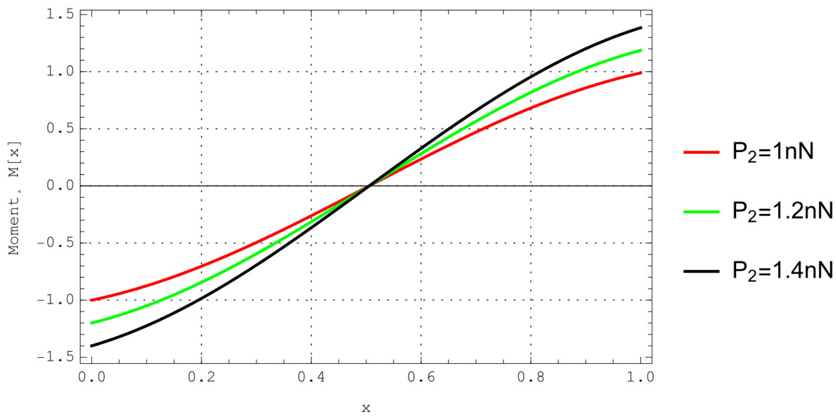

Fig. 7. Moment diagram for constant axial force (P_1 =5.0 nN).

5. Conclusions

In present work, It has been shown that the Laplace transform could be applied to solve nonlocal initial value problem that contains homogeneous linear differential equations. The single walled carbon nanotube is modeled as beam via Euler-Bernoulli theory. Nonlocal elasticity theory is used for small scale effect. One can easily transform the system of differential equations with constant coefficients into a system of (algebraic) equations with constant coefficients. Then these systems of algebraic equations can be solved and takes the inverse Laplace transform to get closed form solutions of the original equations.

References

[1] Eringen, A. C., Nonlocal polar elastic continua. *International Journal of Engineering Science*, 10, 1-16, 1972.

[2] Aydogdu, M., A general nonlocal beam theory: its application to nanobeam bending, buckling and vibration, *Physica E* 41, 1651-1655, 2009.

[3] Liu, T., Hai, M., Zhao, M., Delaminating buckling model based on nonlocal Timoshenko beam theory for microwedge indentation of a film/substrate system, *Eng. Fract. Mech.* 75, 4909-4919, 2008.

[4] Reddy, J.N., Nonlocal theories for bending, buckling and vibration of beams, *Int. J. Eng. Sci.*, 45, 288-307, 2007.

[5] Narendar, S., Buckling analysis of micro-/nano-scale plates based on two variable refined plate theory incorporating nonlocal scale effects, *Compos. Struct.*, 93, 3093-3103, 2011

[6] Pradhan, S.C., Phadikar, J.K., Nonlocal elasticity theory for vibration of nanoplates. *J. Sound Vib.*, 325, 206-223, (2009).

[7] Shen, L., Shen, H.S., Zhang, C.L., Nonlocal plate model for nonlinear vibration of single layer graphene sheets in thermal environments, *Comput. Mater. Sci.*, 48, 680-685, 2010.

[8] Mercan, K., Civalek, Ö., Buckling Analysis of Silicon Carbide Nanotubes (SiCNTs). Int J Eng Appl Sci, 8(2), 101-108, 2016.

[9] Mercan, K., Demir, Ç., Akgöz, B., Civalek, Ö., Coordinate Transformation for Sector and Annular Sector Shaped Graphene Sheets on Silicone Matrix. Int J Eng Appl Sci, 7(2), 56-73, 2015.

[10] Mercan, K., Civalek, Ö., DSC method for buckling analysis of boron nitride nanotube (BNNT) surrounded by an elastic matrix. Compos Struct, 143, 300-309, 2016.

[11] Gürses, M., Akgöz, B., Civalek, Ö., Mathematical modeling of vibration problem of nano-sized annular sector plates using the nonlocal continuum theory via eight-node discrete singular convolution transformation. Appl Math Comput, 219, 3226–3240, 2012.

[12] Yayli M. Ö., Buckling Analysis of a Rotationally Restrained Single Walled Carbon Nanotube Embedded In An Elastic Medium Using Nonlocal Elasticity, Int J Eng Appl Sci, 8(2), 40-50, 2016.

[13] Yayli M. Ö., An Analytical Solution for Free Vibrations of A Cantilever Nanobeam with A Spring Mass System, Int J Eng Appl Sci, 7(4), 10-18, 2016.

[14] Civalek, Ö., Akgöz, B., Free vibration analysis of microtubules as cytoskeleton components: nonlocal Euler–Bernoulli beam modeling, *Sci. Iranica Trans. B: Mech. Eng.*, 17, 367-375, 2010.

[15] Civalek, Ö., Demir, Ç., Bending analysis of microtubules using nonlocal Euler–Bernoulli beam theory, *Appl. Math. Model.*, 35, 2053-2067, 2011.

[16] Wang, C.M., Kitipornchai, S., Lim, C.W., Eisenberger, M., Beam bending solutions based on nonlocal Timoshenko beam theory, *J. Eng. Mech.*, 134, 475-481, 2008.

[17] Lu, P., Lee, H.P., Lu, C., Zhang, P.Q., Dynamic properties of flexural beams using a nonlocal elasticity model, *J. Appl. Phys.*, 99, 73510-73518, 2006.

[18] Murmu, T., Pradhan, S.C., Small-scale effect on the vibration of nonuniform nanocantilever based on nonlocal elasticity theory, Physica E, 41, 1451-1456, 2009.

[19] Rahmani, O., Pedram, O., Analysis and modeling the size effect on vibration of functionally graded nanobeams based on nonlocal Timoshenko beam theory, *Int. J. Eng. Sci*, 77, 55-70, 2014.

[20] Eltaher, M.A., Emam, S.A., Mahmoud, F.F., Static and stability analysis of nonlocal functionally graded nanobeams. *Compos. Struct*, 96, 82-88, 2013.

[21] Thai, H.T., A nonlocal beam theory for bending, buckling, and vibration of nanobeams. *Int. J. Eng. Sci.*, 52, 56-64, 2012.

[22] Reddy J. N., Pang, S. D., Nonlocal continuum theories of beam for the analysis of carbon nanotubes,. *Journal of Applied Physics*, 103, 1-16, 2008.

[23] Setoodeh, A.R., Khosrownejad, M., Malekzadeh, P., Exact nonlocal solution for post buckling of single-walled carbon nanotubes. *Physica E*, 43, 1730-1737, 2011.

[24] Yayli, M.Ö., Buckling Analysis of a Rotationally Restrained Single Walled Carbon Nanotube, *Acta Physica Polonica A*, 127, 3, 678-683, 2015.

[25] Yayli, M.Ö., Stability analysis of gradient elastic microbeams with arbitrary boundary conditions, *Journal of Mechanical Science and Technology*, 29, 8, 3373-3380, 2015.

[26] Artan R., Tepe A., The initial values method for buckling of nonlocal bars with application in nanotechnology. *European Journal of Mechanics-A/Solids*, 27, (3), 469-477, 2008.

[27] Peddieson, J., Buchanan, G. R., McNitt, R. P., Application of nonlocal continuum models to nanotechnology. *Int. J. Eng. Sci*, 41, (3-5), 305-312, 2013.

International Journal of Engineering & Applied Sciences (IJEAS)
Vol.9, Issue 2 (Special Issue: Composite Structures) (2017) 112-126
http://dx.doi.org/10.24107/ijeas.318459
Int J Eng Appl Sci 9(2) (2017) 112-126

Exact Thermal Analysis of Functionally Graded Cylindrical and Spherical Vessels

Vebil Yıldırım

University of Çukurova, Department of Mechanical Engineering
E-mail address: vebil@cu.edu.tr

Received date: June 2017
Accepted Date: July 2017

Abstract

Thermal analyses of radially functionally graded (FG) thick-walled a spherical vessel and an infinite cylindrical vessel or a circular annulus are conducted analytically by the steady-state 1-D Fourier heat conduction theory under Dirichlet's boundary conditions. By employing simple-power material grading pattern the differential equations are obtained in the form of Euler-Cauchy types. Analytical solution of the differential equations gives the temperature field and the heat flux distribution in the radial direction in a closed form. Three different physical metal-ceramic pairs first considered to study the effect of the aspect ratio, which is defined as the inner radius to the outer radius of the structure, on the temperature and heat flux variation along the radial coordinate. Then a parametric study is performed with hypothetic inhomogeneity indexes for varying aspect ratios.

Keywords: Thermal analysis; functionally graded; exact solution; axisymmetric; cylindrical vessel, spherical vessel, inhomogeneity index, aspect ratio, thick-walled, circular annulus.

1. Introduction

As is well known, a temperature difference results in the heat conduction and the heat transfer in structures. Manufacturing processes in factories generally include thermal processes. So the thermal analysis is an important issue in industry related to mechanical, chemical, automotive, petroleum, nuclear engineering and living tissues. A thermal analysis is also the back-bone for the thermal-related analyses such as thermo-mechanical, thermo-electro-mechanical etc. So an accurate solution to the temperature field in the structure is always be very helpful for understanding the real physical thermal response of the structure under consideration at both the manufacturing phase and during its life-time.

To explore the question a number of studies were performed analytically, numerically and experimentally up to now. Chang and Tsou [1-2] used the Green's functions for heat conduction in an anisotropic medium for both steady state and unsteady state cases. Oato et al. [3] studied axisymmetric, transient, thermal stress analysis of a hollow cylinder composed of multilayered composite laminates with temperature changes in the radial and axial directions due to axisymmetric heating from the outer and/or the inner surfaces. They used Fourier cosine transform and Laplace transform for the temperature field and the thermo-elastic potential function and apply Love's displacement function to the thermo-elastic field. They then obtained the exact solutions for the temperature and thermal stress distributions in a transient state. Obata and Noda [4] studied the steady thermal stresses in a hollow cylinder and a hollow sphere made of a functionally gradient material (FGM) and compared their results with those of a FGM plate. Zimmerman and Lutz [5] derived an exact solution for the problem of the uniform heating of FG circular cylinder whose modulus of elasticity and thermal expansion coefficient vary linearly with radius. Tarn [6] found an exact solution for FG anisotropic cylinders subjected to thermal and mechanical loads. Awaji and Sivakumar [7] presented a numerical technique for analyzing one dimensional transient temperature distributions in a circular hollow cylinder that was composed of functionally graded ceramic–metal-based materials, with considering the temperature-dependent material properties. A 1-D steady state mechanical and thermal stress analysis of a thick hollow cylinder under axisymmetric and non-axisymmetric loads was studied by Jabbari et al. [8-10]. Liew et al. [11] sectioned the FGM cylinder into a number of homogeneous sub-cylinders. Displacements and stresses within the homogeneous sub-cylinders are obtained from the homogeneous solutions in Reference [11]. Tarn and Wang [12] worked the end effects of heat conduction in circular cylinders of functionally graded materials and laminated composites. Ruhi et al. [13] presented a semi analytical thermo-elasticity solution for thick-walled finite-length cylinders made of power-graded materials. The stress distribution in a power-graded orthotropic cylindrical body was investigated analytically by Oral and Anlaş [14]. Eslami et al [15] offered a general solution for the one-dimensional steady-state thermal and mechanical stresses in a hollow thick sphere made of a simple-power graded material. By using the Laplace transformation and a series expansion of Bessel functions, Ootao and Tanigawa [16] analyzed one-dimensional transient thermoelastic problem with power-law graded material properties. Pelletier and Vel [17], by using an arbitrary variation of orthotropic material properties in the radial direction, studied analytically the steady-state response of a functionally graded thick cylindrical shell subjected to thermal and mechanical loads and simply supported at the edges by the power series method. Birman and Byrad [18] reviewed related studies published in 2000-2007.

After 2007s, one-dimensional studies are focused especially on the transient thermal analysis, the stress and deformation analyses under steady state case etc. Kayhani et al. [19] presented an exact solution of conductive heat transfer in a cylindrical composite laminate in the radial and azimuthal directions. Kayhani et al. [20] further obtained a general analytical solution for heat conduction in cylindrical multilayered composite laminates in the radial and axial directions. Hosseini and Abolbashari [21] presented a unified formulation to analyze of temperature field in a thick hollow cylinder made of functionally graded materials with various grading patterns. Bayat et al. [22] carried out a thermo-mechanical analysis of functionally graded hollow sphere subjected to mechanical loads and one-dimensional steady-state thermal stresses. Lee and Huang [23] developed an analytic solution method, without integral transformation, to find the exact solutions for the transient heat conduction in functionally graded (FG) circular hollow cylinders with time-dependent boundary conditions. By introducing suitable shifting functions, the governing second-order regular singular differential equation with variable coefficients and time-dependent boundary conditions is transformed into a differential equation with homogenous boundary conditions. In Lee and Huang's [23] study, while the density has a constant value, the variation of specific heat is considered. Wang [24] developed an effective approach to analyze the transient thermal analysis in a functionally graded hollow cylinder based on the laminate approximation theory. The heat conductivity, mass density and specific heat are assumed to vary along the radial direction with arbitrary grading pattern as in the study. Wang [24] divided the transient solution into two parts. He obtained the quasi-static solution by the state space method and the dynamic solution by the initial parameter method in the time domain. By dividing the cylinder into some homogeneous sub-cylinders, an arbitrarily-graded circular hollow cylinder is studied analytically under arbitrarily non-uniform loads on the inner and outer surfaces by Li and Liu [25]. Delouei and Norouzi [26] presented an exact analytical solution for unsteady conductive heat transfer in multilayer spherical fiber-reinforced composite laminates for the most generalized linear boundary conditions consisting of the conduction, convection, and radiation. Arefi [27] performed a nonlinear thermal analysis of a hollow functionally graded cylinder by employing a semi-analytical method of successive approximations. A power function distribution is used for the simulation of non-homogeneity of the material used. A temperature dependence is employed for only the thermal conductivity. Based on the two-points Hermite approximations for integrals, Chen and Jian [28] proposed an improved lumped parameter model for the transient thermal analysis of multilayered composite pipeline with active heating. Daneshjou et .al. [29] presented a non-Fourier heat conduction analysis of infinite 2-D functionally graded (FG) hollow cylinders subjected to a time-dependent heat source. In Daneshjou et .al.'s study [29], a new augmented state space method considering laminate approximation theory is introduced. All material properties are assumed to vary continuously within the cylinder along the specified directions following an arbitrary law.

As seen from the literature survey that the thermal-related analyses are of great importance for both cylindrical and spherical structures. However, most of those studies focused on the computation of thermal stresses in the structure. That is, although they implemented the temperature distribution in their analyses, the thermal behavior of such structures were not studied in a detailed manner. In the present study, because of these reasons, the thermal analysis of such structures is addressed individually for both spherical and cylindrical vessels made of functionally power-law-graded non-homogeneous materials. It may be noted that the heat conduction equations are identical for both a cylindrical structure and a uniform discs or a circular annulus.

2. Derivation and Solution of Heat Conduction Equations

The rate of the heat flux in a solid object is directly proportional to the temperature gradient. The Fourier law governing the heat transfer by conduction is

$$\boldsymbol{q} = -k\nabla T = -k\ grad\ (T) \tag{1}$$

where the temperature gradient is given in cylindrical coordinates, $T(r,\theta,z,t)$, by

$$\nabla T = \frac{\partial T}{\partial r}\boldsymbol{e}_r + \frac{1}{r}\frac{\partial T}{\partial \theta}\boldsymbol{e}_\theta + \frac{\partial T}{\partial z}\boldsymbol{e}_z \tag{2a}$$

and in spherical coordinates, $T(r,\theta,\varphi,t)$, by

$$\nabla T = \frac{\partial T}{\partial r}\boldsymbol{e}_r + \frac{1}{r}\frac{\partial T}{\partial \theta}\boldsymbol{e}_\theta + \frac{1}{r\sin\theta}\frac{\partial T}{\partial \varphi}\boldsymbol{e}_\varphi \tag{2b}$$

By using the first law of thermodynamics, the heat conduction equation is written as follows

$$\rho c_p \frac{\partial T}{\partial t} + div(\boldsymbol{q}) = \dot{q}_{gen} \tag{3}$$

This equation takes the following form without heat generation in the structure [30].

$$\nabla^2 T = \frac{\rho c_p}{k}\left(\frac{\partial T}{\partial t}\right) = \kappa \frac{\partial T}{\partial t} \tag{4}$$

Where Laplacian of the temperature is derived in cylindrical coordinates as

$$\nabla^2 T = \Delta T = \nabla \bullet \nabla T = \frac{1}{r}\frac{\partial}{\partial r}(r\frac{\partial T}{\partial r}) + \frac{1}{r^2}\frac{\partial^2 T}{\partial \theta^2} + \frac{\partial^2 T}{\partial z^2} \tag{5a}$$

and in spherical coordinates as follows

$$\nabla^2 T = \Delta T = \nabla \bullet \nabla T = \frac{1}{r^2}\frac{\partial}{\partial r}(r^2\frac{\partial T}{\partial r}) + \frac{1}{r^2 \sin\theta}\frac{\partial}{\partial \theta}(\sin\theta\frac{\partial T}{\partial \theta}) + \frac{1}{r^2 \sin^2\theta}\frac{\partial^2 T}{\partial \varphi^2} \tag{5b}$$

In recent years functionally graded metal-ceramic composites gain considerable attention due to their attractive properties such as heat resisting, erosion and corrosion resistant, and fracture toughness. For the one-dimensional axisymmetric conditions, $\frac{\partial}{\partial \theta} = 0,\ \frac{\partial}{\partial \varphi} = 0, \frac{\partial}{\partial z} = 0$, the non-steady heat conduction equation of such materials in which the thermal conductivity, density, and the specific heat change along the radial direction becomes (Fig. 1)

$$\frac{1}{r^2}\frac{\partial}{\partial r}\left(r^2 k(r,t)\frac{\partial T(r,t)}{\partial r}\right) = \rho(r,t)c_p(r,t)\frac{\partial T(r,t)}{\partial t} \quad \text{(sphere)} \tag{6a}$$

$$\frac{1}{r}\frac{\partial}{\partial r}\left(r k(r,t)\frac{\partial T(r,t)}{\partial r}\right) = \rho(r,t)c_p(r,t)\frac{\partial T(r,t)}{\partial t} \quad \text{(cylinder/circular annulus)} \tag{6b}$$

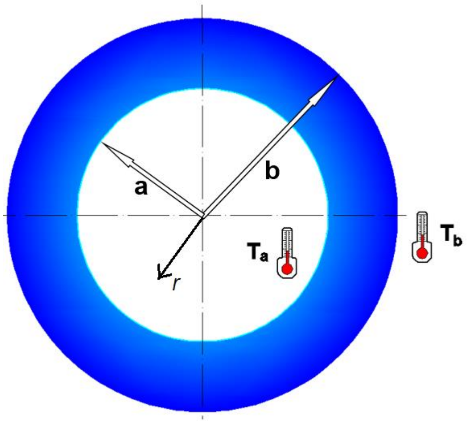

Fig.1. A characteristic section of the structure

After re-arranging of the equations given above, one may get the followings for the spherical structure

$$\frac{\partial^2 T(r,t)}{\partial r^2} + \frac{\partial T(r,t)}{\partial r}\left(\frac{2}{r} + \frac{\frac{\partial k(r,t)}{\partial r}}{k(r,t)}\right) = \frac{\rho(r,t)c_p(r,t)}{k(r,t)}\frac{\partial T(r,t)}{\partial t} \tag{7a}$$

for the cylindrical structure or a disk of uniform thickness or a circular annulus

$$\frac{\partial^2 T(r,t)}{\partial r^2} + \frac{\partial T(r,t)}{\partial r}\left(\frac{1}{r} + \frac{\frac{\partial k(r,t)}{\partial r}}{k(r,t)}\right) = \frac{\rho(r,t)c_p(r,t)}{k(r,t)}\frac{\partial T(r,t)}{\partial t} \tag{7b}$$

By using prime symbol for derivatives with respect to the radial coordinate, for the steady state case ($\frac{\partial T}{\partial t}=0$) one may get the followings.

$$T''(r)+T'(r)\left(\frac{2}{r}+\frac{k'(r)}{k(r)}\right)=0 \text{ (sphere)} \tag{8a}$$

$$T''(r)+T'(r)\left(\frac{1}{r}+\frac{k'(r)}{k(r)}\right)=0 \text{ (cylinder/uniform disk)} \tag{8b}$$

In the above equations, the material grading pattern may be chosen arbitrarily. Solution method to be adopted strictly depends on the material grading pattern considered. Some limited grading rules such as a simple power material grading rule permit to get the differential equation with constant coefficients and offer an analytical solution. For arbitrary grading patterns, the differential equations with variable coefficients are confronted. Consequently in the thermal analysis with arbitrary material grading patterns, it is necessary to use an appropriate numerical technique in the solution process. The material gradation may also be done as full-ceramic at the inner surface and full-metal at the outer surface, or vise-verse, or metal-ceramic mixtures at both surfaces by considering the real working conditions of the structure. Finally, all types of boundary conditions such as Dirichlet's, Neumann's, Robin's and mixed boundary conditions may be applied to the solution of equations (8).

To get exact solutions, in the present study, it is assumed that the thermal conductivity is changed outwardly between the inner and outer surfaces as follows

$$k(r)=k_a\left(\frac{r}{a}\right)^{\gamma} \tag{9}$$

where the inhomogeneity index of a physical material may be determined by

$$\gamma=\frac{\ln\left(\frac{k_a}{k_b}\right)}{\ln\left(\frac{a}{b}\right)} \tag{10}$$

Equation (8) becomes homogeneous Euler-Cauchy type differential equation with constant coefficients under assumptions given in Eq. (9). The solution will be in the form of

$$T(r)=C_1 r^{\mu_1}+C_2 r^{\mu_2} \tag{11}$$

Equation (8) is solved with the first kind boundary conditions (Dirichlet)

$$T(a)=T_a \quad ; \; T(b)=T_b \tag{12}$$

The solutions for each homogeneous/inhomogeneous material types are presented in Tables 1 and 2 for cylindrical and spherical vessels, respectively.

3. Examples with Physical Materials

Metal-ceramic pairs considered in the present study and their material properties are presented in Table 3. It is assumed that the inner surface is to be full-metal, and the outer surface is to be full-ceramic. Between the inner and the outer surfaces the material gradation obeys Eq. (9). The boundary conditions are determined as: $T_a = 220^oC$, and $T_b = 20^oC$. The geometrical properties of the structures are chosen as follows: $a = 0.5m$, $b = 1.0m$.

Table 1. Differential equations and their solutions for cylinders or uniform discs $\{k(r) = k_a(r/a)^\gamma\}$

Cylinder /Uniform Disc Made of a Homogeneous and Isotropic Material	
$\frac{T'(r)}{r} + T''(r) = 0$	$T(r) = C_2 + C_1 lnr$ $C_1 = \frac{T_a - T_b}{lna - lnb}$ $C_2 = \frac{lnaT_b - T_a lnb}{lna - lnb}$ $T(r) = \frac{(-lnb + lnr)T_a + (lna - lnr)T_b}{lna - lnb}$ $= \frac{T_b lna - T_a lnb + (T_a - T_b)lnr}{lna - lnb}$ $q_r(r) = \frac{k_o(-T_a + T_b)}{r(lna - lnb)}$
Cylinder/Uniform Disc Made of a Power-Law-Graded Isotropic and Non-homogeneous Material	
$\frac{(1+\gamma)T'(r)}{r} + T''(r) = 0$	$T(r) = -\frac{r^{-\gamma}}{\gamma}C_1 + C_2$ $C_1 = \frac{\gamma a^\gamma b^\gamma (T_a - T_b)}{a^\gamma - b^\gamma}$ $C_2 = \frac{a^\gamma T_a - b^\gamma T_b}{a^\gamma - b^\gamma}$ $T(r) = \frac{r^{-\gamma}(-a^\gamma(b^\gamma - r^\gamma)T_a + b^\gamma(a^\gamma - r^\gamma)T_b)}{a^\gamma - b^\gamma}$ $= \frac{r^{-\gamma}(-b^\gamma r^\gamma T_b + a^\gamma(r^\gamma T_a + b^\gamma(-T_a + T_b)))}{a^\gamma - b^\gamma}$ $q_r(r) = -\frac{a^\gamma b^\gamma r^{-1-\gamma}(\frac{r}{a})^\gamma \gamma k_a (T_a - T_b)}{a^\gamma - b^\gamma}$

Table 2. Differential equations and their solutions for spherical vessels $\{ k(r) = k_a (r/a)^{\gamma} \}$

Sphere Made of a Homogeneous and Isotropic Material	
$T''(r) + \frac{2}{r}T'(r) = 0$	$T(r) = -\frac{C_1}{r} + C_2$ $C_1 = \frac{ab(T_a - T_b)}{a-b}$ $C_2 = \frac{aT_a - bT_b}{a-b}$ $T(r) = \frac{-brT_b + a(rT_a + b(T_b - T_a))}{(a-b)r}$ $q_r(r) = \left\{ \frac{ab(T_b - T_a)k_o}{r^2(a-b)} \right\}$
Sphere Made of a Power-Law-Graded Isotropic and Non-homogeneous Material	
$T''(r) + \left(\frac{2}{r} + \frac{\gamma}{r} \right) T'(r) = 0$	$T(r) = \frac{r^{-1-\gamma}}{-1-\gamma} C_1 + C_2$ $C_1 = \frac{a^{\gamma+1} b^{\gamma+1} (T_a - T_b)(\gamma+1)}{a^{\gamma+1} - b^{\gamma+1}}$ $C_2 = \frac{(T_a - T_b) a^{\gamma+1}}{a^{\gamma+1} - b^{\gamma+1}} + T_b$ $T(r) = \frac{r^{-1-\gamma}(-b^{1+\gamma} r^{1+\gamma} \mathrm{Tb} + a^{1+\gamma}(r^{1+\gamma}\mathrm{Ta} + b^{1+\gamma}(-\mathrm{Ta} + \mathrm{Tb})))}{a^{1+\gamma} - b^{1+\gamma}}$ $q_r(\mathrm{r}) = \left\{ -\frac{a^{1+\gamma} b^{1+\gamma} r^{-2-\gamma} (T_a - T_b)(1+\gamma)}{a^{1+\gamma} - b^{1+\gamma}} \right\} k(r)$ $= -\frac{a^{1+\gamma} b^{1+\gamma} r^{-2-\gamma} (\frac{r}{a})^{\gamma} (T_a - T_b)(1+\gamma) k_a}{a^{1+\gamma} - b^{1+\gamma}}$

Table 3. Metal-ceramic pairs considered in the present study

	$k\ (\frac{W}{mK})$	Metal/Ceramic pair	γ
Nickel (Ni)	90.7	FGM-1	-6.22922
Silicon Nitride (Si_3N_4)	1.209	(Ni/Si_3N_4)	
Aluminum (Al)	204	FGM-2	-2.76073
Aluminum Oxide (Al_2O_3)	30.1	(Al/Al_2O_3)	
SUS-304 (Stainless Steel)	15.379	FGM-3	-3.11101
Zirconium Oxide (ZrO_2)	1.78	($SUS\text{-}304/ZrO_2$)	

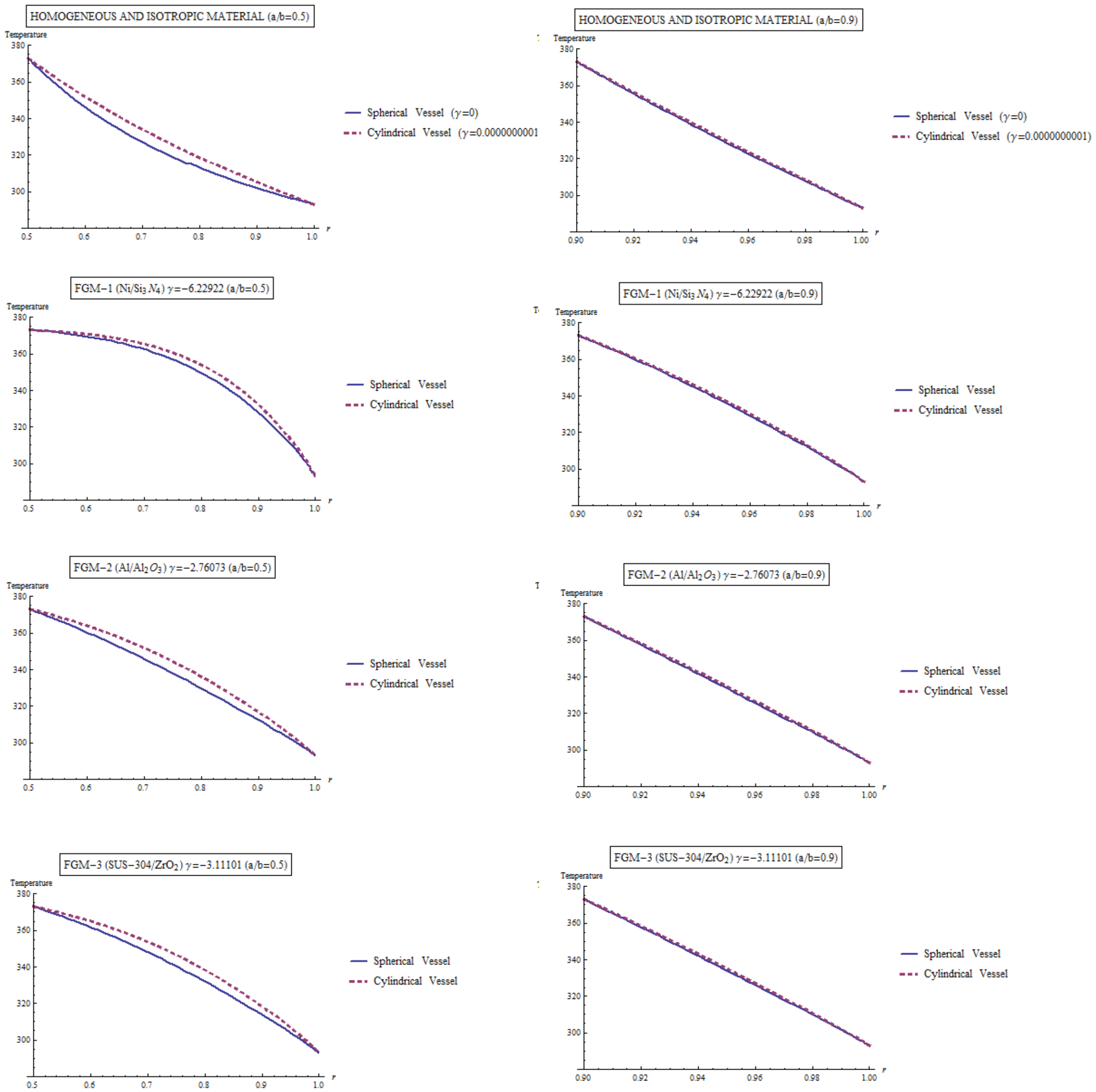

Fig. 2. Temperature variations in physical FGMs with the aspect ratio.

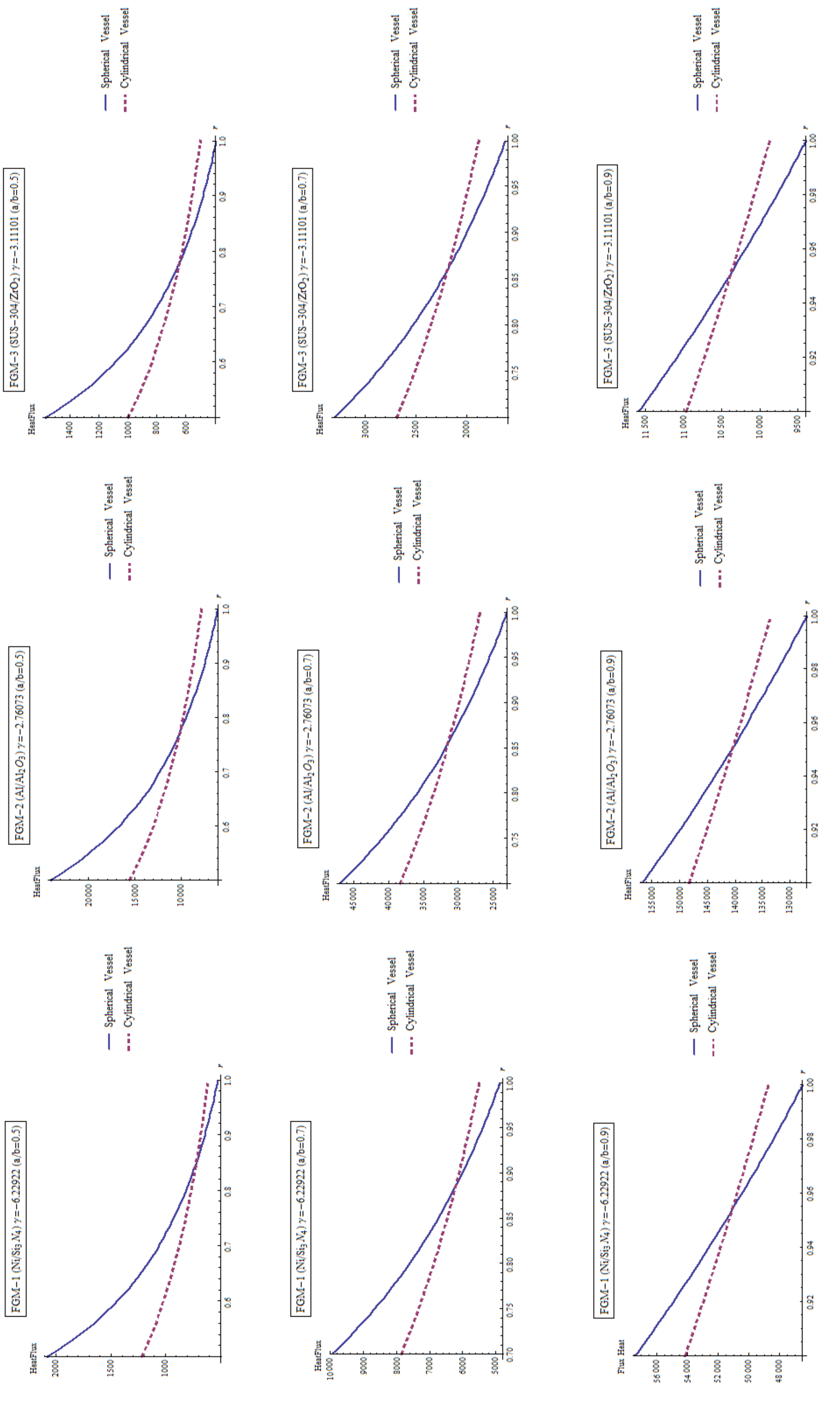

Fig. 3. Heat flux variations in physical FGMs with the aspect ratio.

Figs. 2 and 3 show the temperature and the heat flux variation in FGM-1, FGM-2 and FGM-3 metal-ceramic pairs for different aspect ratios. It is seen from Fig. 2 that the temperature change occurs somewhat rapid in spheres than cylinders. As the aspect ratio increases, that is when the thickness decreases, the temperature distribution differences between a cylinder and a sphere are facing disappearance. The temperature varies slowly in FGM-1 than the others. Heat flux in a sphere is higher than a cylinder as seen Fig. 3. An increase in the aspect ratio results much heat flux in the structure. The maximum heat flux occur at the inner surface of both structural geometries. FGM-2 offers the best metal-ceramic pair regarding the heat flux.

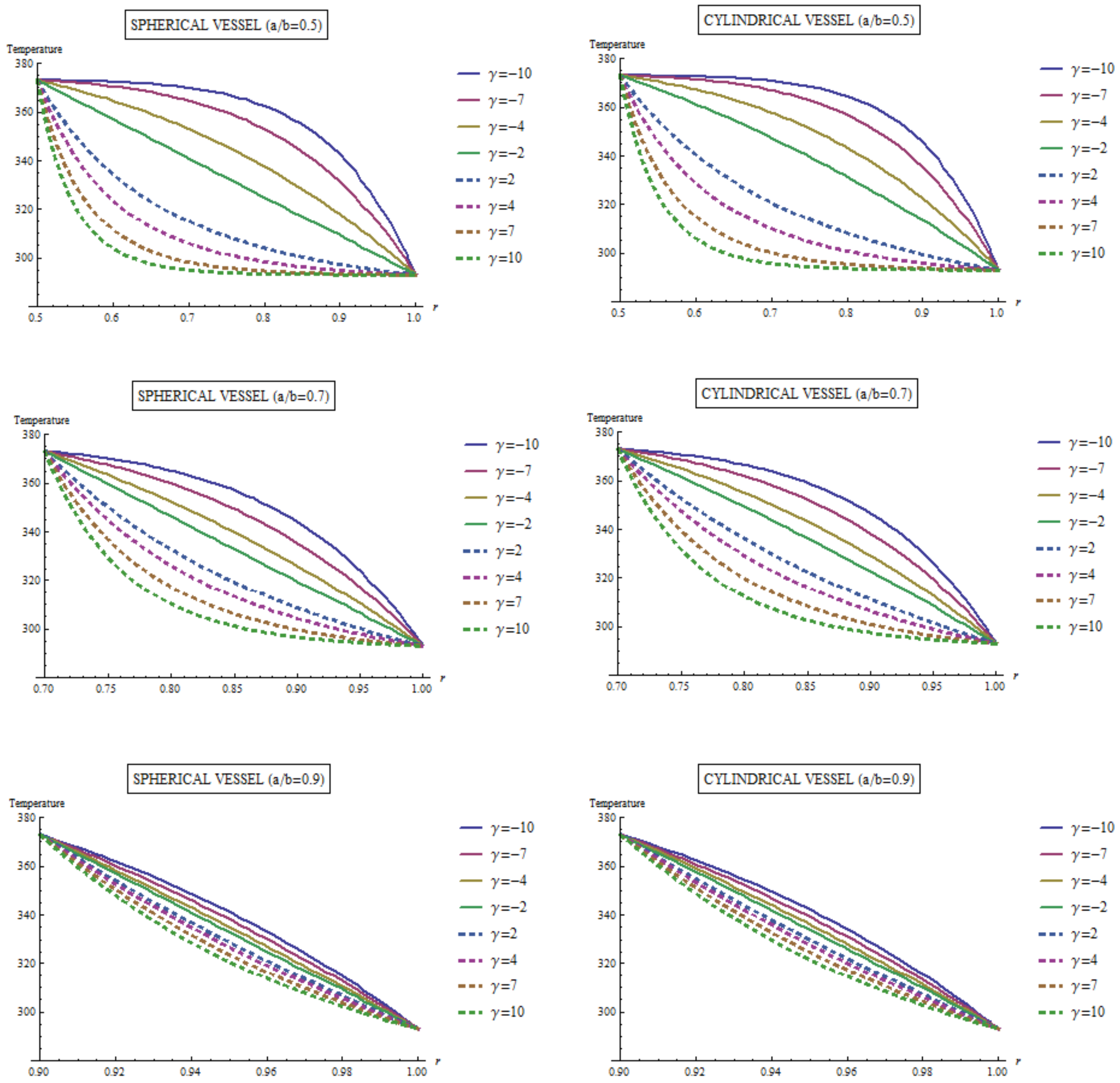

Fig. 4. Variation of temperature with hypothetic inhomogeneity indexes and aspect ratios for both cylinders and spheres ($k_a = 20$ W/mK)

4. A Parametric Study with Hypothetic Inhomogeneity Indexes

In this section, a parametric study is carried out to investigate the temperature variation along the radial direction with both aspect ratios and hypothetic inhomogeneity indexes which vary from $\gamma = -10$ towards $\gamma = 10$. Results are given in Table 4 and Figs. 4 and 5.

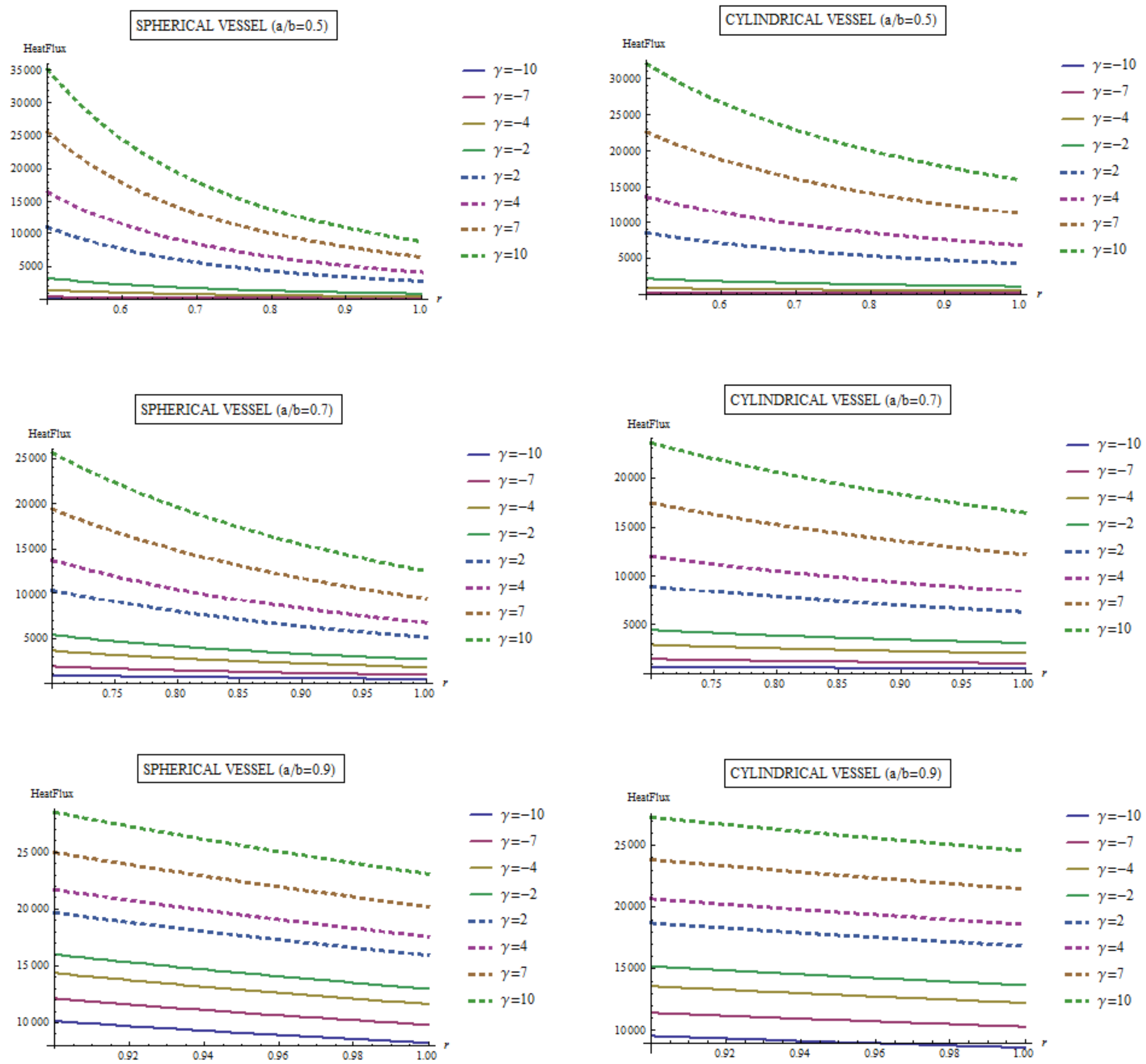

Fig. 5. Variation of heat flux with hypothetic inhomogeneity indexes and aspect ratios for both cylinders and spheres (k_a = 20 W/mK)

Table 3. Radial variation of temperature and heat flux with hypothetic inhomogeneity indexes for both cylinders and spheres having $\frac{a}{b} = 0.5$ and $k_a = 20$ W/mK.

	$\gamma = -10$	$\gamma = -7$	$\gamma = -4$	$\gamma = -2$	$\gamma = 2$	$\gamma = 4$	$\gamma = 7$	$\gamma = 10$
				$T_{sphere}(r)$				
0.5	373.	373.	373.	373.	373.	373.	373.	373.
0.55	372.787	372.02	369.217	365.	350.263	341.695	330.153	321.014
0.6	372.349	370.478	364.68	357.	334.481	323.607	311.365	303.733
0.65	371.496	368.141	359.32	349.	323.187	312.661	302.532	297.427
0.7	369.922	364.709	353.069	341.	314.891	305.774	298.128	294.937
0.75	367.138	359.806	345.857	333.	308.661	301.294	295.82	293.886
0.8	362.398	352.965	337.617	325.	303.893	298.295	294.556	293.416
0.85	354.591	343.619	328.28	317.	300.181	296.235	293.838	293.194
0.9	342.102	331.08	317.777	309.	297.248	294.79	293.415	293.085
0.95	322.638	314.529	306.04	301.	294.901	293.754	293.159	293.03
1.	293.	293.	293.	293.	293.	293.	293.	293.
				$T_{cylinder}(r)$				
0.55	372.875	372.402	370.525	367.4	354.488	345.95	333.746	323.795
0.6	372.594	371.373	367.274	361.267	340.407	328.819	314.872	305.855
0.65	372.	369.677	363.101	354.6	329.45	317.544	305.22	298.731
0.7	370.816	366.99	357.845	347.4	320.755	309.88	300.019	295.69
0.75	368.569	362.867	351.333	339.667	313.741	304.523	297.089	294.31
0.8	364.48	356.721	343.381	331.4	308.	300.688	295.374	293.65
0.85	357.313	347.782	333.789	322.6	303.242	297.884	294.335	293.319
0.9	345.157	335.065	322.346	313.267	299.255	295.796	293.687	293.146
0.95	325.132	317.323	308.829	303.4	295.881	294.215	293.272	293.052
				$q_{r-sphere}(r)$				
0.5	56.3601	304.762	1371.43	3200.	10971.4	16516.1	25700.4	35217.2
0.55	46.5786	251.869	1133.41	2644.63	9067.3	13649.7	21240.	29105.1
0.6	39.1389	211.64	952.381	2222.22	7619.05	11469.5	17847.5	24456.4
0.65	33.3492	180.332	811.496	1893.49	6491.97	9772.86	15207.3	20838.6
0.7	28.7551	155.491	699.708	1632.65	5597.67	8426.6	13112.4	17968.
0.75	25.0489	135.45	609.524	1422.22	4876.19	7340.5	11422.4	15652.1
0.8	22.0157	119.048	535.714	1250.	4285.71	6451.61	10039.2	13756.7
0.85	19.5018	105.454	474.543	1107.27	3796.34	5714.92	8892.87	12185.9
0.9	17.3951	94.0623	423.28	987.654	3386.24	5097.57	7932.22	10869.5
0.95	15.6122	84.4216	379.897	886.427	3039.18	4575.1	7119.22	9755.46
1.	14.09	76.1905	342.857	800.	2742.86	4129.03	6425.1	8804.3
				$q_{r-cylinder}(r)$				
0.5	31.2805	176.378	853.333	2133.33	8533.33	13653.3	22576.4	32031.3
0.55	28.4369	160.344	775.758	1939.39	7757.58	12412.1	20524.	29119.3
0.6	26.0671	146.982	711.111	1777.78	7111.11	11377.8	18813.6	26692.7
0.65	24.062	135.675	656.41	1641.03	6564.1	10502.6	17366.4	24639.4
0.7	22.3432	125.984	609.524	1523.81	6095.24	9752.38	16126.	22879.5
0.75	20.8537	117.585	568.889	1422.22	5688.89	9102.22	15050.9	21354.2
0.8	19.5503	110.236	533.333	1333.33	5333.33	8533.33	14110.2	20019.6
0.85	18.4003	103.752	501.961	1254.9	5019.61	8031.37	13280.2	18841.9
0.9	17.3781	97.9878	474.074	1185.19	4740.74	7585.19	12542.4	17795.2
0.95	16.4634	92.8305	449.123	1122.81	4491.23	7185.96	11882.3	16858.6
1.	15.6403	88.189	426.667	1066.67	4266.67	6826.67	11288.2	16015.6

As seen from Table 3, metals have much greater thermal conductivities than ceramics. If Eq. (10) is considered, that is if a metal is placed on the inner surface, this produces negative inhomogeneity indexes. The converse is true if a ceramic is on the inner surface. When the inhomogeneity index is changed from $\gamma = -10$ to $\gamma = 10$, the temperature declines faster at the vicinity of the inner surface (Fig. 4). Maximum heat flux is at the inner surface for all conditions since the inner surface has greater temperature than the outer. Heat flux decreases with negative inhomogeneity indexes (Fig. 5).

5. Conclusions

This study offers compact expressions in closed forms for the temperature and the heat-flux distributions in radial direction for hollow cylindrical and spherical structures made of radially functionally graded materials. A simple power material grading rule is used to get a differential equation with constant coefficients.

The derived formula for the temperature distribution becomes indefinite at $\gamma = -1$ in spheres and $\gamma = 0$ in cylinders. This disadvantage may be overcome numerically by using real numbers instead integers for those inhomogeneity indexes as seen in Fig. 2.

The formulas in Tables 1 and 2 may be used directly in some thermal and optimization problems. They may also be served as sound benchmark results for advanced studies.

Notations

a	radius at the inner surface
b	radius at the outer surface
c_p	specific heat capacity $\left(J/(kgK)\right)$
C_1, C_2	integration constants
$\boldsymbol{e_r}, \boldsymbol{e_\theta}, \boldsymbol{e_z}$	unit vectors in cylindrical coordinates
$\boldsymbol{e_r}, \boldsymbol{e_\theta}, \boldsymbol{e_\varphi}$	unit vectors in spherical coordinates
k	thermal conductivity $\left(W/(mK)\right)$
q or q_r	Heat flux component in radial direction
$\boldsymbol{q}$	the rate of heat flux vector (W/m^2)
$\dot{q}_{gen}$	heat generation per unit volume
r	radial coordinate
t	time
T	temperature
γ	inhomogeneity constant for simple-power grading rule
$\kappa = \frac{\rho c_p}{k}$	thermal diffusion coefficient (m^2/s)
μ_1, μ_2	characteristic roots of the differential equation
ρ	density (kg/m^3)
θ	Azimuthal angle
φ	Zenith angle
∇	gradient operator

$\nabla^2 = \Delta$	Laplacian operator
$\dfrac{d}{dr}(\,) = (\,)'$	derivative with respect to the radial coordinate
subscripts	
a	value at the inner surface
b	value at the outer surface

References

[1] Chang, Y.P., Tsou, R.C.H., Heat conduction in an anisotropic medium homogeneous in cylindrical regions—steady state. *ASME J. Heat Transfer*, 99(1), 132–134. 1977.

[2] Chang, Y. P., Tsou, R.C.H., Heat conduction in an anisotropic medium homogeneous in cylindrical coordinates-unsteady state. *ASME J. Heat Transfer*, 99(1), 41–46, 1977.

[3] Ootao, Y., Tanigawa, Y., Fukuda T., Axisymmetric transient thermal stress analysis of a multilayered composite hollow cylinder. *J. Therm. Stresses*, 14(2), 201-213, 1991.

[4] Obata, Y., Noda, N., Steady thermal stresses in a hollow circular cylinder and a hollow sphere of a functionally gradient material. *J. Therm. Stresses*, 17(3), 471–487, 1994.

[5] Zimmerman, R.W., Lutz, M.P., Thermal stresses and thermal expansion in a uniformly heated functionally graded cylinder. *J. Therm. Stresses*, 22 (2), 177–188, 1999.

[6] Tarn, J.Q., Exact solutions for functionally graded anisotropic cylinders subjected to thermal and mechanical loads. *Int. J. Solids Struct.*, 38, 8189–8206, 2001.

[7] Awaji, H., Sivakuman, R., Temperature and stress distributions in a hollow cylinder of functionally graded material: the case of temperature-dependent material properties. *Journal of American Ceramic Society*, 1059-1065, 2001.

[8] Jabbari, M., Sohrabpor, S., Eslami, M.R., Mechanical and thermal stresses in a functionally graded hollow cylinder due to radially symmetric loads. *Int. J. Pressure Vessels Piping*, 79, 493–497, 2002.

[9] Jabbari, M., Sohrabpour, S., Eslami, M.R., General solution for mechanical and thermal stresses in a functionally graded hollow cylinder due to nonaxisymmetric steady-state loads. *ASME J. Appl. Mech.*, 70 , 111–118, 2003.

[10] Jabbari, M., Bahtui, A., Eslami, M.R., Axisymmetric mechanical and thermal stresses in thick long FGM cylinders. *J. Therm. Stresses*, 29 (7), 643–663, 2006.

[11] Liew, K.M., Kitipornchai, S., Zhang, X.Z., Lim, C.W., Analysis of the thermal stress behaviour of functionally graded hollow circular cylinders. *Int. J. Solids Struct.*, 40, 2355–2380, 2003.

[12] Tarn, J.Q., Wang, Y.M., End effects of heat conduction in circular cylinders of functionally graded materials and laminated composites. *Int. J. Heat Mass Transfer*, 47, 5741–5747, 2004.

[13] Ruhi, M., Angoshtari, A., Naghdabadi, R., Thermoelastic analysis of thick-walled finite-length cylinders of functionally graded materials. *J. Therm. Stresses*, 28 (4), 391-408, 2005.

[14] Oral, A., Anlas, G., Effects of radially varying moduli on stress distribution of nonhomogeneous anisotropic cylindrical bodies. *International Journal of Solids and Structures*, 5568–5588, 2005.

[15] Eslami, M.R., Babai, M.H., Poultangari, R., Thermal and mechanical stresses in a functionally graded thick sphere. *Int. J. Pressure Vessels Piping*, 82 (7), 522–527, 2005.

[16] Ootao, Y., Tanigawa, Y., Transient thermoelastic analysis for a functionally graded hollow cylinder. *J. Therm. Stresses*, 29(11), 1031–1046, 2006.

[17] Pelletier, J.L., Vel, S.S., An exact solution for the steady-state thermoelastic response of functionally graded orthotropic cylindrical shells. *Int. J. Solids Struct*., 43, 1131–1158, 2006.

[18] Birman, V., Byrd., L.W., Modeling and analysis of functionally graded materials and structures. *Applied Mechanics Reviews*, 60, 195-216, 2007.

[19] Kayhani, M.H., Shariati, M., Nourozi, M., Demneh, M.K., Exact solution of conductive heat transfer in cylindrical composite laminate. *Heat Mass Transfer*, 46, 83–94, 2009.

[20] Kayhani, M.H., Norouzi, M., Delouei, A.A., A general analytical solution for heat conduction in cylindrical multilayer composite laminates. *Int. J. Therm. Sci*., 52, 73–82, 2012.

[21] Hosseini, S.M., Abolbashari, M.H., A unified formulation for the analysis of temperature field in a thick hollow cylinder made of functionally graded materials with various grading patterns. *Heat Transfer Eng*., 33, 261–271, 2012.

[22] Bayat, Y., Ghannad, M., Torabi, H., Analytical and numerical analysis for the FGM thick sphere under combined pressure and temperature loading. *Archive of Applied Mechanics*, 229-242, 2012.

[23] Lee, S.Y., Huang, C.C., Analytic solutions for heat conduction in functionally graded circular hollow cylinders with time-dependent boundary conditions. *Mathematical Problems in Engineering*, Article ID 816385, 1-8. 2013.

[24] Wang, H.M., An effective approach for transient thermal analysis in a functionally graded hollow cylinder. *International Journal of Heat and Mass Transfer*, 67, 499-505, 2013.

[25] Li, H., Liu, Y., Functionally graded hollow cylinders with arbitrary varying material properties under non-axisymmetric loads. *Mechanics Research Communications*, 55, 1-9, 2014.

[26] Delouei, A.A., Norouzi, M., Exact analytical solution for unsteady heat conduction in fiber-reinforced spherical composites under the general boundary conditions. *Journal of Heat Transfer*, 137, 1-8. 2015.

[27] Arefi, M., Nonlinear thermal analysis of a hollow functionally graded cylinder with temperature-variable material properties. *Journal of Applied Mechanics and Technical Physics*, 56(2), 267-273, 2015.

[28] Chen, A., Jian, S., Lumped models for transient thermal analysis of multilayered composite pipeline with active heating. *Applied Thermal Engineering*, 87, 749–759, 2015.

[29] Daneshjou, K., Bakhtiari, M., Parsania H., Fakoor, M., Non-Fourier heat conduction analysis of infinite 2D orthotropic FG hollow cylinders subjected to time-dependent heat source. *Applied Thermal Engineering*, 98, 582–590, 2016.

[30] Hetnarski, B., Eslami, M.R., Thermal Stresses-Advanced Theory and Applications, Springer. Chap. 4-ISBN: 978-1-4020-9246-62009.

International Journal of Engineering & Applied Sciences (IJEAS)
Vol.9, Issue 2 (Special Issue: Composite Structures) (2017) 127-137
http://dx.doi.org/10.24107/ijeas.322884
Int J Eng Appl Sci 9(2) (2017) 127-137

Free Vibration of Functionally Graded Rayleigh Beam

Mehmet Avcar[a], Hiyam Hazim AlSaid Alwan[b]*

[a]Department of Civil Engineering, Faculty of Engineering, Suleyman Demirel University, Cunur, Isparta, Turkey
[b]Graduate School of Natural and Applied Sciences, Suleyman Demirel University, Cunur, Isparta, Turkey
**E-mail address: mehmetavcar@yahoo.com*

Received date: June 2017
Accepted Date: July 2017

Abstract

In the present study, free vibration of Rayleigh beam composed of functionally graded materials (FGMs) is investigated. For this purpose, the equation of the motion of functionally graded (FG) beam derived according to Rayleigh beam theory. The material properties are assumed to vary continuously through the thickness of the beam according to the power-law form. Resulting equations are solved for simply supported boundary conditions. In order to validate the results, a comparison is carried out with available results for homogeneous beam. The effects of varying material properties on the dimensionless free vibration frequency parameters are examined. It is seen that varying material properties have significant effects on dimensionless free vibration frequency parameters of FG Rayleigh beam

Keywords: Beam, Free Vibration, Rayleigh beam theory, Functionally Graded Materials (FGMs).

1. Introduction

FGMs are extensively used in machinery, space, nuclear and civil engineering; high temperature exposed building components, space vehicles, microelectronics, and industrial applications. These types of materials were first introduced by Japanese scientists in 1984 as thermal barrier materials. FGM is typically a mixture of a ceramic and a metal so that the metal can withstand high temperatures in the thermal environment as well as reduce the tensile stresses that would otherwise occur on the ceramic surface during the first stages of cooling [1-4].

Beam structures have large applications in engineering field and studying the vibration behavior of this kind of structural components are important for understanding the behavior of more complex and real structures subjected similar conditions. Therefore, researchers have been focused on the vibration analysis of beam structures using different theories and several solution methods [5-13].

Due to the advantages and increasing use of FGMs and importance of the beam structures in the engineering field, many studies have been performed on the vibration problems of FG beams [14-22].

From the search of open literature, it is seen although there are numerous studies on the vibration analysis of FG beams using different beam theories, the number of works depending on Rayleigh beam theory is still limited. An attempt is made to address this problem. For this purpose, the equation of the motion of FG beam derived using Rayleigh beam theory. The functionally graded material properties are assumed to vary continuously through the thickness direction of the beam according to power law form. Resulting equations are solved for simply supported boundary conditions. In order to validate the results, a comparison is carried out with available results for homogeneous beam. The effects of varying material properties on the dimensionless free vibration frequency parameters are examined.

2. Effective material properties of FGMs

Consider a FGM beam consist of ceramic–metal, which has length, L, width b, and thickness, h, as shown in Fig. 1.

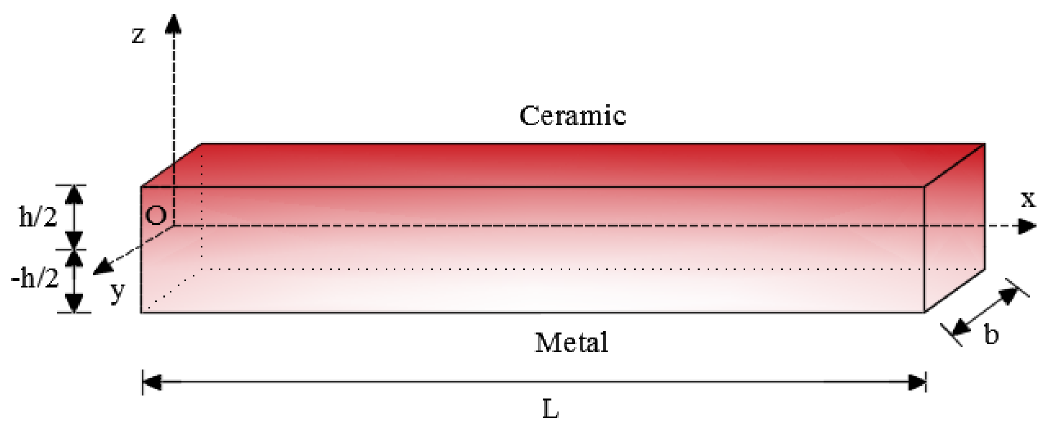

Fig. 1. Geometry of a functionally graded beam

The effective material properties of the FG beam, i.e., Young's modulus E and mass density ρ, vary continuously through the thickness direction according to a function of the volume fractions of the constituents while Poisson's ratio ν is taken to be constant.

According to the rule of mixture, the effective material properties, P, can be expressed as

$$P = P_m V_m + P_c V_c \tag{1}$$

where P_m, P_c, V_m and V_c are the material properties and the volume fractions of the metal and the ceramic constituents respectively.

The total volume fraction of the metal and ceramic as follows

$$V_m + V_c = 1 \tag{2}$$

The power law of volume fraction of the ceramic constituent of the beam as follows

$$V_c = \left(\frac{z}{h} + \frac{1}{2}\right)^d \tag{3}$$

where d is a non-negative number ($0 \le d \le \infty$) called power law or volume fraction index, and z is the distance from the mid-plane of the beam. Note that, FG beam becomes a fully ceramic one as $d = 0$ while it becomes a fully metallic one as $d = \infty$.

The variation of the volume fraction of the ceramic constituent, V_c, through the thickness direction of the FG beam versus various values of power law index, d, is illustrated in Fig. 2. It is clear that the V_c changes rapidly near the bottom surface for $d < 1$ while it changes rapidly near the top surface for $d > 1$.

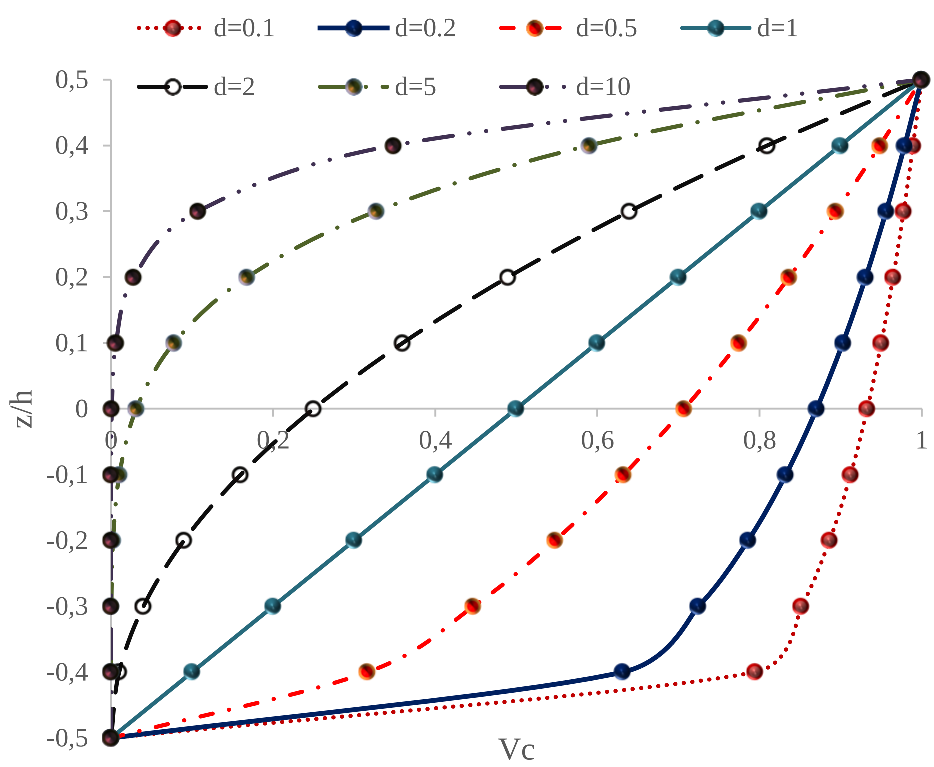

Fig. 2. Variation of volume fraction of the ceramic constituent along thickness of FG beam versus various values of power law index

3. Governing Equation

Using Kirchoff-Love hypothesis, displacements at any point of a FG beam can be expressed as

$$u(x,z,t) = u_0(x,t) + z\,\theta$$
$$w(x,z,t) = w_0(x,t) \tag{4}$$

where $u_0(x,t)$ and $w_0(x,t)$ are the displacements at mid-surface in the x, and z directions, respectively, and θ is the rotation of the cross section at the mid-plane.

The normal strain and shear strain are

$$\varepsilon(x,z,t) = \frac{\partial u_0}{\partial x} + z\frac{\partial \theta}{\partial x} \tag{5}$$

$$\gamma_{xz} = \theta + \frac{\partial w_0}{\partial x} \tag{6}$$

Rayleigh beam theory neglects the shear strain, $\gamma_{xz} = 0$, hence we have

$$\varepsilon(x,z,t) = \frac{\partial u_0}{\partial x} - z\frac{\partial^2 w_0}{\partial x^2} \tag{7}$$

According to the Hooke's law, the normal stress is defined as

$$\sigma(x,z,t) = E(z)\varepsilon = E(z)\left(\frac{\partial u_0}{\partial x} - z\frac{\partial^2 w_0}{\partial x^2}\right) \tag{8}$$

The stress resultants in terms of axial force, N_x, bending moment, M_x, and transverse shear force Q_x, can be written as

$$N_x = \int_A \sigma_x dA = A_1 \frac{\partial u_0}{\partial x} - B_1 \frac{\partial^2 w_0}{\partial x^2} \tag{9}$$

$$M_x = \int_A \sigma_x z dA = B_1 \frac{\partial u_0}{\partial x} - D_1 \frac{\partial^2 w_0}{\partial x^2} \tag{10}$$

$$Q_x = \frac{\partial M_x}{\partial x} = B_1 \frac{\partial^2 u_0}{\partial x^2} - D_1 \frac{\partial^3 w_0}{\partial x^3} \tag{11}$$

where A_1, B_1 and D_1 are the material stiffness components of FG beam and defined as follow

$$(A_1, B_1, D_1) = \int_{-h/2}^{h/2} \frac{E(z)}{1-\nu^2} (1, z, z^2) dz \tag{12}$$

Taking into account the axial and rotary inertias, using Hamilton's Principle and after some mathematical operations, the governing equation of FG Rayleigh beam is derived as follows

$$\Lambda_{11} \frac{\partial^4 w_0}{\partial x^4} + I_0 \frac{\partial^2 w_0}{\partial t^2} - \Gamma_{11} \frac{\partial^4 w_0}{\partial x^2 \partial t^2} = 0 \tag{13}$$

where the following definitions apply

$$\begin{aligned} \Lambda_{11} &= \left(D_1 - \frac{B_1^{\,2}}{A_1} \right) \\ \Gamma_{11} &= \left(I_2 - \frac{I_1^{\,2}}{I_0} \right) \end{aligned} \tag{14}$$

here I_0, I_1 and I_2 are the moment of inertia components of FG beam and defined as follow

$$(I_0, I_1, I_2) = \int_{-h/2}^{h/2} \rho(z) (1, z, z^2) dz \tag{16}$$

4. Solution of Governing Equation

FG Rayleigh beam is assumed to have simply supported boundary conditions in both ends. Hence, the following boundary conditions are satisfied:

$$\begin{aligned} & w_0(0,t)=0, \qquad w_0(L,t)=0 \\ & \frac{\partial^2 w_0}{\partial x^2}(0,t)=0, \qquad \frac{\partial^2 w_0}{\partial x^2}(L,t)=0 \end{aligned} \tag{17}$$

Governing Eq.(13) can be rearranged as follows:

$$a^2\frac{\partial^4 w_0}{\partial x^4}+\frac{\partial^2 w_0}{\partial t^2}-b^2\frac{\partial^4 w_0}{\partial x^2\partial t^2}=0 \tag{18}$$

where the following parameters applied

$$a^2=\frac{\Lambda_{11}}{I_0};\ b^2=\frac{\Gamma_{11}}{I_0} \tag{19}$$

The solution of Eq. (18) satisfying the boundary conditions (17) is assumed as [23]:

$$w(x,t)=C\sin\frac{n\pi x}{L}\cos\omega_n t \tag{20}$$

Substituting the Eq.(20) into Eq. (18) yields

$$a^2\left(\frac{n\pi}{L}\right)^4-\omega^2\left[1+b^2\left(\frac{n\pi}{L}\right)^2\right]=0 \tag{21}$$

Finally, the formula for free vibration frequency of FG Rayleigh beam is obtained as follows

$$\omega = \sqrt{\frac{a^2\left(\frac{n\pi}{L}\right)^4}{\left(1+b^2\left(\frac{n\pi}{L}\right)^2\right)}}, \quad n = 1,2,... \tag{22}$$

5. Numerical Results

In this section examples are given to examine the present problem. At first, a comparison has been performed to show the accuracy of the present formulation. Then, an example is exhibited to show the effect of power law index on the dimensionless free vibration frequency parameters of FG Rayleigh beam.

5.1. Comparison Study

To confirm the formulation given in Eq. (22), the values of natural frequencies of homogeneous beam, $\omega(\mathrm{rad/sn})$, are compared with results of Rao [23] in Table 1. Here the following beam characteristics and material properties are taken into account:

$$L = 1\mathrm{m},\ b = 0.05\mathrm{m},\ h = 0.15\mathrm{m},$$

$$d = 0,$$

$$E = 207\times10^9\ \mathrm{Pa}, \rho = 76.5\times10^3\ \mathrm{N/m^3} \tag{23}$$

Table 1. Comparison of the values of natural frequencies of homogeneous beam with results of Rao [23]

Source	$\omega(\mathrm{rad/sn})$		
	n=1	n=2	n=3
Present Study	696.5834	2713.3651	5857.9512
Rao [23]	696.5987	2713.4221	5858.0654

As it is seen in Table 1, the results are in good agreement and so the accuracy of the formulation is validated.

5.2. Illustrative example

Fig. 3 shows the variation of dimensionless free vibration frequency parameters of FG Rayleigh beam, ϖ, for the first three modes versus power law index, d. Here, FG Rayleigh beam is assumed to be composed of Alumina (Al_2O_3), and Aluminum (Al). Hence, the following beam characteristics and material properties are considered:

$$L/h = 5$$

$$E_c = 380\,\mathrm{GPa};\ \rho_c = 3960\,\mathrm{kg/m^3}$$

$$E_m = 70\,\mathrm{GPa};\ \rho_m = 2702\,\mathrm{kg/m^3} \tag{24}$$

The dimensionless free vibration frequency parameter of Rayleigh beam is defined as follow:

$$\varpi = \frac{\omega L^2}{h}\sqrt{\frac{\rho_m}{E_m}} \tag{25}$$

It is obvious from Fig. 3 that, the highest dimensionless free vibration frequency parameters are found for Al_2O_3 while the lowest ones are found for Al. Furthermore, dimensionless free vibration frequency parameters decrease with increasing power law index, d. As a result, it is concluded that the dimensionless free vibration frequency parameters decrease as the material property of FG Rayleigh beam varies from ceramic to metal component.

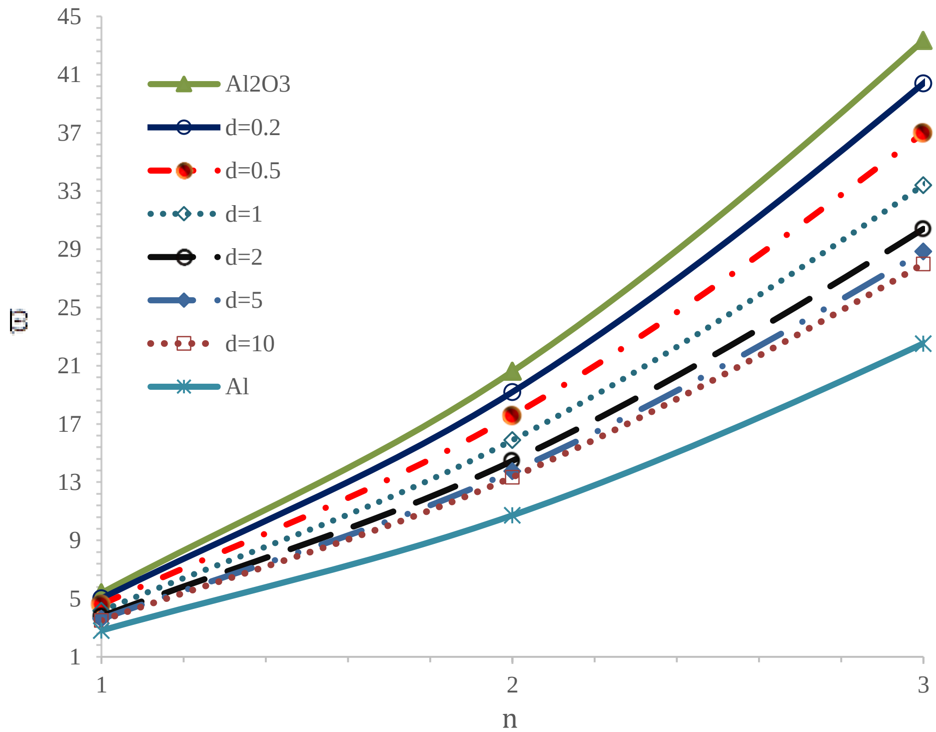

Fig. 3. Variation of dimensionless frequency parameters of FG Rayleigh beam versus power law index, d.

6. Conclusions

In the present study the free vibration of the beam composed of FGMs is investigated using Rayleigh beam theory. The material properties are assumed to vary continuously through the thickness direction of the beam according to the power-law form. Resulting equations are solved considering simply supported boundary conditions. In order to validate the results, a comparison is carried out with available results for homogeneous beam. It is seen that varying material properties have significant effects on dimensionless free vibration frequency parameters of FG Rayleigh beam. Present analysis can be served as a comparative study or data for the different solution methods of future works.

Acknowledgments

The financial support of the Suleyman Demirel University Scientific Research Projects Unit (SDU-BAP) with Grand No. 4857-YL1-17 is gratefully acknowledged. The authors would like to thank institution.

References

[1] Wakashima K., Hirano T., Niino M.. Space applications of advanced structural materials. *ESA SP303-97*, 1990

[2] Koizumi, M., The concept of FGM. *Ceramic Transactions, Functionally Gradient Materials,* vol. 34, pp. 3–10, 1993.

[3] Suresh, S., Mortensen, A.,. *Fundamentals of Functionally Graded Materials*. IOM Communications, London, 1998.

[4] Kieback, B., Neubrand, A., Riedel, H., Processing Technique for Functionally Graded Materials. *Materials Science and Engineering A*, 362 , 81- 105, 2003.

[5] Han, M.S., Benaroya, H., Wei, T., Dynamics of transversely vibrating beams using four engineering theories. *Journal Sound and Vibration*, 225, 935-988. 1999.

[6] Civalek, O., Kiracioglu, O., Free vibration analysis of Timoshenko beams by DSC method. *International Journal of Numerical Methods in Biomedical Engineering*, 26, 1890-1898, 2010.

[7] Carrera, E., Giunta, G. and Petrolo, M., *Beam Structures: Classical and Advanced Theories*. John Wiley and Sons Ltd, 2011.

[8] Coşkun, S.B., Öztürk, B., Atay, M.T., *Transverse Vibration Analysis of Euler-Bernoulli Beams Using Analytical Approximate Techniques*. INTECH Open Access Publisher, 2011.

[9] Li, X.F., Tang, A.Y., Xi, L.Y., Vibration of a Rayleigh cantilever beam with axial force and tip mass. *Journal of Constructional Steel Research*,80, 15-22, 2013.

[10] Avcar M., Free Vibration analysis of beams considering different geometric characteristics and boundary conditions. *International Journal of Mechanics and Applications,* 4, 94-100, 2014.

[11] Avcar, M., Effects of rotary inertia shear deformation and non-homogeneity on frequencies of beam. *Structural Engineering and Mechanics*,55, 871-884. 2015.

[12] Arıbaş, Ü.N., Eratlı, N., Omurtag, M.H., Free Vibration Analysis of Moderately Thick, Sandwich, Circular Beams. *In Proceedings of the World Congress on Engineering* (Vol. 2), 2016.

[13] FF Calim Free Vibration Analysis of Timoshenko Beam with Variable Cross-Section. *Omer Halisdemir University Journal of Engineering Sciences*, 6, 76-82, 2017.

[14] Sankar B.V., An elasticity solution for functionally graded beams. *Composites Science and Technology*, 61 , 689–696. 2001.

[15] Aydogdu, M., Taskin, V., Free vibration analysis of functionally graded beams with simply supported edges. *Materials and Design*, 28 , 1651–1656, 2007.

[16] Li X.F., A unified approach for analyzing static and dynamic behaviors of functionally graded Timoshenko and Euler–Bernoulli beams. *Journal of Sound and Vibration,* 318, 1210–1229, 2008.

[17] Sina S.A., Navazi H.M., Haddadpour H., An analytical method for free vibration analysis of functionally graded beams. *Materials and Design*, 30, 741–747, 2009.

[18] Şimsek, M., Fundamental frequency analysis of functionally graded beams by using different higher-order beam theories. *Nuclear Engineering and Design*, 240, 697-705, 2010.

[19] Nuttawit, W., Variddhi, U., Free vibration analysis of functionally graded beams with general elastically end constraints by DTM. *World Journal of Mechanics*, 2, 297–310, 2012.

[20] Ebrahimia, F., Mokhtaria, M., Semi-analytical vibration characteristics of rotating Timoshenko beams made of functionally graded materials. *Latin American Journal of Solids and Structures*, 12, 1319-1339, 2015.

[21] Chakraverty, S., Pradhan, KK., *Vibration of Functionally Graded Beams and Plates*. Academic Press, 2016.

[22] Al Rjoub, Y.S., Hamad, A.G., Free vibration of functionally Euler-Bernoulli and Timoshenko graded porous beams using the transfer matrix method. *KSCE. Journal of Civil Engineering*, 21, 792-806, 2017.

[23] Rao, S.S., *Vibration of continuous systems*. John Wiley & Sons, 2007.

International Journal of Engineering & Applied Sciences (IJEAS)
Vol.9, Issue 2 (Special Issue: Composite Structures) (2017) 138-146
http://dx.doi.org/10.24107/ijeas.322526
Int J Eng Appl Sci 9(2) (2017) 138-146

What is The Correct Mechanical Model of Aorta Artery

*Kadir Mercan, Ömer Civalek**

Akdeniz University, Civil Engineering Department,
Division of Mechanics, Antalya-TURKIYE
**E-mail address*: civalek@yahoo.com

Received date: June 2017
Accepted Date: July 2017

Abstract:

Aorta artery is the most vital artery in humans and almost all animals. Aorta artery is also the largest artery in human body. This artery is the first artery coming out from the left ventricle of the heart and extending down to the abdomen, where it splits into two smaller iliac arteries. Aorta artery conveys oxygenated blood to all parts of the body so that this artery is the one, which is under the influence of the highest blood pressure. It is well known that aorta artery consists of three main layers, which cover five sub-layers. In this paper, we aimed to show the difference between functionally graded material (FGM) and laminated composite material and to show which model fits to the structure of aorta artery.

Keywords: Aorta artery, composite materials, functionally graded materials, laminated composite materials.

1. Introduction

The mechanic model of aorta artery has a long history and variety in literature. For example, a fundamental paper about mechanic model of aorta artery presented by Gozna et al. in 1974 with the effect of age in man [1]. Gozna et al. have found regression equations between aging and aorta artery mechanic behavior. These equations have showed that there is a linear relation between aging and aorta artery mechanic behavior. More recently, the stability of aorta artery has been investigated in case of buckling under blood pressure by Han in 2007 [2]. Further researches of Han et al. proved that arteries may buckle and become turtous due to reduced axial strain, hypertensive pressure, and weakened artery wall [3-9]. In 2013, Han et al. has introduced new phenotypes, models, and applications of aorta artery [10]. In the review, Han et al. summarized the common forms of buckling that occurs in blood vessels including cross-sectional collapse, longitudinal twist buckling, and bent buckling. Also the phenomena, model analyses, experimental measurements, effect on blood flow, and clinical relevance have been discussed. From this and further works Han et al. clearly showed that mechanical buckling of aorta artery is an important issue for vasculature, in addition to wall stiffness and strength, and requires further studies [11-20].

2. Anatomy of Aorta Artery

It is well known that aorta artery is composed of three main layers like most of other arteries [21]. These layers are "intima", "media", and "adventitia" respectively from inner layer to outermost layer. Intima is the innermost layer of the artery which is covering the lumen side of vessels and it is composed of endothelial cells and lines the entire circulatory system, from the heart and the large arteries all the way down to the very tiny capillary beds. The intima layer also contains extracellular matrix and a supporting layer of collagenous tissue. Endothelial cells sorted in a single layer along the lumen side. Media is the muscular middle layer of the arteries and veins. It is composed of smooth muscle layers. Adventitia is outermost layer of vessels surrounding the media layer. It is mainly composed of collagen and, in arteries, is supported by external elastic lamina . The demonstration of these three main layers have been shown in Fig. 1.

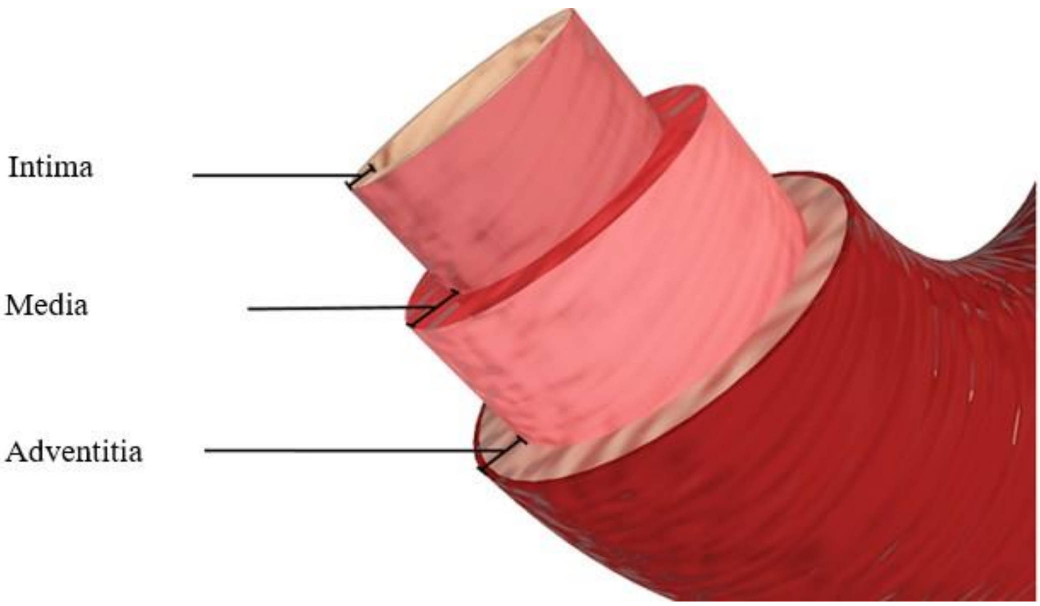

Fig. 1. Main layers of aorta artery

More specifically, these three main layers "intima", "media", and "adventitia" consist of five sub-layers. These sub-layers are Endotel, internal elastic layer, smooth muscle, external elastic layer, collagens and elastic tendons from inside to outside of aorta artery respectively as it is shown in Fig. 2.

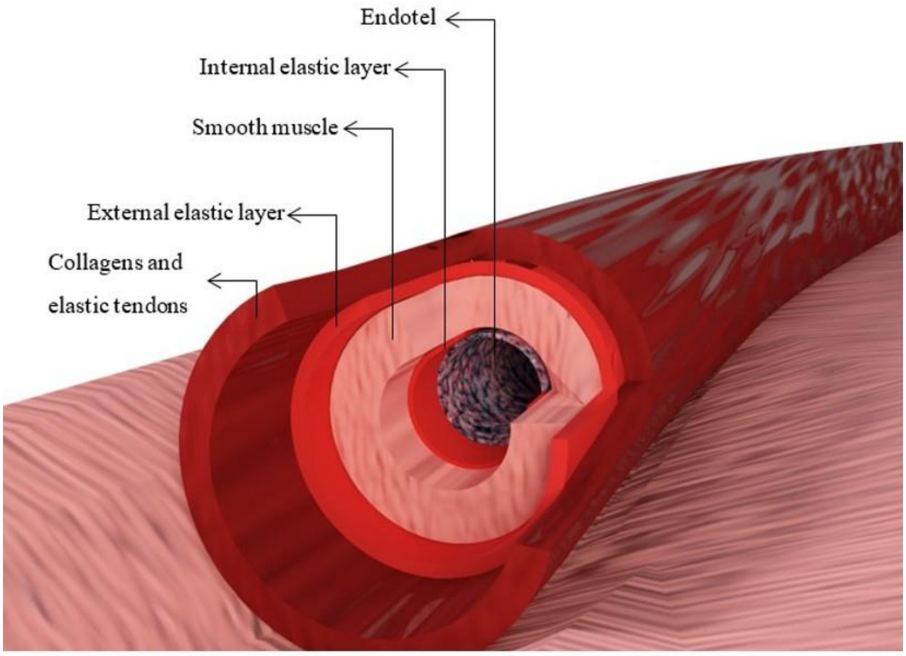

Fig. 2. Sub-layers of aorta artery

In 2005, Holzapfel et al. have made an experimental research to determine the material properties of the layers of aorta artery separately [22]. Within these experiments, 13 nonstenotic human aorta artery have been harvested at autopsies. The age of human were mean 71.5±7.3 years old. The artery samples have been subjected to cyclic quasi-static uniaxial tension tests from the individual layers in axial and circumferential directions. The outer diameter to total wall thickness ratio was 0.189±0.014 and the ratios of intima, media, and adventitia to total thickness were 0.27±0.02, 0.36±0.03, 0.4±0.03 respectively. The axial stretch was 1.044±0.06 and decreased with age of humans. Holzapfel et al. have found that the stress-stretch responses for the individual tissues performed pronounced mechanical heterogeneity. According to researches and experiments, intima have been found to be the stiffest layer and media the softest. Although intima and media have been found the stiffest and softest layers, these two layers have performed similar ultimate tensile stresses. These values have been found three times smaller than ultimate tensile stresses which have been calculated for adventitia (1430±604 kPa circumferential and 1300±692 kPa longitudinal). This study have clearly showed that aorta artery need to be modelled as composite structure which consist of three solid mechanically relevant layers with different material properties. The innermost layer “intima” have performed significant thickness, load-bearing capacity, and mechanical strength compared with other main layers “adventitia and media”. In order to calculate the material properties of the layers of aorta artery, Holzapfel et al. harvested thirteen hearts from ten men and three women within 24 hour of their death. A scalpel has been used in order to separate three main layers. After separating layers, uniaxial tensile tests with bidimensional measurements were performed with the aid computer controlled, screw-driven high-precision tensile testing machine. According to Holzapfel et al., the mean density of adventitia, media, and intima have been calculated dimensionless as 0.55±0.18, 0.25±0.09, 0.51±0.14 and the average stiffness have been calculated as 7.56±4.66 kPa, 1.27±0.63 kPa, 27.90±10.59 kPa respectively [22].

Fig. 3. FGM, single layered, and laminated models of aorta artery

In Fig. 3, different mechanical models of aorta artery have been demonstrated. Functionally graded material (FGM) and laminated composite materials have been chosen to be applied to aorta artery. As it can be seen in the middle, also single layered model have been demonstrated. In vivo, aorta artery is embedded in tissue and this tissue can be modeled as elastic matrix. In literature many paper can be found about static and dynamic analysis of beams and shells with composite materials [23-25].

3. Functionally Graded Materials (FGM)

Functionally graded materials (FGM) are relatively new advanced composite materials compared other composite materials. After the invasion of this composite materials, great deals of research have been made on the production and applications process of this new material concept. Functionally graded materials are characterized by gradually changed physical properties.

$$p = p_0\left[1 + \frac{p_{-1}}{T} + p_1 T + p_2 T^2 + p_3 T^3\right] \tag{1}$$

In Eq. (1) p_i are the coefficients of temperature defined in the unit of Kelvin and them are unique to the constituent materials.

$$p = \sum_{j=1}^{k} p_j V_f \tag{2}$$

In Eq. (2) p_j and V_f are the material property and volume fraction of the constituent material j, respectively. The sum of volume fraction can be stated as

$$\sum_{j=1}^{k} V_f = 1 \tag{3}$$

To adopt the aorta artery as functionally graded material, a shell model with uniform thickness can be used. The volume fraction of the shell can be stated as

$$V_f = \left(\frac{z}{h} + \frac{1}{2}\right)^N \tag{4}$$

The power-law exponent is defined by N. The material properties for a two-constituent functionally graded can be stated as [26]

$$E(z) = (E_1 - E_2)\left(\frac{z}{h} + \frac{1}{2}\right)^N + E_2 \tag{5}$$

$$v(z) = (v_1 - v_2)\left(\frac{z}{h} + \frac{1}{2}\right)^N + v_2 \tag{6}$$

$$\rho(z) = (\rho_1 - \rho_2)\left(\frac{z}{h} + \frac{1}{2}\right)^N + \rho_2 \tag{7}$$

4. Laminated Composite Materials

Laminated composite materials have attracted much attention due to their higher resistance, lighter weight when compared with traditional materials. Laminated composite materials have been widely used in aerospace industry, automotive industry and material engineering. Many researches have been published papers aimed to investigate the applications of laminated composite materials to shells, plates, and beams in case of static and dynamic analyses [27-35].
General equations of laminated composite materials can be stated as follows

$$\sigma_{i1} = \frac{E_{i1}}{1 - v_{i12}v_{i21}}(\varepsilon_{i1} + v_{i21}\varepsilon_{i12}) \tag{8}$$

$$\sigma_{i2} = \frac{E_{i2}}{1 - v_{i12}v_{i21}}(v_{i12}\varepsilon_{i1} + \varepsilon_{i2}) \tag{9}$$

$$\tau_{i12} = G_{i12}\gamma_{i12} = 2G_{i12}\varepsilon_{i12} \tag{10}$$

Where E_{i1} and E_{i2} are the Young's modulus in longitudinal "1" and transverse "2" direction respectively. On the other hand, v_{i12} is the Poisson's ratio for which strains are in longitudinal direction "1" and stress in transverse direction "2". Similarly, G_{i12} is the shear modulus.

Eqs. (8-10) can be written in matrix form as follows

$$\begin{Bmatrix} \sigma_1 \\ \sigma_2 \\ \tau_{12} \end{Bmatrix} = \begin{bmatrix} Q_{11} & Q_{12} & 0 \\ Q_{21} & Q_{22} & 0 \\ 0 & 0 & Q_{66} \end{bmatrix} \begin{Bmatrix} \varepsilon_1 \\ \varepsilon_2 \\ \gamma_{12} \end{Bmatrix} \tag{11}$$

By simplifying Eq. (11) we obtain

$$\{\sigma\} = [Q]\{\varepsilon\} \tag{12}$$

Where

$$Q_{11} = \frac{E_1}{1-v_{12}v_{21}} \tag{13}$$

$$Q_{12} = Q_{21} = v_{21}\frac{E_1}{1-v_{12}v_{21}} = v_{12}\frac{E_1}{1-v_{12}v_{21}} \tag{14}$$

$$Q_{22} = \frac{E_2}{1-v_{12}v_{21}} \tag{15}$$

$$Q_{66} = G_{12} \tag{16}$$

According to Betty-Maxwell theorem the Young's modulus and Poisson's ratios should fulfil the following equation

$$E_1 v_{21} = E_2 v_{12} \tag{17}$$

5. Concluding remarks

In present paper the most convenient mechanical model of aorta artery have been investigated. Two of most used composite materials types have been analyzed. Functionally graded materials and laminated composite materials models fundamental equations have been given. As it can be seen from Fig. 2, aorta artery has a layered structure which is composed of three main layers which consist of five sub-layers. Each layer has their own material properties (density, Young's modulus etc.). To conclude it is possible to say that aorta artery can be modelled by using laminated composite material theories. Three main layers can be adapted in laminated composite theories or to have more accurate result, five sub-layers can be adapted in laminated composite theories in order to investigate the mechanical behavior of aorta artery.

Acknowledgements

The financial support of the Scientific Research Projects Unit of Akdeniz University is gratefully acknowledged.

References

[1] Gozna, E.R., Marble, A.E., Shaw, A., Holland, J.G., Age-Related Changes in Mechanics of Aorta and Pulmonary-Artery of Man. *Journal of Applied Physiology*, 36(4), 407-411, 1974.

[2] Han, H.C., A biomechanical model of artery buckling. *Journal of Biomechanics*, 40(16), 3672-3678, 2007.

[3] Han, H.C., The Theoretical Foundation for Artery Buckling Under Internal Pressure. *Journal of Biomechanical Engineering-Transactions of the Asme*, 131(12), 2009.

[4] Lee, Y.U., Hayman, D., Sprague, E.A., Han, H.C., Effects of Axial Stretch on Cell Proliferation and Intimal Thickness in Arteries in Organ Culture. *Cellular and Molecular Bioengineering*, 3(3), 286-295, 2010.

[5] Lee, Y.U., Luo, J., Sprague, E., Han, H.C., Comparison of Artery Organ Culture and Co-culture Models for Studying Endothelial Cell Migration and Its Effect on Smooth Muscle Cell Proliferation and Migration. *Annals of Biomedical Engineering*, 38(3), 801-812, 2010.

[6] Datir, P., Lee, A.Y., Lamm, S.D., Han, H.C., Effects of Geometric Variations on the Buckling of Arteries. *International Journal of Applied Mechanics*, 3(2), 385-406, 2011.

[7] Hayman, D.M., Xiao, Y.M., Yao, Q.P., Jiang, Z.L., Lindsey, M.L., Han, H.C., Alterations in Pulse Pressure Affect Artery Function. *Cellular and Molecular Bioengineering*, 5(4), 474-487, 2012.

[8] Liu, Q., Han, H.C., Mechanical buckling of artery under pulsatile pressure. *Journal of Biomechanics*, 45(7), 1192-1198, 2012.

[9] Garcia, J.R., Lamm, S.D., Han, H.C., Twist buckling behavior of arteries. *Biomechanics and Modeling in Mechanobiology*, 12(5), 915-927, 2013.

[10] Han, H.C., Chesnutt, J.K.W., Garcia, J.R., Liu, Q., Wen, Q., Artery Buckling: New Phenotypes, Models, and Applications. *Annals of Biomedical Engineering*, 41(7), 1399-1410, 2013.

[11] Lee, A.Y., Sanyal, A., Xiao, Y.M., Shadfan, R., Han, H.C., Mechanical instability of normal and aneurysmal arteries. *Journal of Biomechanics*, 47(16), 3868-3875, 2014.

[12] Liu, Q., Wen, Q., Mottahedi, M., Han, H.C., Artery buckling analysis using a four-fiber wall model. *Journal of Biomechanics*, 47(11), 2790-2796, 2014.

[13] Xiao, Y.M., Hayman, D., Khalafvand, S.S., Lindsey, M.L., Han, H.C., Artery buckling stimulates cell proliferation and NF-kappa B signaling. *American Journal of Physiology-Heart and Circulatory Physiology*, 307(4), H542-H551, 2014.

[14] Zhang, J.Z., Liu, Q., Han, H.C., An In Vivo Rat Model of Artery Buckling for Studying Wall Remodeling. *Annals of Biomedical Engineering*, 42(8), 1658-1667, 2014.

[15] Khalafvand, S.S., Han, H.C., Stability of Carotid Artery Under Steady-State and Pulsatile Blood Flow: A Fluid-Structure Interaction Study. *Journal of Biomechanical Engineering-Transactions of the Asme*, 137(6), 2015.

[16] Luetkemeyer, C.M., James, R.H., Deuarakonda, S.T., Le, V.P., Liu, Q., Han, H.C., Wagenseil, J.E., Critical buckling pressure in mouse carotid arteries with altered elastic fibers. *Journal of the Mechanical Behavior of Biomedical Materials*, 46, 69-82, 2015.

[17] Qi, N., Gao, H., Ogden, R.W., Hill, N.A., Holzapfel, G.A., Han, H.C., Luo, X.Y., Investigation of the optimal collagen fibre orientation in human iliac arteries. *Journal of the Mechanical Behavior of Biomedical Materials*, 52, 108-119, 2015.

[18] Sanyal, A., Han, H.C., Artery buckling affects the mechanical stress in atherosclerotic plaques. *Biomedical Engineering Online*, 14, 2015.

[19] Fatemifar, F., Han, H.C., Effect of Axial Stretch on Lumen Collapse of Arteries. *Journal of Biomechanical Engineering-Transactions of the Asme*, 138(12), 2016.

[20] Mottahedi, M., Han, H.C., Artery buckling analysis using a two-layered wall model with collagen dispersion. *Journal of the Mechanical Behavior of Biomedical Materials*, 60, 515-524, 2016.

[21] Mercan, K., Civalek, Ö., A Simple Buckling Analysis of Aorta Artery. *International Journal of Engineering & Applied Sciences (IJEAS)*, 7(4), 34-44, 2016.

[22] Holzapfel, G.A., Sommer, G., Gasser, C.T., Regitnig, P., Determination of layer-specific mechanical properties of human coronary arteries with nonatherosclerotic intimal thickening and related constitutive modeling. *American Journal of Physiology-Heart and Circulatory Physiology*, 289(5), H2048-H2058, 2005.

[23] Mercan, K., Ersoy, H., Civalek, O., Free vibration of annular plates by discrete singular convolution and differential quadrature methods. *Journal of Applied and Computational Mechanics*, 2(3), 128-133, 2016.

[24] Demir, Ç., Akgöz, B., Erdinç, M.C., Mercan, K., Civalek, Ö., Elastik Bir Malzeme İle Temas Halinde Olan Grafen Tabakanin Titreşim Hesabi. *Gazi Üniversitesi Mühendislik-Mimarlık Fakültesi Dergisi*, 32(2), 2017.

[25] Mercan, K., Civalek, Ö., Buckling analysis of Silicon carbide nanotubes (SiCNTs) with surface effect and nonlocal elasticity using the method of HDQ. *Composites Part B: Engineering*, 114, 34-45, 2017.

[26] Loy, C.T., Lam, K.Y., Reddy, J.N., Vibration of functionally graded cylindrical shells. *International Journal of Mechanical Sciences*, 41(3), 309-324, 1999.

[27] Civalek, Ö., Demir, Ç., Akgöz, B., Static analysis of single walled carbon nanotubes (SWCNT) based on Eringen's nonlocal elasticity theory. *International Journal of Engineering and Applied Sciences*, 2(1), 47-56, 2009.

[28] Civalek, Ö., Korkmaz, A., Demir, Ç., Discrete singular convolution approach for buckling analysis of rectangular Kirchhoff plates subjected to compressive loads on two-opposite edges. *Advances in Engineering Software*, 41(4), 557-560, 2010.

[29] Gürses, M., Akgöz, B., Civalek, Ö., Mathematical modeling of vibration problem of nano-sized annular sector plates using the nonlocal continuum theory via eight-node discrete singular convolution transformation. *Applied Mathematics and Computation*, 219(6), 3226-3240, 2012.

[30] Akgöz, B., Civalek, Ö., A novel microstructure-dependent shear deformable beam model. *International Journal of Mechanical Sciences*, 99, 10-20, 2015.

[31] Demir, Ç., Civalek, Ö., Nonlocal Deflection Of Microtubules Under Point Load. *International Journal of Engineering and Applied Sciences*, 7(3), 33-39, 2015.

[32] Emsen, E., Mercan, K., Akgöz, B., Civalek, Ö., Modal analysis of tapered beam-column embedded in Winkler elastic foundation. *International Journal of Engineering & Applied Sciences*, 7(1), 25-35, 2015.

[33] Mercan, K., Demir, C., Akgöz, B., Civalek, Ö., Coordinate Transformation for Sector and Annular Sector Shaped Graphene Sheets on Silicone Matrix. *International Journal of Engineering & Applied Sciences (IJEAS)*, 7(2), 56-73, 2015.

[34] Demir, Ç., Civalek, Ö., Nonlocal Finite Element Formulation for Vibration. *International Journal of Engineering & Applied Sciences (IJEAS)*, 8(2), 109-117, 2016.

[35] Mercan, K., Civalek, Ö., Buckling Analysis of Silicon Carbide Nanotubes (SiCNTs). *International Journal of Engineering & Applied Sciences (IJEAS)*, 8(2), 101-108, 2016.

International Journal of Engineering & Applied Sciences (IJEAS)
Vol. 9, Issue 2 (Special Issue: Composite Structures) (2017) 147-155
http://dx.doi.org/10.24107/ijeas.322375
Int J Eng Appl Sci 9(2) (2017) 147-155

Stability of A Non-Homogenous Porous Plate by Using Generalized Differantial Quadrature Method

Şeref Doğuşcan AKBAŞ

Bursa Technical University, Department of Civil Engineering, Bursa, Turkey
E-mail address: serefda@yahoo.com

Received date: June 2017
Accepted Date: July 2017

Abstract

This paper presents stability analysis of a non-homogeneous plate with porosity effect. Material properties of the plate vary in the thickness direction and depend on the porosity. In the solution of the problem, the Generalized Differential Quadrature method is used. In the porosity model, uniform porosity distribution is considered. The effects of the porosity and material distribution parameters on the critical buckling of the non-homogeneous plate are investigated.

Keywords: *Non-Homogeneous Plate; Porosity; Generalized Differential Quadrature Method.*

1. Introduction

Non-homogeneous structures, namely functionally graded structures are a type of composites where the volume fraction of the materials constituents vary gradually, giving a non-uniform microstructure with continuously graded macro properties such as elasticity modulus, density, heat conductivity, etc.. Typically, in non-homogeneous structures, one face of a structural component is ceramic that can resist severe thermal corrosion effects and the other face is metal which has excellent structural strength.

Non-homogeneous structures have been an area of intensive research over the last decade. Because of the wide material variations and applications, it is important to study the static and dynamic analysis of Non-homogeneous structures, such as plates. Therefore, an intensive study has been conducted recently on vibration of structures made of FGMs (i.e., [1–42]).

In the literature, some studies about the porosity effect in the Non-homogeneous structures are; Wattanasakulpong and Ungbhakorn [43] investigated vibration analysis of porous FG beams. Mechab et al. [44,45] examined free vibration analysis of a FG nano-plate resting on elastic foundations with the porosities effect. Şimşek and Aydın [46] examined forced vibration of FG microplates with porosity effects based on the modified couple stress theory. Jahwari and Naguib [47] investigated FG viscoelastic porous plates with a higher order plate theory and statistical based model of cellular distribution. Vibration characteristics of FG beams with porosity effect and various thermal loadings are investigated by [48-49]. Linear/ nonlinear analysis of buckling and vibration of FG beams reinforced porous nanocomposite are investigated by Chen et al. [50] and Kitipornchai et al. [51]. Akbaş [52] investigated static and vibration of FG porous plates by using Navier solution.

Stability analysis of a simply supported non-homogeneous plate is investigated with porosity effect by using Generalized Differential Quadrature Method based on the classical plate theory. The effects of the porosity and material distribution parameters on the critical buckling loads of the non-homogeneous plate are examined.

2. Formulations

A simply supported rectangular non-homogeneous porous plate with thickness h in X_3 *direction*, the lengths of L_X and L_Y the in X_1 and X_2 directions, respectively as shown in Figure 1. The non-homogeneous plate is subjected to biaxial plane compressive loads N in both X_1 and X_2 directions, respectively.

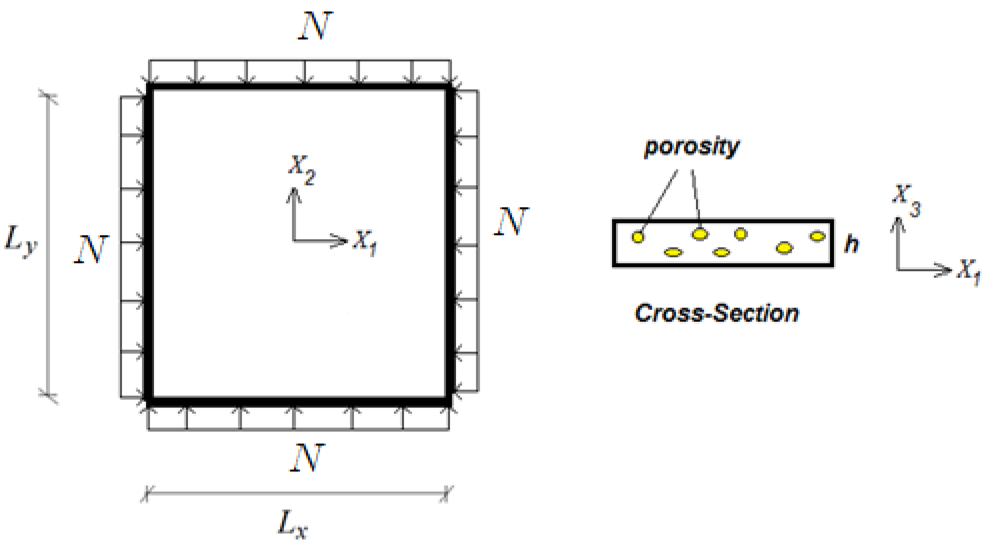

Fig. 1. A non-homogeneous plate subjected biaxial compressive loads with porosity.

The effective material properties of the non-homogeneous plate, P, such as, Young's modulus E, Poisson's ratio v, and shear modulus G vary continuously in the thickness direction (X_3 axis) according to a power-law function. In the porosity model, the porosity spread uniformly though height direction. According to the power law distribution, the effective material property with porosity can be expressed as follows:

$$P(X_3)=(P_T-P_B)\left(\frac{X_3}{h}+\frac{1}{2}\right)^k+P_B-(P_T+P_B)\frac{a}{2} \tag{1}$$

where a (a<<1) is the volume fraction of porosities. When a=0, the plate becomes perfect non-homogeneous plate.

According to classical plate theory, the strain- displacement relations are expressed as

$$\varepsilon_{X_1}=\frac{\partial u}{\partial X_1}=\varepsilon_{X_1}{}^0-X_3\frac{\partial^2 \mathrm{v}}{\partial X_1{}^2} \tag{2a}$$

$$\varepsilon_{X_2} = \frac{\partial v}{\partial X_2} = {\varepsilon_{X_2}}^0 - X_3 \frac{\partial^2 \mathrm{v}}{\partial {X_2}^2} \tag{2b}$$

$$\gamma_{X_1 X_2} = \frac{1}{2}\left({\varepsilon_{X_1 X_2}}^0 - \frac{\partial^2 \mathrm{v}}{\partial X_1 \partial X_2}\right) \tag{2c}$$

where u, v, w are X_1, X_2 and X_3 components of the displacements respectively. The constitutive equations of the non-homogeneous plate are as follows:

$$\sigma_{\mathrm{ij}}(X_{3,}a) = \frac{E(X_3,a)}{(1-\nu^2)}\left[\nu\varepsilon_{kl}\delta_{ij} + (1-\nu)\varepsilon_{ij}\right] \tag{3}$$

The stress resultants of the non-homogeneous plate are given as follows;

$$N_{ij} = \int_{-0.5h}^{0.5h} \sigma_{\mathrm{ij}}\, dX_3 \quad i = j,\ M_{ij} = \int_{-0.5h}^{0.5h} \sigma_{\mathrm{ij}}\, X_3\, dX_3,\ Q_{ij} = \int_{-0.5h}^{0.5h} \sigma_{\mathrm{ij}}\, dX_3 \quad i \neq j \tag{4}$$

where N_{ij}, M_{ij} and Q_{ij} are normal force, moment and shear forces, respectively. The stability equation of the non-homogeneous plate is given as follows:

$$\nabla^4 \nu - \frac{A_1(1-\nu^2)}{A_1 A_3 - {A_2}^2}\left({N_1}^0 \frac{\partial^2 \mathrm{v}}{\partial {X_1}^2} + {N_2}^0 \frac{\partial^2 \mathrm{v}}{\partial {X_2}^2}\right) = 0 \tag{5}$$

where ${N_1}^0$ and ${N_2}^0$ are the pre-buckling force resultants, A_1, A_2, A_3 are expressed as follows:

$$(A_1, A_2, A_3) = \int_{-0.5h}^{0.5h} E(X_3, a)(1, X_3, {X_3}^2)\, dX_3 \tag{6}$$

The boundary conditions at the simple supported plate ends are as follows;

$$v(X_1, 0) = v(L_X, 0) = w(0, X_2) = w(0, L_Y) = 0 \tag{7a}$$

$$M(X_1, 0) = M(L_X, X_2) = M(X_1, L_Y) = M(0, X_2) = 0 \tag{7b}$$

In the solution of the governing equations, the Generalized Differential Quadrature Method is used. In the differential quadrature method, the derivatives of a function are written as linear summation of the values at all points in the domain [53-56];

$$\frac{d^{(p)} w(x_j)}{dx^{(p)}} \approx \sum_{i=1}^{n} B_{ji}^{(p)}\, w(x_i) \tag{8}$$

where n is the number of the points in the domain, p is the order of derivative in the function, $B_{ji}^{(p)}$ is the weighting coefficient with pth derivative of the function with respect to x. The weight coefficients for first-order derivative (p=1) are as follows [53,54];

$$B_{ji}^{(1)} = \begin{cases} \dfrac{\prod_{j=1}^{n}(x_j - x_i)}{(x - x_j)\prod_{j=1}^{n}(x_i - x_j)} & i \neq j \\ -\sum_{j=1, i\neq j}^{n} B_{ji}^{(1)} & i = j \end{cases} \tag{9}$$

For the higher order derivatives, the weight coefficient is expressed as follows:

$$B_{ji}^{(p)} = \sum_{r=1}^{n} B_{jr}^{(1)} B_{ri}^{(p-1)} \quad (i,j=1,n) \tag{10}$$

For determined the sampling points in the domain, Chebyshev–Gauss–Lobatto grid points is employed[53,54];

$$x_j = \frac{1}{2}\left[1 - cos\left(\frac{j-1}{n-1}\pi\right)\right] \quad (j=1,n_{x1}) \tag{11a}$$

$$x_i = \frac{1}{2}\left[1 - cos\left(\frac{i-1}{n-1}\pi\right)\right] \quad (i=1,n_{x2}) \tag{11b}$$

where n_{x1} and n_{x2} are the number of the grid points in X_1 and X_2 direction, respectively.

Substituting eqs. (8-11) into eq. (5), and then using Generalized Differential Quadrature discretization, the governing equations of the problem can be obtained as follows;

$$\left(\sum_{k=1}^{n_{x1}} B_{jk}^{(4)} v_{kj} + 2\sum_{k=1}^{n_{x1}}\sum_{m=1}^{n_{x2}} B_{jk}^{(2)} B_{im}^{(2)} v_{km} + \sum_{k=1}^{n_{x2}} B_{ik}^{(4)} v_{ki}\right) - \frac{A_1(1-\nu^2)}{A_1A_3-{A_2}^2}\left({N_1}^0 \sum_{k=1}^{n_{x1}} B_{jk}^{(2)} v_{kj} + {N_2}^0 \sum_{k=1}^{n_{x2}} B_{ik}^{(2)} v_{ki}\right) = 0 \quad (j=1,n_{x1}),\ (i=1,n_{x2}),\ (k=1,p+1) \tag{12}$$

The dimensionless critical buckling load can be expressed as follows;

$$\bar{N}_{\mathrm{cr}} = N_{cr}\frac{L_X^2}{E_B\,h^3} \tag{13}$$

3. Numerical Results

In the numerical results, the dimensionless critical buckling loads $\bar{N}_{\mathrm{cr}}$ are presented in figures for different porosity parameters and material distributions. The rectangular non-homogeneous porous plate considered in numerical examples is made of Zirconia (E=151*GPa*, ν=0.3) and Steel (E=210*GPa*, ν=0.3). The top surface material of the non-homogeneous plate is Zirconia, the bottom surface material of the non-homogeneous plate is Steel. When k=0 and k=∞, the material of the plate gets homogeneous Zirconia and homogeneous Steel, respectively, according to Eq. (1). The dimensions of the non-homogeneous plate are considered as follows: h = 0.2 *m*, L_X =3 *m*, L_Y=3 *m* in the numerical examples. In the numerical calculations, the numbers of the grid points are taken as n_{x1}=n_{x2}=20.

In figure 2, the effect of the material distribution parameter k on the dimensionless critical buckling loads of the porous non-homogeneous plate is presented for a=0. As seen from figure 2, the dimensionless critical buckling loads increase with increase in the power-law exponents k. With increase in the k, the plate gets to fully Steel. The Young's modulus of Steel is bigger than Zirconia's. As it is expected, with increase the k, the Young's modulus and bending rigidity of the plate increase according to equation (1). So, the strength of material increases and the critical buckling loads increases naturally.

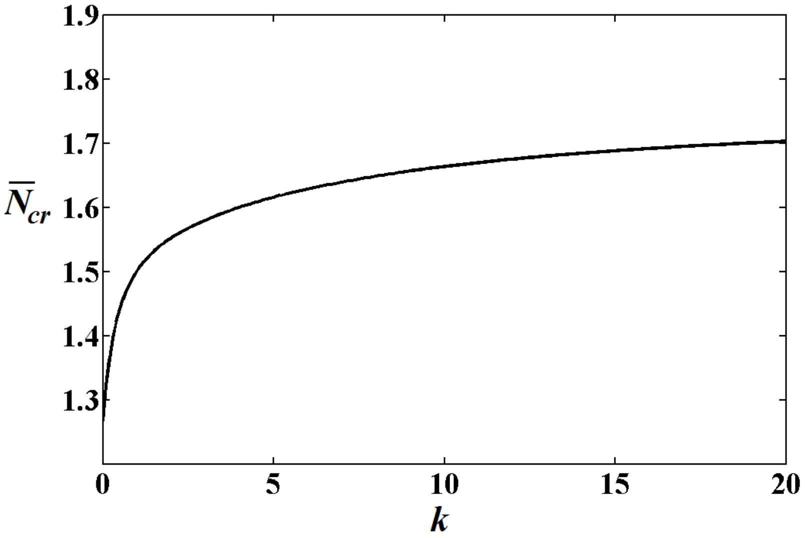

Fig. 2. The effect of the material distribution parameter *k* on the dimensionless critical buckling loads $\overline{N}_{\text{cr}}$.

Figure 3 displays the relationship between of porosity parameter *a* and the dimensionless critical buckling loads of the non-homogeneous porous plate for different the material distribution parameters. It is seen from figure 3 that the dimensionless critical buckling loads decrease with increase with increase porosity parameter *a*. This is because, with increase in the porosity, the strength of the material decreases. So, the critical buckling loads decreases naturally. It shows that Porosity parameters play an important role on the stability of the non-homogeneous porous plates.

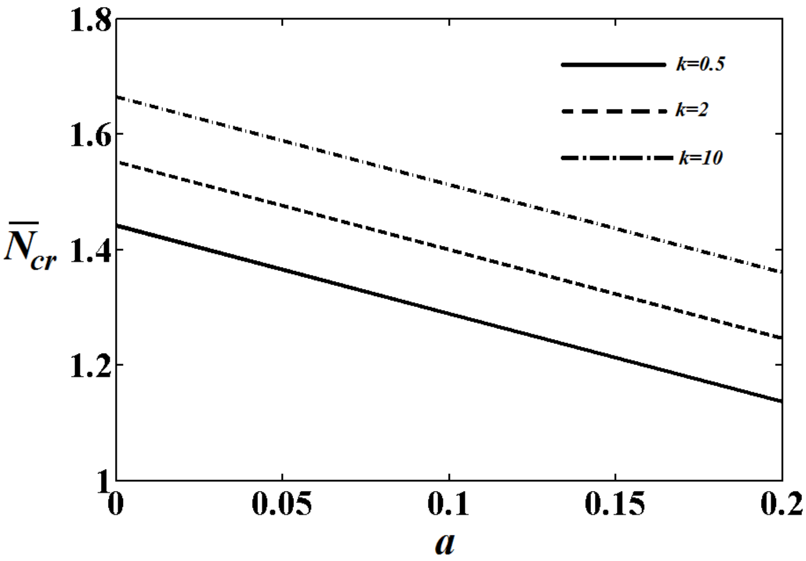

Fig. 3. The effect of the porosity parameter *a* on the dimensionless critical buckling loads $\overline{N}_{\text{cr}}$ for different the material distribution parameters.

4. Conclusions

In this paper, stability analysis of a simply supported porous non-homogeneous plate is studied by using Generalized Differential Quadrature Method. Material properties of the plate depend on both position and porosity. The Classical plate theory is used in the kinematic model of the plate. The effects of the porosity and material distribution parameters on the critical buckling loads of the non-homogeneous plate are presented in figures. Numerical results show that the porosity has important role on the stability of the non-homogeneous plate.

References

[1] Reddy, J.N., and Chin, C.D., Thermomechanical analysis of functionally graded cylinders and plates, *Journal of Thermal Stresses*, 21, 6,.593-626, 1998.
[2] Reddy, J.N., Analysis of functionally graded plates, *International Journal for Numerical Methods in Engineering*, 47, 1-3, 663-684, 2000.
[3] Yanga, J. and Shen, H.S., Non-linear analysis of functionally graded plates under transverse and in-plane loads, *International Journal of Non-Linear Mechanics*, 38, 4, 467-482,2003.
[4] Lanhe, Wu., Thermal buckling of a simply supported moderately thick rectangular FGM plate, *Composite Structures*, 64, 2, 211-218,2004.
[5] Abrate, S., Free vibration, buckling, and static deflections of functionally graded plates, *Composites Science and Technology*, 66, 14, 2383-2394,2006.
[6] Chi, S.H. and Chung, Y.L., Mechanical behavior of functionally graded material plates under transverse load—Part I: Analysis, *International Journal of Solids and Structures*, 43, 13, 3657-3674, 2006.
[7] Samsam Shariat, B.A. and Eslami M.R., Buckling of thick functionally graded plates under mechanical and thermal loads, Composite Structures, 78, 3, 433-439,2007.
[8] Zhao, X., Lee, Y.Y. and Liew, K.M., Mechanical and thermal buckling analysis of functionally graded plates, *Composite Structures*, 90, 2, 161-171,2009.
[9] Akbaş, Ş.D., Static analysis of a functionally graded beam with edge cracks on elastic foundation, *Proceedings of the 9 th International Fracture Conference*, Istanbul, Turkey, 2011.
[10] Zhao, X., Lee, Y. Y. and Liew, K. M., Free vibration analysis of functionally graded plates using the element-free *kp*-Ritz method, *Journal of sound and Vibration*, 319, 3, 918-939,2009.
[11] Mohammadi, M., Saidi, A.R. and Jomehzadeh, E., Levy solution for buckling analysis of functionally graded rectangular plates, *Applied Composite Materials*, 17, 2, 81-93,2010.
[12] Fereidoon, A., Asghardokht Seyedmahalle, M. and Mohyeddin, A., Bending analysis of thin functionally graded plates using generalized differential quadrature method, *Archive of Applied Mechanics*, 81, 11, 1523-1539,2011.
[13] Akbaş, Ş.D. and Kocatürk, T., Post-buckling analysis of a simply supported beam under uniform thermal loading, *Scientific Research and Essays*, *6*,5, 1135-1142, 2011.
[14] Civalek, Ö., Korkmaz, A. and Demir,C., Discrete singular convolution approach for buckling analysis of rectangular Kirchhoff plates subjected to compressive loads on two-opposite edges, *Advances in Engineering Software*, 41, 4, 557-560, 2010.
[15] Kocatürk, T. and Akbas, Ş.D., Post-buckling analysis of Timoshenko beams with various boundary conditions under non-uniform thermal loading, *Structural Engineering and Mechanics*, *40*,3,, 347-371, 2011.
[16] Kocatürk, T., Eskin ,A. and Akbaş Ş.D. Wave propagation in a piecewise homegenous cantilever beam under impact force, *International Journal of Physical Sciences*, *6*, 16, 3867-3874, 2011.

[17] Kumar, J.S., Reddy, B.S., Reddy, C.E. and Reddy, K.V.K., Higher order theory for free vibration analysis of functionally graded material plates, *ARPN J Eng Appl Sci*, 6, 10, 105-111,2011.
[18] Jadhav, P.A. and Bajoria, K.M., Buckling of piezoelectric functionally graded plate subjected to electro-mechanical loading, *Smart Materials and Structures*, 21,.10, 105005,2012.
[19] Akbaş, Ş.D. Free vibration characteristics of edge cracked functionally graded beams by using finite element method. *International Journal of Engineering Trends and Technology, 4*(10), 4590-4597,2013.
[20] Singh, J. and Shukla, K.K., Nonlinear flexural analysis of functionally graded plates under different loadings using RBF based meshless method, *Engineering Analysis with Boundary Elements*, 36, 12, 1819-1827,2012.
[21] Kocatürk and Akbas, Ş.D., Thermal post-buckling analysis of functionally graded beams with temperature-dependent physical properties. *Steel and Composite Structures, 15,* 5, 481-505, 2013.
[22] Daouadji, T.H., Tounsi and Adda Bedia, E-A., Analytical solution for bending analysis of functionally graded plates, *Scientia Iranica,* 20, 3, 516-523, 2013.
[23] Akbaş, Ş.D.. Geometrically nonlinear static analysis of edge cracked Timoshenko beams composed of functionally graded material*, Mathematical Problems in Engineering*, 2013, 201*3.*
[24] Asemi, K. and Shariyat, M., Highly accurate nonlinear three-dimensional finite element elasticity approach for biaxial buckling of rectangular anisotropic FGM plates with general orthotropy directions, *Composite Structures*, 106, 235-249,2013.
[25] Akbaş, Ş. D. and Kocatürk, T., Post-buckling analysis of functionally graded three-dimensional beams under the influence of temperature. *Journal of Thermal Stresses*, 36, 12, 1233-1254, 2013.
[26] Czechowski, L. and Kowal-Michalska, K., Static and dynamic buckling of rectangular functionally graded plates subjected to thermal loading, *Strength of Materials*, 45, 6, 666-673,2013.
[27] Kocatürk, T. and Akbas, Ş.D., Post-buckling analysis of Timoshenko beams made of functionally graded material under thermal loading*, Structural Engineering and Mechanics*, 41,6, 775-789, 2012.
[28] Tahouneh, V., Free vibration analysis of thick CGFR annular sector plates resting on elastic foundations, *Structural Engineering and Mechanics*, 50, 6, 773-796, 2013.
[29] Akbaş, Ş.D., Free vibration of axially functionally graded beams in thermal environment, *International Journal of Engineering and Applied Sciences,* 6(3), 37-51, 2014.
[30] Swaminathan, K., and Naveenkumar, D.T., Assessment of First Order Computational Model for Free Vibration Analysis of FGM Plates, *International Journal of Scientific and Engineering Research*, 4, 5, 115-118, 2013.
[31] Van Long, N., Quoc, T.H. and Tu, T.M., "Bending and free vibration analysis of functionally graded plates using new eight-unknown shear deformation theory by finite-element method", International Journal of Advanced Structural Engineering, vol. 8., No.4, pp.391-399, 2016.
[32] Akbaş, Ş.D., Free vibration and bending of functionally graded beams resting on elastic foundation, *Research on Engineering Structures and Materials,* 1,1, 2015.
[33] Akbaş, Ş.D. On Post-Buckling Behavior of Edge Cracked Functionally Graded Beams Under Axial Loads. *International Journal of Structural Stability and Dynamics*, 15, 4, 1450065, 2015
[34] Akbaş, Ş.D., Post-buckling analysis of axially functionally graded three-dimensional beams. *International Journal of Applied Mechanics, 7,* 3, 1550047, 2015.
[35] Civalek, Ö., Free vibration of carbon nanotubes reinforced (CNTR) and functionally graded shells and plates based on FSDT via discrete singular convolution method, *Composites Part B: Engineering*, 111, 45-59, 2017.

[36] Civalek, Ö. (2017). Buckling analysis of composite panels and shells with different material properties by discrete singular convolution (DSC) method. *Composite Structures*, 161, 93-110, 2017.

[37] Mercan, K., Ersoy, H. and Civalek, Ö., Free vibration of annular plates by discrete singular convolution and differential quadrature methods. *Journal of Applied and Computational Mechanics, 2,*3, 128-133, 2016.

[38] Akbaş, Ş.D., Free vibration of edge cracked functionally graded microscale beams based on the modified couple stress theory, *International Journal of Structural Stability and Dynamics*, 1750033, 2016.

[39] Barati, M.R. and Zenkour, A.M., Electro-thermoelastic vibration of plates made of porous fuctionally graded piezoelectric materials under various boundary conditions, *Journal of Vibration and Control*, doi: 10.1177/1077546316672788, 2016.

[40] Akbaş, Ş.D. (2016). Static Analysis of a Nano Plate by Using Generalized Differential Quadrature Method, *International Journal of Engineering and Applied Sciences, 8,* 2, 30-39, 2016.

[41] Mercan,K., Demir, Ç. And Civalek, Ö., Vibration analysis of FG cylindrical shells with power-law index using discrete singular convolution technique, *Curved and Layered Structures*, 3, 1, 2016.

[42] Akbaş, Ş.D. (2016). Wave propagation in edge cracked functionally graded beams under impact force, *Journal of Vibration and Control, 22,* 10, 2443-2457,2016.

[43] Wattanasakulpong, N. and Ungbhakorn, V.,Linear and nonlinear vibration analysis of elastically restrained ends FGM beams with porosities, *Aerospace Science and Technology*, 32, 1, 111-120, 2014.

[44] Mechab, I., Mechab, B., Benaissa, S., Serier, B., Bouiadjra, B.B., Free vibration analysis of FGM nanoplate with porosities resting on Winkler Pasternak elastic foundations based on two-variable refined plate theories, *Journal of the Brazilian Society of Mechanical Sciences and Engineering*, 38, 8, 2193–2211, 2016.

[45] Mechab, B., Mechab, I., Benaissa, S., Ameri, M. and Serier, B., Probabilistic analysis of effect of the porosities in functionally graded material nanoplate resting on Winkler–Pasternak elastic foundations, *Applied Mathematical Modelling*, 40, 2, 738-749, 2016.

[46] Şimşek, M. and Aydın, M., Size-dependent forced vibration of an imperfect functionally graded (FG) microplate with porosities subjected to a moving load using the modified couple stress theory, *Composite Structures*, 160, 408-421, 2017.

[47] Al Jahwari, F. and Naguib, H.E., Analysis and homogenization of functionally graded viscoelastic porous structures with a higher order plate theory and statistical based model of cellular distribution, *Applied Mathematical Modelling*, 40, 3, 2190-2205, 2016.

[48] Ebrahimi,F. and Jafari, A., A Higher-Order Thermomechanical Vibration Analysis of Temperature-Dependent FGM Beams with Porosities, *Journal of Engineering*, doi:10.1155/2016/9561504, 2016.

[49] Ebrahimi, F., Ghasemi, F. and Salari, E., Investigating thermal effects on vibration behavior of temperature-dependent compositionally graded Euler beams with porosities, *Meccanica*, 51, 1, 223-249, 2016.

[50] Chen, D., Yang, J. and Kitipornchai, S., Nonlinear vibration and postbuckling of functionally graded graphene reinforced porous nanocomposite beams, *Composites Science and Technology*, 142, 235-245, 2017.

[51] Kitipornchai, S., Chen, D. and Yang, J., Free vibration and elastic buckling of functionally graded porous beams reinforced by graphene platelets, *Materials&Design*, 116, 656-665, 2017.

[52] Akbaş, Ş.D., Vibration and Static Analysis of Functionally Graded Porous Plates, Doi: 10.22055/jacm.2017.21540.1107, *Journal of Applied and Computational Mechanics*, 2017.

[53] Shu, C. and Du, H., Implementation of clamped and simply supported boundary conditions in the GDQ free vibration analysis of beams and plates, *Int. J. Solids Struct.* 34, 819–835, 1997.
[54] Shu, C., Differential Quadrature and its Application in Engineering, Springer, 2000.
[55] Chen, C.N., Discrete element analysis methods of generic differential quadrature, Lecture Notes in Applied and Computational Mechanics, vol. 25, Springer, 2006.
[56] Quan, J.R. and Chang, C.T. New insights in solving distributed system equations by the quadrature methods, *Comput. Chem. Eng*. 13, 779–788, 1989.

International Journal of Engineering & Applied Sciences (IJEAS)
Vol.9, Issue 2 (Special Issue: Composite Structures) (2017) 156-168
http://dx.doi.org/10.24107/ijeas.323633
Int J Eng Appl Sci 9(2) (2017) 156-168

Optimum Design of Composite Corrugated Web Beams Using Hunting Search Algorithm

Ferhat Erdal[1], Osman Tunca[2], Erkan Doğan[3]*

[1]Akdeniz University, Civil Engineering Department, Antalya, Turkey*
[2]Karamanoğlu Mehmetbey University, Dep. of Civil Engineering, Karaman, Turkey
[3]Celal Bayar University, Department of Civil Engineering, Manisa, Turkey
[*]E-mail address: eferhat@akdeniz.edu.tr

Received date: June 2017
Accepted Date: July 2017

Abstract

Over the past few years there has been sustainable development in the steel and composite construction technology. One of the recent additions to such developments is the I-girders with corrugated web beams. The use of these new generation beams results in a range of benefits, including flexible, free internal spaces and reduced foundation costs. Corrugated web beams are built-up girders with a thin-walled, corrugated web and wide plate flanges. The thin corrugated web affords a significant weight reduction of these beams, compared with hot-rolled or welded ones. In this paper, optimum design of corrugated composite beams is presented. A recent stochastic optimization algorithm coded that is based on hunting search is used for obtaining the solution of the design problem. In the optimization process, besides the thickness of concrete slab and studs, web height and thickness, distance between the peaks of the two curves, the width and thickness of flange are considered as design variables. The design constraints are respectively implemented from BS EN1993-1:2005 (Annex-D, Eurocode 3) BS-8110 and DIN 18-800 Teil-1. Furthermore, these selections are also carried out such that the design limitations are satisfied and the weight of the composite corrugated web beam is the minimum.

Keywords: Composite structures; corrugated beams; optimum design; structural optimization; stochastic search methods; hunting search algorithm.

1. Introduction

The use of long span steel beams results in a range of benefits, including flexible, free internal spaces and reduced foundation costs. Many large clear-span design solutions are also well adapted to simplify the integration of mechanical or utility services. Corrugated steel web beams provide economical solution and pleasing appearance for space structures. In steel construction applications, the web part of beam usually carries the compressive stress and transmits shear in the beam while the flanges support the applied external loads. By using greater part of the material for the flanges and thinner web, materials saving could be achieved without weakening the load-carrying capability of the beam. In this case, the compressive stress in the web has exceeded the critical point prior to the occurrence of yielding, the flat web loses its stability and deforms transversely. Corrugated web beams shown in Figure 1 are built-up girders with a thin-walled, corrugated web and plate flanges.

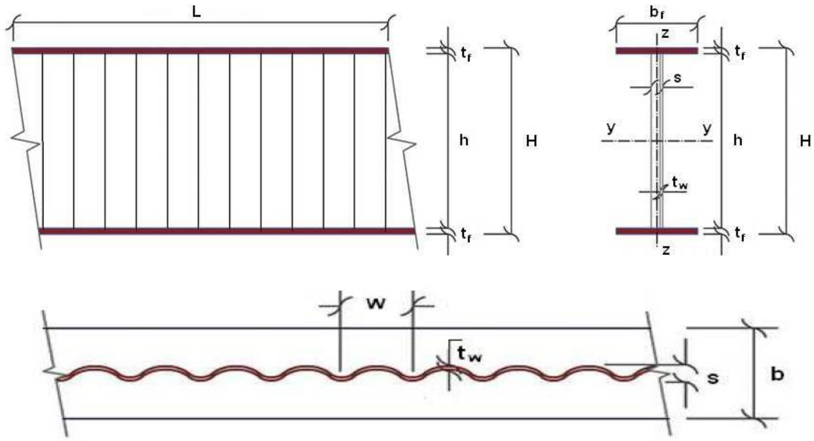

Fig. 1 Geometric properties of Corrugated Web Beam

Corrugated structure of the web cross-section not only increases the resistance of the beam against to shear force and other possible local effects, but also prevents the buckling due to loss of moment of inertia before the plastic limit. This specific structure of the web leads to a decrease in the beam unit weight and increase in the load carrying capacity. These efficient construction materials, commonly used in developed countries over years, can be utilized at the roofs as an alternative to space truss and roof truss, at the slabs as floor beams or columns under axial force. Although the designers are aware of the advantages of the composite systems to be produced with that beams, there is still not a detailed technical specification about their design and behavior. The first studies on the corrugated web beams were focused on the vertically trapezoidal corrugation. Elgaaly investigated the failure mechanisms of trapezoidal corrugation beams under different loading conditions, namely shear mode [1], bending mode [2]. They found that the web could be neglected in the beam bending design calculation due to its insignificant contribution to the beam's load-carrying capability. Besides that, the two distinct modes of failure under the effect of patch loading were dependent on the loading position and the corrugation parameters. These are found agreeable to the investigation by Johnson and Cafolla and were further discussed in their writings [3]. In addition, the experimental tests conducted by Li et al. [4] demonstrated that the corrugated web beam has 2 times higher buckling resistance than the plane web type. According to Pasternak et al., [5], the buckling resistance of presently used sinusoidal corrugated webs is comparable with plane webs.

In the present study, the ultimate load carrying capacities of optimally designed steel corrugated web beams are tested in a self-reacting frame to perform critical loads for all tested specimens. For this purpose, six corrugated beams are tested in a self-reacting frame to determine the ultimate load carrying capacities of mentioned beams under different loading conditions. The tested specimens are designed by using one of the stochastic search techniques called hunting search optimization method. This meta-heuristic algorithm is successfully applied to the optimum design problems of steel cellular beams where the design constraints are implemented from BS EN1993-1:2005 (Annex-D, Eurocode 3) BS-8110 and DIN 18-800 Teil-1 provisions [6-10]. In this formulation, the thickness of concrete slab and studs, web height and thickness, distance between the peaks of the two curves, the width and thickness of flange in the composite corrugated web beams are considered as design variables. The computational steps of the optimization algorithm and the design process are not demonstrated in the paper due to space limitations, yet the detailed implementation specifics of the hunting search method and optimum design process of corrugated web beams can be found in Erdal et al. [11] with parameter sets.

2. The Design of Composite Corrugated Web Beams

The ultimate state design of a steel beam necessitates check of its strength and serviceability. The computation of the strength of a corrugated web beam is determined by considering the interaction of flexure and shear at the sinusoidal web. Consequently, the constraints to be considered in the design of a corrugated web beam include the displacement limitations, transverse force load carrying capacity of webs, normal force load carrying capacity of flanges, lateral torsional buckling capacity of the entire span, rupture of the welded joint, formation of a flexure mechanism and practical restrictions for corrugated web and flanges [9-11].

2.1. Stochastic Optimization Techniques

A combinatorial optimization problem requires exhaustive search and effort to determine an optimum solution which is computationally expensive and in some cases may even not be practically possible. Meta-heuristic search techniques are established to make this search within computationally acceptable time period. Amongst these techniques are simulated annealing [12], evolution strategies [13], particle swarm optimizer [14], tabu search method [15], ant colony optimization [16], harmony search method [17], genetic algorithms [18] and others [19-22]. All of these techniques implement particular meta-heuristic search algorithms that are developed based on simulation of a natural phenomenon into numerical optimization procedure. They have gained a worldwide popularity recently and have proved to be quite robust and effective methods for finding solutions to discrete programming problems in many disciplines of science and engineering, including structural optimization.

2.1.1. Hunting Search Algorithm

Hunting search method based optimum design algorithm has six basic steps, which is outlined in the following [23-24].

Step 1 Initializing design algorithm and parameters: *HGS* defines the group size which is the number of solution vectors in hunting group, *MML* represents the maximum movement toward the leader and *HGCR* is hunting group consideration rate which varies between 0 and 1.

Step 2 Generation of hunting group: On the basis of the number of hunters (*HGS*), hunting group is initialized by selecting randomly sequence number of steel sections (I_i) for each group.

$$I_i = INT\left[I_{min} + r\left(I_{max} - I_{min}\right)\right] \quad i = 1,....,n \tag{1}$$

where; the term *r* represents a random number between 0 and 1, I_{min} is equal to 1 and I_{max} is the total number of values in the discrete set respectively. *n* is the total number of design variables.

Step 3 Moving toward the leader: New hunters' positions are generated by moving toward the leader hunter.

$$I_i^{'} = I_i + r\ MML\left(I_i^L - I_i\right) \qquad i = 1,....,n \tag{2}$$

where; I_i^{L} is the position value of the leader for the *i-th* variable.

Step 4 Position correction-cooperation between hunters: After moving toward the leader, hunters tend to choose another position to conduct the `hunt' efficiently, i.e. better solutions. Position correction is performed in two ways, one of which is real value correction and the other is digital value. In this study, real value correction is employed for the position correction of hunters.

$$I_i^{j'} \leftarrow \begin{cases} I_i^{j'} \in \left\{I_i^1, I_i^2, ..., I_i^{HGS}\right\} & \textit{with probability HGCR} \\ INT\ (I_i^{j'} = I_i \pm Ra) & \textit{with probability (1-HGCR)} \end{cases} \tag{3}$$

Step 5 Reorganizing the hunting group: Hunters must reorganize themselves to get another chance to find the global optimum. If the difference between the objective function values obtained by the leader and the worst hunter in the group becomes smaller than a predetermined constant (ε_1) and the termination criterion is not satisfied, then the group reorganized. By employing the Eq. 6, leader keeps its position and the others randomly select positions.

$$I_i^{'} = I_i^L \pm r\left(\max(I_i) - \min(I_i)\right)\alpha\ (-\beta\ EN) \tag{4}$$

Where; I_i^{L} is the position value of the leader for the *i-th* variable, *r* represents the random number between 0 and 1, $min(I_i)$ and $max(I_i)$ are min. and max. values of variable I_i, respectively, *EN* refers to the number of times that the hunting group has trapped until this step. α and β are determine the convergence rate of the algorithm.

Step 6 Termination: The steps 3 and 5 are repeated until a pre-assigned maximum number of cycles is reached.

3. Optimum Design Problem

The design of a composite corrugated web beam requires the selection of width and thickness of a plate from which the corrugated web is to be produced, distance between the peak points of each corrugate, the length of corrugate web, the selection of width and thickness of a plate for upper and lower flanges in the beam, thickness of the concrete slab and connection members between the concrete slab and corrugated beam are considered as design variables. For this purpose, a design pool is prepared. The optimum design problem formulated considering the design constraints explained in the previous sections yields the following mathematical model [6-11]. Find a integer design vector $\{I\} = \{I_1, I_2, I_3, I_{4,}, I_5, I_6, I_7\}^T$ where I_1 is the sequence number of for the width of upper and lower flanges, I_2 is the sequence number for the thickness values of upper and lower flanges, I_3 is the thickness of corrugated web, I_4 is distance between the peak points of each corrugate web and I_5 the height of corrugate web, I_6 thickness of the concrete slab and I_7 is the connection members between the concrete slab and corrugated beam. Hence the design problem turns out to be minimize the weight of the composite corrugated web beam (W_{kom}).

$$W_{kom} = \rho_s \left(\left(2 \times b_f \times t_f \times L \right) + \left(h \times t_w \times L_{düz} \right) \right) + \rho_{bet} \left[A_{bet} L + \left(A_{stu} N_{stu} \right) \right] \qquad (5)$$

where, ρ_s density of steel, b_f the width of flange, t_f thickness of flange, L span of beam, h height of corrugated web, t_w thickness of corrugated web ve $L_{düz}$ span of beam before corrugation process. ρ_{bet} the density of concrete class, A_{bet} the section area of the concrete slab, A_{stu} the net section are of connection members between the concrete slab and corrugated beam and N_{stu} the number of connection members between the concrete slab and corrugated beam along beam span. The demonstration of composite corrugated web beams under loading conditions is given in Figure 2 with more detail.

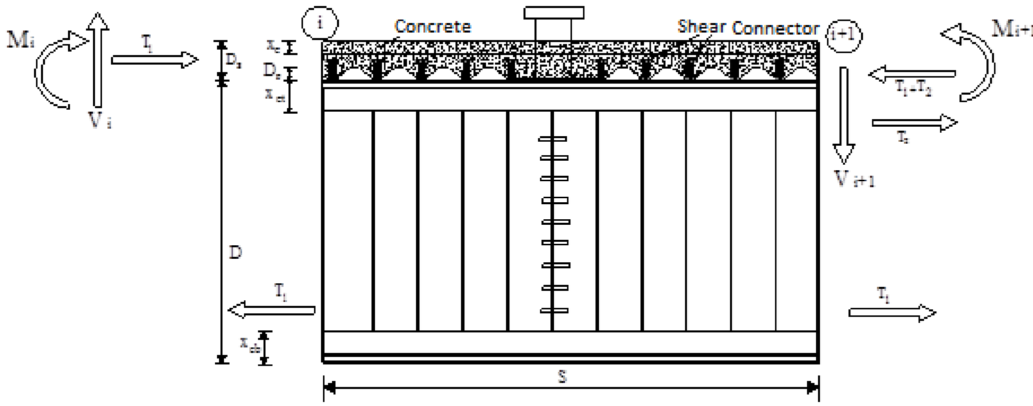

Fig. 2. The demonstration of Composite Corrugated Web Beam

Design of a corrugated beam requires the satisfaction of some geometrical restrictions that are formulated through Eqns. (6-9).

Web dimensions:

$$333\ mm \leq h \leq 1500\ mm \quad (6) \qquad 1.5\ mm \leq t_w \leq 5.0\ mm \quad (7)$$

Flange dimensions:

$$120\ mm \leq b_f \leq 450\ mm \quad (8) \qquad 6.0\ mm \leq t_f \leq 30.0\ mm \quad (9)$$

3.1. Transverse load carrying capacity of corrugated webs

Based upon the experimental tests and finite element analysis results, the following design procedure has been suggested: The corrugated web is regarded as an orthotropic plate with rigidities D*x* and D*y*. According to [5], the following formula therefore applies to the corrugated web:

$$D_x = \frac{E \times w \times t^3}{12 \times s},\ D_y = \frac{E \times I_y}{w} \text{ for } D_x \leq D_y \tag{10}$$

For transverse buckling stress of corrugated web;

$$\tau_{EG} = \frac{162}{5 \times t_w \times h^2} \sqrt{(D_x \times D_y^3)} \tag{11}$$

For slenderness parameter of corrugated web;

$$\lambda_{GN} = \sqrt{\frac{f_y}{\sqrt{3} \times \tau_{EG}}} \tag{12}$$

With the buckling coefficient of corrugated web;

$$K_B = \frac{1}{(\lambda_{GN})^{3/2}} \tag{13}$$

the transverse force load carrying capacity for the corrugated web finally results in:

$$V_{TK-MAX} = \frac{K_B \times f_y \times h \times t_w}{\sqrt{3}} \tag{14}$$

3.2. Normal load carrying capacity of flanges

In determining the normal bearing force of the flanges, a distinction must be made between tensile and compressive stresses. In the case of tensile stress, the load carrying capacity of the flange is derived as follows:

$$\sigma_{ALLOW} = \frac{N_{T-MAX}}{b_f \times t_f} \tag{15}$$

Reformulation of the expression for ψ = 1 leads to the following elastic limit stress:

$$\sigma_{EL} = \frac{4000}{\left(b_f \times t_f\right)^2} \tag{16}$$

Therefore the reduced normal force on the flange:

$$N_{NORMAL} = \sigma_{EL} \times b_f \times t_f \tag{17}$$

Global failure of stability - lateral buckling of the flange - is equivalent to the verification against torsional-flexural buckling. If the restraining effect of the web is ignored, the torsional-flexural verification is carried out as the buckling verification for the "isolated" flange in accordance with [5]. The following condition for the distance between lateral supports is obtained:

$$\tau_{EG} = \frac{\pi}{4\sqrt{3}} \sqrt{E \times f_y} \times \frac{b_f^2 \times t_f}{k_c \times c} \tag{18}$$

3.3. Behavioral and Geometrical Restrictions of Composite Beam

The moment capacity of composite corrugated web beam with sinusoidal web function (M_{RD}) has been defined as following equations.

For the neutral axis on concrete slab;

$$T_{AD} = A \times \frac{f_y}{\gamma_a} \qquad \text{and} \qquad a = \frac{T_{AD} \times \gamma_c}{0.85 \times f_{ck} \times b_c} \tag{19}$$

$$M_{RD} = T_{AD} \times (d_1 + h_F + t_c - a/2) \tag{20}$$

For the neutral axis on steel profile;

$$C_{CD} = 0.85 \times \frac{f_{ck}}{\gamma_c} b_c \times t_c \qquad \text{and} \qquad C_{ad} = \frac{1}{2} \times (T_{AD} - C_{CD}) \tag{21}$$

$$M_{RD} = C_{AD} \times (d - y_t - y_c) + C_{CD}((t_c/2) + h_f + d - y_t) \tag{22}$$

In these equations, d height of steel section, d_1 distance between the centre of steel section and upper part, y_c distance between the centre of pressure region of steel section and upper part, y_t distance between the centre of tension region of steel section and lower part, t_c height of concrete slab, b_c effective slab width, h_F height of steel deck, f_y yield strength of steel, f_{ck} compressive strength of concrete, γ_a and γ_c are coefficients for steel and concrete materials N_{stu} .

3.4. The Design of Concrete Slab for Corrugated Web Beams

The effective length of concrete slab and number of shear connectors have been calculated for OGK_330 corrugated web beams according to EC4, BS-5950 Part-3, Section 3-1.

$$b_{eff=} \frac{l_0}{4} = \frac{470cm}{4} = 117{,}5cm \tag{23}$$

$$R_S = 0{,}95 f_y A_a \tag{24}$$

In these equations, b_{eff} is effective length of concrete slab and l_0 is span of beam.

$$R_C = 0{,}45 f_{cu} b_{eff} h_c \tag{25}$$

In the equation 25, R_c is compressive force of concrete, h_c the depth of the concrete slab, A_a is section area of steel, h height of steel section, h_p the depth of concrete slab at tab of the deck. If plastic neutral axis is on the upper flange of steel section, moment is defined as;

$$M_{pl,Rd} = R_S \frac{h}{2} + R_C \left(\frac{h_c}{2} + h_p\right) \tag{26}$$

The calculation of shear connectors for composite corrugated web beams has been defined in equations 41, 42 and 43. In these equations, f_u maximum tensile stress of steel shear connectors, h the height of shear connectors, d the diameter of shear connectors, γ_v safety factor, and α is constant.

$$P_{Rd} = 0{,}29 \alpha d^2 \frac{\sqrt{f_{ck} E_c}}{\gamma_v} \tag{27}$$

$$P_{Rd} = 0{,}8 f_u \frac{\pi d^2}{4\gamma_v} \tag{28}$$

$$\alpha = 0{,}2 \left(\frac{h}{d} + 1\right) \leq 1 \rightarrow \tag{29}$$

The depth of concrete slab (h_c) and forces (R_s, R_c and $M_{pl,Rd}$) are calculated for OGK_330 corrugated web beam under point loading.

R_s=0,95x355x16x160=863,36 kN

∑Y=0 ; R_s=R_c=0,45x20x1175xh_c ; h_c<=81,64 mm ;h_c=8cm.

$$R_c=0,45x20x1175x80=846 \text{ kN}$$

$$M_{pl,Rd}=863,36x173+846x70=208,58kNm=21,262 \text{ tm}$$

4. Design Example

Optimum design algorithms presented are used to design a corrugated steel web beam (OGK_330) with 5-m span shown in Fig. 3. The beam is subjected to point loading. The upper flange of the beam is laterally supported by the floor system that it supports. The maximum displacement is limited to 17 mm. The modulus of elasticity is 205 kN/mm^2.

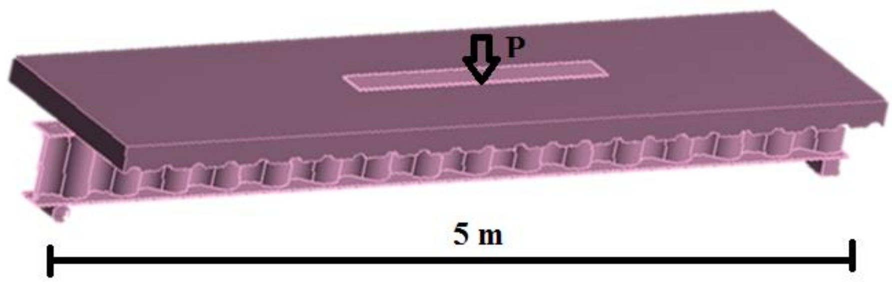

Fig. 3. Loading of 5-m span Corrugated Web beam

The design example is solved by hunting search algorithm (HSA). The maximum number of generations is taken as 5000 (Table 1).

Table 1. The Parameters of HAS and FFO Techniques

Technique	The values of parameters
HSA	$HGS=90$ $MML=0.002$ $HGCR=0.90$ $Ra_{max}=0.01$, $Ra_{min}=0$ $par=0.45$ $\alpha=0.9$, $\beta=0.02$, $IE=25$, $N_{cyc}=50000$

The result of the sensitivity analysis carried out for the HSA parameters is given in Table 2. In steel construction applications, the web part of beam usually carries the compressive stress and transmits shear in the beam while the flanges support the applied external loads. By using greater part of the material for the flanges and thinner web, materials saving could be achieved without weakening the load-carrying capability of the beam. In this case, the compressive stress in the web has exceeded the critical point prior to the occurrence of yielding, the flat web loses its stability and deforms transversely.

Table 2. Optimum Design of Corrugated Beam with 5-m Span

Optimum Section	Conrete Part			Steel Part					Minimum Weight (kg)
	h_c (mm)	b_{eff} (mm)	s_n	t_w (mm)	h(mm)	t_f (mm)	H_c (mm)	L_c (mm)	
OGK_330	80	1175	44	5	330	9	43	155	1317.38

The optimum corrugated web beam should be produced such that it should have 5 mm web thickness 330 mm web height, 9 mm flange thickness and 160 mm flange width for steel part and 80 mm slab depth, 1175 mm effective length of slab, 44 shear connectors for concrete part. HSA produces 1317.38 kg weight for composite corrugated web beam OGK_330. The dimensions of OGK_330 and OGK_500 beam are also given in Table 2. The maximum value of the strength ratio is 0.98 which is almost upper bound. This reveals the fact that the strength constraints are dominant in the problem. The design history curve for HSA techniques is shown in Fig. 4. It is apparent from the figure that HSA method performs good convergence rate and acceptable solution in this design problem.

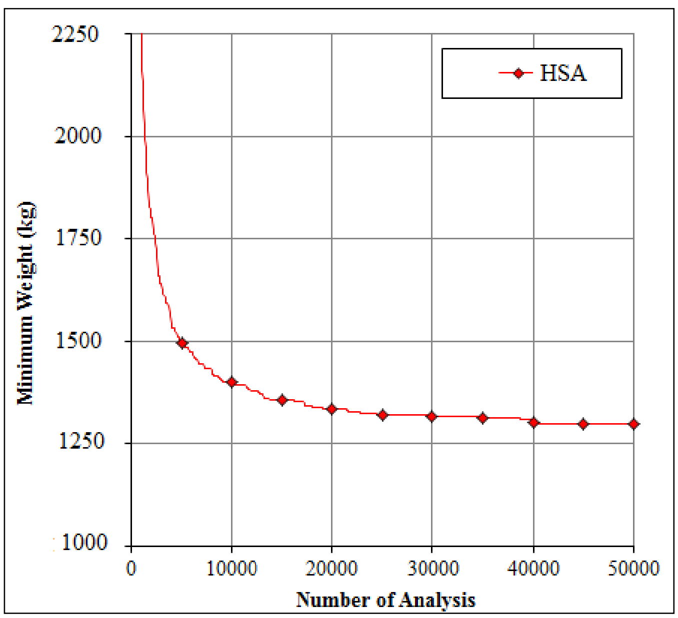

Fig. 4. Design History Graphic of 5-m Corrugated Web Beam

5. Conclusion

This study concerns with the application of a hunting search algorithm to demonstrate the robustness of the proposed algorithm and to find the optimum design of composite corrugated web beams. The design algorithm is mathematically simple but effective in finding the solutions of optimization problems. Fly-back mechanism is employed for handling the problem constraints and feasible ones being candidate solutions to give the minimum weight are determined. A composite corrugated web beam example is designed to illustrate the efficiency of the algorithm. In the optimization process, besides the thickness of concrete slab and studs, web height and thickness, distance between the peaks of the two curves, the width and thickness of flange are considered as design variables. The optimum design attained by HSA method clearly shows that the proposed method give good solution. In view of the results obtained, it can be concluded that the HAS method is an efficient and robust technique that can successfully be used in optimum design of corrugated web beams.

Acknowledgment

This paper is partially based on research supported by the Scientific Research Council of Turkey (TUBITAK Research Grant No: 213M656) which is gratefully acknowledged.

References

[1] Elgaaly M, Hamilton RW ve Seshadri A, Shear Strength of Beams with Corrugated Webs, Journal of Structural Engineering (ASCE), 122, 4, 390-398, 1996.
[2] Elgaaly M, Hamilton RW and Seshadri A, Bending Strength of Steel Beams with Corrugated Webs, Journal of Structural Engineering (ASCE), 123, 6, 772-782, 1997.
[3] Johnson RP ve Cafolla J, Local Flange Buckling in Plate Girders with Corrugated Webs, Structures and Buildings (ICE), 123, 148-156, 1998.
[4] Li Y, Zhang W, Zhou Q, Qi X ve Widera GEO, Development and Research on H-beams with Wholly Corrugated Webs, Journal of Materials Processing Technology, 101, 1-3, 115-118, 2000.
[5] Pasternak H ve Kubieniec G, Plate Girders with Corrugated Webs, Journal of Civil Engineering and Management, 16, 2, 166-171, 2010.
[6] British Standards, BS 5950, Structural Use of Steelworks in Building, Part 1. Code of Practice for Design in Simple and Continuous construction, hot rolled sections, British Standard Institution, London, U.K., 2000.
[7] DIN V ENV 1993-1-1, EUROCODE 3: Design of Steel Structures; Part 1- General Rules and rules for buildings.
[8] DIN 18 800 Teil1-3, Stahbauten; Bemessung und Konstruktion.
[9] British Standards, BS 8110, Structural Use of Concrete, Part 1. Code of Practice for Design and Construction, British Standard Institution, London, U.K.
[10] Steelwork design Guide to BS 5950: Part 1, Section Properties, Member Capacities, Vol.1, 4th edition, The Steel Construction Institute, U.K., 1990.

[11] F. Erdal, O. Tunca, S. Taş, (2016) "Experimental tests of optimally designed steel corrugated beams", 2nd international conference on new advances in civil engineering *(ICNACE 2016), Zagreb,Crotia.*
[12] Kirkpatrick, S., Gerlatt, C. D., Vecchi, M. P., Optimization by Simulated Annealing, Science, 220, 671-680, (1983).
[13] Rechenberg I. Cybernetic solution path of an experimental problem. Royal aircraft establishment, library translation no. 1122. UK: Farnborough, Hants;1965.
[14] Perez, R. E., Behdinan, K., Particle Swarm Approach for Structural Design Optimization, Computers and Structures, 85 (19-20), 1579-1588, 2007.
[15] Glover F. Tabu search-part I. ORSA J Comput, 1(3):190–206, 1989.
[16] Dorigo M, Stutzle T. Ant colony optimization a Bradford book. USA: Massachusetts Institute of Technology; 2004.
[17] Lee K.S., Geem Z.W., A New Structural Optimization Method Based on the Harmony Search Algorithm, Computers and Structures, 82, 781-798, 2004.
[18] Goldberg D.E., Genetic Algorithms in Search, Optimization and Machine Learning, Addison-Wesley Publishing, 1989.
[19] S. Çarbaş, "Design Optimization of Steel Frames Using Enhanced Firefly Algorithm", Engineering Optimization, Vol.10, 12, pp:2007-2025, 2016.
[20] S. Çarbaş, "Optimum Structural Design of Spatial Steel Frames via Biogeography-Based Optimization", Neural Computing and Applications, Vol. 28, 6, pp: 1525-1539, 2017.
[21] I. Aydogdu, S. Çarbaş, A. Akın, "Effect of Levy Flight on the discrete optimum design of steel skeletal structures using metaheuristics", Steel and Composite Structures, Vol.24, 1,, pp:93-112, 2017.
[22] S. Çarbaş, I. Aydoğdu, M.P. Saka, "A Comparative Study of Three Metaheuristics for Optimum Design of Engineering Structures", The 10th World Congress on Structural and Multidisciplinary Optimization, Orlando, Florida, USA, May 19-24, 2013.
[23] Oftadeh ., Mahjoob MJ, Shariatpanahi M, A novel meta-heuristic optimization algorithm inspired by group hunting of animals: Hunting search, Computers and Mathematics with Applications, 60, 2087-2098, 2010.
[24] X. S. Yang, (2008) Nature-Inspired Metaheuristic Algorithms, Luniver Press, UK.